Development of New Displacement-based Methods for the Computation of Notch Stress Intensities of Sharp V-notches

A Thesis Submitted
in Partial Fulfillment of the Requirements
for the Degree of

DOCTOR OF PHILOSOPHY

by

Mirzaul Karim Hussain
(146103035)

Department of Mechanical Engineering
Indian Institute of Technology Guwahati
Guwahati – 781039, India
February 2022

Department of Mechanical Engineering

Indian Institute of Technology Guwahati

Guwahati – 781039, India

CERTIFICATE

It is certified that the work contained in the thesis titled **"Development of New Displacement-based Methods for the Computation of Notch Stress Intensities of Sharp V-notches"** submitted by **Mirzaul Karim Hussain** to the Indian Institute of Technology Guwahati for the award of the degree of Doctor of Philosophy has been carried out under my supervision in the Department of Mechanical Engineering, Indian Institute of Technology Guwahati. This work has not been submitted elsewhere for the award of any other degree.

4th August 2021

(K. S. R. K. Murthy)
Professor
Department of Mechanical Engineering
Indian Institute of Technology Guwahati
Guwahati – 781039

This thesis is dedicated to my parents for

their endless love, support and

encouragement.

ACKNOWLEDGEMENTS

First of all, I express my gratitude to the Almighty for giving me strength and courage in my journey of completion of this thesis. The journey of a PhD is a difficult and challenging path. I am indebted to a lot of people for helping me complete this voyage. Without their support, I would never have completed this thesis.

I would like to express my sincere gratitude and appreciation to my supervisor, Prof. K. S. R. K. Murthy, for his academic guidance and constant encouragement throughout my PhD. I am also highly grateful to him for the efforts he has put in improving the quality of all my manuscripts as well as the thesis. My discussions with him have been insightful and his inputs had definitely improved my research work.

I would like to offer my sincere thanks to my doctoral committee members, Prof. P. S. Robi, Dr. S. S. Gautam of the Mechanical Engineering Department, and Prof. K. D. Singh of the Civil Engineering Department, for their insightful comments and inputs to my dissertation. Thanks are also due to Prof. D. Chakraborty, one of my supervisors of Master thesis, along with Prof. K. S. R. K. Murthy, for the encouragement and motivation.

I express my sincere gratitude to the present and former Heads of the Department of Mechanical Engineering for providing excellent computational facilities and constant encouragement. I am also grateful to the former and present faculties and staff of the Department of Mechanical Engineering for providing me a conducive environment for pursuing my research work. I also offer my sincere thanks to the present Faculty in Charge of the Strength of Materials laboratory, Dr. Nelson Muthu, and the past Faculty in Charge for providing me all the necessary infrastructure and computational facilities for doing my research work. I also thank Mr. Sanjib Sarma, technical superintendent, for providing an amiable environment and essential help in the Strength of Materials laboratory.

I thank my lab mates and friends: Dr. Sajith, Dr. Gayen, Dr. Debaleena, Mr. Pranjol, Mr. Shiv Shukla, Mr. Ankan, Dr. Ashif, Mr. Sibananda, Dr. Rajendra Soni, Mr. Rasool and other research scholars who helped me by discussing and shearing various issues related to research work and my personal life. I also thank my juniors Yaswanth, Vishnuvardhan Naidu and others for their friendly gesture and help. The presence of my AEC friends Dr.

Dhrubajyoti, Dr. Parag, Mr. Subhra and Dr. Bibhuti here in IIT Guwahati gave me a comfort zone. I also thank my batch mates from Hostel-4, AEC, for their well-wishes, phone calls, texts, visits and moral support.

I would like to give my special thanks to my teammates and friends: Durga Prasad, Dr. Kaushik, Dr. Satyannarayana, Dr. Srinu, Ramesh, Dr. Mallikarjunaredy, Shamik, Sunku, Vaibhav, Krishan, Saurav Chaudhary, Dr. Manash Deka, Dr. Prakash Hazam, Dr. Siddesh, Dr. Sumit, Dr. Sohan Bir, Dr. Sunil, Dr. Anshul, Dr. Soumya, Dr. Manish, Dr. Vivek, Dr. Tejas, Dr. Debarshi Mallick, Dr. Ujjwol, Atchuta Rao, Birjit, Sanjib Mog, Srikanth and all the members of *Weekend cricket group*, *Cricket club IITG*, *Mechanical cricket team*, *Spardha Cricket group* and *Spardha Carrom group* for the beautiful memories during my stay in IIT Guwahati. Engaging in various activities with you has helped me stay fit, physically and mentally, over the years.

I would like to acknowledge the Ministry of Education, Govt. of India, for providing the necessary financial support.

Last but not least, in this precious moment of my life, I would like to express my deep sense of gratitude to my beloved parents, grandparents and family members for their endless love, blessings and encouragement.

4th August 2021
Guwahati

Mirzaul Karim Hussain

LIST OF CONTENTS

ABSTRACT

Brittle fracture assessment of engineering components or structures containing sharp V-notches is an important and evolving research area in the field of notch fracture mechanics. A large number of brittle fracture criteria have been developed based on the notch stress intensity factor (NSIF). Therefore, a great deal of effort has been put forward to develop various analytical, experimental, and numerical methods for determining the NSIFs accurately. In the case of complex configurations with complex boundary conditions, many numerical methods, particularly finite element method (FEM) based methods, have been proposed over the years. Different stress-based, displacement-based and energy-based methods have been proposed in connection with the FEM. Many factors of the FEM and of the V-notches have a serious effect on the accuracy of the computed NSIFs. An important aspect of the finite element analysis of the sharp V-notch problems is the lack of special or singular notch tip elements to model the singularity at the notch tip. As a consequence, the current practice is to use the conventional (mostly the isoparametric quadrilateral element (Q8)) elements at the notch tip as well as in the rest of the analysis domain. Moreover, due to the presence of the rigid body terms in the displacement field, unlike the crack problems, the notch opening displacement (NOD) and notch sliding displacement (NSD) are rarely used for the calculation of the NSIFs. Indeed, due to the presence of these rigid body terms, very few displacement-based methods are currently available for the determination of the NSIFs. In the present investigation, two simple, rugged, and efficient finite element displacement-based methods are proposed, which utilize the NOD and NSD to compute the pure mode I, pure mode II and mixed mode (I/II) NSIFs of two-dimensional sharp V-notched configurations subjected to arbitrary in-plane loading. In the first method, certain special properties of the notch tip Q8 elements are investigated, and as a result, an optimum point on the notch tip element is identified for the first time where the displacements are found to be more accurate. Using the NOD and NSD at this point, the NSIFs are calculated. In the second method, the NSIFs are determined using a collocation method in which the NOD and NSD quantities at the recommended collocation nodes along the notch flanks have been employed such that the formulation neatly bypasses the rigid body displacement terms. Both the methods are used to determine the NSIFs of various pure mode I, pure mode II and mixed mode (I/II) benchmark problems, and the results are compared with the available reference solutions. The results obtained using the present methods show an

excellent agreement with the published results. Further, the variation of the computed NSIFs using both the proposed method with the notch angle is in accordance with the theoretical and previous predictions. Many factors of the NSIF extraction methods, such as varied formulations, field variables sampled, location/areas of the sampling points and number of sampling points, etc., are known to affect the accuracy of the NSIFs. Furthermore, the use of the conventional elements at the notch tip in all of these methods also greatly affects the accuracy of the solution. Considering the impact of the above factors on the accuracy, to date, no comprehensive comparison of the above methods exists. Another aim of the present investigation is to conduct a comparison of the various available stress, displacement, and energy-based methods, including the two proposed displacement-based methods in order to study their performance in terms of accuracy of the computed NSIFs and the number of sampling points considered. By comparing all the methods, conclusions of practical relevance have also been provided.

LIST OF FIGURES

LIST OF TABLES

NOMENCLATURE

Latin characters

a	notch length
A_0, B_0, B_2	parameters related to rigid body motion
A, B	constants related to the finite element displacements of the notch tip elements along the notch flanks
A_n $(n = 1, 2, 3, \ldots)$	Williams' coefficients for mode I
B_n $(n = 1, 3, 4, \ldots)$	Williams' coefficients for mode II
C_1, C_2, C_3, C_2', C_3', C_4	constants associated with notch opening and sliding displacements
C_a, C_b, D_a, D_b	constants related to the strain energy density in Lazzarin et al. (2010) method
c_1, c_2, c_3, c_4	constants related to Airy stress function
D, H	matrices related to both analytical and finite element stresses
E	Young's modulus
e_k^{avg}	average percentage relative error
$e_k^{\text{avg-max}}$	maximum of average percentage relative errors
e_k	percentage relative error in normalized notch stress intensity factor

$e_{\lambda^{I(II)}}$	percentage relative error in mode I and mode II eigenvalues
F_E	compressive point load
F_I, F_{II}	normalized notch stress intensity factors under mode I and mode II
$F_{I(II)}^{\mathrm{Ref}}$	available solutions for the normalized notch stress intensity factors
$F_{I(II)}^{\mathrm{Present}}$	present solutions for the normalized notch stress intensity factors
f_{xx}, f_{yy}, f_{xy}	terms related to mode I stress components
f_0, g_0, g_2	terms related to the rigid body displacements
f_1, g_1	singular terms related to u-displacements
f_1', g_1'	singular terms related to v-displacements
G	shear modulus
g_{xx}, g_{yy}, g_{xy}	terms related to mode II stress components
h	semi-height of notched plate
$I_{1,a}$, $I_{2,a}$, $I_{12,a}$, $I_{1,b}$, $I_{2,b}$, $I_{12,b}$	integrals of angular stress functions used in Treifi and Oyadiji (2013c) method
I_1, I_2	integrals of angular stress functions used in Lazzarin et al. (2010) method
K_I, K_{II}, K_{III}	notch stress intensity factors under mode I, mode II and mode III

K_{Ic}, K_{IIc}, K_{IIIc}	critical values of notch stress intensity factors under mode I, mode II and mode III
L_N	notch tip element size
M_a, N_a, Q_a	constants related to the strain energy density in Treifi and Oyadiji (2013c) method
P_1, P_2, P_3	mode I, mode II and mode III loadings
r, θ	polar coordinate components
R	radius
R_I, R_{II}	residuals in displacements for mode I and mode II
r_{op}	optimum radius
r'_{op}	a nearby point of the optimum radius
r_{opt}	optimum point
t	thickness of the specimens
u, v	displacement field near the notch tip
u_R^I, u_R^{II}	rigid body translation and rotation associated with u
U	column matrix containing finite element displacement
u^{FE}, v^{FE}	finite element displacement field near the notch tip
u_R^I, u_R^{II}, v_R^I	rigid body displacements in Cartesian coordinate system
u_{rc}^I, u_{rc}^{II}, $u_{\theta c}^I$, $u_{\theta c}^{II}$	rigid body displacements in polar coordinate system

u_r, u_θ	displacements near notch tip in radial and circumferential directions
v_R^{II}	rigid body translation and rotation associated with v
w	plate width
W_a, W_b	strain energy densities of the areas used in Treifi and Oyadiji (2013c) method
W_1, W_2	strain energy densities of the areas used in Lazzarin et al. (2010) method

Greek letters

α	parameter related to notch angle
α'	direction of additional line
β	notch inclination angle
ε_{xx}, ε_{yy}, ε_{xy}	strain components near the notch tip in Cartesian coordinate system
ε_{rr}, $\varepsilon_{\theta\theta}$, $\varepsilon_{r\theta}$	strain components near the notch tip in polar coordinate system
ϕ	Airy stress function
γ	notch angle
κ	Kolosov constant
κ', η	material dependent parameters
λ_1^I, λ_1^{II}	eigenvalues for mode I and mode II

λ_1^{I*}, λ_1^{II*}	numerical singular eigenvalues for mode I and mode II obtained using Liu et al. (2008) method
ν	Poisson's ratio
σ_{xx}, σ_{yy}, σ_{xy}	stress components near the notch tip in the Cartesian coordinate system
σ_{rr}, $\sigma_{\theta\theta}$, $\sigma_{r\theta}$	stress components near the notch tip in the polar coordinate system
σ, τ	applied stresses
(ξ, ζ)	natural coordinate system
$\Delta u_{\alpha'}$, $\Delta u_{\alpha'}^{FE}$	analytical and finite element sliding displacements along α' direction
Δu_{eff}, Δu_{eff}^{FE}	analytical and finite element effective notch sliding displacements
Δv, Δu	analytical notch opening and sliding displacements
Δv^{FE}, Δu^{FE}	finite element notch opening and sliding displacements

Abbreviations

2D	two-dimensional
3PB	three-point bend
ADENT	angled double edge notched plate under uniform tension
ASENT	angled single edge notched plate under uniform tension
BCM	boundary collocation method

BEM	boundary element method
BFM	body force method
CNT	center notched plate under uniform tension
COD	crack opening displacement
CSD	crack sliding displacement
DENT	double edge notched plate under uniform tension
DIC	digital image correlation
ENSD	effective notch sliding displacement
EPFM	elastic plastic fracture mechanics
EPNFM	elastic plastic notch fracture mechanics
FE	finite element
FEM	finite element method
FFEM	fractal-like finite element method
FT	fracture toughness
LEFM	linear elastic fracture mechanics
LENFM	linear elastic notch fracture mechanics
LSY	large scale yielding
NE	number of elements
NFM	notch fracture mechanics
NFT	notch fracture toughness
NN	number of nodes

NOD	notch opening displacement
NSD	notch sliding displacement
NSIF	notch stress intensity factor
NTOD	notch tip opening displacement
OCNT	off-central center notched plate under uniform tension
ODENT	off-central double edge notched plate under uniform tension
PMMA	polymethyl methacrylate
PSM	peak stress method
QPE	quarter point element
SCB	semi-circular bend
SCF	stress concentration factor
SDZ	singularity dominated zone
SED	strain energy density
SENS	single edge notched plate under shear
SENT	single edge notched plate under uniform tension
SIF	stress intensity factor
SSY	small scale yielding
SV-BD	sharp V-notched Brazilian disc
XFEM	extended finite element method

Chapter 1

Introduction

1.1 Fracture mechanics – a brief introduction

Engineering components or structures are traditionally designed such that peak operating stresses will be much lower than the design stress of the material. The conventional strength-based design approach assumes that the structure to be designed is free of cracks or flaws, and the design criterion only requires the calculated maximum stress to be less than the relevant strength parameter of the material suitably reduced by a factor of safety.

However, the above approach is insufficient because the structures may have existing defects and flaws such as cracks, dislocations or impurities, etc., or they may have sharp corners, notches, or holes. These defects/notches act as stress raisers or stress concentration zones. Such high-stress concentration zones are prone to crack initiation. Once the structure or component attains a sufficient applied load, depending on the material, they experience brittle fracture failure. Brittle fracture is a catastrophic failure mode with relatively less consumption of energy and occurs very often in brittle (e.g., ceramics), quasi-brittle materials (e.g., high-strength metallic materials due to their low ductility) and ductile materials at low temperatures.

As opposed to ductile fractures, brittle fracture usually occurs at stress levels much lower than the anticipated levels and also occurs much before the expected service life of the component. History has shown that such failures are always led to the great loss of human lives and capital investments. Many historic, catastrophic failures of major structures such as bridges, ships, aircrafts, pipelines, and tanks have happened as a result of flaws in the structures, leading not only to the financial losses but also to the loss of many lives. A few notable historical brittle fracture failures include fracture of the World War II Liberty ships, the fatigue failure of the De Havilland Comet from 1952 to 1953, the explosion of a liquid natural gas storage tank that took place in Cleveland in 1944 (Anderson, 2015; Horn and Wilso, 1977). In 1938, the welded Hasselt Bridge across the Albert Canal in Belgium suddenly collapsed and fell into the water. Further, two bridges, namely Kings Bridge (only one-year-old) in Melbourne, Australia, and Point Pleasant Bridge at Point Pleasant, West Virginia, in the US, collapsed due to brittle fracture, costing many lives (Espion, 2012).

Apart from the above characteristic cases, many disasters involving the failure of pipes, weapons, tanks, ships, railways, and aerospace structures occurred throughout the world (Anderson, 2015). All those failures essentially led to the development of the new subject known as "**Fracture mechanics**" which essentially deals with the fracture of engineering materials due to the presence of the cracks. It has been observed that most of these cracks originated from the stress concentration zones or stress raisers such as notches and corrosion pits, etc.

The first significant work in the development of fracture mechanics was the work of Inglis (1913) which discussed the stress analysis of an elliptical hole in an infinite linear elastic tensile plate and the degeneration of the elliptical hole into a sharp crack. Using this work, Griffith (1920) put forward the use of the energy balance approach to study the fracture phenomenon in the cracked bodies. A breakthrough was achieved by Irwin (1948) to extend the Griffith's approach to metals by including the energy dissipated by local plastic flow. He also developed the concept of the strain energy release rate (Irwin, 1957). Based on the linear elastic analysis of cracked bodies in 2D by Westergaard (1938) and Williams (1957), another turning point in the history of fracture mechanics was put forward by Irwin (1957). He showed that the displacements, strains and stress components near a crack tip could be described by a single parameter known as the stress intensity factor (SIF) which can be related to the strain energy rate. Thus, the SIF K became an important parameter in linear elastic fracture mechanics (LEFM) to deal with the control and prevention of brittle fracture.

Fracture mechanics studies can be classified into two broad divisions - brittle fracture and ductile fracture, depending on the ability of the material to undergo plastic deformation before the fracture. In brittle fracture, the crack grows with little or no plastic deformation of the material ahead of the crack tip. In this type of fracture, the existing crack propagates very rapidly at the critical load, and complete failure of the structure occurs without giving any prior warning. Brittle fracture occurs in the brittle (such as ceramics employed in engineering structures as heat shields) and quasi-brittle materials. Many high-strength metallic materials usually exhibit quasi-brittle behavior due to their low ductility. On the other hand, ductile fracture involves large plastic deformation of the materials at the crack tip, thus always will have some amount of stable crack growth before reaching the unstable state.

1.2 Notch fracture mechanics

It is well known that fracture mechanics is widely used in aerospace, naval, shipbuilding, nuclear, locomotive, armament technology, pressure vessel, and other industries. All these engineering structures contain stress concentration zones or notches. These geometric discontinuities are provided to do certain intended functions. Although these notches are useful, however, they become a potential site for the origin of cracks (Leguillon and Yosibash, 2017; Mohammadi et al., 2017; Razavi et al., 2018; Stojceveski et al., 2018) (Figure 1.1). Fracture mechanics defines a material property known as fracture toughness, which deals with the resistance of the material for a crack to form or extend the tip of the existing crack tip.

An important and evolving branch of fracture mechanics is the *notch fracture mechanics,* which deals with the fracture phenomenon at the notches. This is an extension of the principles of the classical fracture mechanics of cracked bodies to the notched bodies. Indeed, currently, notches have been studied using the notch fracture mechanics principles.

Many of these notches are modelled as the sharp V-notch, rounded or blunt V-notch, U-notch and keyhole type notches, etc. Although perfectly sharp V-notches do not exist in practical cases, blunt V-notches with very small notch tip radii can be considered as a sharp V-notch.

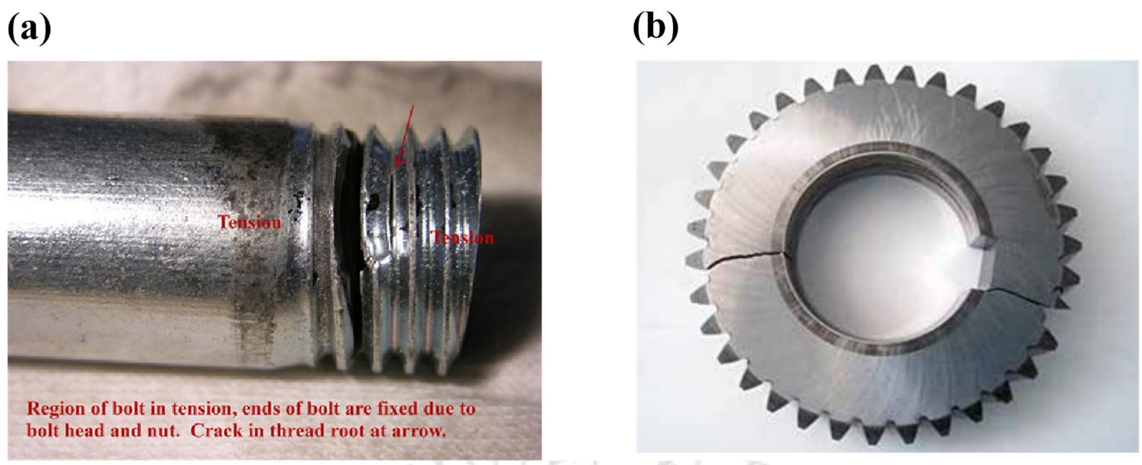

Figure 1.1. (a) Failures bolt thread due to shear stress (Reitz, 2013) and (b) crane gearbox failure (Reed, 2016).

Figure 1.2 shows schematic diagrams of the V-notch and U-notch. Based on the root radius ρ, V-notches are sub-divided into sharp V-notches and blunt or rounded V-notches, shown in Figures 1.2a and 1.2b, respectively. If ρ (Figure 1.2b) is very small compared to the other geometries of the V-notched component, then it is known as the sharp V-notch; otherwise, it is considered as the blunt V-notch or rounded V-notch. Here, γ is the notch opening angle of the V-notches, ρ is the root radius of the blunt V-notch, and r_u is the radius of the U-notch.

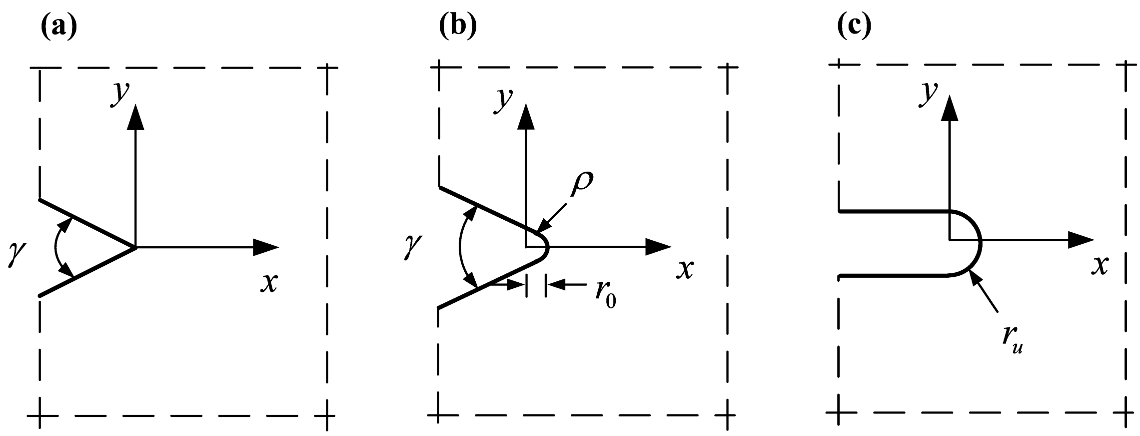

Figure 1.2. (a) Sharp V-notch, (b) blunt V-notch and (c) U-notch.

Of the various shapes of the notches that appear, the sharp V-notch (Figure 1.2a) is the most severe notch and received considerable attention due to the high-stress gradients at the tip of this notch. As a consequence, the V-notched bodies are more prone to brittle fracture. In fact, V- notches do present in many machine components, such as root of the gears, threads of screws and bolts, etc., to serve certain intended functions (Figure 1.3). On the other hand, V-notches also appear due to the nature of some manufacturing methods (Tomari et al., 1990; Dunn et al., 1997b; Rezaee and Adnan, 2018). Further, welds are usually modelled as the V-notches, and the fracture mechanics of the sharp V-notches are also considered in the assessment of static and fatigue strengths of the welds (Verreman and Nie, 1996; Lazzarin and Tovo, 1998; Lazzarin and Livieri, 2001).

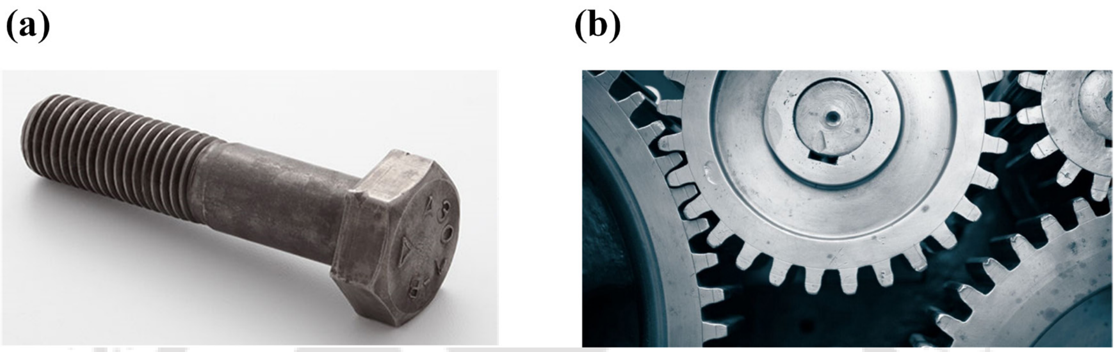

Figure 1.3. Examples of V-notches (a) bolt and (b) gear.

Defects or flaws in many situations in an engineering component do not exactly resemble theoretical cracks. However, treating these defects or notches as sharp cracks will provide excessively conservative solutions and is not desirable in today's design of engineering components. Therefore, for conservative results, these defects or notches are usually modeled as sharp V-notches. It is also evident that a crack is a special case of the sharp V-notch with the notch angle $\gamma = 0°$. Therefore, developing new methods and/or extending existing methods of computing fracture parameters of a crack to compute general fracture parameters of a notch is of high relevance. This would allow interested designers and analysts to compute fracture parameters of any general case of stress intensity, including the cracks (Treifi, 2012).

Due to the high-stress concentration at the notches, cracks originate from these notches. The nucleated crack thus propagates rapidly or slowly depending on the brittleness or ductility of the materials under the operational loads and finally leads to fracture failure. Therefore, it is of great interest to know the critical loads at which the crack initiation from a notch takes place. The theories that predict the critical loads are known as brittle fracture criteria of the notches. It should be noted here that the conventional fracture mechanics deals only after the crack has taken birth and reaches to a detectable crack size and does not pay attention towards the conditions for the crack initiation from the notches. In recent years, the *notch fracture mechanics* principles have been utilized to provide an answer to the above issue.

The notch fracture mechanics starts with the pioneering work of Williams (1952). He is the first to provide stress analysis of the sharp V-notched two-dimensional (2D) body subjected to arbitrary in-plane loading. Later it was extended to the three-dimensional (3D) body by Hartranft and Sih (1968, 1969). Williams (1952) examined the asymptotic stress fields in the vicinity of the sharp V-notch for different boundary conditions (free-free, clamped-free, clamped-clamped) and concluded that under all three loading conditions, the stresses at the notch tip become infinite. However, the strength of the singularity depends only on the notch angle.

1.3 Various fracture parameters of sharp V-notches

Fracture mechanics can be broadly analyzed in two categories, viz. linear elastic fracture mechanics (LEFM) and elastic plastic fracture mechanics (EPFM). In a similar way, the notch fracture mechanics analysis can also be studied by means of the principles of the linear elastic notch fracture mechanics (LENFM) and the elastic-plastic notch fracture mechanics (EPNFM). The use of LENFM is valid under *small scale yielding* (SSY) conditions. In SSY conditions, the plastic zones at the notch tip are sufficiently small compared to the notch length and other relevant geometry parameters. The stress-strain behavior and load-displacement behavior are linear in the LENFM. The size of the plastic zone is small at the notch tip in LENFM; therefore, the effects of the plastic deformations of the notched component during the crack initiation are normally ignored. Thus, the fracture criteria based on the LENFM are applicable for the control and prevention of brittle fractures.

Many of the engineering applications based on the notch fracture mechanics approach are primarily on brittle fracture, which involves brittle materials and high strength materials with low fracture toughness. On the other hand, EPNFM is based on the concept of *large scale yielding* (LSY) conditions. This approach is mainly useful for ductile rupture where the plastic zone size is comparable to the notch length and other geometry parameters.

Because of the presence of more plastic deformation, the specimens under LSY conditions will require more amount of energy for the crack initiation from the notch tip compared to the specimens under SSY conditions.

Depending on whether LENFM or EPNFM is employed, various fracture parameters of the sharp V-notch are the energy release rate, notch stress intensity factor (NSIF), notch tip opening displacement (NTOD), and $J-$integral. The energy release rate and NSIF are used in the LENFM analysis. The NSIF is more popular and widely employed in the LENFM than the energy release rate. On the other hand, the $J-$integral and NTOD are useful in the EPNFM studies. Clearly, these parameters are direct extensions of the crack problems to the notch problems.

1.4 Notch stress intensity factor (NSIF)

Notch stress intensity factor (NSIF) K (sometimes it also written as K^V where the superscript V stands for the V-notch) is the most important notch fracture mechanics parameter of the sharp V-notches in the LENFM. It is a grouped parameter similar to the stress intensity factor (SIF) used for cracked specimens under SSY conditions. The NSIF is a function of the geometry of the V-notched specimen (i.e., notch opening angle, notch length, width, and height of the specimen) and boundary conditions. The stress distribution around the notch tip is generally more complicated than that of a crack. As stated earlier, Williams (1952) was the first to investigate the analytical form of singularities resulting at a notch tip under general in-plane loading. He showed that the stresses in a homogeneous notched body become infinite at the notch tip under any boundary conditions.

Williams (1952) suggests that the singular stress field exists at the tip of the sharp V-notch in the form $\sigma_{ij} = Kr^{\lambda_1 - 1} f_{ij}\left(\theta\right)$ where f_{ij} are angular functions, $\lambda_1 - 1$ is the order of singularity, and K is the NSIF. In the LENFM, K completely characterizes the singular state of the stress field near the notch tip, similar to the case of crack problems. Many important phenomena of fracture of specimens with the sharp V-notches that fall within the scope of the LENFM can be explained with the help of the NSIF approach.

As explained earlier, due to the high-stress gradients at the tip of the V-notch, crack initiation may occur at the notch tip. If the material is brittle or quasi-brittle like high-strength metals, then the crack propagates at high speed, and fracture would occur instantaneously. There is a difference between ductile and brittle materials in the mechanisms of crack initiation and propagation from a notch tip. In the case of brittle materials, the birth of the crack from the notch tip consumes a great portion of the total energy of fracture and consumes very less amount of energy for propagation. On the other hand, as ductile materials exhibit a large amount of plastic deformation around the notches, both crack initiation and propagation consume a significant amount of energy during the ductile fracture (Torabi, 2012). To avoid crack initiation from the borders of notches or stress concentration regions in engineering components, recently, a notch fracture mechanics parameter known as the *notch fracture toughness* (NFT) or *apparent toughnes*s is found to be of great help (Torabi, 2012). The NFT can be determined experimentally and is the material property like fracture toughness (FT) in the classical fracture mechanics. Fracture toughness is the critical SIF of a crack, where propagation of the crack suddenly becomes rapid and unlimited. The FT describes the propagation of a crack from an existing tip of a crack, while the NFT means the resistance of a notch against initiating crack(s) from its tip. Similar to crack problem, NFT is the critical NSIF of a sharp notch, where sudden nucleation and propagation of the cracks take place from the notch tip. The NFT is found useful in providing the solution to the critical loads at which cracks could originate from the notches using the NSIFs. Excellent experimental verifications have been reported to treat the NFT as a material property for a particular notch angle.

Several failure criteria have been proposed for brittle fracture in sharp V-notched components (i.e., a crack onset at a notch) mostly under the pure mode I loading conditions. Amongst, theories based on the NSIF have become very popular. For example, the mean stress criterion suggested by Seweryn (1994), the critical notch stress intensity factor approach by Dunn et al. (1997b), the strain energy density approach by Lazzarin and Zambardi (2001), cohesive zone model approach by Gomez and Elices (2003), $J-$integral based approach by Liviery (2003), strain energy release rate approach by Leguillon and Yosibash (2003) and the point stress and mean stress approaches by Ayatollahi and Torabi (2010). All these approaches present the failure criterion specifically for the mode I loading in the form $K_I = K_{Ic}$, similar to that of the crack problems. Here K_I and K_{Ic} are the mode

I NSIF and critical value of K_I or the NFT, respectively. An important difference between the FT and NFT is that the NFT defined as above depends on the notch angle γ, due to the reason that the NSIF also depends on the same. There are also various criteria available based on the NSIFs for the mixed mode loading (Ayatollahi et al., 2011b).

It is now commonly admitted that the NSIF is the relevant parameter to define a crack onset criterion at a notch tip. Thus, the NSIF approach could be employed for the determination of the safe operating loads without cracks being initiated at the notch tip of the notched components. It is thus, clear that the knowledge of accurate values of the NSIFs of a notched configuration is the chief requirement for successful application of the above criteria in practical applications. Due to its direct practical relevance, a large number of various methods for the accurate determination of the NSIFs under general loading conditions have been developed in recent years, and it is an ongoing and active research field of the fracture mechanics.

1.5 NSIFs for deferent modes of loading

The NSIF (K) is represented according to the mode of loading. As shown in Figure 1.4, the three general cases of load application of a notched configuration are

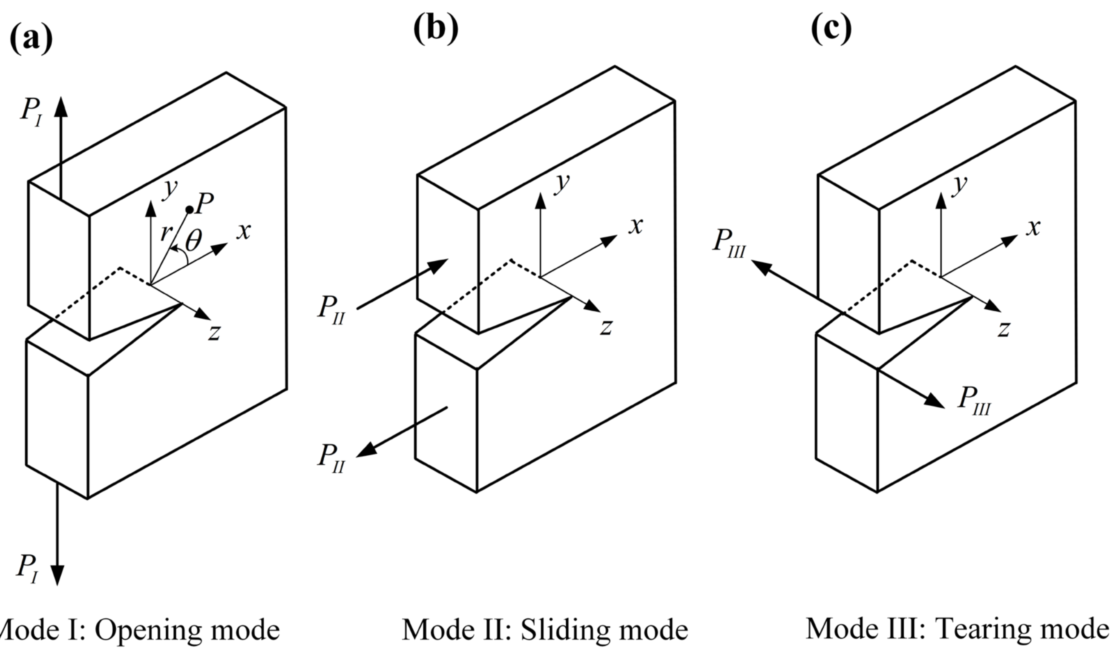

Figure 1.4. Three different modes of loading of a notch.

a) Opening mode or mode I
b) Sliding mode or mode II
c) Tearing mode or mode III

Referring to Figure 1.4, in the mode I loading, the principal load is applied normally to the notch bisector plane and tends to open the notch. Mode II corresponds to the sliding loading and tends to slide one notch flank with respect to the other. The displacement of the notch surface is perpendicular to the leading edge of the notch. Mode III refers to the out-of-plane shearing mode.

A notched body can be loaded in any one of the above three modes or a combination of two or three modes and thus leads to the mixed mode problems. The NSIFs correspond to the mode I, mode II and mode III loading cases are designated as K_I, K_{II} and K_{III}, respectively. Referring to the notch-tip local coordinate system in Figure 1.4, the stress field ahead of a notch tip for the case of linear elastic, isotropic materials under mode I, mode II and mode III loading conditions can be written as

$$\begin{aligned}\sigma_{ij}^{(I)} &= \frac{K_I}{\sqrt{2\pi r^{1-\lambda_1^{I}}}} f_{ij}^{(I)}(\theta)\\ \sigma_{ij}^{(II)} &= \frac{K_{II}}{\sqrt{2\pi r^{1-\lambda_1^{II}}}} f_{ij}^{(II)}(\theta)\\ \sigma_{ij}^{(III)} &= \frac{K_{III}}{\sqrt{2\pi r^{1-\lambda_1^{III}}}} f_{ij}^{(III)}(\theta)\end{aligned} \tag{1.1}$$

where r and θ are the polar coordinates of a point, as shown in Figure 1.4, and f_{ij} are angular functions that only depend on θ and loading mode.

In mixed mode problems (i.e., when more than one loading modes are present), the individual contributions of the stress components are additive, i.e.,

$$\sigma_{ij}^{(total)} = \sigma_{ij}^{(I)} + \sigma_{ij}^{(II)} + \sigma_{ij}^{(III)} \tag{1.2}$$

Thus, in the case of mixed mode (I/II/III) loading, one needs to know the values of K_I, K_{II} and K_{III} for the complete description of the notch tip conditions. This single parameter description of notch tip conditions turned out to be one of the most important concepts in the notch fracture mechanics. If K is accurately known, it is possible to determine all components of the stress, strain, and displacements ahead of a notch tip as a function of r and θ.

The general form of the NSIF is given by (Berto et al., 2012)

$$K = \sigma_{\infty} \sqrt{\pi} a^{1-\lambda_1} \cdot f\left(a/w\right) \tag{1.3}$$

where $f\left(a/w\right)$ is a non-dimensional parameter that depends on the overall geometry of the specimen and σ_{∞} is the remotely applied load. A crack will nucleate from the tip of a sharp V-notch only if (Seweryn, 1994)

$$K > K_c \tag{1.4}$$

where K_c is critical values of the NSIF.

1.6 Various methods for the determination of NSIFs

The NSIFs are found to play a vital role in the application of the LENFM principles to practical problems for analysis and reliable design of the notched configurations. Therefore, accurate estimation of the NSIF is very important for the successful application of the above principles to real-life components. The NSIF can be determined using various analytical, experimental, and numerical methods. Amongst, numerical methods such as the finite element method (FEM) have attracted much attention to determine the NSIFs of complex configurations.

1.6.1 Analytical methods

Analytical methods for determining the NSIFs are very limited in the literature. These methods are most suitable for the idealized geometries, loading, and boundary conditions. Researchers have tried to derive the NSIFs of notch problems from the existing solutions of the SIFs of cracked bodies or stress concentration factors of the notched bodies. However, they are limited to relatively simpler geometries of very idealized material behavior under simple boundary conditions.

1.6.2 Experimental methods

Experimental methods provide new alternatives and opportunities for solving notch fracture mechanics problems. Several experimental methods have been developed for the measurements of the NSIFs of the sharp V-notched configurations. Some of the widely used experimental methods are caustics, photoelasticity, strain gauge method, digital image correlation method, etc.

1.6.3 Numerical methods

Numerical methods are extremely useful for the determination of the NSIFs of complex configurations with complex boundary conditions. Finite element (FE) and boundary element methods (BEM) are widely used for the numerical estimation of the NSIFs of various notched configurations. The use of numerical methods, particularly FEM, has vastly broadened the range of problems that can be solved by computational approaches. A major advantage is that engineers/researchers can easily calculate the NSIFs at their desks, using personal computers and a large number of commercially available FE codes.

In the last few years, there has been a growing interest in the development of new methods to work with the conventional finite element procedures. The NSIFs can be estimated using either displacement-based, stress-based or energy-based methods, etc. Although SIF and NSIF have many similarities, nevertheless there is a remarkable difference in the estimation of these quantities using the conventional FEM. In case of the crack problems, the crack tip singularity is usually modelled using the quarter-point elements (QPEs) (Henshel and Shaw, 1976; Barsoum, 1976), and this element is commonly available in all commercial software. As far as the notch problem is concerned, due to the variability of the notch singularity, to the best of the author's knowledge, no special notch tip or singular elements are formulated till date under mixed mode (I/II) loading. The current practice is the use of conventional elements at the notch tips for the computation of the field variables. These field variables are finally employed by various post-processing methods to compute the NSIFs.

1.7 Motivation

The following issues and problems while computing the accurate NSIFs of the sharp V-notched configurations using the conventional FE method are the motivating factors of the present investigation.

1. Development of brittle fracture criteria of various types of notches, specifically the sharp V-notch is an important and ongoing research area in the notch fracture mechanics. This is because, sharp V-notches occur in many engineering components, and some classes of defects can also be treated successfully and conservatively with the help of sharp V-notches. A large number of fracture criteria admitted that the NSIF of the V-notch is an extremely useful parameter in the formulation of the failure criteria. As a consequence, the determination of the accurate NSIFs has gained importance in recent years, especially using the conventional finite element methods. Therefore, development of new methods for the accurate computation of the NSIFs is highly desirable as many factors of the sharp V-notches have a great influence on the performance of the NSIF extraction methods.

2. One striking feature of the FE notch analyses is the lack of special notch tip elements or singular elements for use at the notch tip to model the variable singularity under mixed mode loading. In contrast, powerful QPEs are available in the case of crack problems where the strength of the singularity remains the same in all problems. Despite knowing the fact that the notch tips are the strong singular regions, the current practice is to use the conventional elements (mostly isoparametric quadrilateral elements (Q8)) at the notch tip in the V-notch FE analyses. At the notch tip, these elements are collapsed to the triangular elements to form a spider-web pattern. Since no singular elements like that of QPEs are available for the notch problems, it is of great advantage in the field of the notch fracture mechanics to investigate whether or not any special and useful properties (specifically in the displacement fields) exhibited by the Q8 elements when they are attached to the sharp V-notch tips. It is also important to the field of the notch fracture mechanics to develop a

NSIF extraction method based on these special properties in the displacement fields of the Q8 elements.

3. It is well-known that the displacement components are more accurate than the stress components in the conventional FE analysis (displacement-based). Moreover, experience in the crack problems strongly suggests that the FE displacements along the notch flanks are more accurate and valuable in the extraction of the NSIFs than at the other regions around the notch tip. These two aspects are very well documented and implemented in the crack problems and gained excellent benefits from the use of these aspects. Despite these facts, only very limited number of methods are currently available (Ayatollahi and Nejati, 2011a) that use the displacement components on a circular arc/boundary of a body for the evaluation of the NSIFs. Experience from the crack problems and the above discussion clearly motivates to develop methods based on the displacements sampled at the notch flanks is very important in the field of the sharp V-notches.

4. One of the important aspects of the V-notch problems that strongly differ from the crack problems is the presence of the rigid body displacement terms in the displacement field of the notches. Experience shows that neglecting these terms from the displacement series led to highly erroneous values of the NSIFs. Moreover, these rigid body terms make the displacement components less tractable in making simple formulations for the accurate estimation of the NSIFs. In other words, they introduce many complications while formulating post-processing methods with the displacement fields. In view of the benefits of using the displacement components (as stated above) and inseparable presence of the rigid body displacement terms therein, there is a need to develop displacement-based methods that neatly bypass these rigid body terms (rather than neglecting them) for the very accurate computation of the NSIFs of the sharp V-notched configurations.

5. Collocation (i.e., solving overdeterministic system of equations using the least-squares and boundary conditions) is a well-recognized numerical estimation of the SIFs of crack problems. It is mostly applied along the boundaries of the cracked configurations. In view of its excellent efficacy in the extraction of the SIFs and benefits of the notch flank displacements, it is important to develop a displacement-based method for accurate determination of the NSIFs that combines the benefits of the collocation method and the notch flank displacements.

6. As mentioned earlier, many conventional finite element based post-processing methods have been developed for the computation of the NSIFs. These methods have different formulations, different field variables to be sampled, locations/areas of the sampling points and the number of sampling points, etc. Till date, no comprehensive comparison among these published methods is available. Such comparison provides better insight in the strengths and, possibly more important, the weaknesses of the various methods. Taking into the account the direct practical relevance of the various post-processing methods for the determination of the NSIF, a comprehensive numerical comparison study among the published works on stress, displacement and energy-based methods is extremely important to the field of the notch fracture mechanics.

Based on the above motivating factors, objectives of the present investigation have been laid as presented in Chapter 2.

1.8 Outline of the thesis

The present thesis is divided into seven chapters. ***Chapter 1*** (present chapter) describes the fracture mechanics in brief and presents notch fracture mechanics succinctly. The significance and need of accurate determination of the NSIF are also discussed in this chapter. Further, the motivation behind the present study is also presented in this chapter.

Chapter 2 presents a detailed literature review of various methods that have been developed and used to determine the mixed mode (I/II) NSIFs of 2D sharp V-notched configurations under various loading conditions. The importance of the NSIFs as a brittle fracture criterion is also discussed in this chapter. Finally, the summary of the literature review, research gaps, and the objectives of the present investigation have been presented in this chapter.

The necessary theoretical background needed for understanding and implementation of the present work is presented in ***Chapter 3***. The closed-form expressions of the stress, strain, and displacement components around a notch tip are also provided in this chapter. A brief theory on the collocation method, the Muller's method, and finite element formulation for modeling notched bodies are also presented here.

Chapter 4 proposes a *"point substitution method"* for the determination of pure mode I, pure mode II and mixed mode (I/II) NSIFs of the sharp V-notched configurations. This chapter presents the theoretical formulation of the proposed method. Numerical results and discussion related to the validations of the proposed method are also presented here. The results of the various benchmark example problems in pure mode I, pure mode II and mixed mode (I/II) NSIFs have been presented in this chapter.

Another displacement-based method, a *"collocation method"* proposed in the present work is presented in ***Chapter 5***. The theoretical formulations and the validations of the proposed *collocation method* have been described in this chapter. The proposed method is used to calculate the mode I, mode II and mixed mode (I/II) NSIFs of various specimens with the sharp V-notches.

In ***Chapter 6***, various FE based methods are compared along with the proposed two methods (in ***Chapters 4*** and ***5***) on a common set of problems and on the common FE meshes to study their efficacy in terms of accuracy of the computed NSIFs.

In ***Chapter*** *7*, the summary of the present work and important conclusions drawn from the present investigation are discussed. Future directions in this field are also listed in this chapter. The contributions and limitations of the present work are also discussed here.

Finally, a list of references has been presented after ***Chapter*** *7*.

Chapter 2

Literature Review

2.1 Introduction

In this chapter, a detailed review of the literature on the application of the NSIFs in studies of the sharp V-notched bodies has been presented. One of the current research directions in the notch fracture mechanics is the assessment of brittle fracture of the notched components. Because of the success of such assessments based on the notch fracture toughness (which is in terms of the NSIF), and due to the widespread use of the NSIF in brittle fracture studies, a great deal of effort has been put forward for the development of various post-processing methods for the accurate estimation of the NSIF. Due to the complex geometry and loading conditions of the engineering components, many numerical methods, specifically finite element-based methods, have been developed over recent years for the accurate determination of the NSIFs. Although several publications have appeared on the development of different methods, however, to the author's best knowledge, no work is reported till date on comprehensive numerical comparison of the published works, which usually have various theoretical backgrounds and computational strategies. Therefore, keeping in view the above-mentioned important factors, the literature review has been broadly categorized under the following headings:

1. NSIFs for the assessment of failure initiation
2. NSIF determination methods
    a. Analytical/semi-analytical methods

   b. Experimental methods
   c. Numerical methods
3. Finite element-based methods
4. Comparison among various NSIF determination FE methods

Based on the exhaustive literature review, a summary of the literature and research gap are presented. Finally, the specific objectives of the present thesis are laid down.

2.2 NSIFs for the assessment of failure initiation

2.2.1 Static loading

The well-known brittle fracture criteria based on the LEFM principles for the crack (where the notch opening angle $\gamma = 0°$) problems were proposed by Griffith (1920) and Irwin (1957). However, their criteria cannot be directly used for other notched problems (where $\gamma \neq 0°$). In an attempt to extend the fracture mechanics of crack problems, many researchers have derived the fracture criteria of the sharp V-notched bodies using the critical values of the NSIFs, as is done by Irwin (1957).

Carpinteri (1987) was first to determine the critical loads of the sharp V-notches experimentally for the different notch angles under the mode I loading conditions using the PPMA specimens. From the averaged critical failure loads obtained from the experiments, he then calculated the critical values of the NSIFs for a wide range of the notch opening angles. Later, Seweryn (1994) proposed a brittle fracture criterion based on the critical values of the NSIFs by conducting experiments on the PMMA notched specimens. According to this criterion, a crack will propagate from a tip of a notch when the actual value of the NSIFs reaches a critical value. In an analogy to the crack problems, Seweryn (1994) suggested that a general brittle fracture criterion for the sharp V-notched bodies can be given as

$$K_{I,II,III} \geq K_{Ic,IIc,IIIc} \tag{2.1}$$

where K_{Ic}, K_{IIc} and K_{IIIc} are the critical values of the NSIFs of the mode I, mode II and mode III loading, respectively. These critical values of the NSIFs K_{Ic}, K_{IIc} and K_{IIIc} depend not only on materials but also on the notch angles. In another research, Seweryn and Mroz (1995) proposed another brittle failure criterion for the notched components under mixed mode (I/II) loading conditions based on the critical values of NSIFs. This criterion can predict the critical loads at the onset of propagation of the crack at the tip of a sharp V-notch undergoing brittle fracture. Further, Seweryn et al. (1997) applied the above brittle fracture criteria to determine the critical loads and the crack deflection angles for a notched body under the mixed mode (I/II) loading conditions. They also conducted experiments using PMMA material, and satisfactory agreement was observed between the experimental and theoretical predictions. Knésl (1991) suggested the stability criterion of the sharp V-notched configurations based on the critical value of the NSIF.

Dunn et al. (1997b) supported the contention that the critical NSIFs can be used to correlate brittle fracture initiation at the sharp V-notches by finding critical NSIF under mode I loading from the critical loads observed in the experiments. For this purpose, the NSIFs were obtained using finite element analysis. To support further their findings, they conducted finite element analyses and concluded that the plastic zone size is smaller than the singularity dominated zone, and hence LENFM conditions are applicable. Further experimental studies were carried out by Dunn et al. (1997a) and Dunn and Suwito (1997) to provide more evidence on using the critical value of the NSIF to correlate the brittle failure. Their data showed that excellent failure correlation is obtained in both the mode I, mode II and mixed mode (I/II) loading conditions using the critical stress intensity.

Minor et al. (2003) investigated the fracture toughness of U-notched circular ring specimens made of high-strength steel using the NSIF and volumetric approach. Ayatollahi and Torabi (2010) and Ayatollahi et al. (2011b) developed various NSIFs based on the maximum tangential stress (MTS) criteria to predict the brittle fracture in rounded and sharp V-notched configurations under mixed mode (I/II) loading conditions. Bahrami et al. (2018) predicted the fracture load, crack initiation angles, and trajectories for the sharp V-notched Brazilian disk (SV-BD) specimens under mixed mode (I/II) conditions utilizing the MTS criterion (Erdogan and Sih, 1963) and mixed mode NSIFs. In a recent publication, Bahrami et al. (2020b) predicted the fracture load of a semi-circular bend specimen under mode I loading conditions using the MTS criterion and NSIFs.

It can be observed that many criteria were developed in the past based on the critical values of the NSIFs for the assessment of brittle fracture of notched components under static loading conditions. The use of NSIFs under fatigue loading conditions will be discussed in the next section.

2.2.2 Fatigue loading

The pioneering work of Griffith (1920) and Irwin (1957) was fulfilled in 1961 when Paris (Paris et al., 1961) developed the fatigue crack growth law in terms of the SIF of the mode I loading. They developed a correlation for the fatigue crack growth rate as a function of the SIF range (ΔK). On the other hand, in 1974, Tanaka (Tanaka, 1974) proposed a modified form of the Paris law for components subjected to the mixed mode (I/II) loading, which is now widely in use for the fatigue life prediction. However, the above-mentioned works were limited to the cracked specimens and not ideal for the notched specimens. Consequently, significant attention has been received among researchers (Boukharouba et al., 1995; Verreman and Nie, 1996; Lazzarin and Tovo, 1998; Atzori et al., 1999; 2001; Lazzarin and Livieri, 2001; Fischer et al., 2016b; Hu et al., 2019) on failure under high cycle fatigue loading conditions of the sharp V-notches based on the critical values of the NSIFs. Boukharouba et al. (1995) proposed two different approaches for the fatigue crack initiation based on the NSIFs. The first one can predict both crack initiation and crack propagation. The second one is more conservative and deals with crack initiation only.

Verreman and Nie (1996) proposed another NSIF based approach for evaluating the crack initiation life at the fillet-weld joints. They did an experimental study on the early development of fatigue cracking along the wavy toe of manual fillet welds between structural steel plates. They showed that the NSIFs of singular stress fields at the V-notched geometries are a promising parameter to rationalize crack initiation live.

Lazzarin and Tovo (1998) presented a stress field approach wherein the NSIFs were used to describe the stress distributions in the neighborhood of the weld toes so as to assess the fatigue strength. They investigated the applicability of the NSIF approach in the fatigue strength assessment of the welded joints not only for zero toe radius but also for non-zero ones. They demonstrated that the NSIF can be used as a fatigue parameter for the life prediction of cyclically loaded welded joints.

In another research, Atzori et al. (1999) used the NSIF to predict the fatigue behavior of mechanical components weekend by the V-shaped reentrant corners. They successfully correlated the mode I NSIFs to the fatigue strength properties of the fillet welded joints. Later, Atzori et al. (2001) developed a new approach for predicting the high cycle fatigue behavior of the welded joints based on the NSIFs of the uncracked geometries.

Lazzarin and Livieri (2001) and Livieri and Lazzarin (2005) modeled the weld toe region as a sharp, zero radius, and V-shaped notch and determined the NSIFs using the asymptotic stress distributions obeying Williams (1952) solution. Lazzarin and Livieri (2001) performed fatigue life assessments on various aluminum welded joints with a thickness ranging from 3 to 24 mm. In their later publication (Livieri and Lazzarin, 2005), they considered welded joints made of steel or aluminium alloy of thickness 3 to 100 mm subjected to tension and bending loads. They predicted the total fatigue life of the welded joints using the values of the mode I NSIFs.

Fischer and his co-workers (Fischer et al., 2011, 2012, 2016a) applied NSIFs as the fatigue assessment of various welded structural components. Fischer et al. (2016b) presented a review of the literature which used the critical values of NSIFs as the fatigue strength parameter of the welded joints. Recently, Hu et al. (2019) investigated fatigue strength assessment of tube-flange welded joints. In their investigation, the mode III NSIF was considered as a fatigue failure parameter of the welded joints.

Most of the above research is on welded joints, as it is said that the welded joints are a practical example of the NSIF's use in fatigue strength prediction. It has been observed that many studies have indicated that the NSIFs can be used in brittle fracture criteria of the sharp V-notched structures under static and fatigue loading conditions. Therefore, a great deal of effort has been put forward to develop various methods for determining the NSIFs accurately. The available methods will be discussed in the next section.

2.3 NSIF determination methods

It has been discussed in the previous section (Section 2.2) that the NSIF plays a vital role in the application of the notch fracture mechanics. Accurate determination of the NSIFs for engineering components containing the sharp V-notches is, therefore, crucial for the prediction of failure and structural integrity assessment of these components. NSIF can be calculated by means of various analytical/semi-analytical, experimental, and numerical methods. Figure 2.1 shows various methods available for the determination of the NSIFs. A detailed review of these methods is described in the following sections.

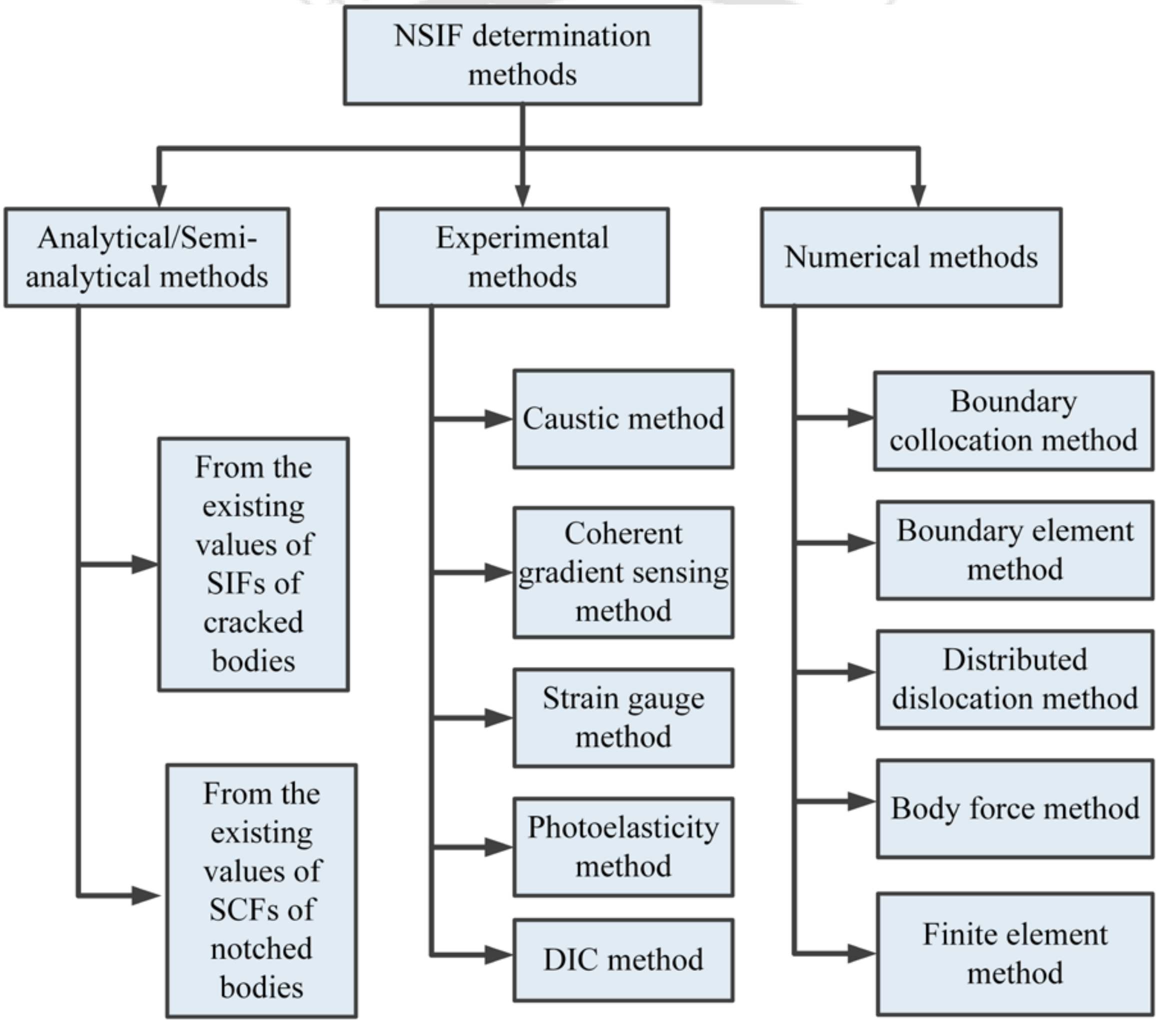

Figure 2.1. Various methods available for the determination of NSIFs.

2.3.1 Analytical/semi-analytical methods

Due to the complex nature of the sharp V-notch problems, only a few analytical/semi-analytical methods are available in the literature for the determination of NSIF. Some researchers (Hasebe and Kutana, 1978; Hart, 1976; Zhao et al., 1988; Zhao and Hahn, 1992; Loua and Barltrop, 2020) attempted to determine the NSIFs of a V-notched problem directly from the existing solutions of other problems, for example, from the stress concentration factor (SCF) of a sharp V-notch (Hasebe and Kutana, 1978) and the SIF of a crack problem (Hart, 1976; Zhao et al., 1988; Zhao and Hahn, 1992), etc. Hasebe and Kutana (1978) showed that the mode I NSIFs of the V-notches with a small tip radius could be determined from the corresponding SCF. These SCF expressions can be obtained either from the experiments or from the handbooks. Alternatively, some researchers (Hart, 1976; Zhao et al., 1988; Zhao and Hahn, 1992) tried to provide a correlation between the values of NSIF of a V-notch to a linear crack for which the SIF solutions are available.

Hart (1976) suggested closed-form expressions for the NSIFs of the V-notches using the SIFs of the crack problems with correction factors to account for the plate width and notch angle. Zhao et al. (1988) determined the NSIFs based on a theoretical analysis and hypothesis (concerning the plate shape and boundary conditions) correlated the SIFs of a linear crack to that of the NSIF of a V-notched plate under various boundary conditions. Their (Hart, 1976; Zhao et al., 1988) results suggested that NSIFs could be obtained from the existing results of a linear crack with some error. However, most of their (Hart, 1976; Zhao et al., 1988) results are confined to the mode I cases only. In another research, Zhao and Hahn (1992) proposed a methodology for determining both the mode I and mode II NSIFs directly from the existing solutions of the crack problems. Using their method, they obtained the NSIFs in mode I and mode II problems. In a recent publication, Loua and Barltrop (2020) proposed a simple methodology to find the NSIFs of the V-notched plates with and without cracks (emanating from the notch) from the available empirical formulae for the finite width cracked plates. Their approach is limited only to the edge cracked/notched configurations.

From the above discussion, it can be seen that the analytical/semi-analytical methods are very limited in the literature. Moreover, they are confined only to the simple mode I problems. Only a few results of the mode II problem are reported. All the results reported are showing some errors. Further, till date, there are no analytical/semi-analytical methods that can determine the mixed mode (I/II) NSIFs of the sharp V-notched configurations. Therefore, many experimental and, more specifically, numerical methods have been developed over the past decades for the accurate estimation of the mixed mode (I/II) NSIFs. A detailed review of the various experimental and numerical methods is discussed in the following sections.

2.3.2 Experimental methods

The experimental methods are indispensable for validating the numerical results and obtaining the NSIFs of complex configurations. Various experimental methods such as caustics (Prassianakis and Theocaris, 1980; Xu et al., 2004; Yazdanmehr and Soltani, 2014), coherent gradient sensing (Yao et al., 2006), strain gauge (Kondo et al., 2001; Kondo et al., 2014; Paul et al., 2018), photoelasticity (Murthy et al., 1983; Murthy and Rao, 1985; Mahinfalah and Zackery, 1995; Ayatollahi and Nejati, 2011b) and digital image correlation (DIC) (Ju, 2010; Dehnavi et al., 2013; Torabi et al., 2019; Bahrami et al., 2020a) have been developed in the past decades to determine the NSIFs of the V-notches.

2.3.2.1 Caustics method

Prassianakis and Theocaris (1980) determined the NSIFs of the sharp V-notched elastic and symmetrically loaded plates using the method of caustics. They developed an experimental solution for the determination of the NSIFs based on the theory of reflected caustics. In another research, Xu et al. (2004) determined the mode I NSIFs of the sharp V-notches of specimens under three-point bending using an optical caustics method. Recently, Yazdanmehr and Soltani (2014) developed another experimental method of caustics to calculate the mixed mode (I/II) NSIFs for the rounded V and U-notches. All the above-mentioned researchers used specimens made of PMMA material in their experiments.

2.3.2.2 Coherent gradient sensing method

Yao et al. (2006) utilized the coherent gradient sensing (CGS) method to calculate the mode I NSIFs of the sharp V-notched three-point bending specimen. They experimentally investigated the local deformation field and fracture characterization under mode I for the different notch angles.

2.3.2.3 Strain gauge method

Another frequently used method in the area of fracture mechanics is strain gauge methods. These methods are gaining importance in the notch fracture mechanics. Strain gauge methods have been utilized in many works (Kondo et al., 2001; 2014; Paul et al., 2018) for the determination of the NSIFs of the sharp V-notches.

Based on the strain gauge method, Kondo et al. (2001) attempted to find the mixed mode NSIF of sharp inclined notch strips made of aluminum alloy 5052 under tension. In another research, Kondo et al. (2014) developed a strain gauge method for the determination of the NSIFs under transverse bending.

In addition to the above works, another strain gauge method was proposed by Paul et al. (2018) to determine the mode I NSIFs of single edge notch specimens under uniform tension. They (Paul et al., 2018) also proposed the optimal locations of the strain gauges to determine accurate values of the NSIFs.

2.3.2.4 Photoelastic method

Photoelasticity was used by Murthy and his co-authors (Murthy et al., 1983; Murthy and Rao, 1985) to determine the mode I NSIFs under bending and tensile loading conditions. Mahinfalah and Zackery (1995) used the photoelasticity and digital image analysis to study the singular stress field at the sharp reentrant corners. They evaluated the mixed mode (I/II) NSIFs of plates made of PSM-1 photoelastic material with 90^{o} reentrant corners.

In another study, Ayatollahi and Nejati (2011b) utilized the photoelastic method to calculate the pure mode I, pure mode II, and mixed mode (I/II) NSIFs of sharp V-notched Brazilian disk (SV-BD) specimen made of PMMA. To minimize the error in the experimental data, they used the overdeterministic least-squares method of Sanford (1980) combined with the Newton-Raphson iterative method.

2.3.2.5 Digital image correlation method

The DIC method has also been used by many researchers in different branches of fracture mechanics. Ju (2010) calculated the NSIFs of the sharp V-notches of isotropic and composite materials using DIC. Recently, this method has been used by Dehnavi et al. (2013), Torabi et al. (2019) and Bahrami et al. (2020a) to determine the NSIFs notched specimens. Dehnavi et al. (2013) and Torabi et al. (2019) developed two different methods for determining the mode I NSIFs using the experimental displacement field near the notch tip region. Later, Bahrami et al. (2020a) extended the works of Torabi et al. (2019) to determine the mixed mode (I/II) NSIFs using the displacement field obtained from the DIC experiments.

2.3.3 Numerical methods

In the case of complex configurations with complex boundary conditions, one has to recourse to the numerical methods such as the boundary collocation method (BCM), body force method (BFM), FE method, boundary element method (BEM), etc. It can be observed that, amongst all available numerical methods, the FE method has been extensively used for the accurate estimation of the NSIFs of complex configurations. All these different methods are reviewed in the following sections.

2.3.3.1 Boundary collocation method

Gross and Mendelson (1972) were the first to compute the NSIFs using the numerical methods. They employed the boundary collocation method (BCM) to determine the NSIFs of various 2D plates having sharp V-notches and subjected to different loading conditions. They determined the NSIFs of single edge notched plate under tensile and in-plane bending loading conditions for various notch depth to width ratios and the notch opening angles. Gross and Mendelson (1972) also estimated the NSIFs of a double cantilever beam under mode I and mode II loading conditions.

Carpenter (1984a) proposed an overdetermined collocation method for determining the NSIFs of V-notched problems. Carpenter (1984a) showed that the use of more than one eigenvector, stresses, and displacements at the collocation points could circumvent many problems that normally can be found with the collocation method. He applied the proposed collocation method to calculate the NSIFs of two test problems with the notch angles 0° and 90°.

Recently, Ayatollahi and Nejati (2011a) determined NSIFs of the sharp V-notches using the BCM. They calculated the unknown coefficients of Williams (1952) expansion by fitting the stresses and displacements to specified boundary conditions at the remote boundaries. They found the NSIFs for single and double edge notched problems under mode I and mixed mode (I/II) loading conditions. They also found the mode II NSIFs for the single edge notched problem for the different notch angles.

2.3.3.2 Boundary element method

The boundary element method (BEM) is another effective numerical approach used to solve engineering problems having cracks and sharp V-notches. Many researchers (Portela et al., 1991; Xu et al., 1999; Cheng et al., 2009; Niu et al., 2009; Barroso et al., 2012; Cheng et al., 2016; Zhang et al., 2018; Han et al., 2019) employed the BEM to determine the NSIFs.

Portela et al. (1991) proposed a boundary element singularity subtraction technique to compute the NSIFs of the V-notched problems. Their method requires extra boundary conditions that they referred to as singularity conditions of the regularization procedure. They provide a simple and efficient method to obtain the mixed mode (I/II) NSIFs.

Xu et al. (1999) determined the multiple stress singularities and the NSIFs of the bi-material notched problems by using the solutions obtained from the BEM. They proposed a new method to find all the orders of the stress singularities at an interface and the NSIFs by the extrapolation method.

Cheng et al. (2009) proposed a new technique for the evaluation of multiple stress singularity orders of a V-notch using the BEM. The asymptotic displacement field around the notch tip region of a sharp V-notch linear elastic material was expressed as a series expansion with respect to the distance from the notch tip. This series was substituted into the boundary integral equation and then transformed into an eigen-equation. Finally, the eigenvalues were obtained by solving the eigen-equation.

Niu et al. (2009) proposed another new BEM to calculate the NSIFs of planar V-notched bodies. In their method, a small circular portion around the notch tip is isolated from the entire component as a free body. Thereafter, stress singularities in the notch tip region are transformed into an eigenvalue problem of ordinary differential equations. The orders of the singularity and the associated eigenvectors of the V-notch were then solved using the interpolating matrix method (Niu, 1993). For the remaining part of the V-notched body, the boundary integral equation is applied to find the displacement and stress fields. Finally, the NSIFs were determined using the stress solutions or stress eigenfunctions.

Barroso et al. (2012) proposed a post-processing procedure for the evaluation of the mixed mode (I/II) NSIFs of multimaterial corners based on the BEM. Based on the simple least-squares fitting using numerical results of the displacements and/or stresses along boundary edges, the NSIFs of the multimaterial corners are determined.

Cheng et al. (2016) determined the thermal mixed mode (I/II) NSIFs of the sharp V-notched bodies by solving the natural boundary integral equations using both the BEM and FEM.

Zhang et al. (2017, 2018) presented a new singular element (expanding element), which can increase the polynomial order of the shape functions by two by considering the virtual nodes. By using the developed element, the NSIFs of sharp V-notches subjected to the mixed-mode (I/II) loading conditions were estimated by Zhang et al. (2018). It is evident that the conventional element cannot model the singularity at the notch tip; therefore, it requires extremely fine meshes at the notch tip for better results. Moreover, the special elements developed for the crack problems (Blandford et al., 1981) will only provide singularity of order -0.5, are not suitable for analyzing the structure with V-shaped notches.

Recently, Han et al. (2019) calculated the NSIFs of sharp V-notches by characteristic analysis coupled with isogeometric BEM. They determined the NSIFs of sigle edge notched specimens under mode I and mixed mode (I/II) loading conditions.

2.3.3.3 Distributed dislocation method

Larrosa et al. (2015) estimated the mode I NSIFs of the sharp V-notches by means of the distributed dislocation method (DDM). In their work, the NSIFs were determined using the strain energy approach (SEA) which was originally developed by Treifi and Oyadiji (2013c). In this method, the stresses at the vicinity of the notch tip were assessed by DDM. Larrosa et al. (2015) showed that the DDM could be applied to model the singular fields accurately for the notch problems. They determined the mode I NSIFs using DDM and observed that good accuracy could be obtained when the ratio of the notch length to width of the plate is less than 0.35. The application of the DDM in the area of notch problems is still very limited and requires further research.

2.3.3.4 Body force method

Apart from the above-mentioned numerical methods, researchers (Chen, 1995; Noda et al., 1996; Noda and Takase, 2003) developed and used the body force method (BFM) to calculate the mixed mode (I/II) NSIFs. Chen (1995) proposed a body force method to find the mixed mode (I/II) NSIFs of a strip plate with single and double edge notches subjected to the tension and in-plane bending loading conditions for varying notch angles, notch inclination angles, and notch length to width ratios. In his analysis, basic density functions of the body force were introduced to characterize the stress singularity at the notch tip.

Noda et al. (1996) determined NSIFs of the sharp V-notches using the BFM for various geometrical and loading conditions. They formulated a system of singular integral equations of the BFM to calculate the mixed mode (I/II) NSIFs of the angular corners. In their investigation, various problems such as parallelogram holes in an infinite plate, angled V-shaped notch in a semi-infinite plate, array of diamond-shaped holes under various loading conditions were analyzed.

In another research, Noda and Takase (2003) determined the NSIFs of sharp V-shaped notches using BFM. In their work, NSIFs K_I, K_{II} and K_{III} for mode I, mode II and mode III, respectively, were determined for a round bar using the BFM. In their approach, the singular integral equations of the BFM were used to calculate the NSIFs of the sharp V-notches.

2.3.3.5 Finite element method

The conventional finite element method has been extensively used for the evaluation of the mixed mode (I/II) NSIFs of the sharp V-notches. Various methods, such as displacement-based, stress-based, energy-based, have been developed over the years for the determination of the NSIFs. Many of these methods that are developed in conjunction with the conventional finite element method are reviewed in the following sections. An important aspect of the finite element-based methods is that all of these methods employ conventional finite elements at the notch tip, unlike crack problems where the quarter-point elements (Barsoum, 1976; Henshel and Shaw, 1976) are usually deployed at the crack tip. Therefore, the accuracy of the NSIFs using a particular method also depends on the suitability of their formulation with the use of conventional elements at the notch tip.

2.4 Finite element-based methods

2.4.1 Path-independent integrals

It is well-known that the stress singular behavior of a sharp notch tip is different from that of the crack tip. Therefore, the conventional concepts of the contour integrals available for crack problems are no longer valid for a sharp V-notch and need to be modified to determine the associated NSIFs. Several path-independent integrals (e.g., $H-$integral, $A-$integral, $J_{kR}-$integral, $M_{1\varepsilon}-$integral, reciprocal work contour integral, etc.) have been proposed for the calculation of the generalized NSIFs at the sharp notches. Sinclair et al. (1984) developed a set of path-independent integrals ($H-$integrals) to calculate the generalized NSIFs at sharp corners. Their work is based on the works of Stern and Soni (1976). Independently, Labossiere and Dunn (1998) presented another procedure to calculate the mixed mode (I/II) NSIFs in anisotropic materials using the path-independent $H-$integral. They obtained the mode I NSIFs of a 70.53° notch silicon beam in flexure and the mixed mode (I/II) NSIFs of a T-structure with 90° notches under tensile loading. Later, Hwu and Kuo (2007) and Hwu and Huang (2012) calculated the mixed mode (I/II) NSIFs of interface notches using the $H-$integral. Carpenter (1984 b, c) applied the reciprocal work contour integral method (RWCIM) of Stern and Soni (1976) to compute the mixed mode (I/II) NSIFs of 90º sharp V-notches. In another research, Kim and Cho (2009) also used the RWCIM to determine the mode I NSIFs of the sharp V-notches.

Atkinson et al. (1988) used a path-independent integral known as $A-$integral to evaluate the singularity state by making use of suitable auxiliary fields of the displacements and stresses obtained from the FE method. They found the NSIFs using the proposed integral for both the static and dynamic cases of a single notch specimen under the mode I loading condition. Chang and Kang (2002) propose a pair of contour integrals $\left(J_{kR}\right)$ to find the NSIFs for notched problems under the mixed mode (I/II) conditions. Later, Chang and Fan (2009) extended the work of Chang and Kang (2002) to the curved notches. They employed these integrals to determine the NSIFs under the mixed mode (I/II) loading conditions of diamond-shaped center-notched specimens and curved notched specimens. Chang and Wu (2003) proposed another path independent integral termed as $M_{1\varepsilon}$ to evaluate the mixed mode (I/II) NSIFs. They found the mode I NSIFs for a double edge notched specimen and the mixed mode (I/II) NSIFs for a diamond-shaped center notch specimen for the various notch angles.

Although the above path independent integrals neatly avoid the problems near the notch tips, however, they are in the general complex to implement. Therefore, apart from these various path-independent integrals, researchers have developed methods to extract the NSIFs directly from the stress field, displacement components, and energy obtained from the standard FE analysis.

2.4.2 Stress-based methods

Ju and Chung (2007) developed a least-square method (LSM) for the evaluation of the NSIFs of the sharp V-notches by minimizing the errors in the stresses at the nodes around the notch tip. They have suggested that higher-order stress terms should be considered for the higher accuracy of the NSIFs. Another simple yet highly efficient stress-based method was developed by Liu et al. (2008). They considered a number of successive nodes along a radial line slightly away from the notch tip in a selected direction to determine the mixed mode (I/II) NSIFs. They evaluated the NSIFs by minimizing the errors in the analytical and FE stresses at the selected nodes along the radial line. Although these LSMs are simple and easy to implement in the existing codes, they require more refined meshes due to the use of the FE stresses instead of the displacement components, which are known to be more accurate.

Meneghetti and Lazzarin (2007) extended the peak stress method (PSM) to determine mode I NSIFs at the tip of sharp V-notches for a wide range of notch opening angles ranging from 0° to 135° using the peak stresses. The PSM is an FE stress-based method used to estimate the NSIFs from the elastic peak stress. Later, this PSM was used by many researchers (Meneghetti, 2012; Meneghetti and Guzzella, 2014; Meneghetti et al., 2018) to estimate the mode I, mode II and mode III NSIFs of 2D and 3D configurations.

2.4.3 Displacement-based methods

It is well-known that the displacement components are more accurate than the stress components in the conventional FEM. To the best of the author's knowledge, the methods based on the displacements are scarcely available. In the work of Ayatollahi and Nejati (2011a), they proposed an overdeterministic method with displacements as the sampling points along a circular arc and verified their results of the mixed mode (I/II) NSIFs with the boundary collocation method using the displacement field along the boundary of the domain. They proposed the method for the computation of the NSIFs and higher-order coefficients of the Williams (1952) series expansion using the FE displacements from the nodes around the notch tip. In their method, by employing the displacements of the nodes falling on a circular contour around the notch tip, an over-determined set of simultaneous linear equations were derived by minimizing the error in the least-squares sense. They also discussed the importance of the rigid body modes of displacements in the accurate determination of the NSIFs. It should be noted that, in contrast to the displacement-based methods, the stress and energy-based methods are free of rigid body displacement components.

2.4.4 Energy-based methods

The idea of using the strain energy to compute the SIFs goes back to the work of Sih (1974) and Sih and Macdonald (1974), who proposed a strain energy density method for cracks.

Later, the strain energy density concept was utilized by many researchers to calculate NSIFs of the sharp (Lazzarin and Zambardi, 2001, Lazzarin et al., 2010; Treifi and Oyadiji, 2013c) and blunt V-notches (Lazzarin and Berto, 2005; Lazzarin and Filippi, 2006). These works established an approach to compute the NSIFs for sharp and rounded notches based on the averaged strain energy density (SED) over a control volume around the notch tip. Lazzarin and Zambardi (2001) determined the NSIFs of isotropic homogeneous notches under the pure mode I loadings. However, Lazzarin and Zambardi (2001) method is extended by Lazzarin et al. (2010) for the computation of the mixed mode (I/II) NSIFs by sampling the field variable on two concentric volumes around the notch tip. Nevertheless, this method (Lazzarin et al., 2010) cannot be used for the crack problems under mixed mode loading conditions.

Recently, Treifi and Oyadiji (2013c) developed an improved strain energy density method to determine the mixed mode (I/II) NSIFs. In their approach, the SED of two semi-circles of the same radius was considered for the calculation of the mixed mode (I/II) NSIFs. Unlike Lazzarin et al. (2010) method, Treifi and Oyadiji (2013c) method can be used for the determination of the mixed mode (I/II) SIFs of a crack problem. Recently, Pittarello et al. (2016) proposed a new method based on the evaluation of the total and deviatoric strain energy density averaged over a control volume to compute the mixed mode NSIFs. Moreover, researches used the strain energy density to calculate the NSIFs of notched plates of orthotropic matrerials (Zappalorto, 2019; Zappalorto and Ricotta, 2019; Zappalorto and Carraro, 2020) and plastic materials (Lazzarin and Zambardi, 2002; Lazzarin and Zappalorto, 2008).

2.4.5 Other numerical methods

Apart from the conventional FEM and BEM methods, researchers also used fractal-like finite element method (FFEM) (Treifi et al. 2008; 2009a; b; 2013a; b), extended finite element method (XFEM) (Yu and Shi, 2012; Yi et al., 2017; 2018) and method of analytical constrain (Seweryn, 2002) for the computation of NSIFs. Treifi et al. (2008) have developed the fractal-like finite element method (FFEM) to analyze the singularity resulting at a notch tip and to determine the NSIF at the notch tip. Treifi et al. (2008; 2009a) used the FFEM to compute the mixed mode (I/II) NSIFs of the sharp notched plates under the in-plane shear, bending, and tensile loading conditions. Treifi et al. (2009b) utilized the FFEM to calculate the NSIFs of double-edge and center V-notched plates under the tension and anti-plane shear loading. Recently, Treifi et al. (2013a) evaluated the mixed mode (I/II) NSIFs for the bi-material notched bodies using the FFEM.

The XFEM is a very effective numerical method for the fracture analysis of crack problems. However, the application of XFEM for the determination of NSIFs of the sharp V-notches is rather limited in the literature. Recently, only a few XFEM based methods were developed by Yu and Shi (2012) and Yi et al. (2017; 2018) for the evaluation of the NSIFs of the sharp V-notches. Yu and Shi (2012) and Yi et al. (2017) developed different stress-based and SED-based methods, respectively, for determining the NSIFs of isotropic homogeneous sharp V-notched geometries. In another work, Yi et al. (2018) proposed a method based on an effective conservative integral for the determination of the mixed mode NSIFs in bi-material V-notches using XFEM.

2.5 Various methods for the determination of mode III NSIFs

There are only a few papers available that have developed the methods for determining the NSIFs of notched components under out-of-plane loading (mode III) in comparison to the in-plane ones (mode I and mode II). Seweryn and Molski (1996) provided the stress and displacement field solution around the notch tip under out-of-plane shear loading conditions. Noda and Takase (2003) determined the NSIFs under mode III loading condition for sharp V-shaped notched round bar under torsion loading using the singular integral equation of the body force method. They also calculated the mode III NSIFs of V-notched semi-infinite plates under out-of-plane shear loading conditions.

Ju and Chung (2007) developed a least-squares-based method to determine mode III NSIFs of a cylinder with a round sharp V-notch subjected to a torsion loading. They determined the mode III NSIFs by minimizing the error in the analytical and stresses in an annulus region near the notch tip. They also considered higher-order terms in the calculation of the NSIFs. In another research, Ju (2014) determined the mode I, mode II, and mode III NSIFs of 3D notched bodies using the least-squares method. Recently, Yang et al. (2021) determined the mode III NSIFs for isotropic homogeneous and bi-material sharp V-notched configurations using the FE stresses along the notch bisector line. They (Yang et al., 2021) studied the influence of the first two non-singular stress terms on the stress field around the anti-plane sharp notch vertex. They concluded that their method would provide accurate mode III NSIFs if the first two non-singular stress terms were considered in the calculation.

Zappalorto et al. (2009) proposed the analytical expressions for the mode III NSIFs for circumferentially-sharply-notched rounded bars under torsion loading using the theoretical stress concentration factors of the corresponding notch problem. They determined the mode III NSIFs for the rounded bars for various notch angles and notch depths.

Treifi and Oyadiji (2013b) extended the FFEM to compute the mode III stress intensity factors for bi-material notched configurations subjected to anti-plane shear loading. In another research, Treifi and Oyadiji (2013c) proposed another strain energy approach to calculate the NSIFs for isotropic homogeneous and bi-material sharp V-notched plates subject to various mode I, mode II and mode III loading conditions.

Recently, Mehraban et al. (2021) determined the mode III NSIFs and higher-order stress coefficients using an overdeterministic method utilizing FE displacements. They considered the FE displacement at nodes lying in a circular ring around the notch tip on the mid-plane of the 3D specimens to calculate the mode III NSIFs.

2.6 Comparison among various NSIF determination FE methods

The review presented in the previous sections clearly indicates there has been a growing interest for the last few years for the accurate determination of the NSIFs of the sharp V-notched bodies. The above review clearly indicates that much research has been carried in this direction, and especially the conventional FE method is extensively employed in the computation of the NSIFs. These finite element-based methods have different theoretical foundations, computational strategies, the number of nodes at which field variables are sampled, and their locations. A similarity between all these methods is that they use conventional elements at the notch tip. To the knowledge of the author, no work is available till date on comprehensive numerical comparison of these methods, which have different theoretical backgrounds except for a few works by Berto and co-workers (Pittarello et al., 2016; Berto et al., 2017; Lepore et al., 2019). They (Pittarello et al., 2016; Berto et al., 2017; Lepore et al., 2019) investigated the efficiency of two energy-based methods proposed by Lazzarin et al. (2010) and Triefi et al. (2013c) for the different V-notched configurations.

2.7 Summary of the literature review and research gap

2.7.1 Summary

- NSIF is found to be a very important and most frequently used fracture parameter in the notch fracture mechanics.
- Determining the NSIF of the sharp V-notched configurations is generally more involved. Therefore, only a limited number of analytical/semi-analytical methods are available for the determination of NSIFs. These methods are confined only to simple configurations under the pure mode I and pure mode II loading conditions.
- NSIFs of complex notched configurations with complex boundary conditions are obtained using numerical methods.
- Many numerical methods have been developed in the past for the estimation of NSIFs of the sharp V-notches under the mode I, mode II and mixed mode (I/II) loadings.
- Among all the numerical methods, FEM is found to be the most widely used numerical method for the determination of NSIFs of sharp V-notches under complex geometries and loading conditions.
- All methods based on the FEM employ the conventional elements at the notch tip. This is because no special notch tip or singular elements are available till date for providing the exact singularity for all the notch angles under mixed mode loading.
- Path independent integrals, stress, energy, and displacement-based methods have been developed in conjunction with the conventional FEM.
- Stress and energy-based methods are free of the rigid body displacement terms. On the other hand, these terms are always associated with displacement-based methods.

- Despite knowing that the finite element displacements are more accurate than the stress components, very limited displacement-based methods are available till date.
- Except for some comparison between two energy-based methods, no literature is available till date on comprehensive numerical comparison among the stress, displacement, and energy-based methods.
- Apart from the traditional numerical methods, some nonconventional FE methods are also available to compute the NSIFs of the sharp V-notched configurations.
- Researchers also proposed various experimental methods to determine the NSIFs of the sharp V-notches.

2.7.2 Research gap

From the above literature study, the following gaps are observed

- Literature review on the conventional finite element-based methods (such as stress, displacement, and energy-based methods) clearly indicates the necessity of the development of new methods that are simple, rugged, and efficient for the accurate estimation of the NSIFs.
- In spite of the fact that FE displacement components are more accurate than other field variables, only two methods employed by Ayatollahi and Nejati (2011a) are available till date for the estimation of the mixed mode (I/II) NSIFs. Alternatively saying, the methods that need to deal with the rigid body displacement terms are highly scarce.
- Till date, notch flank displacements are rarely being used for the determination of mixed mode (I/II) NSIFs.
- The conventional quadratic quadrilateral element or eight noded isoparametric element is widely used in the FE analyses of various notches. The literature review does not show any attempt till date to study the behavior of these elements when used as the notch tip elements in the FE analyses of the sharp V-noted bodies.
- No comparative study among the stress, displacement, and energy-based FE methods is available till date for a deeper understanding of these methods.

2.8 Objectives of the present study

Based on the motivation, literature review, and gaps in the literature review on the available methods for the determination of NSIFs of the sharp V-notched bodies, the objectives of the present investigation are laid as

1. To investigate for special and useful properties of the conventional Q8 element when used as the notch tip element in the problems of the sharp V-notches.
2. To extend the widely availed concepts in the crack problems viz., the crack opening displacement (COD) and crack sliding displacement (CSD) to the sharp V-notch problems for the purpose of exploring these quantities in the notch problems to neatly bypass the rigid body displacement terms rather than discarding them.
3. To develop a very simple, rugged, and efficient displacement-based method using the special properties of the notch tip Q8 elements and the above extended quantities viz., the notch opening displacement (NOD) and notch sliding displacement (NSD) to determine the accurate NSIFs of the 2D V-notched bodies subjected to general in-plane loading.
4. To explore the benefits of the collocating the quantities NOD and NSD by sampling along the notch flanks.
5. To develop another simple, rugged, and efficient displacement-based method for the accurate estimation of the NSIFs using the collocation of the quantities NOD and NSD along the notch flanks and by neatly bypassing the rigid body displacement terms.
6. To conduct a comparison examination of the widely referred stress, displacement, and energy-based methods along with the two proposed methods in order to study their performance in terms of accuracy of the computed NSIFs on the common set of problems and FE meshes.
7. To suggest the methods that consistently provide accurate values of both the mode I and mode II NSIFs using the above comparison study.

Chapter 3

Theoretical background

3.1 Introduction

In this chapter, the theoretical background needed for understanding and implementation of the proposed methods is presented. Closed-form expressions of the stresses, strains, and displacement components around the tip of a sharp V-notch of an isotropic plate subjected to an arbitrary in-plane loading are presented in this chapter. These closed-form expressions are derived using an eigenfunction expansion method and are employed later in the development of the proposed methods. The formulation for obtaining the eigenvalues using the Muller's iteration method is also presented in this chapter. Theory and finite element formulation for modeling the sharp notch tip and discretization of the V-notched geometries are also presented here.

3.2 Williams eigenfunction expansion method

Williams (1952) proposed an eigenfunction approach based on the Airy's stress function for analysis of the sharp V-notches and cracks. Using this approach, one can conveniently obtain the stress, strain, and displacement fields in a closed-form fashion in bodies having sharp V-notches.

Let us consider a planar V-notched linear elastic body made of an isotropic material with a notch opening angle $\gamma\left(=360°-2\alpha\right)$ as shown in Figure 3.1 and subjected to an arbitrary in-plane loading. Such a loading produces the mixed mode (I/II) loading conditions in the notched body. According to Williams (1952), let ϕ be the Airy stress function in the polar coordinate system (r, θ) whose origin coincides with the tip of the V-notch (Figure 3.1). The line $\theta = 0°$ coincides with the axis of the notch or Cartesian $x-$axis, which is the bisector of the notch angle γ. $y-$axis is considered such that it forms the right-handed coordinate system, as shown in Figure 3.1. In the absence of the body forces and for the traction free notch flanks, the differential equations of equilibrium are automatically satisfied (in the polar coordinate system shown in Figure 3.1) if the stress components are defined in terms of the stress function ϕ as (Timoshenko and Goodier, 1970)

$$\sigma_{rr} = \frac{1}{r}\frac{\partial \phi}{\partial r} + \frac{1}{r^2}\frac{\partial^2 \phi}{\partial \theta^2} \tag{3.1}$$

$$\sigma_{\theta\theta} = \frac{\partial^2 \phi}{\partial r^2} \tag{3.2}$$

$$\sigma_{r\theta} = -\frac{\partial}{\partial r}\left(\frac{1}{r}\frac{\partial \phi}{\partial \theta}\right) = \frac{1}{r^2}\frac{\partial \phi}{\partial \theta} - \frac{1}{r}\frac{\partial^2 \phi}{\partial r \partial \theta} \tag{3.3}$$

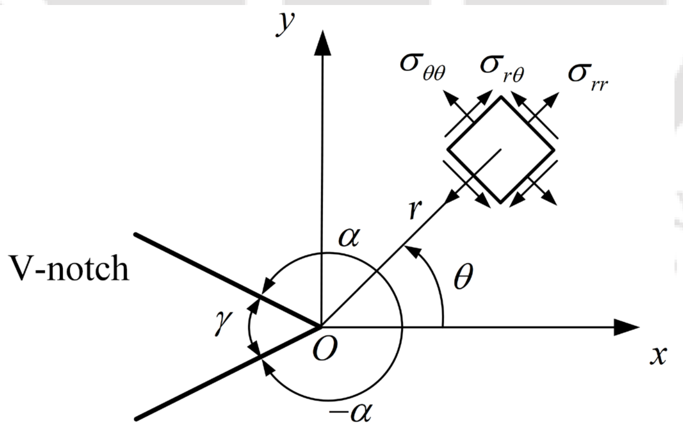

Figure 3.1. Stresses near the notch tip in the polar coordinate system.

As the Airy stress function approach is a stress-based approach, it is necessary that the stress components need to satisfy the two-dimensional compatibility equation in the polar coordinate system. It can be shown that (Timoshenko and Goodier, 1970) this leads to the satisfaction of the bi-harmonic equation in terms of the Airy stress function $\phi(r,\theta)$ as given by the following equation

$$\nabla^4\phi = \nabla^2\left(\nabla^2\phi\right) = 0 \tag{3.4}$$

where the Laplacian operator

$$\nabla^2 = \frac{\partial^2}{\partial r^2} + \frac{1}{r}\frac{\partial}{\partial r} + \frac{1}{r^2}\frac{\partial^2}{\partial \theta^2} \tag{3.5}$$

The Airy stress function $\phi(r,\theta)$ for a sharp V-notch problem under arbitrary loading conditions is given as (Williams, 1952)

$$\phi(r,\,\theta) = r^{\lambda-1}F(\theta) \tag{3.6}$$

where r is the radius from the notch-tip (Figure 3.1) and F is a function of the polar coordinate θ which is yet to be determined as explained below. Consequently, the first and second partial derivatives of $\phi(r,\theta)$ can be written as

$$\begin{aligned} &\frac{\partial}{\partial r}\left(r^{\lambda+1}F\right) = (\lambda+1)r^{\lambda}F, && \frac{\partial^2}{\partial r^2}\left(r^{\lambda+1}F\right) = (\lambda+1)\lambda r^{\lambda-1}F, \\ &\frac{\partial}{\partial \theta}\left(r^{\lambda+1}F\right) = r^{\lambda+1}F', && \frac{\partial^2}{\partial \theta^2}\left(r^{\lambda+1}F\right) = r^{\lambda+1}F'' \end{aligned} \tag{3.7}$$

where the prime stands for the differentiation of $F(\theta)$ with respect to θ. Here, F is used instead of $F(\theta)$ for simplicity.

Now, substituting Eqs. (3.6) and (3.7) into Eq. (3.4), one can get

$$\left\{(\lambda-1)^2 + \frac{\partial^2}{\partial\theta^2}\right\}\left\{(\lambda+1)^2 + \frac{\partial^2}{\partial\theta^2}\right\} r^{\lambda-3}F = 0 \tag{3.8}$$

Since $r^{\lambda-1} \neq 0$ in general, Eq. (3.8) is satisfied if

$$\left[(\lambda-1)^2+\frac{\partial^2}{\partial\theta^2}\right]\left[(\lambda+1)^2+\frac{\partial^2}{\partial\theta^2}\right]F(\theta)=0 \tag{3.9}$$

From above, either of the below two cases must be valid

$$\left[(\lambda-1)^2+\frac{\partial^2}{\partial\theta^2}\right]F(\theta)=0 \tag{3.10}$$

and

$$\left[(\lambda+1)^2+\frac{\partial^2}{\partial\theta^2}\right]F(\theta)=0 \tag{3.11}$$

The solution of Eq. (3.10) is

$$F(\theta)=c_1\cos(\lambda-1)\theta+c_2\sin(\lambda-1)\theta \tag{3.12}$$

and the solution of Eq. (3.11) is

$$F(\theta)=c_3\cos(\lambda+1)\theta+c_4\sin(\lambda+1)\theta \tag{3.13}$$

Considering Eqs. (3.12) and (3.13), the general solution of $F(\theta)$ is

$$F(\theta)=c_1\cos(\lambda-1)\theta+c_2\sin(\lambda-1)\theta+c_3\cos(\lambda+1)\theta+c_4\sin(\lambda+1)\theta \tag{3.14}$$

Consequently, the Airy stress function in Eq. (3.6) can now be written as

$$\phi=r^{\lambda-1}\left[c_1\cos(\lambda-1)\theta+c_2\sin(\lambda-1)\theta+c_3\cos(\lambda+1)\theta+c_4\sin(\lambda+1)\theta\right] \tag{3.15}$$

Thus $\phi(r,\theta)$ obtained from Eq. (3.15) is an acceptable Airy stress function because it satisfies the bi-harmonic equation (Eq. (3.8)) and hence satisfies the compatibility condition.

Substituting Eq. (3.15) into Eqs. (3.1) – (3.3), the stress components can be obtained as

$$\sigma_{rr} = \frac{1}{r}\frac{\partial \phi}{\partial r} + \frac{1}{r^2}\frac{\partial^2 \phi}{\partial \theta^2} = r^{\lambda-1}\begin{bmatrix} -\lambda(\lambda-3)c_1\cos(\lambda-1)\theta - \lambda(\lambda-3)c_2\sin(\lambda-1)\theta \\ -\lambda(\lambda+1)c_3\cos(\lambda+1)\theta - \lambda(\lambda+1)c_4\sin(\lambda+1)\theta \end{bmatrix} \tag{3.16}$$

$$\sigma_{\theta\theta} = \frac{\partial^2 \phi}{\partial r^2} = r^{\lambda-1}\begin{bmatrix} \lambda(\lambda+1)c_1\cos(\lambda-1)\theta + \lambda(\lambda+1)c_2\sin(\lambda-1)\theta \\ +\lambda(\lambda+1)c_3\cos(\lambda+1)\theta + \lambda(\lambda+1)c_4\sin(\lambda+1)\theta \end{bmatrix} \tag{3.17}$$

and

$$\sigma_{r\theta} = \frac{1}{r^2}\frac{\partial \phi}{\partial \theta} - \frac{1}{r}\frac{\partial^2 \phi}{\partial r \partial \theta} = r^{\lambda-1}\begin{bmatrix} \lambda(\lambda-1)c_1\sin(\lambda-1)\theta - \lambda(\lambda-1)c_2\cos(\lambda-1)\theta \\ +\lambda(\lambda+1)c_3\sin(\lambda+1)\theta - \lambda(\lambda+1)c_4\cos(\lambda+1)\theta \end{bmatrix} \tag{3.18}$$

The unknowns $c_i\,(i=1,\,2,\,3,\,4)$ and λ (which may be real or complex) can be determined by applying the boundary conditions. For the traction-free notch surfaces, referring to Figure 3.1, these conditions can be written as

$$\sigma_{\theta\theta}(r,\pm\alpha) = 0 \tag{3.19}$$

and

$$\sigma_{r\theta}(r,\pm\alpha) = 0 \tag{3.20}$$

Substituting the $\sigma_{\theta\theta}$ from Eq. (3.17) into Eq. (3.19) at $\theta = +\alpha$ and $\theta = -\alpha$, one will get

$$\begin{aligned} \sigma_{\theta\theta(\theta=+\alpha)} &= \lambda(\lambda+1)c_1\cos(\lambda-1)\alpha + \lambda(\lambda+1)c_2\sin(\lambda-1)\alpha \\ &\quad + \lambda(\lambda+1)c_3\cos(\lambda+1)\alpha + \lambda(\lambda+1)c_4\sin(\lambda+1)\alpha = 0 \end{aligned} \tag{3.21}$$

and

$$\sigma_{\theta\theta(\theta=-\alpha)} = \lambda(\lambda+1)c_1\cos(\lambda-1)\alpha - \lambda(\lambda+1)c_2\sin(\lambda-1)\alpha \\ +\lambda(\lambda+1)c_3\cos(\lambda+1)\alpha - \lambda(\lambda+1)c_4\sin(\lambda+1)\alpha = 0 \tag{3.22}$$

Similarly, substituting the shear stress from Eq. (3.18) into Eq. (3.20) at $\theta=+\alpha$ and $\theta=-\alpha$, one obtains as

$$\sigma_{r\theta(\theta=+\alpha)} = \lambda(\lambda-1)c_1\sin(\lambda-1)\alpha - \lambda(\lambda-1)c_2\cos(\lambda-1)\alpha \\ +\lambda(\lambda+1)c_3\sin(\lambda+1)\alpha - \lambda(\lambda+1)c_4\cos(\lambda+1)\alpha = 0 \tag{3.23}$$

and

$$\sigma_{r\theta(\theta=-\alpha)} = -\lambda(\lambda-1)c_1\sin(\lambda-1)\alpha - \lambda(\lambda-1)c_2\cos(\lambda-1)\alpha \\ -\lambda(\lambda+1)c_3\sin(\lambda+1)\alpha - \lambda(\lambda+1)c_4\cos(\lambda+1)\alpha = 0 \tag{3.24}$$

Using simple algebra, the above equations, i.e., Eqs. (3.21) – (3.24) can be separated into two uncoupled systems of equations and can be shown in a matrix form as

$$\begin{bmatrix} \cos(\lambda-1)\alpha & \cos(\lambda+1)\alpha \\ (\lambda-1)\sin(\lambda-1)\alpha & (\lambda+1)\sin(\lambda+1)\alpha \end{bmatrix} \begin{Bmatrix} c_1 \\ c_3 \end{Bmatrix} = \begin{Bmatrix} 0 \\ 0 \end{Bmatrix} \tag{3.25}$$

and

$$\begin{bmatrix} \sin(\lambda-1)\alpha & \sin(\lambda+1)\alpha \\ (\lambda-1)\cos(\lambda-1)\alpha & (\lambda+1)\cos(\lambda+1)\alpha \end{bmatrix} \begin{Bmatrix} c_2 \\ c_4 \end{Bmatrix} = \begin{Bmatrix} 0 \\ 0 \end{Bmatrix} \tag{3.26}$$

The constants c_1 and c_3 are coefficients of cosine functions in Eq. (3.15); therefore, Eq. (3.25) leads to solutions that are symmetric with respect to the $x-$axis, i.e., mode I. Similarly, as the constants c_2 and c_4 are coefficients of sine functions in Eq. (3.15); therefore, Eq. (3.26), leads to solutions that are anti-symmetric with respect to the $x-$axis, i.e., mode II.

For non-trivial solutions of Eqs. (3.25) and (3.26), the determinant of their corresponding matrices should be equal to zero. By equating the determinant of Eq. (3.25) to zero, one can get

$$\lambda^{I} \sin 2\alpha + \sin 2\lambda^{I}\alpha = 0 \tag{3.27}$$

and similarly, equating the determinant of Eq. (3.26) to zero, one can get

$$-\lambda^{II} \sin 2\alpha + \sin 2\lambda^{II}\alpha = 0 \tag{3.28}$$

where λ^{I} and λ^{II} are the eigenvalues corresponding to mode I and mode II, respectively, and are always different from each other except for the special case viz., the sharp crack problems for which the notch angle $\gamma = 0°$. With $\alpha = \pi$, for a crack problem, the eigenvalues can be obtained as

$$\lambda^{I} = \lambda^{II} = \frac{n}{2} \tag{3.29}$$

where $n = 1,\ 2,\ 3,\ldots$ (Kundu, 2008). The singular stress field around the crack tip is characterized by the first eigenvalue $(n = 1)$. As far as the sharp V-notch problems are concerned, the characteristic equations (Eqs. (3.27) and (3.28)) need to be solved numerically. For this purpose, the Muller's iterative method (Press et al., 2007) is widely employed for determining n-th eigenvalues of λ_n^{I} and λ_n^{II} for mode I and mode II, respectively. It should be noted that, unlike the crack problems, the eigenvalues of the sharp V-notch problems depend on the notch angel γ. The advantage of the Muller's method is that the iteration can converge to a complex root, even if it has started with a real number (Press et al., 2007). This iterative method will be discussed in detail in Section 3.4.

For different values of $\lambda_n^{I/II}$, the function $F(\theta)$ given in Eq. (3.14) will have different expressions with different constants, c_{in} ($i = 1, 2, 3, 4$ and n =1, 2, 3, …). As a consequence, the stress, strain, and displacement expressions are represented by an infinite series function in terms of the $\lambda_n^{I/II}$ and c_{in}. For convenience, the term n is omitted for the time being, and it will be included in the final expression of the stress, strain, and displacement components.

From Eq. (3.25), a relation between c_1 and c_3 can be obtained as

$$c_1 = -\frac{\cos\left(\lambda^I+1\right)\alpha}{\cos\left(\lambda^I-1\right)\alpha}c_3 = -\frac{\left(\lambda^I+1\right)\sin\left(\lambda^I+1\right)\alpha}{\left(\lambda^I-1\right)\sin\left(\lambda^I-1\right)\alpha}c_3 \tag{3.30}$$

Similarly, from Eq. (3.26), it can be shown that the constants c_2 and c_4 are related as

$$c_2 = -\frac{\sin\left(\lambda^{II}+1\right)\alpha}{\sin\left(\lambda^{II}-1\right)\alpha}c_4 = -\frac{\left(\lambda^{II}+1\right)\cos\left(\lambda^{II}+1\right)\alpha}{\left(\lambda^{II}-1\right)\cos\left(\lambda^{II}-1\right)\alpha}c_4 \tag{3.31}$$

Thus, $F(\theta)$ can now be rewritten as

$$\begin{aligned} F(\theta) = F^I + F^{II} &= c_1\cos\left(\lambda^I-1\right)\theta + c_3\cos\left(\lambda^I+1\right) \\ &+ c_2\sin\left(\lambda^{II}-1\right)\theta + c_4\sin\left(\lambda^{II}+1\right)\theta \end{aligned} \tag{3.32}$$

where

$$F^I = c_1\cos\left(\lambda^I-1\right)\theta + c_3\sin\left(\lambda^I+1\right)\theta \tag{3.33}$$

which corresponds to the mode I problems and

$$F^{II} = c_2\sin\left(\lambda^{II}-1\right)\theta + c_4\cos\left(\lambda^{II}+1\right)\theta \tag{3.34}$$

which pertains to the mode II problems. The first and second derivatives of the function $F(\theta)$ for mode I and mode II can be obtained as

$$\begin{aligned} F^{I\prime} &= -c_3\left(\lambda^I+1\right)\sin\left(\lambda^I+1\right)\theta - c_1\left(\lambda^I+1\right)\sin\left(\lambda^I+1\right)\theta \\ F^{I\prime\prime} &= -c_3\left(\lambda^I+1\right)^2\cos\left(\lambda^I+1\right)\theta - c_1\left(\lambda^I+1\right)^2\cos\left(\lambda^I+1\right)\theta \\ F^{II\prime} &= c_4\left(\lambda^{II}+1\right)\cos\left(\lambda^{II}+1\right)\theta + c_2\left(\lambda^{II}+1\right)\cos\left(\lambda^{II}+1\right)\theta \\ F^{II\prime\prime} &= -c_4\left(\lambda^{II}+1\right)^2\sin\left(\lambda^{II}+1\right)\theta - c_2\left(\lambda^{II}+1\right)^2\sin\left(\lambda^{II}+1\right)\theta \end{aligned} \tag{3.35}$$

Rearranging Eq. (3.30), one obtains

$$\frac{c_3}{c_1}=\frac{-\left(\lambda^I-1\right)\sin\left(\lambda^I-1\right)\alpha}{\left(\lambda^I+1\right)\sin\left(\lambda^I+1\right)\alpha}=\frac{-1}{\left(\lambda^I+1\right)}X \tag{3.36}$$

where

$$X=\lambda^I\cos 2\alpha+\cos 2\lambda^I\alpha \tag{3.37}$$

Similarly, rearranging Eq. (3.31),

$$\frac{c_4}{c_2}=\frac{-\left(\lambda^{II}-1\right)\cos\left(\lambda^{II}-1\right)\alpha}{\left(\lambda^{II}+1\right)\cos\left(\lambda^{II}+1\right)\alpha}=\frac{-1}{\left(\lambda^{II}+1\right)}Y \tag{3.38}$$

where

$$Y=\lambda^{II}\cos 2\alpha-\cos 2\lambda^{II}\alpha \tag{3.39}$$

3.2.1 Stress components in the polar coordinate system

Expressions for the mode I stress components (σ_{rr}, $\sigma_{\theta\theta}$ and $\sigma_{r\theta}$) in the polar coordinate system can now be written using Eqs. (3.1) – (3.3), (3.6) and (3.35) as

$$\begin{aligned}\sigma_{rr}^I&=r^{\lambda^I-1}\left[\left(\lambda^I+1\right)F^I+F^{I''}\right]\\&=\lambda^I r^{\lambda^I-1}c_1\left[\left(3-\lambda^I\right)\cos\left(\lambda^I-1\right)\theta+X\cos\left(\lambda^I+1\right)\theta\right]\end{aligned} \tag{3.40}$$

$$\begin{aligned}\sigma_{\theta\theta}^I&=r^{\lambda^I-1}\lambda^I\left(\lambda^I+1\right)F^I\\&=\lambda^I r^{\lambda^I-1}c_1\left[\left(\lambda^I+1\right)\cos\left(\lambda^I-1\right)\theta-X\cos\left(\lambda^I+1\right)\theta\right]\end{aligned} \tag{3.41}$$

and

$$\begin{aligned}\sigma_{r\theta}^{I} &= r^{\lambda^{I}-1}\left(-\lambda^{I}F^{I\prime}\right)\\ &= \lambda^{I}r^{\lambda^{I}-1}c_1\left[\left(\lambda^{I}-1\right)\sin\left(\lambda^{I}-1\right)\theta - X\sin\left(\lambda^{I}+1\right)\theta\right]\end{aligned} \tag{3.42}$$

Similarly, the stress expressions for the mode II in the polar coordinate system can be rewritten as (using Eqs. (3.1) – (3.3), (3.6) and (3.35))

$$\begin{aligned}\sigma_{rr}^{II} &= r^{\lambda^{II}-1}\left[\left(\lambda^{II}+1\right)F^{II}+F^{II\prime\prime}\right]\\ &= \lambda^{II}r^{\lambda^{II}-1}c_2\left[\left(3-\lambda^{II}\right)\sin\left(\lambda^{II}-1\right)\theta + Y\sin\left(\lambda^{II}+1\right)\theta\right]\end{aligned} \tag{3.43}$$

$$\begin{aligned}\sigma_{\theta\theta}^{II} &= r^{\lambda^{II}-1}\left[\lambda^{II}\left(\lambda^{II}+1\right)F^{II}\right]\\ &= \lambda^{II}r^{\lambda^{II}-1}c_2\left[\left(\lambda^{II}+1\right)\sin\left(\lambda^{II}-1\right)\theta - Y\sin\left(\lambda^{II}+1\right)\theta\right]\end{aligned} \tag{3.44}$$

and

$$\begin{aligned}\sigma_{r\theta}^{II} &= r^{\lambda^{II}-1}\left[-\lambda^{II}F^{II\prime}\right]\\ &= \lambda^{II}r^{\lambda^{II}-1}c_2\left[\left(1-\lambda^{II}\right)\cos\left(\lambda^{II}-1\right)\theta + Y\cos\left(\lambda^{II}+1\right)\theta+\right]\end{aligned} \tag{3.45}$$

Finally, using the principle of superposition, the mixed mode (I/II) stress expressions in the polar coordinate system can be written as (using Eqs. (3.40) – (3.45))

$$\begin{aligned}\sigma_{rr} &= \sigma_{rr}^{I}+\sigma_{rr}^{II}\\ &= \lambda^{I}r^{\lambda^{I}-1}c_1\left[\left(3-\lambda^{I}\right)\cos\left(\lambda^{I}-1\right)\theta + X\cos\left(\lambda^{I}+1\right)\theta\right]\\ &\quad+\lambda^{II}r^{\lambda^{II}-1}c_2\left[\left(3-\lambda^{II}\right)\sin\left(\lambda^{II}-1\right)\theta + Y\sin\left(\lambda^{II}+1\right)\theta\right]\end{aligned} \tag{3.46}$$

$$\begin{aligned}\sigma_{\theta\theta} &= \sigma_{\theta\theta}^{I}+\sigma_{\theta\theta}^{II}\\ &= \lambda^{I}r^{\lambda^{I}-1}c_1\left[\left(\lambda^{I}+1\right)\cos\left(\lambda^{I}-1\right)\theta - X\cos\left(\lambda^{I}+1\right)\theta\right]\\ &\quad+\lambda^{II}r^{\lambda^{II}-1}c_2\left[\left(\lambda^{II}+1\right)\sin\left(\lambda^{II}-1\right)\theta - Y\sin\left(\lambda^{II}+1\right)\theta\right]\end{aligned} \tag{3.47}$$

and

$$\begin{aligned}\sigma_{r\theta} &= \sigma_{r\theta}^{I} + \sigma_{r\theta}^{II} \\ &= \lambda^{I} r^{\lambda^{I}-1} c_1 \left[\left(\lambda^{I}-1\right) \sin\left(\lambda^{I}-1\right)\theta - X \sin\left(\lambda^{I}+1\right)\theta \right] \\ &\quad + \lambda^{II} r^{\lambda^{II}-1} c_2 \left[\left(1-\lambda^{II}\right) \cos\left(\lambda^{II}-1\right)\theta + Y \cos\left(\lambda^{II}+1\right)\theta \right]\end{aligned} \tag{3.48}$$

Note that the above expressions (Eqs. (3.46) – (3.48)) are infinite series expansions. Rewriting the above infinite series form of the stress components in the mixed mode (I/II) loading in a more convenient form as

$$\begin{Bmatrix}\sigma_{rr}\\ \sigma_{\theta\theta}\\ \sigma_{r\theta}\end{Bmatrix} = \sum_{n=1}^{\infty} \mathrm{Re}\left\{ \frac{\lambda_n^{I} A_n}{r^{1-\lambda_n^{I}}} \begin{Bmatrix} \left(3-\lambda_n^{I}\right)\cos\left(\lambda_n^{I}-1\right)\theta + \left(\lambda_n^{I}\cos 2\alpha + \cos 2\lambda_n^{I}\alpha\right)\cos\left(\lambda_n^{I}+1\right)\theta \\ \left(\lambda_n^{I}+1\right)\cos\left(\lambda_n^{I}-1\right)\theta - \left(\lambda_n^{I}\cos 2\alpha + \cos 2\lambda_n^{I}\alpha\right)\cos\left(\lambda_n^{I}+1\right)\theta \\ \left(\lambda_n^{I}-1\right)\sin\left(\lambda_n^{I}-1\right)\theta - \left(\lambda_n^{I}\cos 2\alpha + \cos 2\lambda_n^{I}\alpha\right)\sin\left(\lambda_n^{I}+1\right)\theta \end{Bmatrix} \right\}$$
$$+ \sum_{n=1}^{\infty} \mathrm{Re}\left\{ \frac{\lambda_n^{II} B_n}{r^{1-\lambda_n^{II}}} \begin{Bmatrix} \left(\lambda_n^{II}-3\right)\sin\left(\lambda_n^{II}-1\right)\theta - \left(\lambda_n^{II}\cos 2\alpha - \cos 2\lambda_n^{II}\alpha\right)\sin\left(\lambda_n^{II}+1\right)\theta \\ -\left(\lambda_n^{II}+1\right)\sin\left(\lambda_n^{II}-1\right)\theta - \left(\lambda_n^{II}\cos 2\alpha - \cos 2\lambda_n^{II}\alpha\right)\sin\left(\lambda_n^{II}+1\right)\theta \\ \left(\lambda_n^{II}-1\right)\cos\left(\lambda_n^{II}-1\right)\theta - \left(\lambda_n^{II}\cos 2\alpha - \cos 2\lambda_n^{II}\alpha\right)\cos\left(\lambda_n^{II}+1\right)\theta \end{Bmatrix} \right\} \tag{3.49}$$

Here, the constant c_1 is renamed as A_1 and c_2 is termed as $-B_1$ as they are more frequently employed in the recent literature in place of the c_1 and c_2. This has been adopted throughout the thesis. Thus, in Eq. (3.49), the terms associated with the coefficient A_n represent the mode I stress components, and those associated with B_n represent the mode II components. Further, in Eq. (3.49), n is the number of terms in the infinite series, $\mathrm{Re}(\ )$ denotes real part of the variables, A_n and B_n ($n \neq 2$ for B_n, as $n = 2$ produces only rigid body displacements and which will be discussed in Chapter 4 elaborately) are the Williams' coefficients corresponding to the n-th term.

3.2.2 Stress components in the Cartesian coordinate system

The stress components in the Cartesian coordinate system (Figure 3.2) can be obtained in terms of the polar coordinates (r, θ) using the following stress transformation equations

$$\sigma_{xx} = \frac{\sigma_{rr} + \sigma_{\theta\theta}}{2} + \frac{\sigma_{rr} - \sigma_{\theta\theta}}{2}\cos 2\theta - \sigma_{r\theta}\sin 2\theta \tag{3.50}$$

$$\sigma_{yy} = \frac{\sigma_{rr} + \sigma_{\theta\theta}}{2} - \frac{\sigma_{rr} - \sigma_{\theta\theta}}{2}\cos 2\theta + \sigma_{r\theta}\sin 2\theta \tag{3.51}$$

and

$$\sigma_{xy} = \frac{\sigma_{rr} - \sigma_{\theta\theta}}{2}\sin 2\theta + \sigma_{r\theta}\cos 2\theta \tag{3.52}$$

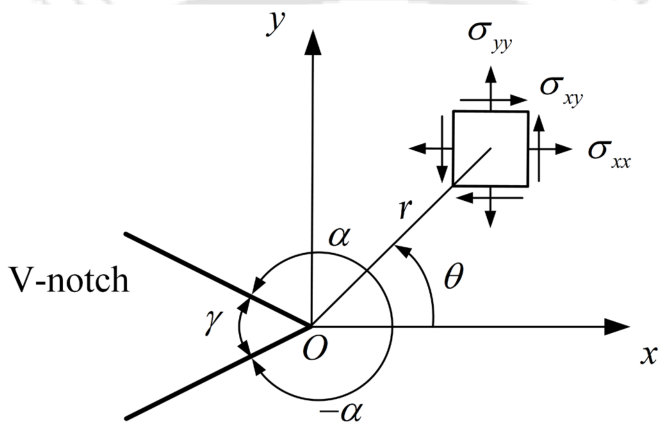

Figure 3.2. Stresses near the notch tip in the Cartesian coordinate system.

Using the above equations, it can be shown that the infinite series form of the Cartesian stress components under mixed mode (I/II) loading can be written as

$$\begin{Bmatrix} \sigma_{xx} \\ \sigma_{yy} \\ \sigma_{xy} \end{Bmatrix} = \sum_{n=1}^{\infty} \mathrm{Re}\left\{ \frac{\lambda_n^I A_n}{r^{1-\lambda_n^1}} \begin{Bmatrix} (2+\lambda_n^I \cos 2\alpha + \cos 2\alpha \lambda_n^I)\cos(\lambda_n^I - 1)\theta - (\lambda_n^I - 1)\cos(\lambda_n^I - 3)\theta \\ (2-\lambda_n^I \cos 2\alpha - \cos 2\alpha \lambda_n^I)\cos(\lambda_n^I - 1)\theta + (\lambda_n^I - 1)\cos(\lambda_n^I - 3)\theta \\ -(\lambda_n^I \cos 2\alpha + \cos 2\alpha \lambda_n^I)\sin(\lambda_n^I - 1)\theta + (\lambda_n^I - 1)\sin(\lambda_n^I - 3)\theta \end{Bmatrix} \right\}$$
$$+ \sum_{n=1}^{\infty} \mathrm{Re}\left\{ \frac{\lambda_n^{II} B_n}{r^{1-\lambda_n^{II}}} \begin{Bmatrix} -(2+\lambda_n^{II} \cos 2\alpha - \cos 2\alpha \lambda_n^{II})\sin(\lambda_n^{II} - 1)\theta + (\lambda_n^{II} - 1)\sin(\lambda_n^{II} - 3)\theta \\ (-2+\lambda_n^{II} \cos 2\alpha - \cos 2\alpha \lambda_n^{II})\sin(\lambda_n^{II} - 1)\theta - (\lambda_n^{II} - 1)\sin(\lambda_n^{II} - 3)\theta \\ -(\lambda_n^{II} \cos 2\alpha - \cos 2\alpha \lambda_n^{II})\cos(\lambda_n^{II} - 1)\theta + (\lambda_n^{II} - 1)\cos(\lambda_n^{II} - 3)\theta \end{Bmatrix} \right\} \tag{3.53}$$

In the above equation, $n \neq 2$ for B_n as $n = 2$ produces only rigid body displacements, which will be discussed in Chapter 4 elaborately. Thus, similar to the polar stress components, in Eq. (3.53), the terms associated with the coefficient A_n represent the mode I stress components, and that associated with the B_n represent the mode II components.

It can be noticed from Eqs. (3.49) and (3.53) that these are infinite series due to the parameters A_n, B_n, and $\lambda_n^{I/II}$. It is worth discussing the nature of these parameters here. Eigenvalues $\lambda_n^{I/II}$, can be real or complex depending on the notch angle γ as shown in Figure 3.3. The first eigenvalues of mode I and mode II, i.e., λ_1^I and λ_1^{II} are always real for all the notch angles and are measure of the singularity $(\lambda_1^{I\,or\,II}-1)$ (see Eqs. (3.49) and (3.53)). Figure 3.3 shows the variation of the computed eigenvalues for $n=1$ to 3 for mode I and $n=1$ to 4 for mode II. It can be noticed from Figure 3.3 that crack has the strongest singularity (–0.5) in both the mode I and mode II loading. As the notch angle increases, the singularity decreases, i.e., $\lambda_1^{I\,or\,II}$ increases and vanishes at the larger notch angles. In case of mode I loading, $\lambda_1^I=1$ for the notch angle 180° whereas in mode II when $\gamma=102.5466°$ the first eigenvalue $\lambda_1^{II}>1$. Thus, the singularity prevails up to $\gamma<180°$ in the mode I and $\gamma<102.5466°$ in the mode II loading. As mentioned previously, the second eigenvalue in mode II, i.e., λ_1^{II} is always real and equals to 1(one) for all the notch angles (Figure 3.3), and thus results in the rigid body modes of deformation.

It can be shown that in the mode I loading, there are infinite number of complex conjugate roots for Eq. (3.27) possible when $45°<\gamma<152°$. While in the mode II loading, infinite number of complex conjugate roots for Eq. (3.28) occurs when $32°<\gamma<160°$ as shown in Figure 3.3. If n-eigenvalue of Eq. (3.27) or (3.28) is a complex number (i.e., $\lambda_n^I=\mathrm{Re}\,\lambda_n^I+\mathrm{Im}\,\lambda_n^I$ or $\lambda_n^{II}=\mathrm{Re}\,\lambda_n^{II}+\mathrm{Im}\,\lambda_n^{II}$) then its conjugate value ($\overline{\lambda}_n^I=\mathrm{Re}\,\lambda_n^I-\mathrm{Im}\,\lambda_n^I$ or $\overline{\lambda}_n^{II}=\mathrm{Re}\,\lambda_n^{II}-\mathrm{Im}\,\lambda_n^{II}$) is also a root of the characteristic equations (Ayatollahi and Nejati, 2011a). Consequently, the Williams coefficient corresponding to the n^{th} term will also be a complex number ($A_n=\mathrm{Re}\,A_n+\mathrm{Im}\,A_n$ or $B_n=\mathrm{Re}\,B_n+\mathrm{Im}\,B_n$) and its conjugate ($\overline{A}_n=\mathrm{Re}\,A_n-\mathrm{Im}\,A_n$ or $\overline{B}_n=\mathrm{Re}\,B_n-\mathrm{Im}\,B_n$) is the coefficient related to the conjugate of the eigenvalue (Seweryn, 2002).

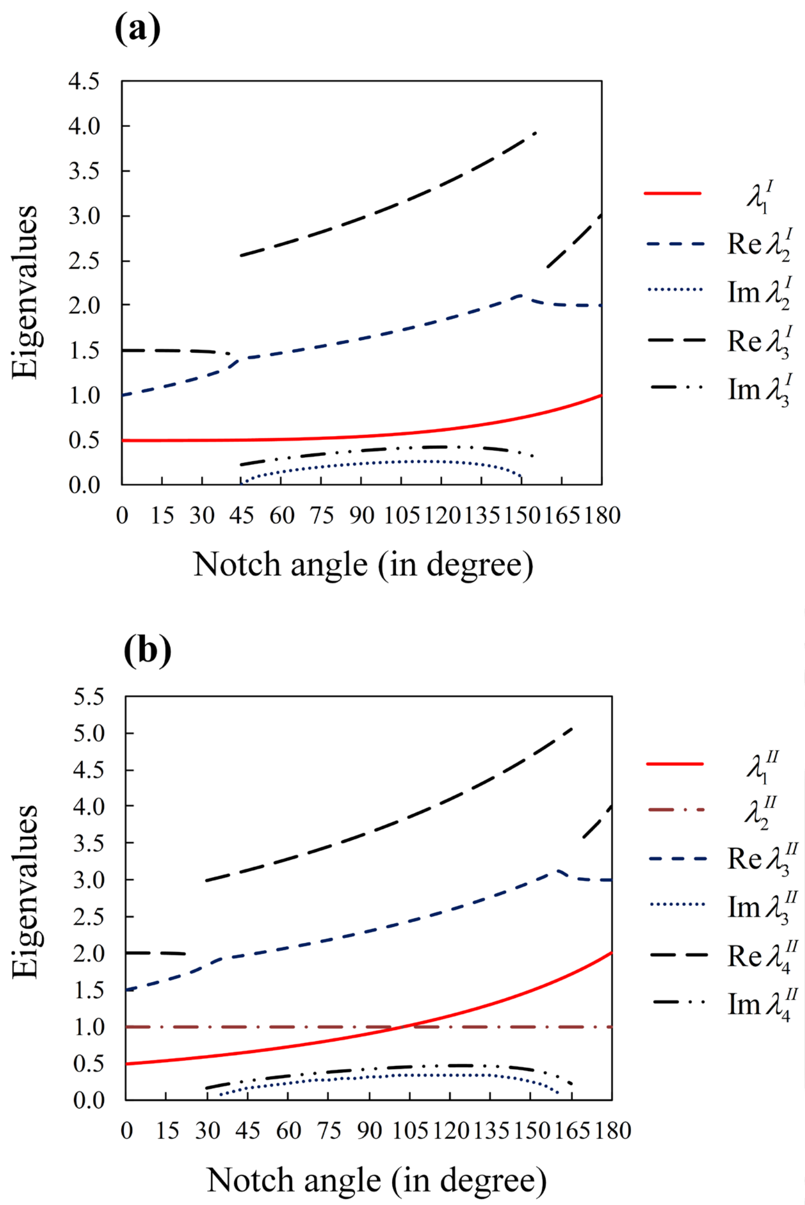

Figure 3.3. Variation of (a) first three eigenvalues for mode I and (b) first four eigenvalues for mode II in terms of notch angle.

As only the real values of the stresses can exist around the notch tip and such values can be obtained only when the complex conjugate Williams coefficients (A_n and $\overline{A}_n$ or B_n and $\overline{B}_n$) correspond to the complex conjugate of eigenvalues (λ_n^I and $\overline{\lambda}_n^I$ or λ_n^{II} and $\overline{\lambda}_n^{II}$) (Ayatollahi and Nejati, 2011a). However, in this work, the first eigenvalues, i.e., λ_1^I and λ_1^{II} are only considered for the development of the proposed methods. As the first eigenvalue of mode I (λ_1^I) and mode II (λ_1^{II}) are always real; therefore, the corresponding Williams coefficients will always be real.

3.2.3 Strain components in the polar coordinate system

The stress-strain relations in the polar coordinate system for the plane stress conditions are given as

$$\begin{aligned} E\varepsilon_{rr} &= \sigma_{rr} - \nu\sigma_{\theta\theta} \\ E\varepsilon_{\theta\theta} &= \sigma_{\theta\theta} - \nu\sigma_{rr} \\ G\gamma_{r\theta} &= \sigma_{r\theta} \end{aligned} \tag{3.54}$$

Using the above relations (Eq. (3.54)), the strain components in the polar coordinate system in the infinite series form under mixed mode (I/II) loading conditions can be obtained as

$$\begin{aligned} \begin{Bmatrix} \varepsilon_{rr} \\ \varepsilon_{\theta\theta} \\ \gamma_{r\theta} \end{Bmatrix} = &\sum_{n=1}^{\infty} \mathrm{Re}\left\{ \frac{\lambda_n^I r^{\lambda_n^I - 1} A_n}{2G} \begin{Bmatrix} \left(3\kappa' + 2\eta - \lambda_n^I\right)\cos\left(\lambda_n^I - 1\right)\theta + \left(\lambda_n^I \cos 2\alpha + \cos 2\lambda_n^I \alpha\right)\cos\left(\lambda_n^I + 1\right)\theta \\ \left(\kappa' - 2\eta + \lambda_n^I\right)\cos\left(\lambda_n^I - 1\right)\theta - \left(\lambda_n^I \cos 2\alpha + \cos 2\lambda_n^I \alpha\right)\cos\left(\lambda_n^I + 1\right)\theta \\ 2\left(\lambda_n^I - 1\right)\sin\left(\lambda^I - 1\right)\theta - 2\left(\lambda_n^I \cos 2\alpha + \cos 2\lambda_n^I \alpha\right)\sin\left(\lambda_n^I + 1\right)\theta \end{Bmatrix} \right\} \\ &+ \sum_{n=1}^{\infty} \mathrm{Re}\left\{ \frac{\lambda_n^{II} r^{\lambda_n^{II} - 1} B_n}{2G} \begin{Bmatrix} \left(\lambda_n^{II} - 3\kappa' - 2\eta\right)\sin\left(\lambda_n^{II} - 1\right)\theta - \left(\lambda_n^{II} \cos 2\alpha - \cos 2\lambda_n^{II} \alpha\right)\sin\left(\lambda_n^{II} + 1\right)\theta \\ \left(-\lambda_n^{II} - \kappa' + 2\eta\right)\sin\left(\lambda_n^{II} - 1\right)\theta + \left(\lambda_n^{II} \cos 2\alpha - \cos 2\lambda_n^{II} \alpha\right)\sin\left(\lambda_n^{II} + 1\right)\theta \\ 2\left(\lambda_n^{II} - 1\right)\cos\left(\lambda_n^{II} - 1\right)\theta - 2\left(\lambda_n^{II} \cos 2\alpha - \cos 2\lambda_n^{II} \alpha\right)\cos\left(\lambda_n^{II} + 1\right)\theta \end{Bmatrix} \right\} \end{aligned} \tag{3.55}$$

where $n \neq 2$ for B_n ($n = 2$ for B_n produces rigid body displacements as similar to the stress equation (Eq. (3.49)) and

$$\kappa' = \begin{cases} \dfrac{1-\nu}{1+\nu} & \text{for plane stress} \\ 1-2\nu & \text{for plane strain} \end{cases} \tag{3.56}$$

and

$$\eta = \begin{cases} \dfrac{\nu}{1+\nu} & \text{for plane stress} \\ \nu & \text{for plane strain} \end{cases} \tag{3.57}$$

3.2.4 Strain components in the Cartesian coordinate system

Either using the stress-strain relations in the Cartesian coordinate system or using the strain transformation laws, the strain components in the infinite series form in a sharp V-notched body subjected to an arbitrary in-plane loading conditions can be obtained as

$$\begin{Bmatrix}\varepsilon_{xx}\\ \varepsilon_{yy}\\ \gamma_{xy}\end{Bmatrix}=\sum_{n=1}^{\infty}\mathrm{Re}\left\{\frac{\lambda_n^I A_n}{2Gr^{1-\lambda_n^I}}\begin{Bmatrix}(2\kappa'+\lambda_n^I\cos 2\alpha+\cos 2\alpha\lambda_n^I)\cos(\lambda_n^I-1)\theta-(\lambda_n^I-1)\cos(\lambda_n^I-3)\theta\\ (2\kappa'-\lambda_n^I\cos 2\alpha-\cos 2\alpha\lambda_n^I)\cos(\lambda_n^I-1)\theta+(\lambda_n^I-1)\cos(\lambda_n^I-3)\theta\\ -2(\lambda_n^I\cos 2\alpha+\cos 2\alpha\lambda_n^I)\sin(\lambda_n^I-1)\theta+2(\lambda_n^I-1)\sin(\lambda_n^I-3)\theta\end{Bmatrix}\right\}$$
$$+\sum_{n=1}^{\infty}\mathrm{Re}\left\{\frac{\lambda_n^{II} B_n}{2Gr^{1-\lambda_n^{II}}}\begin{Bmatrix}-(2\kappa'+\lambda_n^{II}\cos 2\alpha-\cos 2\alpha\lambda_n^{II})\sin(\lambda_n^{II}-1)\theta+(\lambda_n^{II}-1)\sin(\lambda_n^{II}-3)\theta\\ (-2\kappa'+\lambda_n^{II}\cos 2\alpha-\cos 2\alpha\lambda_n^{II})\sin(\lambda_n^{II}-1)\theta-(\lambda_n^{II}-1)\sin(\lambda_n^{II}-3)\theta\\ -2(\lambda_n^{II}\cos 2\alpha-\cos 2\alpha\lambda_n^{II})\cos(\lambda_n^{II}-1)\theta+2(\lambda_n^{II}-1)\cos(\lambda_n^{II}-3)\theta\end{Bmatrix}\right\}\tag{3.58}$$

In the above equation, $n \neq 2$ for B_n, as $n = 2$ produces only rigid body displacements. The values of κ' and η can be obtained from Eqs. (3.56) and (3.57), respectively.

3.2.5 Displacement components in the polar coordinate system

The displacement components can be easily derived by integrating the strain components (Timoshenko and Goodier, 1970). Following the standard procedure, the displacement components in the infinite series form in a sharp V-notched body subjected to the mixed mode (I/II) loading are

$$u_r=\sum_{n=1}^{\infty}\mathrm{Re}\left[\frac{r^{\lambda_n^I}A_n}{2G}\left[\begin{matrix}\left(3-4\eta-\lambda_n^I\right)\cos\left(\lambda_n^I-1\right)\theta\\ +\left(\lambda_n^I\cos 2\alpha+\cos 2\lambda_n^I\alpha\right)\cos\left(\lambda_n^I+1\right)\theta\end{matrix}\right]\right]+u_{rc}^I$$
$$+\sum_{n=1}^{\infty}\mathrm{Re}\left[\frac{r^{\lambda_n^{II}}B_n}{2G}\left[\begin{matrix}-\left(3-4\eta-\lambda_n^{II}\right)\sin\left(\lambda_n^{II}-1\right)\theta\\ -\left(\lambda_n^{II}\cos 2\alpha-\cos 2\lambda_n^{II}\alpha\right)\sin\left(\lambda_n^{II}+1\right)\theta\end{matrix}\right]\right]+u_{rc}^{II}\tag{3.59}$$

and

$$u_\theta = \sum_{n=1}^{\infty} \mathrm{Re}\left[\frac{r^{\lambda_n^I} A_n}{2G}\left[\begin{array}{c}\left(3-4\eta+\lambda_n^I\right)\sin\left(\lambda_n^I-1\right)\theta \\ -\left(\lambda_n^I\cos 2\alpha+\cos 2\lambda_n^I\alpha\right)\sin\left(\lambda_n^I+1\right)\theta\end{array}\right]\right] + u_{\theta c}^I$$

$$+\sum_{n=1}^{\infty} \mathrm{Re}\left[\frac{r^{\lambda_n^{II}} B_n}{2G}\left[\begin{array}{c}\left(3-4\eta+\lambda_n^{II}\right)\cos\left(\lambda_n^{II}-1\right)\theta \\ -\left(\lambda_n^{II}\cos 2\alpha-\cos 2\lambda_n^{II}\alpha\right)\cos\left(\lambda_n^{II}+1\right)\theta\end{array}\right]\right] + u_{\theta c}^{II} \tag{3.60}$$

$$\left(n \neq 2 \text{ for } B_n\right)$$

where the constant η can be obtained from Eq. (3.57) for plane stress and plane strain conditions. Those constants u_{rc}^I, u_{rc}^{II}, $u_{\theta c}^I$ and $u_{\theta c}^{II}$ represent the rigid body modes of deformation and can be given as

$$\begin{array}{ll} u_{rc}^I = 4\dfrac{A_0}{2G}(1-\eta)\cos\theta, & u_{rc}^{II} = 4\dfrac{B_0}{2G}(1-\eta)\sin\theta, \\ u_{\theta c}^I = -4\dfrac{A_0}{2G}(1-\eta)\sin\theta, & u_{\theta c}^{II} = 4\dfrac{B_0}{2G}(1-\eta)\cos\theta + 4r\dfrac{B_2}{2G}(1-\eta), \end{array} \tag{3.61}$$

3.2.6 Displacement components in the Cartesian coordinate system

Displacement fields in the Cartesian coordinate system can be obtained from the displacement fields in the polar coordinates using the following equation

$$\begin{Bmatrix} u \\ v \end{Bmatrix} = \begin{bmatrix} \cos\theta & -\sin\theta \\ \sin\theta & \cos\theta \end{bmatrix} \begin{Bmatrix} u_r \\ u_\theta \end{Bmatrix} \tag{3.62}$$

The displacement fields in the infinite series form under the mixed mode (I/II) loading conditions in the Cartesian coordinate system can be obtained using Eq. (3.62) as

$$u = \sum_{n=1}^{\infty} \mathrm{Re}\left[\frac{A_n}{2G} r^{\lambda_n^I}\left\{\left(\kappa+\lambda_n^I\cos 2\alpha+\cos 2\alpha\lambda_n^I\right)\cos\lambda_n^I\theta-\lambda_n^I\cos\left(\lambda_n^I-2\right)\theta\right\}\right]+u_R^I$$

$$+\sum_{n=1}^{\infty} \mathrm{Re}\left[\frac{B_n}{2G} r^{\lambda_n^{II}}\left\{\left(-\kappa-\lambda_n^{II}\cos 2\alpha+\cos 2\alpha\lambda_n^{II}\right)\sin\lambda_n^{II}\theta+\lambda_n^{II}\sin\left(\lambda_n^{II}-2\right)\theta\right\}\right]+u_R^{II}$$

$$\left(n \neq 2 \text{ for } B_n\right)$$

$$\tag{3.63}$$

and

$$v=\sum_{n=1}^{\infty}\mathrm{Re}\left[\frac{A_n}{2G}r^{\lambda_n^I}\left\{\left(\kappa-\lambda_n^I\cos 2\alpha-\cos 2\alpha\lambda_n^I\right)\sin\lambda_n^I\theta+\lambda_n^I\sin\left(\lambda_n^I-2\right)\theta\right\}\right]$$
$$+\sum_{n=1}^{\infty}\mathrm{Re}\left[\frac{B_n}{2G}r^{\lambda_n^{II}}\left\{\left(\kappa-\lambda_n^{II}\cos 2\alpha+\cos 2\alpha\lambda_n^{II}\right)\cos\lambda_n^{II}\theta+\lambda_n^{II}\cos\left(\lambda_n^{II}-2\right)\theta\right\}\right]+v_R^{II}$$
$$\left(n\neq 2 \text{ for } B_n\right) \tag{3.64}$$

where κ is Kolosov constant and can be given as

$$\kappa=\begin{cases}\dfrac{(3-\nu)}{1+\nu} & \text{for plane stress}\\ 3-4\nu & \text{for plane strain}\end{cases} \tag{3.65}$$

and the constants u_R^I and u_R^{II} represent rigid body translation and rotation associated with the u-displacement field in the mode I and mode II loading conditions, respectively, and v_R^{II} in Eq. (3.64) comprises both the rigid body translation and rotation associated with the v-displacement field in the mode II loading. There are no translation or rotational components in the v-displacement field under the mode I loading. Considering $\lambda_0^I=\lambda_0^{II}=0$ (Ayatollahi and Nejati, 2011a) and $\lambda_2^{II}=1$, these constants can be obtained as

$$u_R^I=\frac{\kappa+1}{2G}A_0;\quad u_R^{II}=-\frac{\kappa+1}{2G}B_2 r\sin\theta;\quad v_R^{II}=\frac{\kappa+1}{2G}(B_0+B_2 r\cos\theta) \tag{3.66}$$

where A_0 and B_0 are the Williams' coefficients corresponding to the rigid body translation and B_2 is the Williams' coefficient corresponding to the rigid body rotations. It is to be noted that these rigid body coefficients should not be omitted from Eqs. (3.63) and (3.64) and should be considered for the accurate computation of the NSIFs. The role of the rotational coefficient B_2 in the mode II displacement field will be discussed in the next chapter (Section 4.2).

3.3 NSIFs of a sharp V-notch

The notch stress intensity factor (NSIF) is defined in a way similar to that of the SIF of a crack (Gross and Mendelson, 1972). It is a group parameter combining three main variables, the far-field stress (σ_∞ for mode I and τ_∞ for mode II), notch length a and notch angle γ (Figure 3.4). It is a function of the notch angle γ because the strength of singularity $(\lambda_1^{I/II}-1)$ depends on the notch angle. Irwin (1958) combined the two variables σ_∞ and a to form a new variable (K) for the crack problems. Thus, the SIF is regarded as an important parameter for the cracked components and is a measure of the strength of the singularity at the crack tip. For example, for an infinite plate containing center crack of length $2a$ subjected to the far-field stresses σ_α (mode I) and τ_α (mode II) can be given as (Irwin, 1958)

$$K_I = \sigma_\infty \sqrt{\pi a} \quad \text{and} \quad K_{II} = \tau_\infty \sqrt{\pi a} \tag{3.67}$$

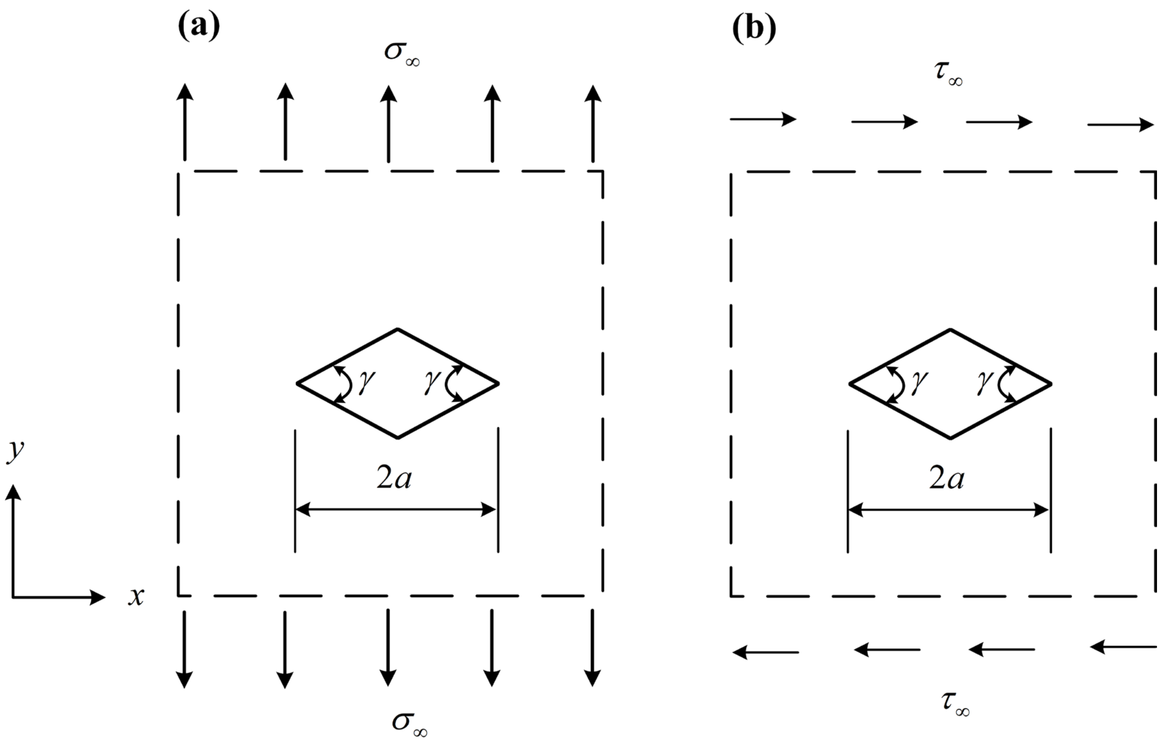

Figure 3.4. Infinite notched plates with a central notch of length $2a$ and notch angle γ .

Similar to the cracked configurations, the NSIF also measures the strength of singularity of the notch tip and can be given, say for example, for the center notched infinite plates (Figure 3.4) subjected to the mode I and mode II loading as

$$K_I = \sigma_\infty \sqrt{\pi} a^{1-\lambda_1^I} \quad \text{and} \quad K_{II} = \tau_\infty \sqrt{\pi} a^{1-\lambda_1^{II}} \tag{3.68}$$

Thus, realizing the similarity, the NSIF (K) has been defined formally as (Gross and Mendelson, 1972)

$$K_I = \sqrt{2\pi} \lim_{r \to 0} r^{1-\lambda_1^I} \sigma_{\theta\theta}\left(\theta = 0\right) \tag{3.69}$$

in the mode I loading and

$$K_{II} = \sqrt{2\pi} \lim_{r \to 0} r^{1-\lambda_1^{II}} \sigma_{r\theta}\left(\theta = 0\right) \tag{3.70}$$

in the mode II loading.

For calculating the NSIFs K_I and K_{II} (Eqs. (3.69) and (3.70)), the first eigenvalues λ_1^I and λ_1^{II} are required for the mode I and mode II, respectively. This is because, only the first eigenvalue provides the strength of the singularity $(\lambda_1^{I\,or\,II} - 1)$ at the notch tip (Gross and Mendelson, 1972). Substituting $\sigma_{\theta\theta}$ and $\sigma_{r\theta}$ from Eqs. (3.47) and (3.48), respectively, in Eqs. (3.69) and (3.70), one would get a more convenient form of the NISFs in terms of the Williams' coefficients A_1 and B_1 as

$$K_I = \sqrt{2\pi} \lambda_1^I \left(1 + \lambda_1^I - \lambda_1^I \cos 2\alpha - \cos 2\alpha\lambda_1^I\right) A_1 \tag{3.71}$$

and

$$K_{II} = \sqrt{2\pi} \lambda_1^{II} \left(-1 + \lambda_1^{II} - \lambda_1^{II} \cos 2\alpha + \cos 2\alpha\lambda_1^{II}\right) B_1 \tag{3.72}$$

The above definitions of K_I and K_{II} are employed in the present work.

3.4 Muller's method of solving the characteristic equations

As discussed earlier, Eqs. (3.27) and (3.28) represent the characteristic equations, and the roots of these equations or eigenvalues depend on the notch angle γ. The Muller's method (Press et al., 2007) is one of the efficient and widely used methods in sharp V-notch problems. This method is a generalization of the secant method. Instead of starting with two initial values and then joining them with a straight line as in the secant method, the Muller's method starts with the three initial approximations of the root. The method then joins these roots with a second-degree polynomial (a parabola), and a quadratic formula is used to find the root of the quadratic for the next approximation. The benefit of using quadratic interpolation is that complex roots can also be determined conveniently. Given three previous guesses for the root of a eigenvalue λ_{i-2}, λ_{i-1} and λ_i, and the values of the polynomial $P(\lambda)$ at those points, the next approximation λ_{i+1} is produced by the following formulas (Press et al., 2007),

$$q \equiv \frac{\lambda_i - \lambda_{i-1}}{\lambda_{i-1} - \lambda_{i-2}} \tag{3.73}$$

Defining,

$$A_m \equiv qP(\lambda_i) - q(1+q)P(\lambda_{i-1}) + q^2 P(\lambda_{i-2}) \tag{3.74}$$

$$B_m \equiv (2q+1)P(\lambda_i) - (1+q)^2 P(\lambda_{i-1}) + q^2 P(\lambda_{i-2}) \tag{3.75}$$

$$C_m \equiv (q+1)P(\lambda_i) \tag{3.76}$$

Using the values of A_m, B_m and C_m, the constants D_1 and D_2 can be defined as

$$D_1 = B_m + \sqrt{B_m^2 - 4A_m C_m} \tag{3.77}$$

$$D_2 = B_m - \sqrt{B_m^2 - 4A_m C_m} \tag{3.78}$$

$$D = \max\left(\left|D_1\right| \text{ or } \left|D_2\right|\right) \tag{3.79}$$

and considering the initial guess values of λ_{i-2}, λ_{i-1} and λ_i, the value of λ in the next iteration can be found as (Press et al., 2007)

$$\lambda_{i+1} = \lambda_i - \left(\lambda_i - \lambda_{i-1}\right)\frac{2C_m}{D} \tag{3.80}$$

If $er = \left|\lambda_{i+1} - \lambda_i\right|$ and $er_{\max}$ is the user-defined maximum allowable error limit, when $er > er_{\max}$ the iteration is continued, otherwise, the iteration is stopped and λ_{i+1} will be the desired eigenvalue for the particular notch angle γ. It should be noted that because of the presence of a complex denominator D in Eq. (3.80), the eigenvalues can be complex in the next iteration even though the initial guess was real. Using the Muller's method (Press et al., 2007), the n-th eigenvalues for both mode I and mode II (Eqs. (3.27) and (3.28)) can be obtained. However, only the first eigenvalues of mode I and mode II eigenvalues are required to determine the NSIFs and the singular stress fields. The first three eigenvalues of mode I and the first four eigenvalues of mode II for various notch angles are shown in Figure 3.3, which are obtained using the Muller's method.

3.5 Finite element formulation

The proposed techniques in the present investigation are post-processing techniques and hence require various field variables from the numerical analyses for the accurate determination of the NSIFs under mode I, mode II and mixed mode (I/II) loading conditions. Thus, all the numerical analyses of the sharp V-notched configurations of the present investigation have been carried out using the displacement-based FE method available in the commercial software ANSYS® (ANSYS, 2007). In the present work, PLANE183 element available in ANSYS® (ANSYS, 2007) is used for discretization of the notched domains. PLANE183 is a standard eight-noded isoparametric quadrilateral element (Q8). These Q8 elements can be used for the analysis under both plane stress and plane strain conditions. The Q8 element is collapsed into triangular elements to form a standard spider-web pattern at the notch tip.

One of the striking features of the sharp V-notched problems is the absence of singular or special elements (such as quarter-point elements in the crack problems) at the notch tip for modeling the varying singularity (which depends on the notch angle) at the sharp V-notch. Despite knowing that the tip of the sharp V-notch is a high-stress gradient zone, due to the unavailability of the singular elements, conventional finite elements such as the collapsed Q8 elements are usually deployed around the notch tip in a spider-web pattern (Carpenter, 1984c; Liu et al., 2008, Labossiere and Dunn, 1998; Chang and Kang, 2002; Chang and Wu, 2003; Kim and Cho, 2009; Lazzarin et al., 2010; Ayatollahi and Nejati, 2011a; Treifi and Oyadiji, 2013c). Solution of the field variables at such conventional elements around the notch is then employed to compute the NSIFs. Thus, the conventional Q8 elements are employed throughout the notched configuration for the FE analyses, including the notch tips in the present work. A brief finite element formulation of the standard Q8 is element is also presented here. Figure 3.5 shows the typical Q8 element in the physical and natural coordinate systems.

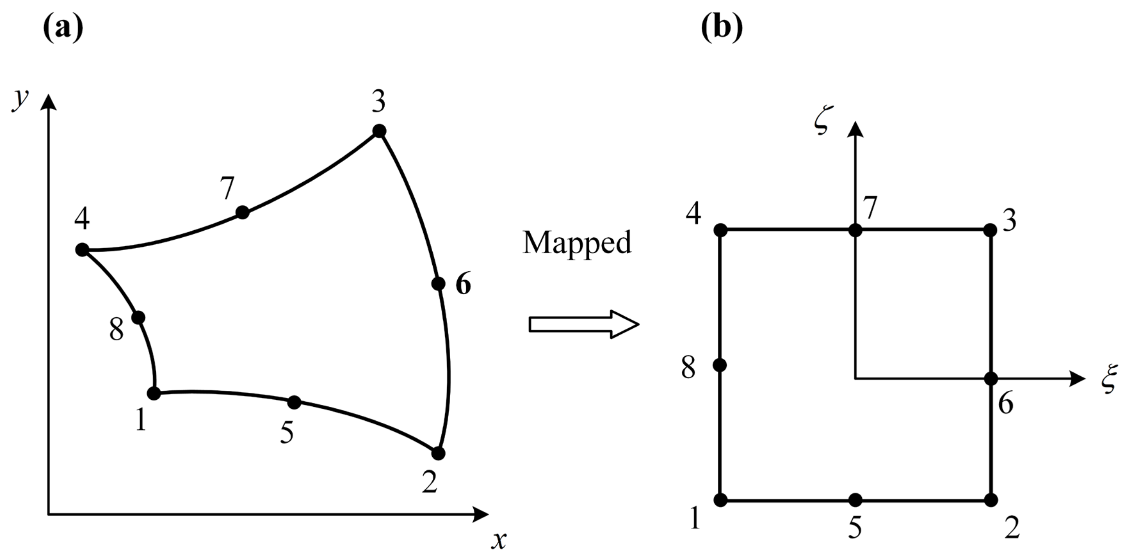

Figure 3.5. Eight noded quadrilateral isoparametric element represented in the natural coordinates.

Being isoparametric element, the geometric variables are expressed in a similar way as the field variables. Therefore, the geometric variables are expressed as

$$x = \sum_{i=1}^{8} N_i x_i \quad \text{and} \quad y = \sum_{i=1}^{8} N_i y_i \tag{3.81}$$

Similarly, the field variables are also represented as

$$u = \sum_{i=1}^{8} N_i u_i \quad \text{and} \quad v = \sum_{i=1}^{8} N_i v_i \tag{3.82}$$

where $(x_i,\, y_i)$ and $(u_i,\, v_i)$ are the nodal coordinates and nodal displacements, respectively, $N_i\,(i = 1,\, 2...,\, 8)$ are the shape functions. The shape function must be expressed in a natural coordinate system for numerical integration. Natural coordinate (ξ, ζ) systems are dimensionless and have a maximum absolute magnitude of one (Figure 3.5b). They are defined with reference to the element rather than with reference to the global coordinate system in which the element resides (Figure 3.5a). The shape functions for a Q8 element can be expressed in the natural coordinates as

$$\begin{aligned}
N_1 &= \frac{1}{4}(1+\xi)(1-\zeta) - \frac{1}{2}(N_8 + N_5) \qquad & N_5 &= \frac{1}{2}(1-\xi^2)(1-\zeta) \\
N_2 &= \frac{1}{4}(1-\xi)(1+\zeta) - \frac{1}{2}(N_5 + N_6) \qquad & N_6 &= \frac{1}{2}(1+\xi)(1-\zeta^2) \\
N_3 &= \frac{1}{4}(1-\xi)(1-\zeta) - \frac{1}{2}(N_6 + N_7) \qquad & N_7 &= \frac{1}{2}(1-\xi^2)(1-\zeta) \\
N_4 &= \frac{1}{4}(1+\xi)(1-\zeta) - \frac{1}{2}(N_7 + N_8) \qquad & N_8 &= \frac{1}{2}(1+\xi)(1-\zeta^2)
\end{aligned} \tag{3.83}$$

The displacements within the element in terms of the nodal displacements can be expressed as

$$\{U\} = \begin{Bmatrix} u \\ v \end{Bmatrix} = [N]\{X\}_e \tag{3.84}$$

where $\{U\}$ is the displacement vector of an element, with the shape function matrix

$$[N] = \begin{bmatrix} N_1 & 0 & N_2 & 0 & \ldots & N_7 & 0 & N_8 & 0 \\ 0 & N_1 & 0 & N_2 & \ldots & 0 & N_7 & 0 & N_8 \end{bmatrix} \tag{3.85}$$

and the nodal displacement

$$\{X\}_e^T = \{u_1 \quad v_1 \quad u_2 \quad v_2 \quad \ldots \quad u_7 \quad v_7 \quad u_8 \quad v_8\} \tag{3.86}$$

The governing equations of equilibrium for the plane elastostatic problems are given by

$$\frac{\partial \sigma_{xx}}{\partial x} + \frac{\partial \sigma_{xy}}{\partial y} + f_x = 0 \tag{3.87}$$

and

$$\frac{\partial \sigma_{xy}}{\partial x} + \frac{\partial \sigma_{yy}}{\partial y} + f_y = 0 \tag{3.88}$$

where f_x and f_y denote the body force per unit volume along the x and $y-$directions, respectively, σ_{xx} and σ_{yy} are the normal stresses and σ_{xy} is the in-plane shear stress. The strain matrix associated with the plane stress and plane strain problems in terms of the nodal displacement vector is then given by

$$\{\varepsilon\} = \begin{Bmatrix} \varepsilon_{\mathrm{xx}} \\ \varepsilon_{\mathrm{yy}} \\ \gamma_{\mathrm{xy}} \end{Bmatrix} = \begin{Bmatrix} \dfrac{\partial u}{\partial x} \\ \dfrac{\partial v}{\partial y} \\ \dfrac{\partial u}{\partial y} + \dfrac{\partial v}{\partial x} \end{Bmatrix} = \begin{bmatrix} \dfrac{\partial}{\partial x} & 0 \\ 0 & \dfrac{\partial}{\partial y} \\ \dfrac{\partial}{\partial y} & \dfrac{\partial}{\partial x} \end{bmatrix} \begin{Bmatrix} u \\ v \end{Bmatrix} = \begin{bmatrix} \dfrac{\partial}{\partial x} & 0 \\ 0 & \dfrac{\partial}{\partial y} \\ \dfrac{\partial}{\partial y} & \dfrac{\partial}{\partial x} \end{bmatrix} [N]\{X\}_e \tag{3.89}$$

According to the standard notation, the strain matrix is

$$\{\varepsilon\} = [B]\{X\}_e \tag{3.90}$$

The matrix $[B]$ can be written as

$$[B] = \begin{bmatrix} \partial/\partial x & 0 \\ 0 & \partial/\partial y \\ \partial/\partial y & \partial/\partial x \end{bmatrix} [N] \tag{3.91}$$

The stress-strain relationship for an element is given by

$$\{\sigma\}=\begin{Bmatrix}\sigma_{xx}\\ \sigma_{yy}\\ \sigma_{xy}\end{Bmatrix}=[D]_e\{\varepsilon\}=[D]_e[B]\{X\}_e \tag{3.92}$$

where $[D]_e$ is the elasticity matrix and is given for the plane stress and plane strain problems for isotropic materials as

$$[D]_{Plane-Stress}=\frac{E}{1-\gamma^2}\begin{bmatrix}1 & \gamma & 0\\ \gamma & 1 & 0\\ 0 & 0 & \frac{1-\gamma}{2}\end{bmatrix} \tag{3.93}$$

and

$$[D]_{Plane-Strain}=\frac{E(1-\gamma)}{(1-2\gamma)(1+\gamma)}\begin{bmatrix}1 & \frac{\gamma}{1-\gamma} & 0\\ \frac{\gamma}{1-\gamma} & 1 & 0\\ 0 & 0 & \frac{1-2\gamma}{2(1-\gamma)}\end{bmatrix} \tag{3.94}$$

Here E, ν and G are the Young's modulus, Poisson's ratio, and shear modulus, respectively. The displacements, derivatives of the displacements, strains, and stresses at any point within the element can be easily computed once $\{X\}_e$ of an element is known. The element stiffness matrix which relates the unknown nodal displacements to the applied forces on an element can be given as

$$[K]_e=t\int_A [B]^T[D][B]\,dxdy \tag{3.95}$$

where $[D]$ is the elasticity matrix consisting of element material constants. The matrix $[B]$ relates strains and displacements, is a function of (x, y) and t is the thickness of the element (assumed constant). The differential area $dxdy$ can be replaced by

$$dxdy = |J| \ d\xi \, d\zeta \tag{3.96}$$

where $|J|$ is the determinant of the Jacobian matrix and is given by

$$|J| = \frac{\partial x}{\partial \xi}\frac{\partial y}{\partial \zeta} - \frac{\partial x}{\partial \zeta}\frac{\partial y}{\partial \xi} \tag{3.97}$$

Then Eq. (3.95) becomes

$$[K]_e = t\int_{-1}^{1}\int_{-1}^{1}\left[B(\xi,\zeta)\right]^T [D]\left[B(\xi,\zeta)\right]|J|\,d\xi d\zeta \tag{3.98}$$

where

$$\left[B(\xi,\eta)\right] = \begin{pmatrix} \dfrac{\delta\xi}{\delta x} & \dfrac{\delta\zeta}{\delta x} & 0 & 0 \\ 0 & 0 & \dfrac{\delta\xi}{\delta y} & \dfrac{\delta\zeta}{\delta y} \\ \dfrac{\delta\xi}{\delta x} & \dfrac{\delta\zeta}{\delta y} & \dfrac{\delta\xi}{\delta x} & \dfrac{\delta\zeta}{\delta x} \end{pmatrix} \begin{pmatrix} \dfrac{\delta}{\delta\xi} & 0 \\ \dfrac{\delta}{\delta\zeta} & 0 \\ 0 & \dfrac{\delta}{\delta\xi} \\ 0 & \dfrac{\delta}{\delta\zeta} \end{pmatrix} [N] \tag{3.99}$$

The above equation is now entirely a function of local coordinates (ξ, ζ). Numerical integration is required to be employed over the area for the evaluation of the element stiffness matrix $[K]_e$.

3.6 Collocation method

The collocation method is a point-matching technique used for computing the stress intensity factors of cracks and sharp V-notches (Kobayashi et al., 1964; Gross and Srawley, 1965; Anderson, 2015). This approach involves finding stress or displacement functions that satisfy the boundary conditions at various nodes of a finite element mesh and determining the NSIFs from these functions. In a collocation method, the Williams coefficients are inferred from nodal quantities (i.e., stresses or displacements). The minimum number of nodes used in the collocation method corresponds to the number of unknown coefficients. However, the results can be improved by considering more than the minimum number of nodes and solving for the unknown coefficients by least-squares methods. In the collocation method, the selection of nodal positions and node numbers play an important role in the accuracy of the calculated NSIFs. A robust and simple collocation method is proposed in this thesis (Chapter 5) to determine the mixed mode (I/II) NSIFs of sharp V-notched configurations. In the proposed collocation method, the unknown Williams coefficients A_1 and B_1 for mode I and mode II, respectively, are determined using the collocation method using the finite element displacements at nodes along the notch flanks (which will be discussed in Chapter 5 elaborately). Two approaches for selecting the appropriate collocation nodes are also discussed in Chapter 5.

3.7 Summary

In this chapter, the theoretical background required for understanding and implementation of the proposed methods is presented. This includes an exposition of the stress, strain, and displacement components in the polar and Cartesian coordinate systems under mixed mode (I/II) conditions for a sharp V-notched problem. These are presented with the help of the Williams eigenfunction expansion approach. The procedure for the numerical estimation of the eigenvalues using the Muller's iteration method is also presented in this chapter. Some issues of the FE simulation of the notched configurations and formulation of the eight nodded isoparametric quadrilateral element is also discussed here.

Chapter 4

Proposed point substitution method

4.1 Introduction

In this chapter, a simple, robust, and efficient point substitution type displacement-based method for the finite element computation of the NSIFs of the sharp V-notched configurations under the mode I, mode II and mixed mode (I/II) loading conditions has been proposed. A novel feature of the proposed method is that it utilizes the notch flank displacements only at a single point for mode I and at two points for mode II loading conditions for the computation of the NSIFs. These critical points of the notch tip elements have been identified using the least-square minimization of the error and the slope of the displacement within the notch tip elements. The NSIFs of the various mode I, mode II and mixed mode (I/II) benchmark problems have been estimated and compared with the available or published reference solutions in this chapter. The convergence characteristics of the proposed method have also been studied using meshes of various mesh densities.

4.2 Formulation of the proposed point substitution method

This section first presents the formulation of the proposed point substitution method for the accurate estimation of the NSIFs. Let us consider a two-dimensional sharp V-notched linear elastic body made of isotropic and homogeneous material with a notch opening angle

$\gamma\left(=360^\circ-2\alpha\right)$ and subjected to an arbitrary in-plane loading as shown in Figure 4.1. The displacement field around the notch tip using Eqs. (3.63) and (3.64) under the mixed mode (I/II) loading can be written as

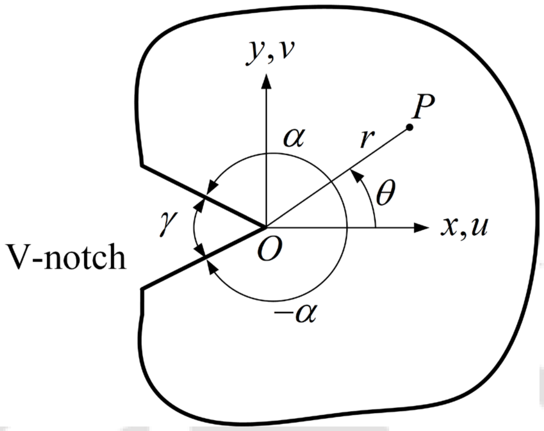

Figure 4.1. Notch tip local coordinate system.

$$u=\frac{\kappa+1}{2G}A_0+\frac{A_1}{2G}r^{\lambda_1^I}\left\{\left(\kappa+\lambda_1^I\cos 2\alpha+\cos 2\alpha\lambda_1^I\right)\cos\lambda_1^I\theta-\lambda_1^I\cos\left(\lambda_1^I-2\right)\theta\right\}$$
$$+\frac{B_1}{2G}r^{\lambda_1^{II}}\left\{\left(-\kappa-\lambda_1^{II}\cos 2\alpha+\cos 2\alpha\lambda_1^{II}\right)\sin\lambda_1^{II}\theta+\lambda_1^{II}\sin\left(\lambda_1^{II}-2\right)\theta\right\}-\frac{\kappa+1}{2G}B_2 r\sin\theta \tag{4.1}$$

and

$$v=\frac{A_1}{2G}r^{\lambda_1^I}\left\{\left(\kappa-\lambda_1^I\cos 2\alpha-\cos 2\alpha\lambda_1^I\right)\sin\lambda_1^I\theta+\lambda_n^I\sin\left(\lambda_1^I-2\right)\theta\right\}+\frac{\kappa+1}{2G}B_0$$
$$+\frac{B_1}{2G}r^{\lambda_1^{II}}\left\{\left(\kappa-\lambda_1^{II}\cos 2\alpha+\cos 2\alpha\lambda_1^{II}\right)\cos\lambda_1^{II}\theta+\lambda_1^{II}\cos\left(\lambda_1^{II}-2\right)\theta\right\}+\frac{\kappa+1}{2G}B_2 r\cos\theta \tag{4.2}$$

where κ is Kolosov constant and can be given as

$$\kappa=\begin{cases}3-4\nu & \text{for plane strain}\\ \dfrac{\left(3-\nu\right)}{1+\nu} & \text{for plane stress}\end{cases} \tag{4.3}$$

and u and v are the displacement components in the x and $y-$directions (Figure 4.1), respectively. In Eqs. (4.1) and (4.2), the displacement components contain only the leading term of the infinite series and the rigid body displacements. The leading terms of displacement components correspond to the first eigenvalues λ_1^I and λ_1^{II} for mode I and mode II, respectively. The rigid body rotation corresponds to the second eigenvalue of mode II λ_1^{II}. The first eigenvalue of mode I and the first and second eigenvalues of mode II are listed in Table 4.1. Although they are presented in Figure 3.3, the numerical values of λ_1^I, λ_1^{II} and λ_2^{II} are listed in Table 4.1 for convenience as these values will be more frequently used in the numerical sections (Sections 4.3, 5.4 and 6.4) for determining the NSIFs.

Table 4.1. First eigenvalues for mode I and mode II for different notch angles.

$\gamma(°)$	λ_1^I	λ_1^{II}	λ_2^{II}
0	0.5000000	0.5000000	1
15	0.5001793	0.5452545	1
30	0.5014530	0.5981919	1
45	0.5050097	0.6597016	1
50	0.5069328	0.6822948	1
60	0.5122214	0.7309007	1
75	0.5247234	0.8132210	1
90	0.5444837	0.9085292	1
105	0.5738686	1.0193039	1
120	0.6157311	1.1489128	1
135	0.6735834	1.3020860	1
150	0.7519746	1.4858117	1
165	0.8573319	1.7113300	1
180	1.0000000	2.0000000	1

As discussed earlier (in Chapter 3), the constants A_0 and B_0 are the Williams' coefficients corresponding to the rigid body translations in the mode I and mode II, respectively, and B_2 is the Williams' coefficient corresponding to the rigid body rotation in mode II. The rotational coefficient B_2 plays an important role in the accurate determination of the mode II NSIFs. Discarding the above constants introduces significant errors in the computation of the NSIFs (Ayatollahi and Nejati, 2011a). The rigid body rotation of the notch with respect to the notch tip can be shown as $\varphi = -(\kappa+1)B_2/2G$. It can be noticed that the magnitude of the rigid body rotation of a V-notch, denoted by φ, is equal to the angle between the bisectors of the notch before and after the deformation (Figure 4.2). The rigid body translation of the notch tip $u_0 = (\kappa+1)A_0/2G$ and $v_0 = (\kappa+1)B_0/2G$, and the rigid body rotation φ with respect to the notch tip are shown in Figure 4.2.

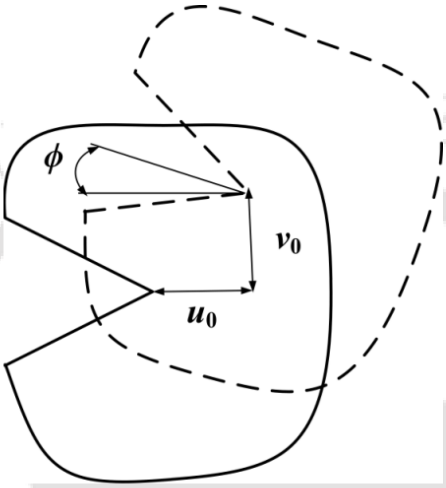

Figure 4.2. Rigid body translation and rigid body rotation with respect to the notch tip.

Let us consider the $v-$displacement field in the vicinity of the notch tip as given by Eq. (4.2) above. Analytical notch opening displacement (NOD) under the mode I loading conditions can be defined using Eq. (4.2) as

$$\Delta v = v^I_{\theta=+\alpha} - v^I_{\theta=-\alpha} = 2v^I_{\theta=+\alpha} = 2\frac{A_1}{2G}r^{\lambda_1^I}\left[\begin{array}{c}\left(\kappa - \lambda_1^I\cos 2\alpha - \cos 2\alpha\lambda_1^I\right)\sin\lambda_1^I\alpha \\ +\lambda_1^I\sin\left(\lambda_1^I - 2\right)\alpha\end{array}\right] = 2A_1C_1r^{\lambda_1^I} \tag{4.4}$$

where $v^I_{\theta=+\alpha}$ and $v^I_{\theta=-\alpha}$ are the mode I $v-$component in Eq. (4.2). Similarly, the notch sliding displacement (NSD) for the mode II loading can be defined using Eq. (4.1) as

$$\begin{aligned}\Delta u = u^{II}_{\theta=+\alpha} - u^{II}_{\theta=-\alpha} = 2u^{II}_{\theta=+\alpha} = 2\frac{B_1}{2G}r^{\lambda_1^{II}}&\left[\begin{array}{c}\left(-\kappa - \lambda_1^{II}\cos 2\alpha + \cos 2\alpha\lambda_1^{II}\right)\sin\lambda_1^{II}\alpha \\ +\lambda_1^{II}\sin\left(\lambda_1^{II} - 2\right)\alpha\end{array}\right] \\ &-2\frac{\kappa+1}{2G}B_2 r\sin\alpha \quad = 2B_1C_2r^{\lambda_1^{II}} + 2B_2C_3r\end{aligned} \tag{4.5}$$

where $u^{II}_{\theta=+\alpha}$ and $u^{II}_{\theta=-\alpha}$ are the mode II $u-$component in Eq. (4.1) and C_1, C_2 and C_3 are constants which depend upon the notch angle, eigenvalue, and κ. It can be easily shown that in the case of mixed mode (I/II) loading conditions also that the NOD and NSD equal to $v^{I}_{\theta=+\alpha} - v^{I}_{\theta=-\alpha}$ and $u^{II}_{\theta=+\alpha} - u^{II}_{\theta=-\alpha}$, respectively. Thus, in all loading conditions, A_1 and B_1 can be computed from the NOD equation (Eq. (4.4)) and NSD equation (Eq. (4.5)), respectively.

4.2.1 Determination of mode I NSIF

As discussed in Chapter 3, the collapsed Q8 elements are placed around the notch tip in a spider-web pattern for modeling the singularity in the finite element analysis. A collapsed Q8 element is a six-node quadratic triangular element with mid-side nodes at the mid-sides as shown in Figure 4.3a. Let us consider two such notch tip triangular elements which are connected to the notch flanks, as shown in Figure 4.3a. The u and $v-$displacements along the entire domain of the notch tip elements can be written in a quadratic form as

$$u = a_1 + a_2 x + a_3 y + a_4 x^2 + a_5 xy + a_6 y^2 \tag{4.6}$$

and

$$v = a_7 + a_8 x + a_9 y + a_{10} x^2 + a_{11} xy + a_{12} y^2 \tag{4.7}$$

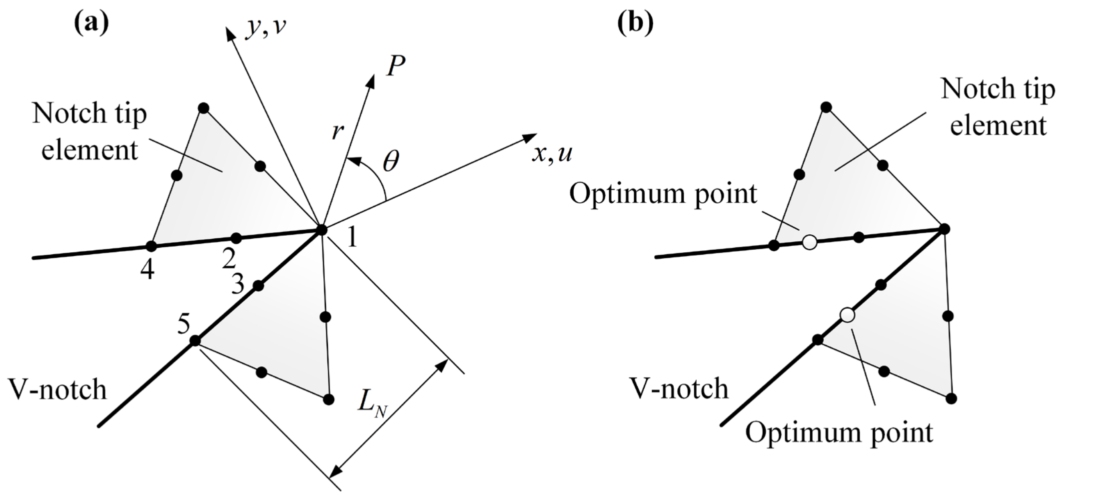

Figure 4.3. (a) Typical six-node quadratic triangular notch tip elements and (b) optimum points in the notch tip elements.

where $a_i\left(i=1-12\right)$ are arbitrary constants of the polynomials.

Referring to Figure 4.3a, node 1 is situated at the notch tip and is common to both the triangles. The edges of the two triangular elements 1–2–4 and 1–3–5 are along the notch flanks above and below the notch bisector line (i.e., $x-$axis), respectively. Let r be the radial distance from the notch tip. It can be noted that both the notch tip elements are exactly the same and are placed symmetrically above and below the notch bisector line (due to the spider-web pattern at the notch tip). Using Eq. (4.7), the finite element solution of the $v-$displacement component along the line 1–2–4 can be estimated as

$$\begin{aligned} v_{1-2-4}^{FE} &= a_7 + a_8\left(r\cos\alpha\right) + a_9\left(r\sin\alpha\right) + a_{10}\left(r\cos\alpha\right)^2 \\ &\qquad + a_{11}\left(r\cos\alpha\right)\left(r\sin\alpha\right) + a_{12}\left(r\sin\alpha\right)^2 \\ &= r^2\left(a_{10}\cos^2\alpha + a_{11}\cos\alpha\sin\alpha + a_{12}\sin^2\alpha\right) \\ &\qquad + r\left(a_8\cos\alpha + a_9\sin\alpha\right) + a_7 \\ &= Ar^2 + Br + C \end{aligned} \tag{4.8}$$

where v^{FE} represents the finite element solution. In the pure mode I loading, displacement of the node 1 (i.e., notch tip) along $y-$direction is zero; therefore

$$v_{1-2-4}^{FE}\left(r=0\right)=0 \tag{4.9}$$

From Eqs. (4.8) and (4.9), it can be shown that

$$C=0 \tag{4.10}$$

Therefore, the v^{FE} displacement along the line 1–2–4 in mode I and in the notch tip local coordinate system can be written as

$$v_{1-2-4}^{FE} = v_{\theta=+\alpha}^{FE} = Ar^2 + Br \tag{4.11}$$

where r is the distance from the notch tip $(0\le r\le L_N)$, L_N is the length of the notch tip element, and A and B are constants which can be determined from the nodal displacements at nodes 2 and 4 as

$$\begin{Bmatrix} A \\ B \end{Bmatrix} = \begin{bmatrix} r_2^2 & r_2 \\ r_4^2 & r_4 \end{bmatrix}^{-1} \begin{Bmatrix} v_2^{FE} \\ v_4^{FE} \end{Bmatrix} \tag{4.12}$$

where r_2 and r_4 are the radial distances from the notch tip to the nodes 2 and 4, respectively. The FE value of the NOD is thus can be written as

$$\Delta v^{FE} = 2Ar^2 + 2Br \tag{4.13}$$

Now the residual $\Re$ between the analytical NOD (Eq. (4.4)) and the FE NOD (Eq. (4.11)) can be written as

$$\Re = \left(\Delta v - \Delta v^{FE}\right)^2 = \left(2A_1C_1r^{\lambda_1^I} - 2Ar^2 - 2Br\right)^2 \tag{4.14}$$

In order that the residual $\Re$ reaches the minimum, the partial derivative of it with respect to the r must vanish, i.e.,

$$\frac{\partial \Re}{\partial r} = 0 \tag{4.15}$$

which simplifies to two simultaneous equations as

$$Ar^2 + Br = A_1C_1r^{\lambda_1^I} \tag{4.16}$$

and

$$2Ar + B = \lambda_1^I A_1C_1r^{\lambda_1^I - 1} \tag{4.17}$$

By solving Eqs. (4.16) and (4.17), r and A_1 can be determined as

$$r = r_{op} = -\frac{B\left(1-\lambda_1^I\right)}{A\left(2-\lambda_1^I\right)} \tag{4.18}$$

and

$$A_1 = \frac{Ar_{op}^2 + Br_{op}}{C_1 r_{op}^{\lambda_1^I}} = \frac{\Delta v^{FE}\big|_{r=r_{op}}}{C_1 r_{op}^{\lambda_1^I}} \tag{4.19}$$

where r_{op} is the optimum radius. In the above equations, A and B can be estimated using Eq. (4.12). Thus, by computing the r_{op} using Eq. (4.12) and $\Delta v^{FE}\big|_{r=r_{op}}$ at the point r_{op} (Figure 4.3b), the coefficient A_1 can then be determined using Eq. (4.19). Here, $\Delta v^{FE}\big|_{r=r_{op}}$ can be interpolated at r_{op} using shape functions or using Eq. (4.13). Thus, the mode I NSIF can be easily estimated in mode I and mixed mode (I/II) problems using Eq. (3.71). For convenience, this equation is presented here as

$$K_I = \sqrt{2\pi}\lambda_1^I \left(1 + \lambda_1^I - \lambda_1^I \cos 2\alpha - \cos 2\alpha\lambda_1^I\right) A_1 \tag{4.20}$$

From the study of various benchmark problems (with various notch angles and notch length to width ratios (a/w)), the ratio, $r_{opt} = r_{op}/L_N$ for the various notch angles is found and presented in Table 4.2. An important observation is that these values are close to each other and centered around the average value of 0.785. Further, these r_{opt} values are found to be independent of the notched configuration and depend only on the notch angle. Thus, one could employ the results in Table 4.2 directly for the estimation of the r_{op} or use Eq. (4.18). It will be shown later that the computed NSIFs at these points (Table 4.2) are found to be very accurate.

For graphical interpretation of Eq. (4.15), let us take logarithm on both sides of $v_{\theta=+\alpha}^I$ or $v_{\theta=-\alpha}^I$ (Eq. (4.4)), then the analytical $v-$displacement can be written as

$$\ln v = \lambda_1^I \ln r + \ln A_1 C_1 \tag{4.21}$$

Equation (4.21) is a straight line with a slope equals to λ_1^I on a logarithmic scale until a radial distance, which is the validity of Eq. (4.2). However, the logarithmic plot of the FE values of $v_{\theta=+\alpha}^{FE}$ (Eq. (4.11)) at various radial locations along the notch flank 1–2–4 of the notch tip element obviously does not show the theoretical trend as depicted in Eq. (4.21).

Figure 4.4a shows a plot of the $\ln\left(v_{\theta=+\alpha}^{FE}\right)$ versus $\ln\left(r/L_N\right)$. Evidently, the slope of $\ln\left(v_{\theta=+\alpha}^{FE}\right)$ is not constant and changes from point to point. The plot in Figure 4.4 is plotted from the results of a mode I example in Section 4.3.1 for $a/w = 0.4$ and $\gamma = 30°$.

Table 4.2. r_{opt} values for different notch angles.

$\gamma(°)$	$r_{opt} = r_{op}/L_N$
0	0.809
15	0.795
30	0.787
45	0.777
60	0.776
75	0.769
90	0.776
105	0.778
120	0.790

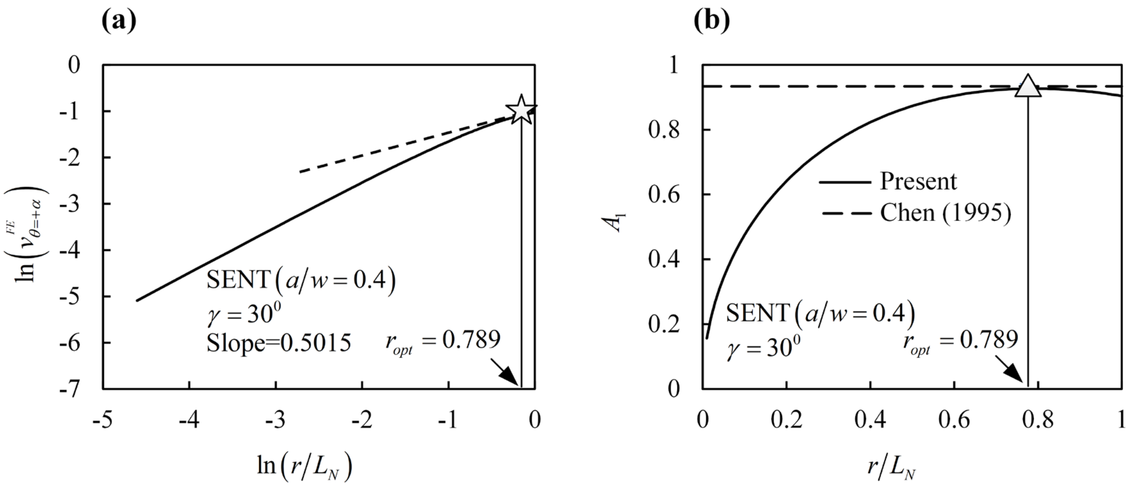

Figure 4.4. (a) A typical variation of $\ln\left(v_{\theta=+\alpha}^{FE}\right)$ with $\ln\left(r/L_N\right)$ along the notch flank 1–2–4 in Figure 4.3 and (b) accuracy of the coefficient A_1 (and hence $v_{\theta=+\alpha}^{FE}$) with r/L_N along the notch flank 1–2–4.

A close inspection of the graphs in Figure 4.4a shows that the slope is found to be equal to λ_1^I (as in Eq. (4.21)) at $\ln\left(r_{opt}\right)$ (Table 4.2), which further substantiates Eq. (4.15). It is furthermore interesting to mention here that, as shown in Figure 4.4b, A_1 and hence $v_{\theta=+\alpha}^{FE}$ at this point is more accurate as compared with other radii along the element edge 1–2–4.

Similar trends have been noticed in many benchmark examples on the mode I and mixed mode (I/II) loading conditions. Importantly, then $r_{opt} = r_{op} / L_N$ at which the slope becomes λ_1^I is also the same as given in Table 4.2 and depends only on the notch angle and independent of the geometry of the V-notched configuration. All these aspects are demonstrated further with the help of examples in Section 4.3.1.

To the knowledge of the author, for the first time, such characteristic of the Q8 element has been noticed within problems of the sharp V-notch. It will be shown later that very accurate mode I NSIFs can be computed even on the coarse meshes by the mere substitution of the Δv^{FE} at r_{op} in Eq. (4.19).

4.2.2 Determination of mode II NSIF

For the determination of the mode II NSIFs, the notch flank mode II $u-$displacement component is considered here (Eq. (4.1)). Estimation of the r_{op} or r_{opt} corresponding to this $u-$displacement using either the least-squares approach or by matching the slope by plotting $\ln\left(u_{\theta=+\alpha}^{FE}\right)$ and $\ln\left(r\right)$ along the notch flank 1–2–4 (as is done in the mode I loading conditions in the previous section) is not feasible as $u_{\theta=+\alpha}^{FE}$ (or $u_{\theta=-\alpha}^{FE}$) is always accompanied by the rigid body rotation term u_R^{II} (see Eq. (4.5)). Experience has shown that neglecting this rigid body term induces substantial error in the mode II NSIF. Therefore, to facilitate the computation of the mode II NSIFs in a simple manner, it is assumed that the mode II $u-$displacement component displays the same characteristics as that of mode I $v-$displacement component such that it provides maximum accuracy at the same r_{op} (hence same r_{opt}) as given in Table 4.2. Conversely, it is assumed that the slope of the mode II $u_{\theta=+\alpha}^{FE}$ displacement component along the notch flank 1–2–4 also approaches the theoretical value at the same optimum point r_{opt} in Table 4.2 and $u_{\theta=+\alpha}^{FE}$ is also accurate at this point. Accurate results of the mode II NSIFs in the following sections clearly demonstrate that this assumption is sufficiently reasonable for the mode II problems.

With this assumption, the finite element NSD value $\left(\Delta u^{FE}\right)$ can now be equated with the theoretical value given by Eq. (4.5) along the notch flank 1–2–4 of the notch tip element

$$\Delta u^{FE} = \Delta u = u^{II}_{\theta=+\alpha} - u^{II}_{\theta=-\alpha} = 2B_1C_2r^{\lambda_1^{II}} + 2B_2C_3r \tag{4.22}$$

Consistent with the assumption made previously and in order to estimate the two unknown coefficients B_1 and B_2, Eq. (4.22) is solved at two closely spaced radii given $r_{op} = r_{opt} \times L_N$ and $r'_{op} = r_{op} \pm \Delta r_{opt} \times L_N$. From solving numerous mode II and mixed mode (I/II) problems, it has been observed that Δr_{opt} may be taken in the range 0.002 to 0.01.

With the above radii and after some algebraic manipulations, the Williams' coefficient B_1 can be calculated as

$$B_1 = \frac{\Delta u^{FE}_{r_{op}} r'_{op} - \Delta u^{FE}_{r'_{op}} r_{op}}{2C_2 r_{op} r'_{op}\left(r_{op}^{\lambda_1^{II}-1} - r'^{\lambda_1^{II}-1}_{op}\right)} \tag{4.23}$$

Using the B_1 value, the mode II NSIF can be estimated using Eq. (3.72). For the reason of convenience, the same equation is presented here as

$$K_{II} = \sqrt{2\pi}\lambda_1^{II}\left(-1 + \lambda_1^{II} - \lambda_1^{II}\cos 2\alpha + \cos 2\alpha\lambda_1^{II}\right)B_1 \tag{4.24}$$

Thus, once again, the mere substitution of Δu^{FE} values at two recommended points on either of the notch flanks into the Eq. (4.24), the mode II NSIF can be computed in the pure mode II and mixed mode (I/II) problems.

The FE displacements Δu^{FE} at r_{op} and r'_{op} for mode II can be determined using the shape functions or quadratic equation Eq. (4.13). It should be noted that the numerical results of the present investigation for the mode II NSIF are based on $\Delta r_{opt} = 0.002$, and no significant change in the NSIF has been noticed with other values of Δr_{opt} in the range mentioned above.

4.2.3 Determination of mixed mode (I/II) NSIFs

In the proposed method, the NOD Δv and NSD Δu are employed for the computation of the mode I and mode II NSIFs, respectively. It can be seen that the NOD (Eq. (4.4)) and NSD (Eq. (4.5)) equations are valid for the problems under mixed mode (I/II) loading conditions. Therefore, Eqs. (4.19) and (4.23) can also be directly used in the mixed mode (I/II) problems. Utilizing NOD at r_{op}, the mode I NSIF K_I can be calculated for mixed mode (I/II) problems using Eqs. (4.19) and (4.20). Again, utilizing NSDs at r_{op} and r'_{op}, the mode II NSIF K_{II} can be obtained for mixed mode (I/II) problems using Eqs. (4.23) and (4.24).

4.3 Numerical results and discussion

In this section, the NSIFs of several benchmark examples of pure mode I, pure mode II and mixed mode (I/II) problems have been determined using the proposed method described in the previous sections and compared with the published results to demonstrate the efficacy of the proposed method. The FE analyses of all the example problems are carried out using ANSYS® (ANSYS, 2007), as discussed in Section 3.5. Conventional Q8 elements are utilized throughout this work. At the notch tip, the Q8 elements are collapsed to form triangular elements in a standard spider web pattern. No singular or any special elements are employed at the notch tip. Eqs. (4.12) and (4.13) have been solved using the codes written in MATLAB (MATLAB, 2015).

In all example problems of this section, Young's modulus $E = 1.0$, Poisson's ratio $\nu = 0.25$, thickness of all the specimens $t = 1$, applied stresses σ, $\tau = 1.0$ and point load $F_E = 1$ are considered. Plane stress conditions are assumed in all problems, and width of the plate $w = 1.0$ is set in all examples. Units are consistent. Normalized NSIFs $\left(F_I, F_{II}\right)$ for various V-notched configurations with the notch length a are computed using the following expressions. For plates under tension or shear (Sub-sections 4.3.1 – 4.3.3)

$$F_{I(II)} = \frac{K_{I(II)}}{\sigma(\tau)\sqrt{\pi} a^{\left(1-\lambda_1^{I(II)}\right)}} \qquad (4.25)$$

In the above equation F_I reaches a value equals to $\sqrt{2}$ when the notch angle attains $\gamma = 180°$. On the other hand, $F_{II} = 1.67$ when the notch angle $\gamma = 102.56°$ (Savruk and Kazberuk, 2007; 2009; 2010; 2017).

For the circular specimen
$$F_{I(II)} = \frac{K_{I(II)} R^{\lambda_1^{I(II)}} t}{F_E} \tag{4.26}$$

For the semi-circular specimen
$$F_I = \frac{2RtK_I}{F_E \sqrt{\pi} a^{1-\lambda_1^I}} \tag{4.27}$$

For the three-point bend specimen
$$F_I = \frac{K_I w^{\lambda_1^I} t}{6F_E} \tag{4.28}$$

The circular specimen is discussed in Sub-section 4.3.3, and the semi-circular and three-point-bending specimens are analyzed in Sub-section 4.3.1. The percent relative error (e_k) in F_I and F_{II} is calculated as

$$e_k(\%) = \left| \frac{F_{I(II)}^{\text{Ref}} - F_{I(II)}^{\text{Present}}}{F_{I(II)}^{\text{Ref}}} \right| \times 100 \tag{4.29}$$

where $F_{I(II)}^{\text{Ref}}$ refers to the available analytical or numerical values of the F_I or F_{II}, and $F_{I(II)}^{\text{Present}}$ is the values of F_I or F_{II} obtained using the proposed point substitution method. These percent relative errors are used in the convergence and comparison studies.

4.3.1 Mode I examples

Five sharp V-notched benchmark example problems have been considered under the mode I loading viz. (a) A single edge notched plate under uniform tension (SENT), (b) a double edge notched plate under uniform tension (DENT), (c) a center notched plate under uniform tension (CNT), (d) a three-point bending (3PB) and (e) a semi-circular bend (SCB) specimens as shown in Figure 4.5. Various notch angles $\gamma = 0°$ to $120°$ in steps of $15°$ and the notch length to width ratios $a/w = 0.2$ and 0.4 are considered for all the specimens except the SCB specimen. For SCB specimen, $\gamma = 0°$ to $90°$ in steps of $15°$ and the notch length to radius ratios $a/R = 0.3$ and 0.5 are considered. The height to width ratio $h/w = 1.2$ is chosen for the SENT specimen. The radius (R) of the SCB specimen is set at 40. The height to width ratio for the DENT, CNT and 3PB specimens is considered as $h/w = 2.0$. Due to the symmetry in the geometry and loading, only one-half of the SENT, 3PB, and SCB specimens and one-quarter of the DENT and CNT specimens as shown by the shaded regions in Figure 4.5 are used for the FE analyses. Boundary conditions employed in all the example problems are also shown in Figure 4.5. The geometric and loading parameters of the above specimens are summarized in Table 4.3 for convenience.

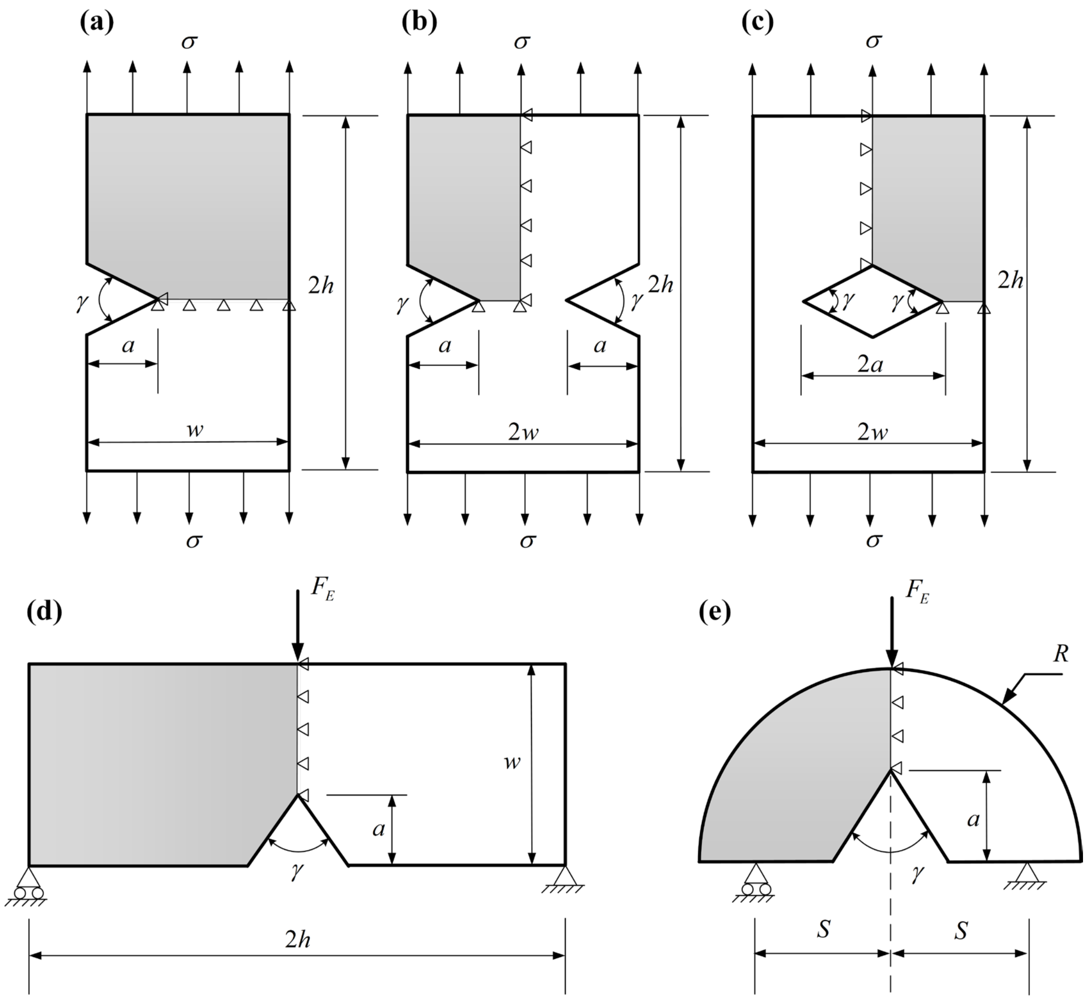

Figure 4.5. (a) Single edge notched plate under uniform tension (SENT), (b) double edge notched plate under uniform tension (DENT), (c) center notched plate under uniform tension (CNT), (d) three-point bending (3PB), and (e) semi-circular bend (SCB) specimens along with boundary conditions for FE analysis.

Table 4.3. Summary of geometric and loading parameters of the mode I example problems.

	SENT	DENT	CNT	3PB	SCB
a/w	0.2, 0.4	0.2, 0.4	0.2, 0.4	0.2, 0.4	-----
h/w	1.2	2.0	2.0	2.0	-----
γ	0° to 120°	0° to 120°	0° to 120°	0° to 120°	0° to 90°
w	1.0	1.0	1.0	1.0	-----
R	-----	-----	-----	-----	40
a/R	-----	-----	-----	-----	0.3 and 0.5
σ	1.0	1.0	1.0	-----	-----
F_E	-----	-----	-----	1.0	1.0

Validation of the existence of the optimum radius $r_{opt}\left(=r_{op}/L_N\right)$ and the accuracy of the field variables thereat is first demonstrated here. Figure 4.6 shows the variation of r_{opt} determined using Eq. (4.18) with the notch angle γ for both the SENT and DENT specimens and for both the a/w values. It can be noticed from Figure 4.6 that r_{opt} values are almost the same for a given notch angle γ for both the specimens and for both the a/w values. These values are the same as that the values presented in Table 4.2. Further, all these values are centered around $r_{opt}=0.785$, which is the average of all the values in Table 4.2.

Figure 4.7 shows the logarithmic plots of $v_{\theta=+\alpha}^{FE}$ versus r/L_N for the SENT specimen for $a/w=0.2$ and 0.4 and for the various notch angles $\gamma=30°$, 60°, and 90°. Similarly, the logarithmic plots of $v_{\theta=+\alpha}^{FE}$ versus r/L_N for the DENT specimen for $a/w=0.2$ and 0.4 and for the notch angles $\gamma=30°$, 60°, and 90° are plotted in Figure 4.8. As discussed earlier in Section 4.2.1, it can be clearly seen from Figures 4.7 and 4.8 that the slope of $v_{\theta=+\alpha}^{FE}$ along the notch flank (along 1–2–4 in Figure 4.3) is equal to the respective theoretical slope λ_1^I only at $r_{opt}=r_{op}/L_N$ (as given in Table 4.2) for both the specimens and for different a/w values.

Further, Figures 4.9 and 4.10 show plots of variation of the Williams' coefficient A_1 obtained at different r/L_N values using Eq. (4.19) along the notch flank 1–2–4 for the SENT and DENT specimens, respectively, for both the values of a/w. The results of Chen (1995) are also plotted in Figures 4.9 and 4.10 as a reference. Results in Figures 4.9 and 4.10 substantiate that $v_{\theta=+\alpha}^{FE}$ is more accurate (because A_1 is accurate) at the r_{opt} when compared to the other points along the notch flank 1–2–4. From the above discussion, it is evident that r_{opt} point in the notch tip element is a potential location for the accurate determination of the NSIFs. In fact, the plots in Figure 4.4 belong to the SENT specimen with $a/w = 0.4$ and $\gamma = 30°$. Although not presented here, similar observations have been noticed in many other benchmark problems.

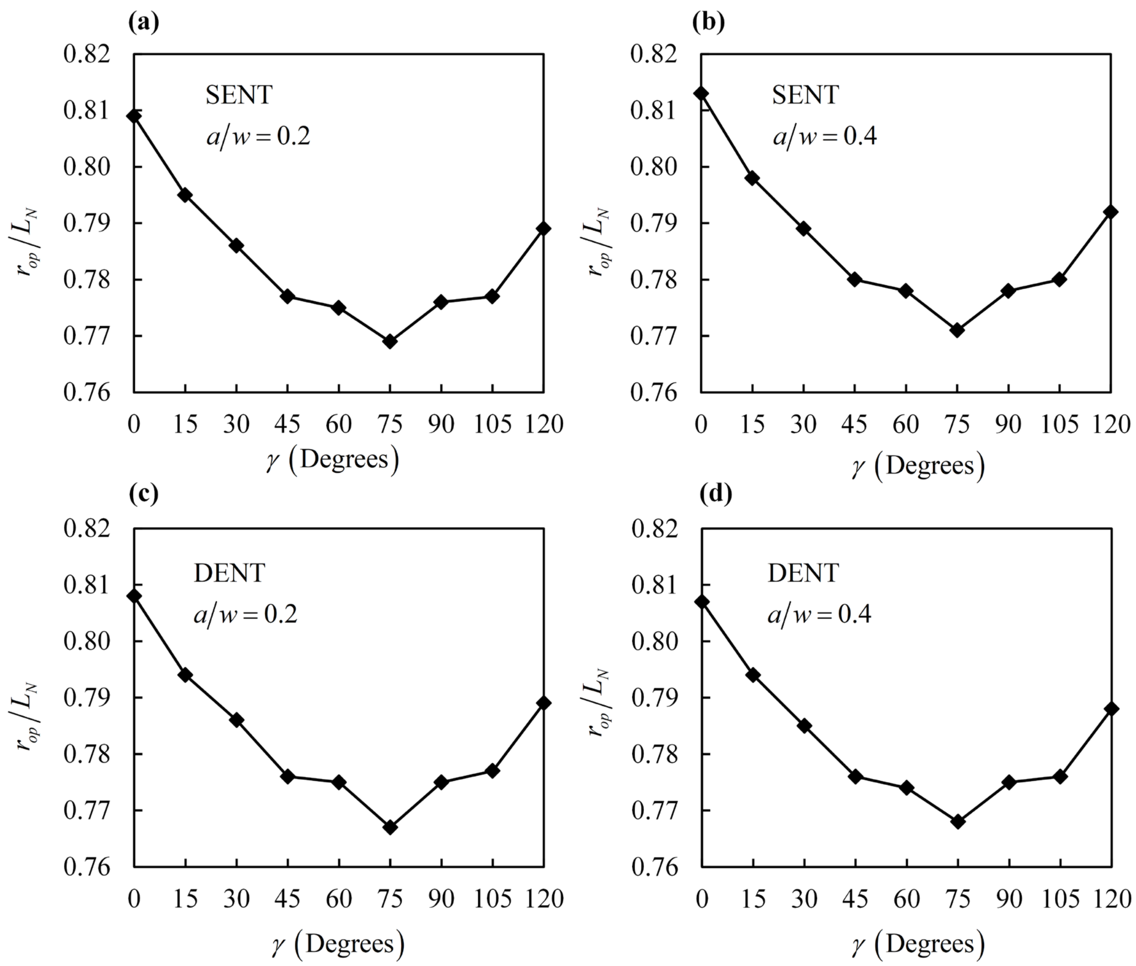

Figure 4.6. Variation of $r_{opt} = r_{op}/L_N$ with notch angle γ for (a) SENT $a/w = 0.2$, (b) SENT $a/w = 0.4$, (c) DENT $a/w = 0.2$, and (d) DENT $a/w = 0.4$.

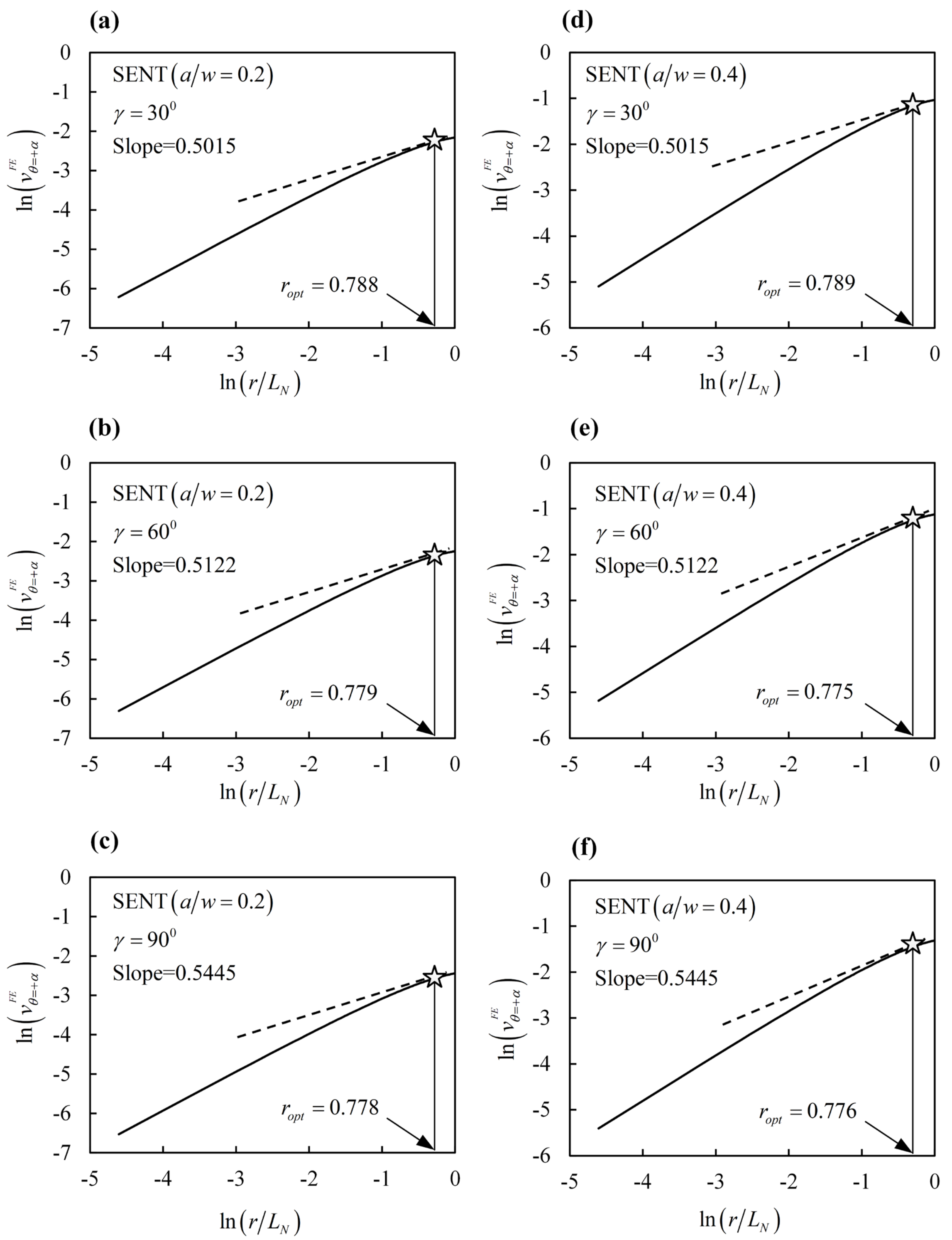

Figure 4.7. Variation of $\ln\left(v_{\theta=+\alpha}^{FE}\right)$ with $\ln(r/L_N)$ along the notch flank 1–2–4 for the SENT specimen (a) to (c) for $a/w = 0.2$ and (d) to (f) for $a/w = 0.4$.

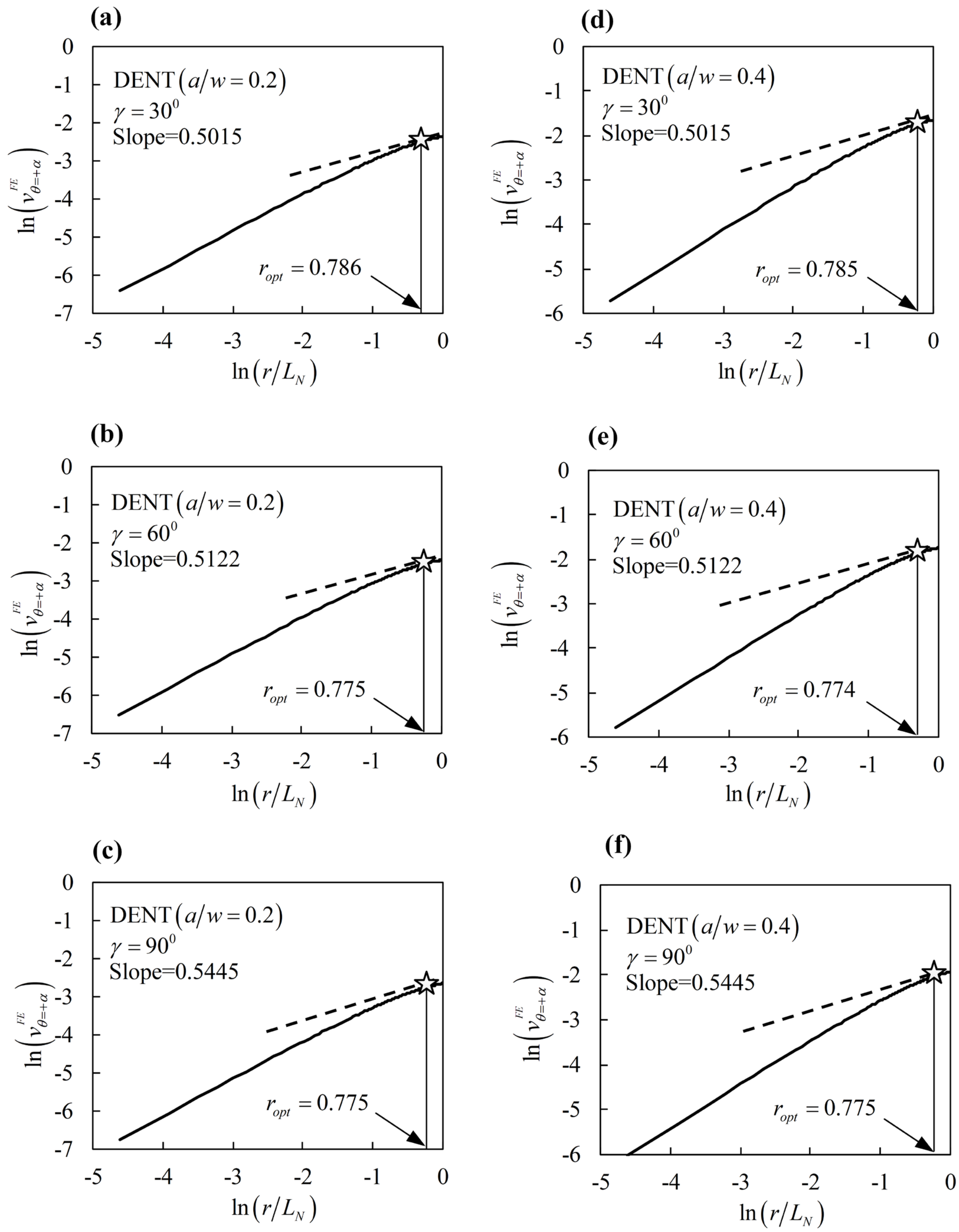

Figure 4.8. Variation of $\ln\left(v_{\theta=+\alpha}^{FE}\right)$ with $\ln\left(r/L_N\right)$ along the notch flank 1–2–4 for the DENT specimen (a) to (c) for $a/w=0.2$ and (d) to (f) for $a/w=0.4$.

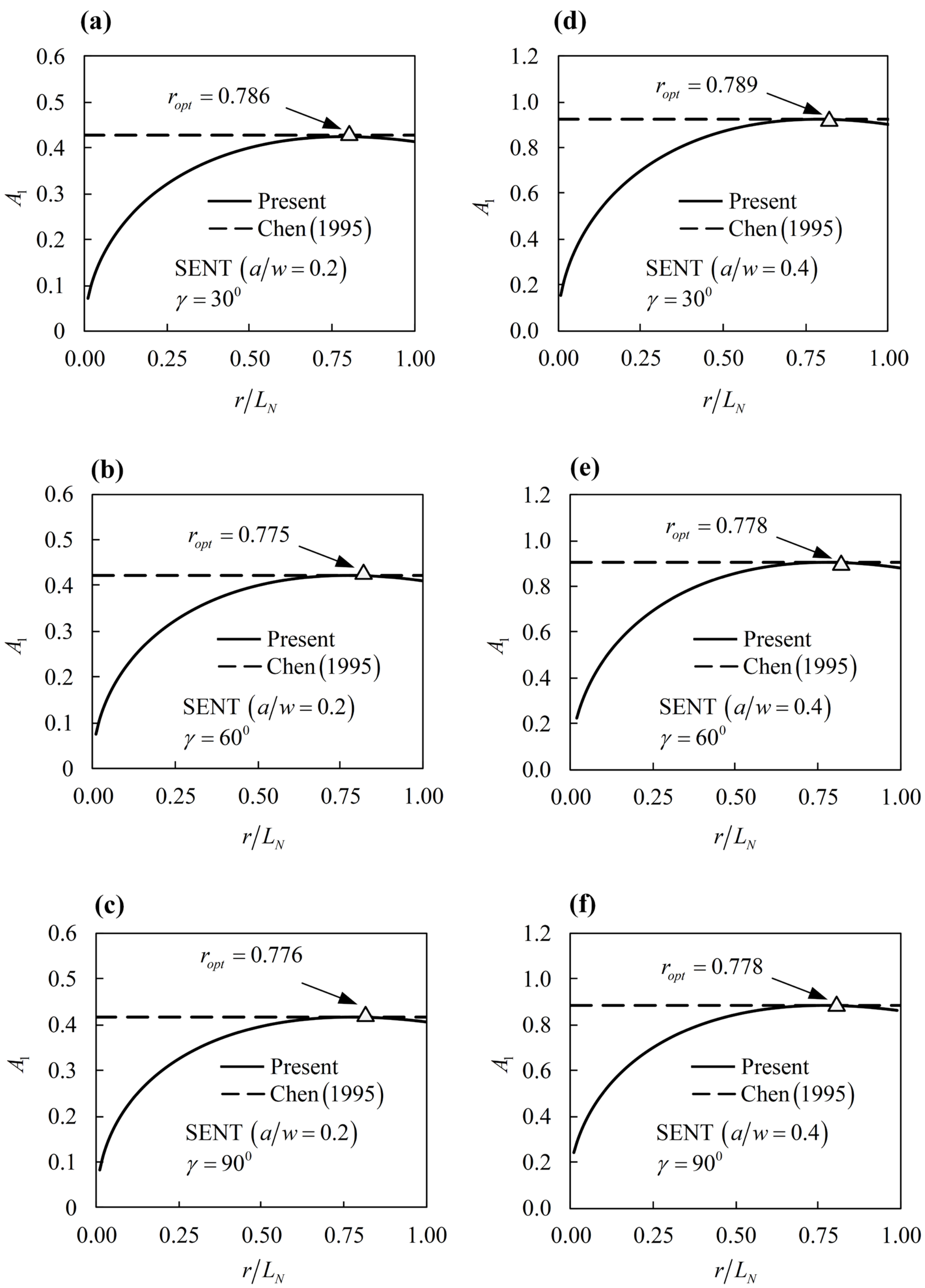

Figure 4.9. Accuracy of the coefficient A_1 (and hence $v^{FE}_{\theta=+\alpha}$) with r/L_N along the notch flank 1–2–4 for the SENT specimen (a) to (c) for $a/w = 0.2$ and (d) to (f) for $a/w = 0.4$.

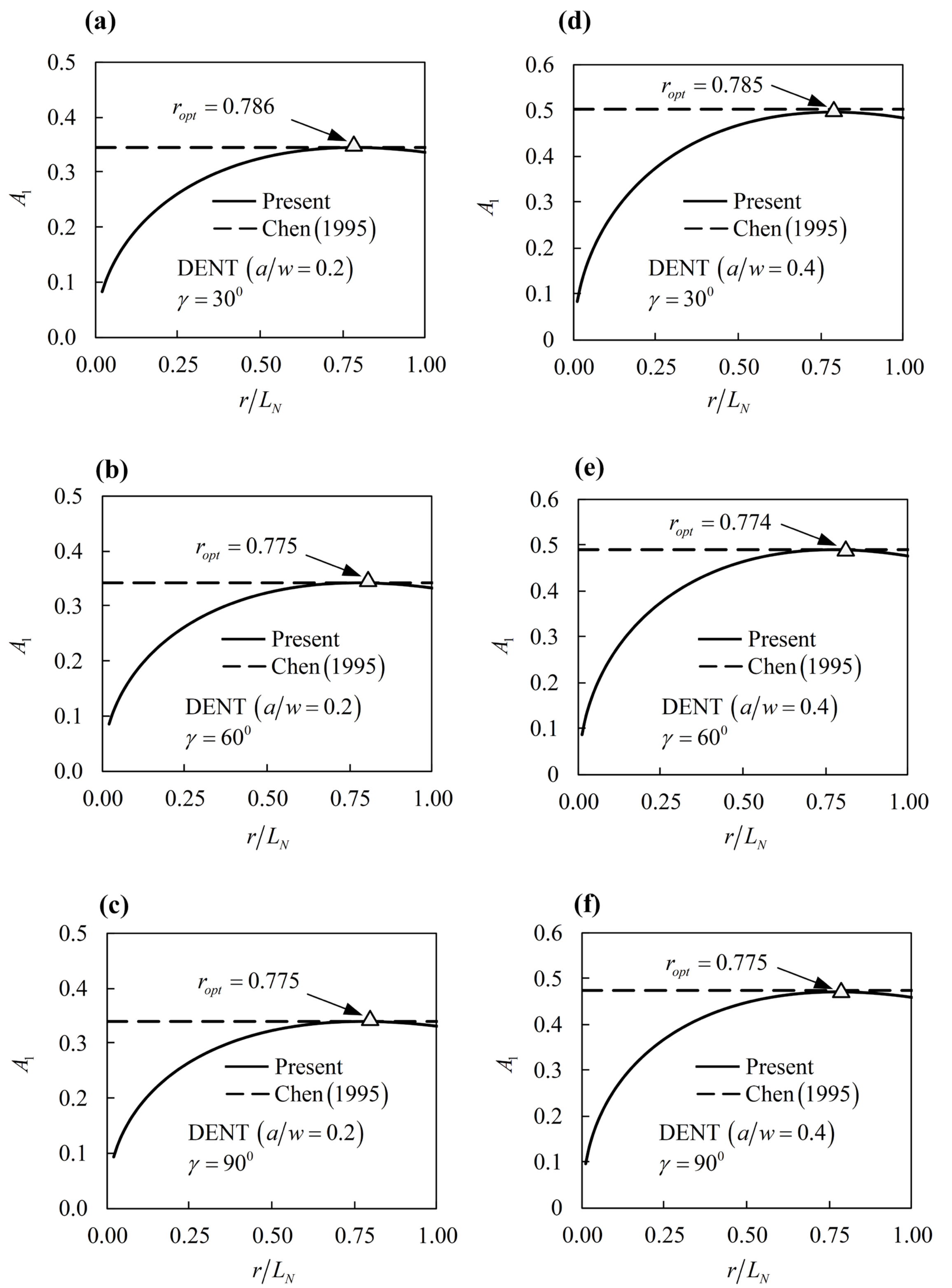

Figure 4.10. Accuracy of the coefficient A_1 (and hence $v^{FE}_{\theta=+\alpha}$) with r/L_N along the notch flank 1–2–4 for the DENT specimen (a) to (c) for $a/w = 0.2$ and (d) to (f) for $a/w = 0.4$.

With the above properties at r_{opt}, the next step is the numerical demonstration of the accurate estimation of the mode I NSIFs by substituting the finite element solution of the NOD, i.e., Δv^{FE} at the optimum radius $r_{op} (= r_{opt} \times L_N)$ in Eq. (4.19). In the present investigation r_{op} is determined in all the examples using the r_{opt} values presented in Table 4.2. Nonetheless, the same can also be obtained directly from Eq. (4.18). In order to study the influence of the mesh refinement on the convergence of the estimated mode I NSIFs, four different meshes of the SENT with $a/w = 0.4$ and $\gamma = 30°$, and the DENT with $a/w = 0.4$ and $\gamma = 30°$ specimens with increasing mesh density such that L_N/a equals to 0.25, 0.0833, 0.0333 and 0.025, respectively, are considered. Typical meshes used are shown in Figure 4.11. The number of elements (NE) and the number of nodes (NN) present in these Q8 element meshes are also shown in Figure 4.11. The densest mesh (Mesh 4 in Figure 4.11) considered for the SENT specimen (for $a/w = 0.4$ and $\gamma = 30°$) consists of number of elements (NE) = 218 and number of nodes (NN) = 725. It is worth mentioning here that the plots presented in Figures 4.6 – 4.10 for understanding the r_{opt} were obtained using the results from the typical meshes such as the Mesh 4 in Figure 4.11.

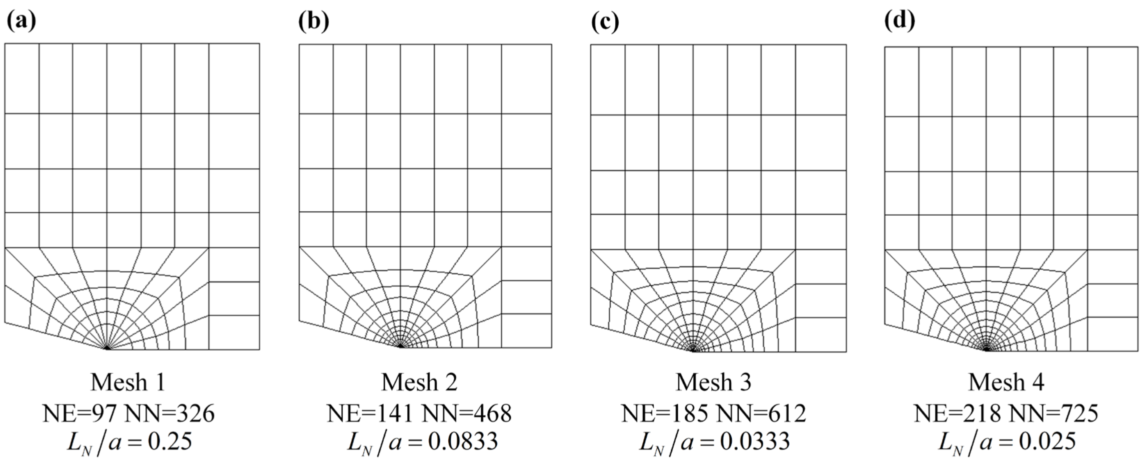

Figure 4.11. Typical finite element meshes used for the convergence study.

Following the procedure outlined in Section 4.2.1, the mode I NSIF is computed for all the four meshes (Figure 4.11) and compared with the reference solution given by Chen (1995). Figure 4.12 shows the convergence of F_I with the mesh refinement for both specimens. In Mesh 4 the absolute percent relative error in F_I for the SENT and DENT specimens is reduced to 0.78% and 0.96%, respectively, from 1.06% and 3.28%, respectively, in Mesh

1. It can be noticed from Figure 4.12 that the estimated NSIFs using the proposed method are converging as the meshes are refined.

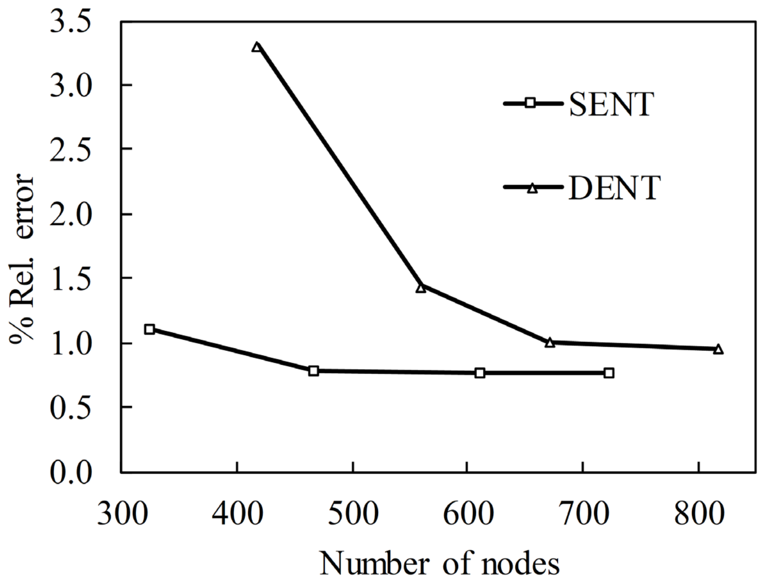

Figure 4.12. Convergence of F_I with the mesh refinement for the SENT and DENT specimens.

In order to demonstrate the efficacy of the proposed point substitution method, the mode I NSIFs have been determined for the SENT, DENT, CNT, and 3PB specimens for the notch angles $\gamma = 0°$, 15°, 30°, 45°, 60°, 75°, 90°, 105°, and 120°. For this purpose, meshes of the type Mesh 4 in Figure 4.11d are employed for the rectangular specimens (Figure 4.5a – d), where L_N/a = 0.025. Similarly, the mode I NSIFs for the SCB specimens are determined for a/R =0.3 and 0.5 and notch angles $\gamma = 0°$, 15°, 30°, 45°, 60°, 75°, and 90°. For this specimen (Figure 4.5e), the mesh has a ratio of L_N/a = 0.025, as shown in Figure 4.13. The typical mesh (Figure 4.13) considered for this specimen consists of NE = 402 and NN = 1281 (for $\gamma = 30°$). A point load $F_E = 1.0$ is applied at the top in the vertical direction as shown in Figure 4.5e. The distance between the two supports is considered as $2S = 40$ (Figure 4.5e). Tables 4.4 and 4.5 show the estimated normalized mode I NSIF of the SENT specimen along with the published results for the purpose of comparison of the accuracy. Results corresponding to the DENT specimen have been presented in Tables 4.6 and 4.7. Estimated normalized mode I NSIFs of the CNT specimen have been shown in Tables 4.8 and 4.9. While the 3PB specimen results have been presented in Tables 4.10 and 4.11. Finally, Tables 4.12 and 4.13 show the results of the SCB specimen. In all these tables, published results are also presented for the purpose of comparison of the accuracy of extraction of the proposed method. A hyphen (–) is used in the tables wherever published data is not available. It can be observed from the results presented in Tables 4.4 – 4.13 that the NSIFs obtained from the proposed method are in very good agreement with the published results for all the notch angles and a/w values considered. Only a limited number of reference values are available for the SCB specimen. From the results in Tables 4.12 and 4.13, it can be seen that the present results are in good agreement with the published results for $\gamma = 0°$. For other notch angles, the NSIFs are also calculated using Ayatollahi and Nejati (2011a) method using the present meshes. It can be observed that the results obtained using the proposed point substitution method are in good agreement with the results obtained using Ayatollahi and Nejati (2011a) method for all the notch angles and a/R values considered. Due to the use of the notch flank displacements at the proposed locations $\left(r_{opt}\right)$, very accurate mode I NSIFs are determined using the proposed method even on the relatively coarse meshes such as Mesh 4 in Figure 4.11. It is worth reemphasizing that by the mere substitution of the finite element NOD value in Eq. (4.19), one can easily determine the very accurate mode I NSIFs of the sharp V-notched configurations.

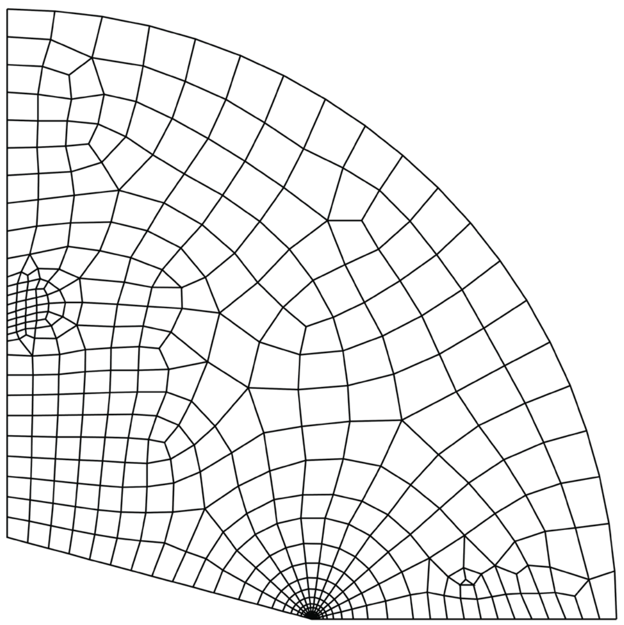

Figure 4.13. Typical FE mesh for the SCB specimen (NE=402, NN=1281).

Table 4.4. Normalized NSIFs F_I for the SENT specimen (a/w =0.2).

	F_I								
$\gamma(°)\rightarrow$	0	15	30	45	60	75	90	105	120
Present	1.3421	1.3525	1.3686	1.3958	1.4379	1.5008	1.5912	1.7148	1.8771
Chen (1995)	–	–	1.3810	–	1.4450	–	1.5970	–	–
Gross and Mendelson (1972)	1.3688	–	1.3807	–	1.4460	–	1.6042	–	1.8891
Zhao and Hahn (1992)	1.3738	–	1.3769	–	1.4374	–	1.5714	–	1.7812

Table 4.5. Normalized NSIFs F_I for the SENT specimen (a/w =0.4).

	F_I								
$\gamma(°)\rightarrow$	0	15	30	45	60	75	90	105	120
Present	2.0768	2.0908	2.1124	2.1512	2.2142	2.3137	2.4655	2.6898	3.0166
Chen (1995)	–	–	2.1290	–	2.2230	–	2.4720	–	–
Gross and Mendelson (1972)	2.1133	–	2.1283	–	2.2230	–	2.4734	–	3.1105
Zhao and Hahn (1992)	2.1062	–	2.1140	–	2.2230	–	2.4854	–	2.9597
Kim and Cho (2009)	2.1130	–	2.1300	–	2.2250	–	2.4740	–	–
Ayatollahi and Nejati (2011a)	2.1100	2.1125	2.1273	2.1610	2.2250	2.3214	2.4718	–	–
Yi et al. (2017)	2.1100	–	2.1270	–	2.2240	–	2.4690	–	3.195

Table 4.6. Normalized NSIFs F_I for the DENT specimen (a/w =0.2).

	F_I								
$\gamma(°)\rightarrow$	0	15	30	45	60	75	90	105	120
Present	1.0913	1.1000	1.1134	1.1361	1.1707	1.2216	1.2928	1.3868	1.5021
Treifi et al. (2009b)	1.1110	–	1.1220	1.1250	1.1650	–	1.3020	–	–
Chen (1995)	–	–	1.1230	–	1.1760	–	1.2980	–	–

Table 4.7. Normalized NSIFs F_I for the DENT specimen (a/w =0.4).

	F_I								
$\gamma(°)\rightarrow$	0	15	30	45	60	75	90	105	120
Present	1.1113	1.1202	1.1340	1.1571	1.1925	1.2443	1.3171	1.4136	1.5343
Treifi et al. (2009b)	1.1320	–	1.1430	1.1530	1.1910	–	1.3230	–	–
Chen (1995)	–	–	1.1450	–	1.1990	–	1.3230	–	–
Ayatollahi and Nejati (2011a)	1.1326	1.1343	1.1439	1.1641	1.1984	1.2499	1.3221	–	–

Table 4.8. Normalized NSIFs F_I for the CNT specimen (a/w =0.2).

	F_I								
$\gamma(°)\rightarrow$	0	15	30	45	60	75	90	105	120
Present	1.0034	1.0205	1.0473	1.0872	1.1419	1.2150	1.3115	1.4315	1.5801
Triefy et al. (2009b)	10240	–	1.0530	1.0670	1.1310	–	1.3210	–	–

Table 4.9. Normalized NSIFs F_I for the CNT specimen (a/w =0.4).

	F_I								
$\gamma(°)\rightarrow$	0	15	30	45	60	75	90	105	120
Present	1.0866	1.1097	1.1446	1.1954	1.2652	1.3604	1.4914	1.6626	1.9004
Triefy et al. (2009b)	1.1090	–	1.1510	1.1840	1.2610	–	1.4970	–	–

Table 4.10. Normalized NSIFs F_I for the 3PB specimen (a/w =0.2).

	F_I								
$\gamma(°)\rightarrow$	0	15	30	45	60	75	90	105	120
Present	0.7631	0.7682	0.7772	0.7950	0.8255	0.8752	0.9527	1.0697	1.2440
Gross and Mendelson (1972)	0.7770	–	0.7850	–	0.8320	–	0.9630	–	1.2610
Zhao and Hahn (1992)	0.7780	–	0.7810	–	0.8300	–	0.9550	–	1.2150

Table 4.11. Normalized NSIFs F_I for the 3PB specimen (a/w =0.4).

	F_I								
$\gamma(°)\rightarrow$	0	15	30	45	60	75	90	105	120
Present	1.3005	1.3068	1.3181	1.3419	1.3845	1.4565	1.5725	1.7539	2.0355
Gross and Mendelson (1972)	1.3180	–	1.3250	–	1.3900	–	1.5780	–	2.0340
Zhao and Hahn (1992)	1.3150	–	1.3220	–	1.4040	–	1.6170	–	2.0050

Table 4.12. Normalized NSIFs F_I for the SCB specimen (a/R =0.3).

	F_I						
$\gamma(°)\rightarrow$	0	15	30	45	60	75	90
Present	2.5491	2.5649	2.5908	2.6351	2.7116	2.8329	3.0184
Ayatollahi and Aliha (2006)	2.6040	–	–	–	–	–	–
Tutluoglu and Keles (2011)	2.5380	–	–	–	–	–	–
Using Ayatollahi and Nejati (2011a) method	2.5729	2.5809	2.5995	2.6385	2.7087	2.8238	3.0017

Table 4.13. Normalized NSIFs F_I for the SCB specimen (a/R =0.5).

	F_I						
$\gamma(°)\rightarrow$	0	15	30	45	60	75	90
Present	3.5839	3.6079	3.6480	3.7191	3.8456	4.0508	4.6417
Ayatollahi et al., (2011a)	3.6000	–	–	–	–	–	–
Tutluoglu and Keles (2011)	3.5500	–	–	–	–	–	–
Using Ayatollahi and Nejati (2011a) method	3.5932	3.6045	3.6337	3.6960	3.8113	4.0049	4.6140

In order to substantiate the performance of the proposed method further, variation of the F_I of the SENT and DENT specimens with the notch angle has been made, as shown in

Figure 4.14. It can be seen from the plots of Figure 4.14 that, as expected F_I value increases with the notch angle being minimum at $\gamma = 0°$. Though not presented here, this value increases until a notch angle is reached $(\approx 158°)$ from which it decreases to $\sqrt{2}$ at the notch angle 180° where a uniform stress state is attained (Savruk and Kazberuk, 2007; 2009; 2010, 2017). It can also be seen from Figure 4.14 that, as expected F_I values increase with the increase in a/w ratio. Similar trends have also been noticed from the results of the other example problems considered in this section.

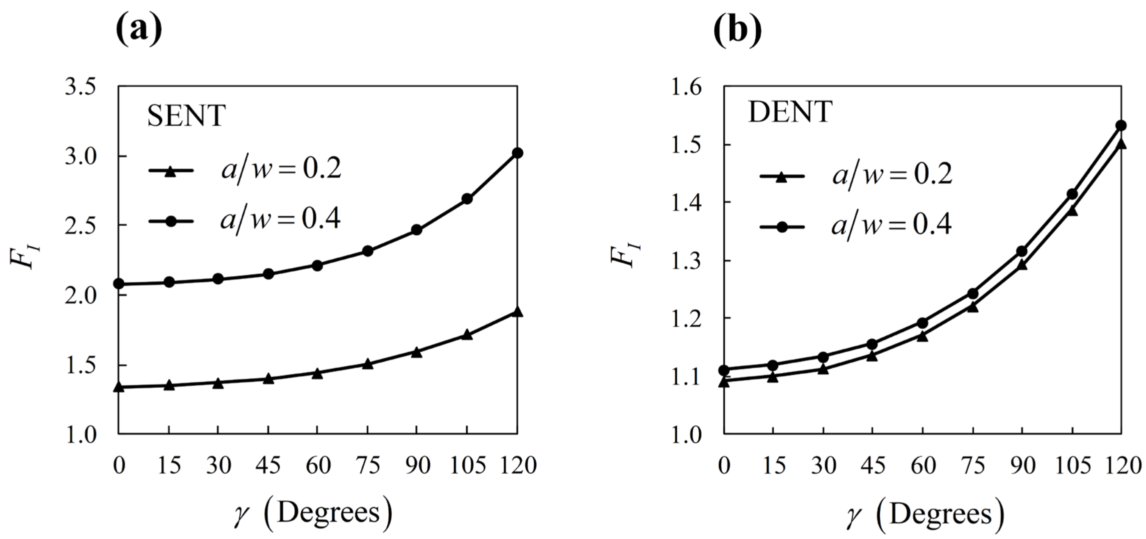

Figure 4.14. Variation of F_I with notch angle γ for the (a) SENT and (b) DENT specimens.

4.3.2 Mode II examples

This section presents example problems that are under pure mode II loading conditions. For this purpose, a single edge notched specimen under shear (SENS) is considered, as shown in Figure 4.15. The counter-moment (modeled as a couple) is applied to counterbalance the shear load. Mode II NSIF is determined for this specimen for $\gamma = 0°$, 15°, 30°, 45°, 60°, 75°, and 90°, and $a/w = 0.2$ and 0.4 with $h/w = 1.0$. Further, for the notch angle $\gamma = 50°$, the NSIFs have also been determined for $a/w = 0.2 - 0.5$. Due to the symmetry in the geometry and antisymmetry in the loading, only one-half of the SENS specimen shown as the shaded area in Figure 4.15 is considered for the FE analyses. Boundary conditions are also shown in Figure 4.15.

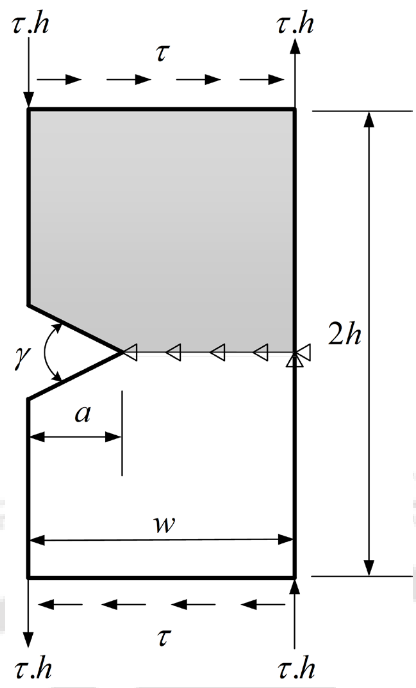

Figure 4.15. Mode II example: Single edge notched plate under shear (SENS).

In line with the assumption made in Section 4.2.2, to estimate the mode II NSIF, the FE NSD, i.e., Δu^{FE} at two radii on the notch flank 1–2–4 (Figure 4.3) of the notch tip element is computed. In the present investigation, for both the mode II and mixed mode (I/II) problems, these two radii are selected close to each other as $r_{op} = r_{opt} \times L_N$ and $r'_{op} = r_{op} - \Delta r_{opt} \times L_N$ (Section 4.2.2). Here r_{opt} is taken directly from Table 4.2 depending on the notch angle and Δr_{opt} is set to 0.002. Subsequently, Δu^{FE} at these two radial locations is substituted into Eq. (4.23) to determine the Williams' coefficient B_1, and then the mode II NSIF is calculated using Eq. (3.72 or 4.24). For this purpose, FE mesh, whose mesh density is similar to Mesh 4 in Figure 4.11d, is employed in all the calculations of this section.

As most of the published data is available for $a/w = 0.4$, results of which is presented first than the $a/w = 0.2$. Table 4.14 shows the estimated normalized mode II NSIF for the SENS specimen with $a/w = 0.4$ using the proposed method for the various notch angles. Table 4.14 also shows the available NSIFs in the published works. It can be noticed from the results presented in Table 4.14 that the computed mode II NSIFs using the proposed method is very well in agreement with the published results even on the relatively coarser meshes (such as Mesh 4 in Figure 4.11). Thus, by the mere substitution of Δu^{FE} at two radial locations into the Eq. (4.23), one can evaluate very accurate mode II NSIFs. The results in Table 4.14 clearly indicate that r_{opt} values in Table 4.2 (which have been identified under mode I loading conditions) can also be employed for the accurate estimation of the mode II NSIFs and hence strongly substantiate the assumption made in Section 4.2.2. Results corresponding to the $a/w = 0.2$ are presented in Table 4.15. Although very limited published results are available for this configuration, the present results are once again very well in agreement with the available published results. To substantiate further the efficacy of the proposed method for the mode II problems, Table 4.16 shows the results of the SENS specimen with $a/w = 0.2 - 0.5$ in steps of 0.1 and for the notch angle $\gamma = 50°$. The results in Table 4.16 also show that the present results are in very well agreement with the published results.

Table 4.14. Normalized NSIFs F_{II} for the SENS specimen $(a/w = 0.4)$.

$\gamma(°)$ ↓	F_{II} Present	Treifi et al. (2008)	Ayatollahi and Nejati (2011a)	Zhao and Hahn (1991)	Zhao and Hahn (1992)	Kim and Cho (2009)	Yi et al. (2017)
0	1.1903	1.1800	1.1735	1.1660	1.1500	1.1780	1.1820
15	1.3907	–	1.3817	–	–	–	–
30	1.6429	1.6350	1.6287	1.6250	1.8630	1.6330	1.6290
45	1.9537	–	1.9365	–	–	–	–
60	2.3347	2.3070	2.2986	2.2920	2.3550	2.2970	2.3040
75	2.7152	–	2.7309	–	–	–	–
90	3.1637	3.1750	3.2134	3.2150	3.1260	3.2040	3.1760

Table 4.15. Normalized NSIFs F_{II} for the SENS specimen $(a/w = 0.2)$.

γ →	F_{II} 0°	15°	30°	45°	60°	75°	90°
Present	0.7027	0.8253	0.9788	1.1701	1.4024	1.6365	1.9043
Treifi et al. (2008)	0.6960	–	–	–	–	–	–

Table 4.16. Normalized NSIFs F_{II} for the SENS specimen $(\gamma = 50°)$.

	F_{II}			
$a/w \rightarrow$	0.2	0.3	0.4	0.5
Present (Eq. (5.13))	1.2513	1.6972	2.0456	2.4013
Treifi et al. (2008)	1.2580	1.6980	2.0610	2.3880

To further demonstrate the performance of the proposed method in the mode II problems, a plot of the NSIF versus the notch angle is made, as shown in Figure 4.16 for $a/w = 0.2$ and 0.4. Similar to the mode I examples, F_{II} increases with the increase in the notch angle γ as expected (Savruk and Kazberuk, 2007; 2009; 2010; 2017). Moreover, F_{II} is also increasing with the increase in a/w. It is observed that accurate mode II NSIFs have been obtained using $\cos(\alpha)$ instead of $\cos(2\alpha)$ while calculating the constant C_2 using Eq. (4.5). This advantage is utilized throughout this work.

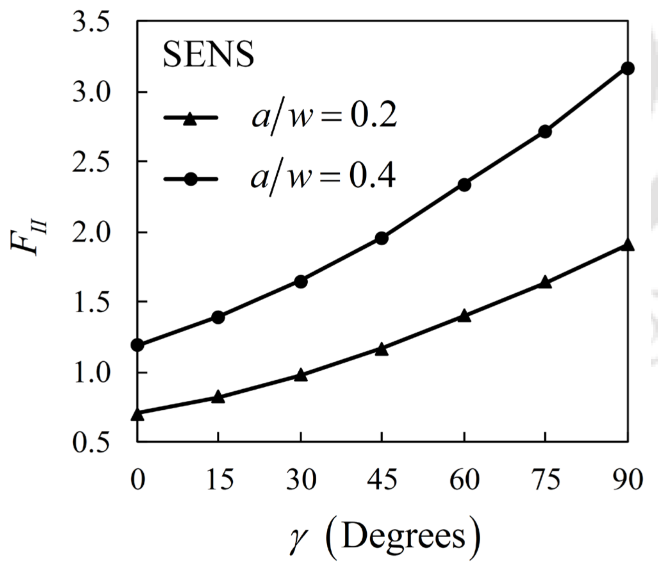

Figure 4.16. Variation of F_{II} with notch angle γ for the SENS specimen.

4.3.3 Mixed mode (I/II) examples

This section presents example problems that are under mixed mode (I/II) loading conditions. For this purpose, five example problems viz. (a) An angled single edge notched plate under uniform tension (ASENT), (b) an angled double edge notched plate under uniform tension (ADENT), (c) an off-central double edge notched plate under uniform tension (ODENT), (d) an off-central center notched plate under uniform tension (OCNT), and (e) a sharp V-notched Brazilian disc (SV-BD) specimens as shown in Figures 4.17 – 4.19 are selected to substantiate the efficacy of the proposed point substitution method in the determination of the accurate mixed mode (I/II) NSIFs.

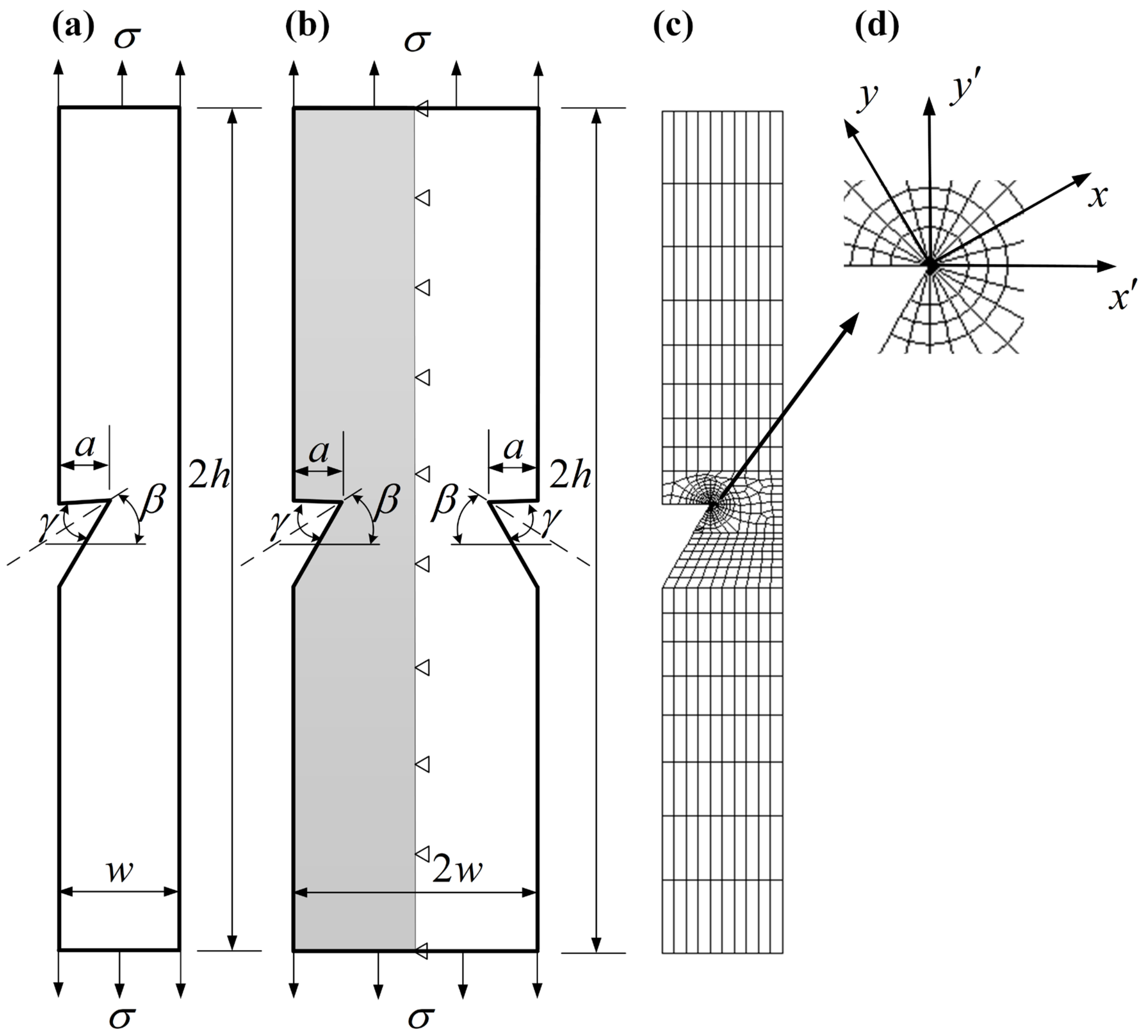

Figure 4.17. (a) Angled single edge notched plate under uniform tension (ASENT), (b) angled double edge notched plate under uniform tension (ADENT), (c) typical FE mesh used for the ASENT and ADENT (NE=563 and NN=1829) and (d) enlarge view of the notch tip portion.

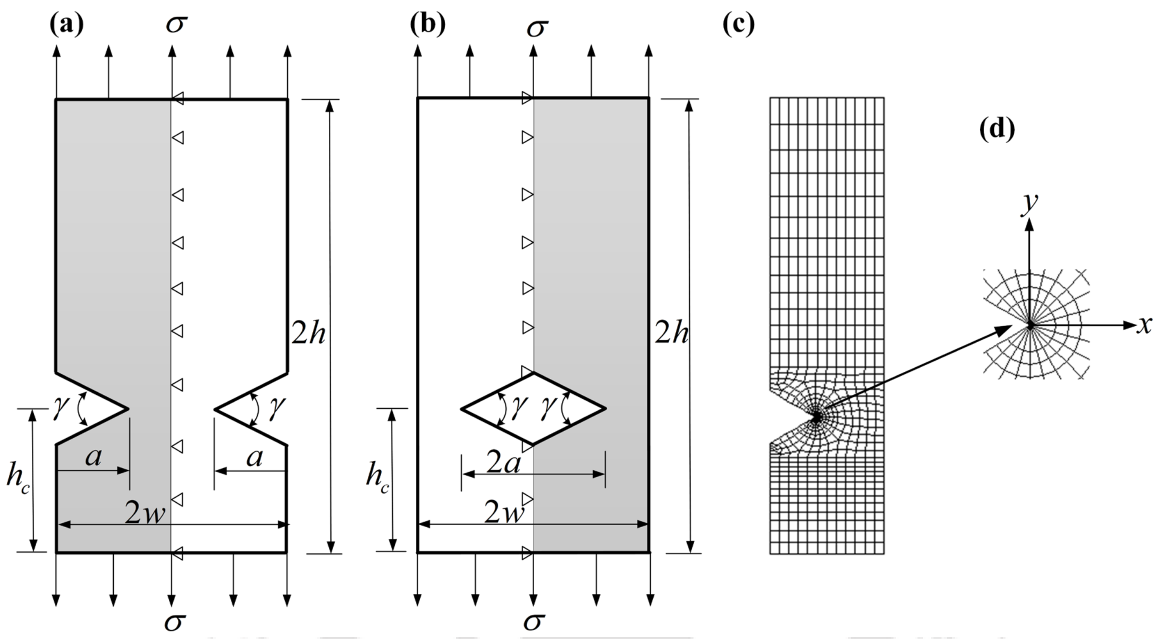

Figure 4.18. (a) Off-central double edge notched plate under uniform tension (ODENT), (b) off-central center notched plate under uniform tension (OCNT), (c) typical FE mesh used for the ODENT and OCNT (NE=680 and NN=2190) and (d) enlarge view of the notch tip portion.

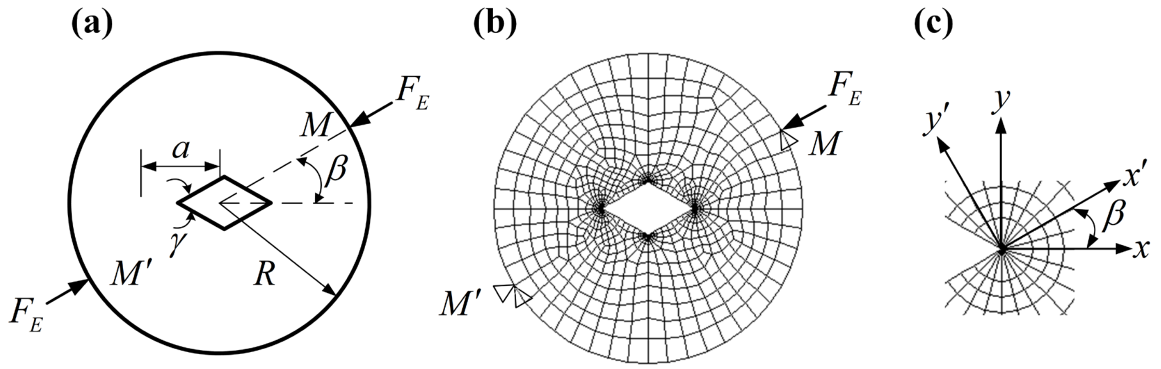

Figure 4.19. (a) Sharp V-notched Brazilian disc (SV-BD), (b) typical FE mesh used (NE=1040 and NN=3192) and (c) enlarge view of the notch tip portion.

The ASENT and ADENT specimens are shown in Figure 4.17 along with the typical FE mesh used for the FE analysis. The typical mesh (for $a/w = 0.4$, $\beta = 15°$ and $\gamma = 30°$) consists of NE = 563 and NN = 1829. The enlarged portion of the notch tip region is shown in Figure 4.17d. In Figure 4.17, β is the notch inclination angle. For both the ASENT and ADENT specimens $a/w = 0.2$ and 0.4, $h/w = 3.5$, $\gamma = 0°$, 30°, 60°, and 90° and the applied stress $\sigma = 1.0$ have been chosen. The effect of the notch inclination angle on the mixed mode NSIFs is studied for $\beta = 15°$, 30°, and 45° for both the specimens. For the ASENT specimen, the bottom edge has been restrained from both the displacements and the tensile load is applied at the top edge. Due to the symmetry in the geometry and loading conditions, only one-half of the ADENT (shaded area with boundary conditions in Figure 4.17) is considered. For the ADENT specimen, the displacements at the bottom edge have been restrained in the $y'-$direction, and the displacements on the right side of the shaded portion have been restrained in the $x'-$direction, as shown in Figure 4.17.

Figure 4.18 shows the geometry and loading conditions of the ODENT and OCNT specimens along with the typical FE mesh with the enlarged portion of the mesh region near the notch tip used for the FE analyses. This typical mesh consists of NE = 680 and NN = 2190 (for $a/w = 0.4$, $h_c/2h = 0.3$ and $\gamma = 60°$). For these specimens, the notch length to width ratios $a/w = 0.2$ and 0.4 and notch angles $\gamma = 0°$, 30°, 60°, and 90° are considered. The height to width ratio of $h/w = 3.5$ and 2.0 is chosen for the ODENT and OCNT specimens, respectively. The effect of the different notch positions $(h_c/2h)$ (see Figure 4.18) on the mixed mode NSIFs has also been studied for $h_c/2h = 0.1 - 0.4$ in steps of 0.1 for both the ODENT and OCNT specimens. It is to be noted that pure mode I occurs when $h_c/2h = 0.5$ and mode-mixity increases with the decrease in $h_c/2h$ values. One-half of the ODENT and OCNT specimens are considered for the FE analyses, and these are shown as shaded regions in Figure 4.18. The top edge of the ODENT and OCNT are restrained in the $y-$direction, and the loads are applied at the bottom edge. The displacements on the vertical edge (shaded portions in Figure 4.18) are restrained in the $x-$direction in the right-hand side of the ODENT specimen and the left-hand side of the OCNT specimens, as shown in Figure 4.18.

The SV-BD specimen is shown in Figure 4.19 along with the typical FE mesh used (NE = 1040, NN = 3192 for $a/R = 0.3$ and $\gamma = 60°$) for the FE analyses. For this specimen $a/R = 0.3$ and 0.5, $R = 60$, $\gamma = 30°$, 60°, and 90°, and the applied point load $F_E = 1.0$ are chosen. The notch inclination angle β=0°, 10°, 20°, 25°, 29°, and 35° are considered for this specimen. The displacements are restrained in the $y'-$ direction at the point M and in both x' and y' directions at the point M' of the SV-BD specimen, as shown in Figure 4.19. Here, the points M and M' are on the circumference of the disc at the opposite sides of a diagonal line shown in Figure 4.19b. Figure 4.19c shows the enlarged portion of the notch tip portion showing the details of the mesh near the notch tip. Table 4.17 shows the summary of the geometric and loading parameters of all five mixed mode (I/II) configurations.

Table 4.17. Details of the geometry and loading parameters of the mixed mode specimens.

	ASENT	ADENT	ODENT	OCNT	SV-BD
a/w	0.2, 0.4	0.2, 0.4	0.2, 0.4	0.2, 0.4	-----
γ	0° – 90°	0° – 90°	0° – 90°	0° – 90°	30° – 90°
β	15° – 45°	15° – 45°	-----	-----	0° – 35°
w	1.0	1.0	1.0	1.0	-----
$h_c/2h$	-----	-----	0.1 – 0.4	0.1 – 0.4	-----
a/R	-----	-----	-----	-----	0.3, 0.5
R	-----	-----	-----	-----	60
h/w	3.5	3.5	2.0	2.0	-----
σ	1.0	1.0	1.0	1.0	-----
F_E	-----	-----	-----	-----	1.0

As is done in the case of mode I and mode II, Δv^{FE} at r_{opt} is used in Eq. (4.19) for determination of the mode I NSIF and Δu^{FE} at two radii ($r_{op} = r_{opt} \times L_N$ and $r'_{op} = r_{op} - 0.002 \times L_N$) are substituted in Eq. (4.23) for the determination of the mode II NSIF in the present mixed mode problems as well. The computed normalized mixed mode NSIFs using the proposed method for the ASENT specimen are presented in Tables 4.18 and 4.19 for $a/w = 0.2$ and 0.4, respectively. Similarly, Tables 4.20 and 4.21 present the computed normalized NSIFs corresponding to the ADENT specimen for $a/w = 0.2$ and 0.4, respectively. Published results for the purpose of comparison are also presented in Tables 4.18 – 4.21. It can be observed from the results presented in Tables 4.18 – 4.21 that the mixed mode NSIFs obtained using the present method are in very good agreement with the various published results regardless of the notch angle, a/w and notch inclination angle. This is true for both the F_I and F_{II}.

Table 4.18. Normalized NSIFs F_I and F_{II} for the ASENT specimen $(a/w = 0.2)$.

$\beta(°)$	$\gamma(°)$	F_I		F_{II}	
		Present	Chen (1995)	Present	Chen (1995)
15	0	1.3014	–	0.2145	–
	30	1.3246	1.3360	0.2952	0.2940
	60	1.3848	1.3920	0.4076	0.4020
	90	1.5185	1.5250	0.5227	0.5220
30	0	1.1867	–	0.3991	–
	30	1.1973	1.2100	0.5322	0.5360
	60	1.2327	1.2420	0.7166	0.7170
	90	1.3212	1.3280	0.8903	0.9050
45	0	1.0123	–	0.5226	–
	30	1.0073	1.0200	0.6950	0.6870
	60	1.0114	1.0200	0.8957	0.8830

Table 4.19. Normalized NSIFs F_I and F_{II} for the ASENT specimen $(a/w = 0.4)$.

$\beta(°)$	$\gamma(°)$	F_I			F_{II}		
		Present	Chen (1995)	Ayatollahi and Nejati (2011a)	Present	Chen (1995)	Ayatollahi and Nejati (2011a)
15	0	2.0184	–	2.0482	0.3095	–	0.3086
	30	2.0502	2.0660	2.0648	0.4238	0.4240	0.4238
	60	2.1448	2.1540	2.1525	0.5878	0.5870	0.5869
	90	2.3842	2.3910	2.3902	0.8158	0.8060	0.8062
30	0	1.8510	–	1.8761	0.5772	–	0.5747
	30	1.8734	1.8890	1.8870	0.7835	0.7830	0.7835
	60	1.9500	1.9600	1.9600	1.0805	1.0760	1.0770
	90	2.1583	2.1660	2.1645	1.4934	1.4900	1.4900
45	0	1.5998	–	–	0.7685	–	–
	30	1.6121	1.6260	–	1.0299	1.0300	–
	60	1.6659	1.6770	–	1.4220	1.4080	–

Table 4.20. Normalized NSIFs F_I and F_{II} for the ADENT specimen $(a/w = 0.2)$.

$\beta(°)$	$\gamma(°)$	F_I		F_{II}	
		Present	Chen (1995)	Present	Chen (1995)
15	0	1.0577	–	0.1779	–
	30	1.0767	1.0870	0.2444	0.2430
	60	1.1242	1.1310	0.3393	0.3340
	90	1.2250	1.2310	0.4222	0.4300
30	0	0.9631	–	0.3302	–
	30	0.9699	0.9810	0.4486	0.4440
	60	0.9915	1.0000	0.6046	0.5890
	90	1.0306	1.0370	0.7180	0.7140
45	0	0.8184	–	0.4323	–
	30	0.8079	0.8180	0.5618	0.5630
	60	0.7860	0.7940	0.7054	0.6990

Table 4.21. Normalized NSIFs F_I and F_{II} for the ADENT specimen $(a/w = 0.4)$.

$\beta(°)$	$\gamma(°)$	F_I			F_{II}		
		Present	Chen (1995)	Ayatollahi and Nejati (2011a)	Present	Chen (1995)	Ayatollahi and Nejati (2011a)
15	0	1.0768	–	1.0979	0.1812	–	0.1789
	30	1.0957	1.1070	1.1076	0.2489	0.2480	0.2474
	60	1.1457	1.1530	1.1531	0.3421	0.3380	0.3373
	90	1.2526	1.2590	1.2591	0.4207	0.4260	0.4241
30	0	0.9799	–	0.9995	0.3349	–	0.3309
	30	0.9889	1.0000	1.0005	0.4509	0.4520	0.4491
	60	1.0158	1.0240	1.0263	0.5990	0.5960	0.5944
	90	1.0834	1.0900	1.0920	0.7180	0.7220	0.7194
45	0	0.8329	–	–	0.4406	–	–
	30	0.8278	0.8390	–	0.5766	0.5740	–
	60	0.8292	0.8370	–	0.7278	0.7210	–

To understand further the performance of the proposed method, the variation of the F_I and F_{II} with the notch inclination angle β are presented here for the ASENT specimen. Figure 4.20 shows the F_I and F_{II} versus β for the $a/w = 0.4$, and $\gamma = 0°$, 30°, 60° and 90°. The results correspond to $\beta = 0°$ (i.e., for pure mode I condition) are presented in Table 4.5. It can be observed from the plots in Figure 4.20 and results presented in Tables 4.4, 4.5, 4.18 and 4.19 that (a) when loading changes from pure mode I ($\beta = 0°$) to the mixed mode, F_I decreases and F_{II} increases with the increase in β for a given notch angle, (b) when $\beta = 0°$, F_{II} vanishes for all the notch angles and for all a/w values, (c) both the NSIFs increase with the increase in the notch angle for a given β, (d) in the specimens like ASENT, the mode II NSIF is less than the mode I NSIF regardless of the notch angle and (e) both the NSIFs increase with the increase in the value of a/w. All of these observations are consistent with the theory and previous studies (Dunn et al., 1997b; Savruk and Kazberuk, 2007; 2009; 2010; 2017). Similar trends can also be noticed for the ADENT specimen from Tables 4.20 and 4.21.

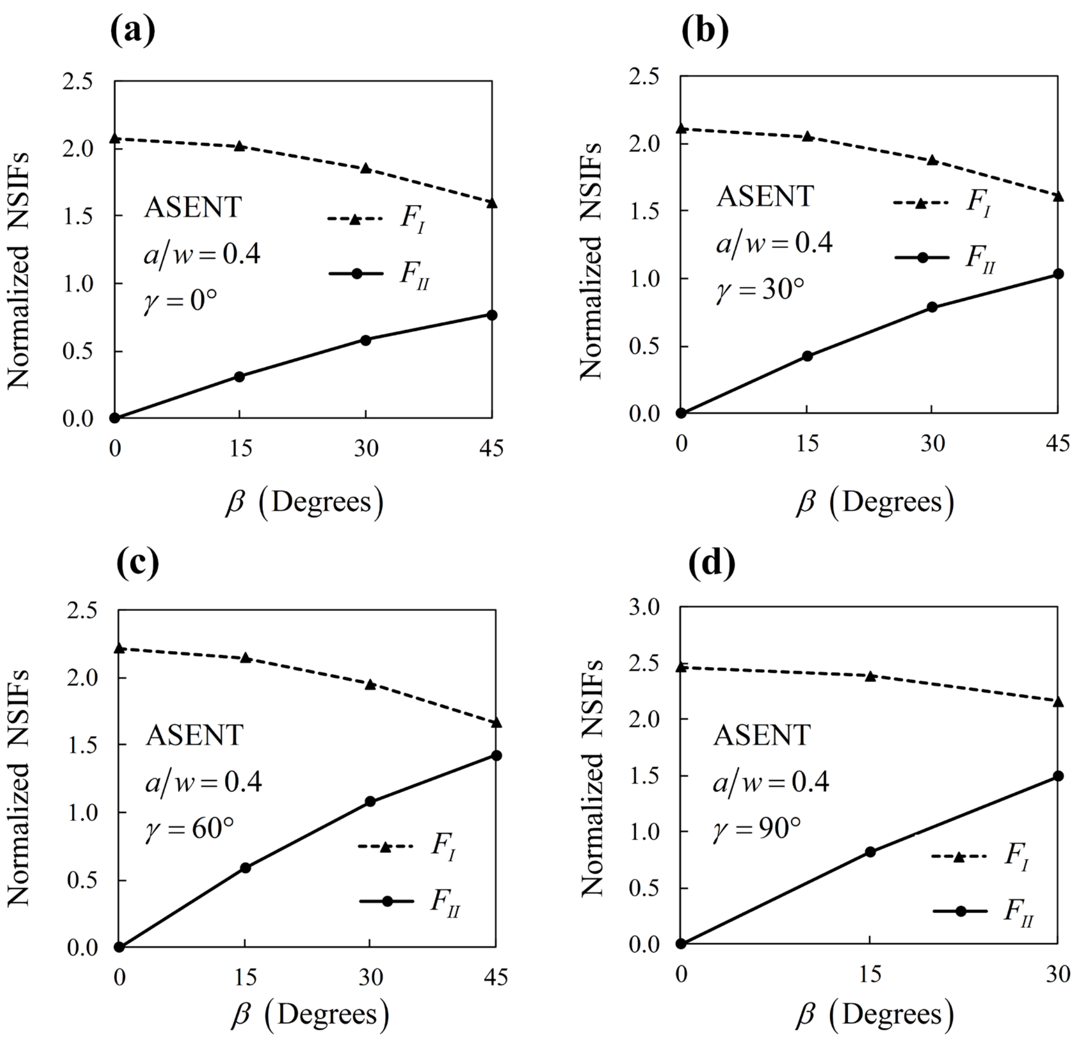

Figure 4.20. Variation of F_I and F_{II} with notch inclination angle β for the ASENT specimen.

Computed normalized mixed mode NSIFs using the proposed method for the ODENT and OCNT specimens are listed in Tables 4.22 and 4.23, respectively, for both $a/w = 0.2$ and 0.4, along with the reference solutions. An inspection of the results in Tables 4.22 and 4.23 clearly shows that once again, the normalized NSIFs obtained using the proposed method are in very good agreement with the published data for all the notch angles, a/w and notch positions considered here. This is true for both the NSIFs, F_I and F_{II}.

Table 4.22. Normalized NSIFs F_I and F_{II} for the ODENT specimen $(a/w = 0.2$ and $0.4)$.

$\frac{h_c}{2h}$	$\gamma(°)$	$a/w=0.2$		$a/w=0.4$			
		F_I	F_{II}	F_I		F_{II}	
		present	present	present	Treifi et al. (2009b)	present	Treifi et al. (2009b)
0.1	0	1.4175	0.0829	1.9109	1.9300	0.3639	0.3770
	30	1.4419	0.1188	1.9409	1.9490	0.5063	0.5110
	60	1.5117	0.1646	2.0307	2.0470	0.7199	0.7030
	90	1.6705	0.2237	2.2524	2.2500	1.0382	1.0230
0.2	0	1.1647	0.0181	1.2739	1.2950	0.0928	0.0960
	30	1.1864	0.0266	1.2963	1.3060	0.1291	0.1310
	60	1.2472	0.0382	1.3587	1.3610	0.1814	0.1800
	90	1.3764	0.0503	1.4972	1.5030	0.2470	0.2480
0.3	0	1.1065	0.0040	1.1403	1.1630	0.0198	0.0230
	30	1.1268	0.0059	1.1623	1.1740	0.0278	0.0310
	60	1.1853	0.0085	1.2234	1.2230	0.0437	0.0440
	90	1.3083	0.0118	1.3496	1.3550	0.0574	0.0590
0.4	0	1.0939	0.0005	1.1162	1.1360	0.0038	0.0040
	30	1.1152	0.0010	1.1379	1.1470	0.0052	0.0060
	60	1.1723	0.0011	1.1962	1.1950	0.0073	0.0090
	90	1.2942	0.0017	1.3212	1.3270	0.0101	0.0120

Table 4.23. Normalized NSIFs F_I and F_{II} for the OCNT specimen $(a/w = 0.2 \text{ and } 0.4)$.

$\frac{h_c}{2h}$	$\gamma(°)$	$a/w=0.2$		$a/w=0.4$			
		F_I	F_{II}	F_I		F_{II}	
		present	present	present	Treifi et al. (2009b)	present	Treifi et al. (2009b)
0.1	0	1.1508	0.0356	1.5456	1.5640	0.1752	0.1740
	30	1.2085	0.0660	1.6703	1.6770	0.3324	0.3330
	60	1.3304	0.1142	1.8738	1.8800	0.5934	0.5770
	90	1.5411	0.1809	2.2075	2.1850	0.8328	0.8350
0.2	0	1.0375	0.0059	1.1982	1.2190	0.0384	0.0390
	30	1.0842	0.0103	1.2778	1.2850	0.0707	0.0720
	60	1.1885	0.0190	1.4444	1.4400	0.1310	0.1320
	90	1.3736	0.0258	1.7537	1.7590	0.2154	0.2280
0.3	0	1.0130	0.0014	1.1125	1.1320	0.0106	0.0110
	30	1.0556	0.0030	1.1743	1.1810	0.0207	0.0210
	60	1.1542	0.0045	1.3090	1.3040	0.0397	0.0420
	90	1.3287	0.0057	1.5655	1.5720	0.0790	0.0810
0.4	0	1.0072	0.0002	1.0922	1.1120	0.0020	0.0030
	30	1.0486	0.0009	1.1486	1.1550	0.0044	0.0050
	60	1.1439	0.0012	1.2725	1.2670	0.0090	0.0110
	90	1.3145	0.0029	1.5037	1.5100	0.0198	0.0220

To demonstrate further the accuracy of extraction of the NSIFs using the proposed method, Figure 4.21 shows the plot of the variation of the NSIFs with the $h_c/2h$ of the ODENT specimen for $a/w = 0.4$ and $\gamma = 0°$, 30°, 60° and 90°. The results correspond to $h_c/2h = 0.5$ (i.e., for pure mode I condition) are presented in Table 4.7. From the results of Tables 4.6, 4.7 and 4.22 and Figure 4.21, the following observations can be made (a) when the notch is at the center position, i.e., $h_c/2h = 0.5$ (Figure 4.18), the ODENT is under pure mode I loading (Tables 4.6 and 4.7). At this ratio, for all the notch angles, the value of F_{II} is zero, (b) as the notch moves towards the bottom of the plate, i.e., when the $h_c/2h$ decreases, the asymmetry in the plate increases both the F_{II} and F_I increases, (c) both the NSIFs increase with the increase in the value of a/w for all the notch angles and $h_c/2h$ values, (d) both the NSIFs increases with the increase in the notch angle for a given

$h_c/2h$ value and (e) the mode II NSIF is less than the mode I NSIF regardless of the notch angle. All the above observations are anticipated and are in line with the previous predictions. Similar observations can also be noticed from the results of the OCNT specimen.

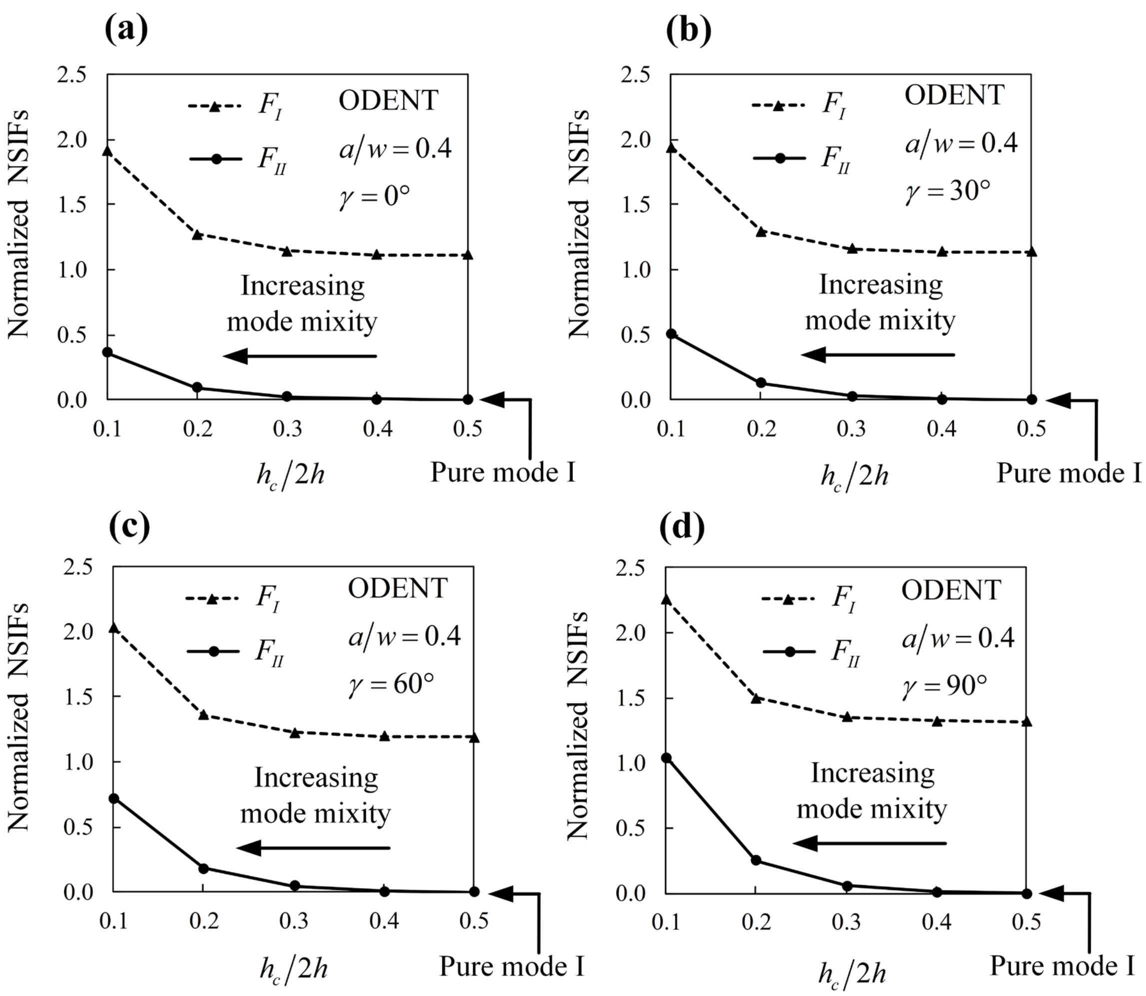

Figure 4.21. Variation of F_I and F_{II} with $h_c/2h$ for the ODENT specimen.

The results of the SV-BD specimen for a/R=0.3 and 0.5 and for the notch inclination angles $\beta = 0°$, 10°, 20°, 25°, 29°, and 35° are listed in Table 4.24. It can also be noticed from Table 4.24 that for $a/R = 0.5$ and for the combination of angles $(\gamma = 30°,\ \beta = 25°)$, $(\gamma = 60°,\ \beta = 29°)$ and $(\gamma = 90°,\ \beta = 35°)$, the SV-BD specimen will be under pure mode II loading condition. Similar observations have also been made by Ayatollahi and Nejati (2011b) for this same specimen. Once again, an excellent agreement of the present results with the published results can be clearly seen in Table 4.24 regardless of the notch angles, a/R and the notch inclination angles.

Table 4.24. Normalized NSIFs F_I and F_{II} for the SV-BD specimen ($a/R = 0.3$ and 0.5).

$\beta(°)$	$\gamma(°)$	$a/w = 0.3$		$a/w = 0.5$					
		F_I	F_{II}	F_I			F_{II}		
		Present	Present	Present	Ayatollahi and Nejati (2011b) (FEM)	Ayatollahi and Nejati (2011b) (Exp.)	Present	Ayatollahi and Nejati (2011b) (FEM)	Ayatollahi and Nejati (2011b) (Exp.)
0	30	0.4176	0.0036	0.7213	0.7100	0.7400	0.0027	0.0000	0.0200
	60	0.5980	0.0009	1.1530	1.1300	1.1700	0.0000	0.0000	0.0500
	90	1.0194	0.0036	2.3108	2.2900	2.2900	0.0000	0.0000	0.0600
10	30	0.3609	0.3984	0.5727	0.5600	0.6000	0.7470	0.7200	0.7200
	60	0.5258	0.6753	0.9599	0.9400	0.9900	1.2619	1.1700	1.1100
	90	0.9162	0.9183	2.0187	2.0000	1.9500	2.1169	2.0200	2.1300
20	30	0.1966	0.7171	0.2148	0.2000	0.2200	1.1800	1.1800	1.1800
	60	0.3236	1.0542	0.4940	0.4800	0.4800	1.8600	1.8600	1.8900
	90	0.6327	1.8366	1.3013	1.2900	1.2700	3.1200	3.1200	3.0300
25	30	0.0912	0.8305	0.0082	0.0000	0.0100	1.3036	1.2800	1.2600
	60	0.1877	1.3024	0.2185	–	–	2.0429	–	–
	90	0.4409	2.0932	0.8742	–	–	3.2716	–	–
29	30	0.0313	0.9126	1.9800	–	–	1.3447	–	–
	60	0.0425	1.4375	0.0555	-0.0100	0.0900	2.0788	2.0200	1.9200
	90	0.2298	2.2958	0.4395	–	–	3.2716	–	–
35	30	0.1569	0.9054	0.3947	–	–	1.3073	–	–
	60	0.1116	1.4471	0.3206	–	–	1.9924	–	–
	90	0.0078	1.8366	0.0082	0.0100	0.1500	3.2716	3.1900	3.3100

Figure 4.22 shows the variation of F_I and F_{II} of the SV-BD specimen with respect to the notch inclination angle β for $a/R = 0.5$ and $\gamma = 30°$, $60°$ and $90°$. The following observations can be made using the results presented in Figure 4.22 and Table 4.24 that (a) at $\beta = 0°$, the specimen is under pure mode I loading condition and consequently the values of F_{II} is zero for all the notch angles, (b) when the loading changes from pure mode I $(\beta = 0°)$ to the mixed mode, F_I decreases, becomes zero and then increases. On the other hand, F_{II} increases with the increase in β and then decreases for a given notch angle, (c)

when $a/R = 0.5$, for some combination of the γ and β (as mentioned above), F_I becomes zero and the specimen will be under pure mode II loading condition; however, the value of β at which the specimen undergoes pure mode II loading condition is different for different notch angles, (d) both the NSIFs increase with the increase in the value of a/R, (e) in most of the cases the NSIFs increases with the increase in the notch angle and (f) unlike rectangular boundary specimens, this specimen exhibits higher F_{II} values than F_I for the different notch angles. Most of these expected trends are similar to that of the previous specimens considered in this section.

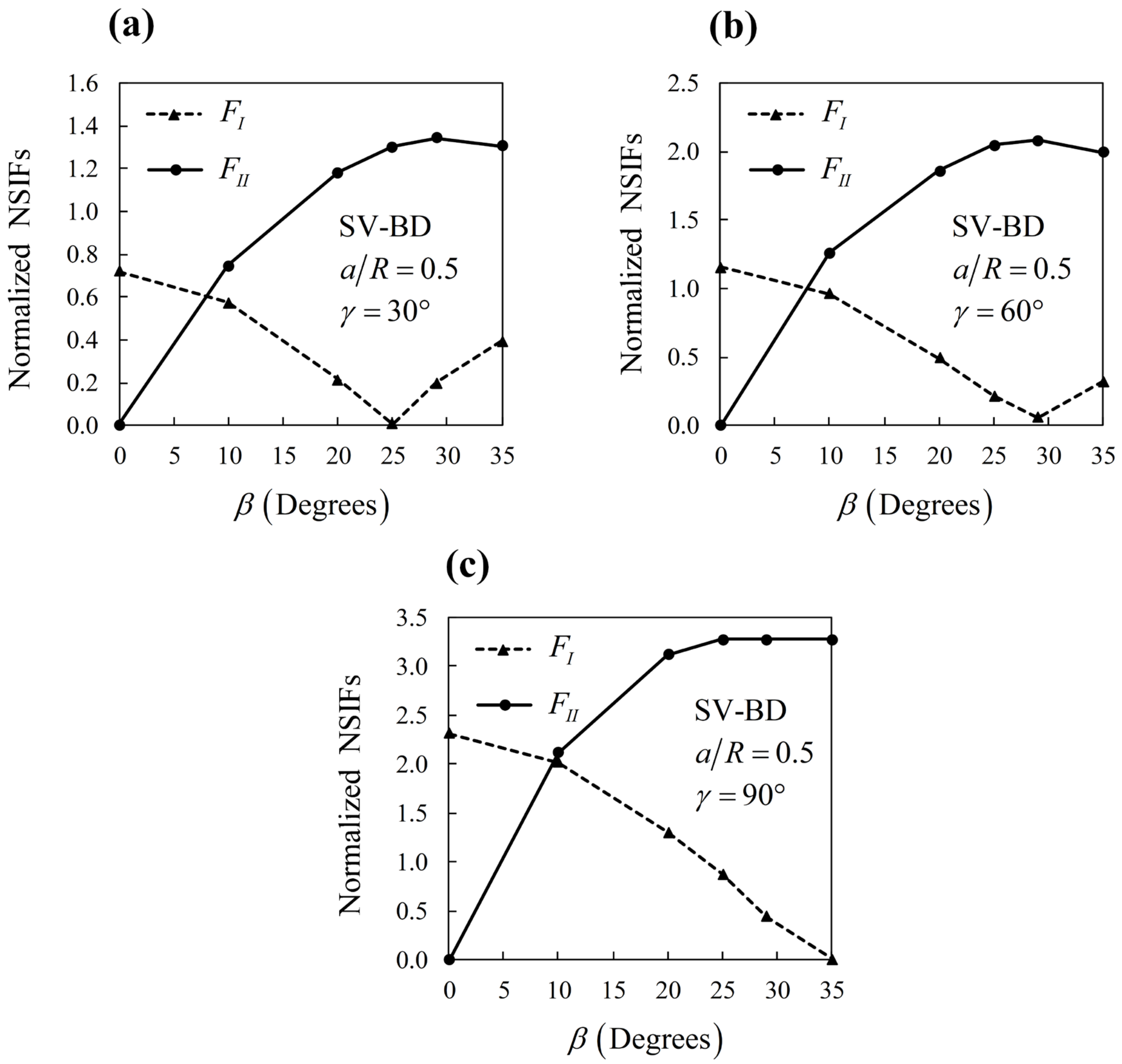

Figure 4.22. Variation of F_I and F_{II} with β for the SV-BD specimen.

Finally, the results and comparison presented in this section clearly demonstrate that very accurate mode I, mode II and mixed mode NSIFs can be easily computed using the proposed method in a simple way by substitution of the NOD and NSD values in Eq. (4.19) and Eq. (4.23) respectively.

4.4 Summary

In this chapter, a simple, efficient, and robust method for the accurate determination of the NSIFs from the FE notch flank displacements at specific radial locations termed as "optimum points" is proposed. The presence of these points in the Q8 elements is demonstrated for the first time for the sharp V-notch problems using the least-square and slope matching approach. In the proposed method, the notch opening and notch sliding displacements at these points are employed for the accurate estimation of the NSIFs. The proposed method can be easily incorporated into the existing FE codes, and the NSIFs can even be calculated by hand calculations if the displacements of these optimum point(s) are available. The convergence of the results has been demonstrated. Various mode I, mode II and mixed mode (I/II) benchmark problems have been analyzed for different notch angles and notch length to width ratios and compared with the published data. A very good agreement between the present results and that of the published data is observed in all problems considered here. Using the proposed method, accurate NSIFs can be obtained using coarse meshes. The formulation of the proposed method is quite general and can be applied to the complex 2D sharp V-notched configurations subjected to arbitrary in-plane loading.

Chapter 5

Proposed collocation method

5.1 Introduction

In this chapter, another yet simple and efficient method based on the collocation has been proposed for the accurate estimation of the NSIFs of the sharp V-notched configurations using FE notch opening and sliding displacements at the selected number of nodes along the notch flanks. The theoretical formulation of the proposed method is described in the following sections. It has been observed that, unlike the crack problems, the displacement field is rarely employed in the notch problems due to the complexities introduced by the presence of the rigid body displacements. Therefore, one of the main emphasis of the present work is to neatly bypass these rigid body displacements and develop a simple approach for the accurate computation of the NSIFs so that they can be easily incorporated into the existing codes.

The notch opening displacement (NOD) and notch sliding displacement (NSD) defined in the previous chapter will be employed in this chapter. In the present investigation, several benchmark problems under mode I, mode II and mixed mode (I/II) have been analyzed and compared with the published reference solutions. In addition, the procedures for the selection of valid collocation points for the accurate estimation of the NSIFs have also been explained in this chapter. Further, the convergence characteristics of the proposed method have also been studied using meshes of varying element sizes.

5.2 Formulations of the proposed collocation method

In this section, the theoretical formulation of the proposed collocation method for the calculation of the NSIFs is presented.

5.2.1 Determination of mode I NSIF

Formulation of the proposed collocation method for the determination of the mode I NSIF is described in the present section. Referring to Figure 4.1, the analytical NOD of the V-notch under the mixed mode (I/II) loading condition can be given by rewriting Eq. (4.4) as

$$\Delta v = v_{\theta=+\alpha} - v_{\theta=-\alpha} = 2\frac{A_1}{2G} r^{\lambda_1^I} \begin{bmatrix} \left(\kappa - \lambda_1^I \cos 2\alpha - \cos 2\alpha \lambda_1^I\right) \sin \lambda_1^I \alpha \\ + \lambda_1^I \sin\left(\lambda_1^I - 2\right)\alpha \end{bmatrix} = 2A_1 C_1 r^{\lambda_1^I} \tag{5.1}$$

where C_1 is a constant as described in Section 4.2.1. One can observe the absence of rigid body displacements in Eq. (5.1). Thus, by considering the NOD, the coefficients A_0, B_1 and B_2 are eliminated without being discarded. Now, taking logarithm on both the sides of Eq. (5.1), the NOD can be written as

$$\ln(\Delta v) = \ln(2A_1 C_1) + \lambda_1^I \ln(r) \tag{5.2}$$

Equation (5.2) represents a straight line with the slope equals to λ_1^I on the logarithmic scale and is valid within the so-called singularity dominated zone (SDZ). Here SDZ is the zone in which the leading terms of the infinite series of the displacement components are dominant. In accordance with the least-square method, the residual R_I between the analytical NOD and the FE NOD Δv^{FE} can be written as

$$R_I = \sum_{i=1}^{N} \left[\ln\left(\Delta v_i^{FE}\right) - \ln(A_1) - \ln(2C_1) - \lambda_1^I \ln(r_i) \right]^2 \tag{5.3}$$

In order that the function R_I to be minimum, the partial differentiation of R_I with respect to $\ln(A_1)$ must vanish, i.e.

$$\frac{\partial R_I}{\partial \ln(A_1)} = -2\sum_{i=1}^{N}\left[\ln\left(\Delta v_i^{FE}\right) - \ln(A_1) - \ln(2C_1) - \lambda_1^I \ln(r_i)\right] = 0 \tag{5.4}$$

After some algebraic manipulations, the Williams constant A_1 can be obtained as

$$A_1 = \frac{\exp\left[\frac{1}{N}\sum_{i=1}^{N} \ln\left(\Delta v_i^{FE} r_i^{-\lambda_1^I}\right)\right]}{2C_1} \tag{5.5}$$

The idea of the present method is to employ the collocation method to solve Eq. (5.5) for the solution of the unknown coefficient A_1. Thus, by computing the FE NOD, Δv^{FE} using the notch flank displacements at the collocation nodes lying on the notch flanks (Figure 5.1a), one can easily find A_1 using Eq. (5.5). Subsequently, the mode I NSIF K_I can be computed using Eq. (3.71). The suggested procedure for the selection of the valid collocation nodes to be used in Eq. (5.5) is described in Section 5.3.

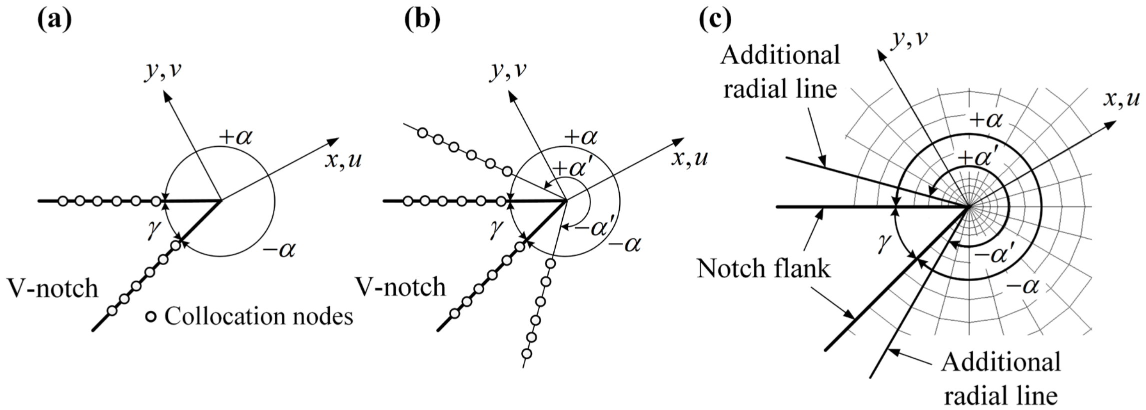

Figure 5.1. Selection of the collocation nodes for (a) mode I and (b) mode II, and (c) typical mesh arrangement around the notch tip.

5.2.2 Determination of mode II NSIF

This section describes the proposed method for the mode II problems. Similar to the mode I loading, the analytical notch sliding displacement (NSD) under the mixed mode loading condition can be written by rewriting Eq. (4.5) as

$$\begin{aligned}\Delta u = u_{\theta=+\alpha} - u_{\theta=-\alpha} &= 2\frac{B_1}{2G} r^{\lambda_1^{II}} \begin{bmatrix} \left(-\kappa - \lambda_1^{II}\cos 2\alpha + \cos 2\alpha \lambda_1^{II}\right)\sin \lambda_1^{II}\alpha \\ + \lambda_1^{II}\sin\left(\lambda_1^{II} - 2\right)\alpha \end{bmatrix} - 2\frac{\kappa+1}{2G} B_2 r \sin\alpha \\ &= 2B_1 C_2 r^{\lambda_1^{II}} + 2B_2 C_3 r \end{aligned} \tag{5.6}$$

Details of the various constants in the above equation have already been described in Section 4.2.2. The least-square approach implemented for the mode I loading is not feasible using Eq. (5.6) as Δu in Eq. (5.6) is accompanied by the rigid body rotation term B_2. Such minimization results into a single equation with two unknowns B_1 and B_2. It is worth mentioning here that substantial error in B_1 (and hence K_{II}) has been observed if B_2 is forcibly neglected in Eq. (5.6). Similar observations were noticed in the point substitution method presented in Chapter 4. Without discarding the constant B_2 in Eq. (5.6), if it can be eliminated as is done with A_0 and A_1, then the mode II NSIFs can be easily estimated using the coefficient B_1. Therefore, to facilitate computation of the accurate mode II NSIFs without neglecting the term B_2, a simplified procedure which neatly bypasses this term is developed in the present section and is explained in the following paragraphs.

Let us consider two additional radial lines at $\theta = +\alpha'$ and $\theta = -\alpha'$ as shown in Figure 5.1b apart from the notch flanks which are at $\theta = +\alpha$ and $\theta = -\alpha$. These two additional lines could be the radial lines, one above the top notch-flank and one below the bottom notch-flank in a typical spider-web FE mesh around the notch tip, as shown in Figure 5.1c. The NSD $\left(\Delta u_{\alpha'}\right)$ measured now between the above two additional lines ($\theta = +\alpha'$ and $\theta = -\alpha'$) can be written using Eq. (5.6) as

$$\Delta u_{\alpha'} = u_{\theta=+\alpha'} - u_{\theta=-\alpha'} = 2B_1 C_2' r^{\lambda_1^{II}} + 2B_2 C_3' r \tag{5.7}$$

where C_2' and C_3' are constants which depend upon the notch angle, eigenvalue, κ and the direction of the new line (α'). Eliminating B_2 from Eqs. (5.6) and (5.7) and after some algebraic manipulations, the effective notch sliding displacement (ENSD) Δu_{eff} in terms of the Williams' coefficient B_1 can be obtained as

$$\Delta u_{eff} = \Delta u C_3' - \Delta u_{\alpha'} C_3 = 2B_1\left(C_2 C_3' - C_2' C_3\right) r^{\lambda_1^{II}} = 2B_1 C_4 r^{\lambda_1^{II}} \tag{5.8}$$

where

$$\begin{aligned}
C_2 &= \frac{1}{2G}\left[\left(-\kappa - \lambda_1^{II}\cos 2\alpha + \cos 2\alpha \lambda_1^{II}\right)\sin \lambda_1^{II}\alpha + \lambda_1^{II}\sin\left(\lambda_1^{II} - 2\right)\alpha\right] \\
C_2' &= \frac{1}{2G}\left[\left(-\kappa - \lambda_1^{II}\cos 2\alpha + \cos 2\alpha \lambda_1^{II}\right)\sin \lambda_1^{II}\alpha' + \lambda_1^{II}\sin\left(\lambda_1^{II} - 2\right)\alpha'\right] \\
C_3 &= -\frac{\kappa+1}{2G}\sin\alpha \\
C_3' &= -\frac{\kappa+1}{2G}\sin\alpha' \\
C_4 &= \frac{1}{2G}\begin{bmatrix} (\kappa+1)\left(-\kappa - \lambda_1^{II}\cos 2\alpha + \cos 2\alpha\lambda_1^{II}\right)\left\{\sin\lambda_1^{II}\alpha'\sin\alpha - \sin\lambda_1^{II}\alpha\sin\alpha'\right\} \\ +\lambda_1^{II}(\kappa+1)\left\{\sin\left(\lambda_1^{II}-2\right)\alpha'\sin\alpha - \sin\left(\lambda_1^{II}-2\right)\alpha\sin\alpha'\right\} \end{bmatrix}
\end{aligned} \tag{5.9}$$

Now Eq. (5.8) contains only one coefficient B_1 and is similar to Eq. (5.1) of the mode I loading. Therefore, the least-square procedure used for the determination of the mode I NSIFs can now be implemented for the mode II problems using Eq. (5.8), i.e., using Δu_{eff}.

Taking logarithm on both the sides of Eq. (5.8), one can obtain

$$\ln\left(\Delta u_{eff}\right) = \ln\left(2B_1C_4\right) + \lambda_1^{II}\ln(r) \tag{5.10}$$

Equation (5.10) will also be a straight line in the double logarithmic plot, with the slope equals to λ_1^{II} and is valid within the SDZ. Now, the residual R_{II} between the analytical (Eq. (5.10)) and the FE values of the ENSD Δu_{eff}^{FE} for mode II can be written as

$$R_{II} = \sum_{i=1}^{N} \left[\ln\left(\Delta u_{eff,i}^{FE}\right) - \ln\left(B_1\right) - \ln\left(2C_4\right) - \lambda_1^{II} \ln\left(r_i\right) \right]^2 \tag{5.11}$$

For the minimum R_{II}, the partial differentiation of R_{II} with respect to $\ln\left(B_1\right)$ must be equal to zero, i.e.,

$$\frac{\partial R_{II}}{\partial \ln\left(B_1\right)} = -2\sum_{i=1}^{N} \left[\ln\left(\Delta u_{eff,i}^{FE}\right) - \ln\left(B_1\right) - \ln\left(2C_4\right) - \lambda_1^{II} \ln\left(r_i\right) \right] = 0 \tag{5.12}$$

After simplification of Eq. (5.12), the unknown coefficient B_1 can be obtained as

$$B_1 = \frac{\exp\left[\frac{1}{N} \sum_{i=1}^{N} \ln\left(\Delta u_{eff,i}^{FE} r_i^{-\lambda_1^{II}} \right) \right]}{2C_4} \tag{5.13}$$

where the constant C_4 can be obtained from Eq. (5.9).

Referring to Eq. (5.8), Δu_{eff}^{FE} in Eq. (5.13) can be computed as $\Delta u_{eff}^{FE} = \Delta u^{FE} C_3' - \Delta u_{\alpha'}^{FE} C_c$ where Δu^{FE} and $\Delta u_{\alpha'}^{FE}$ are the finite element NSD values between the two pairs of the radial lines $\theta = +\alpha$ and $\theta = -\alpha$ (i.e., notch flanks) and $\theta = +\alpha'$ and $\theta = -\alpha'$ (radial lines immediately adjacent to the notch flanks), respectively. Thus, the unknown coefficient B_1 in Eq. (5.13) can be found by employing the collocation method using the nodes lying on the above two pairs of radial lines. Subsequently, using this value, the mode II NSIFs can be estimated by employing Eq. (3.72). Thus, for the computation of the mode II NSIFs, sliding displacements along two additional radial lines are required apart from at the top and bottom notch flanks. It can be noticed from Eqs. (5.5) and (5.13) that the selection of the proper collocation points or nodes is vital for the accurate determination of the NSIFs using these equations. The procedure for the selection of these valid nodes is described in Section 5.3.

5.2.3 Determination of mixed mode (I/II) NSIFs

In the proposed method, the notch opening displacements Δv and sliding displacements Δu are employed for the computation of the NSIFs K_I and K_{II}, respectively. Referring to Eqs. (5.1) and (5.6), it can be seen that the same Eqs. (5.5) and (5.13) can also be directly used in the mixed mode (I/II) problems.

5.3 Selection of the valid collocation nodes

It can be noticed from the discussion in Section 5.2 that not all nodes available on the notch flanks and/or adjacent radial lines can be considered as the valid collocation points for the evaluation of Eqs. (5.5) and (5.13). In fact, as the leading terms are employed in Eqs. (5.1) and (5.6), valid or selected collocation nodes to be used in Eqs. (5.5) and (5.13) should be within the extent of validity of Eqs. (5.1) and (5.6), i.e., within the SDZ.

Two approaches can be devised for the selection of the valid collocation points. Let us consider the mode I loading first. Figure 5.2a shows a typical plot of the FE NOD $\left(\Delta v^{FE}\right)$ versus the radial distance (r) along the notch flank on a log-log scale and a superposed straight line with a slope equals to λ_1^I (Eq. (5.2)). Clearly, the nodes on the right-hand side that deviate from the straight line do not fall within the extent of validity of Eq. (5.2) and should not be considered as the valid collocations points. Further, results of a few nodes close to the notch tip (on the left-hand side) may not fall on the superposed straight line (may be due to the use of conventional elements at the notch tip as mentioned in Section 3.5) and should also be omitted from the list of the valid collocation nodes (Figure 5.2a). Thus, the nodes that are almost near to the superposed line should be considered as the valid collocation points.

As only one unknown is involved in Eq. (5.5), the use of the multiple collocation nodes leads to overdeterministic approach, and the above visual selection of the valid nodes do not introduce any significant error in the evaluation of Eq. (5.5). Even though this approach computes very accurate values of the NSIFs, the selection of these nodes in this way is time-consuming and difficult to implement the proposed method in the existing FE codes.

Therefore, another simple, straightforward, and robust approach based on the experience has been presented as follows.

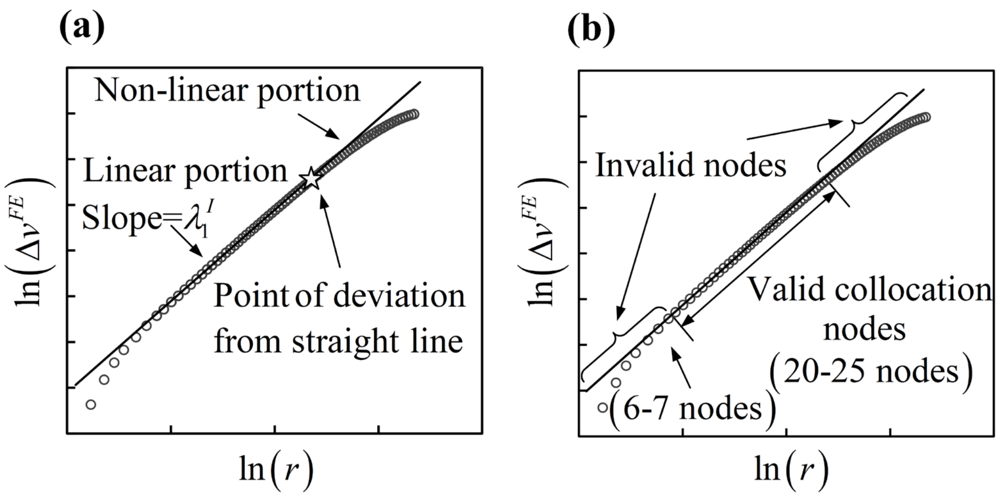

Figure 5.2. (a) Variation of $\ln(\Delta v^{FE})$ against $\ln(r)$ along notch flank and (b) valid and invalid collocation nodes.

In this second approach, irrespective of the density of the mesh chosen, one can omit the first 6 to 7 number of nodes from the notch tip along the notch flank and select the following 20 to 25 numbers of nodes (Figure 5.2b) as the valid collocation nodes for use in Eq. (5.5). Experience shows that this approach results in an infallible method for the selection of valid collocation points for reasonably fine meshes. More numbers of valid collocation nodes will be available on the dense meshes, and one can choose more than 20 numbers in such cases. However, 20 number of nodes are found to be a conservative set, and such procedures are proved very successful (Liu et al., 2008). Further, the same collocation nodes can also be used for the mode II and mixed mode (I/II) problems. These two approaches are demonstrated in Section 5.4.

5.4 Numerical results and discussion

In this section, the same benchmark examples of the pure mode I, pure mode II and mixed mode (mode I/II) presented in Chapter 4 have been considered here for demonstrating the efficacy of the proposed collocation method. FE analyses of the benchmark example problems have been carried out using ANSYS® (ANSYS, 2007), and the nodes on the notch flanks are considered as the collocation points. As is done in the previous chapter, the conventional Q8 elements are utilized throughout the domain, and Q8 elements are collapsed to form triangular elements in a standard spider web pattern at the notch tip. No singular or special elements are employed at the notch tip to model the singularity. The proposed collocation method including solving Eqs. (5.5) and (5.13) have been implemented in MATLAB (MATLAB, 2015) by writing codes.

The material properties for all the example problems of this chapter are Young's modulus $E=1.0$ and Poisson's ratio $\nu=0.25$. The thickness of all the specimens is considered as unity. Applied stresses $\sigma, \tau=10$ and point load $F_E=1.0$ are considered in this chapter. Plane stress conditions are assumed in all the problems, and the width of the plate $w=10$ is set in all the examples. The radius (R) of the Brazilian disc (SV-BD) and the semi-circular bend (SCB) specimens is set at $R=60$ and 40, respectively. Units are consistent. The NSIFs obtained using the proposed method are normalized using Eqs. (4.25) – (4.28). The percent relative error in the calculated $F_{I(II)}$ is obtained using Eq. (4.29).

5.4.1 Mode I examples

To demonstrate the efficacy of the proposed collocation method, the same mode I examples in Chapter 4 are considered once again here. The five mode I examples considered are (a) SENT, (b) DENT, (c) CNT, (d) 3PB, and (e) SCB, as shown in Figure 4.5. The notch angles (γ), the notch length to width ratios (a/w), notch length to radius ratios (a/R), and the height to width ratios (h/w) are also the same as discussed in Section 4.3.1. For convenience, a summary of the geometric and loading parameters of the above example problems has been presented in Table 5.1.

At first, to study the convergence of the estimated normalized NSIFs using the proposed collocation method, four meshes (Figure 5.3) are designed with increasing mesh density for the SENT specimen with $a/w=0.4$ and $\gamma=60°$. Figure 5.3 also shows the number of elements (NE) and the number of nodes (NN) used in the FE analyses. The ratio of the notch tip element size to the notch length (L_N/a) decreases from 0.050 to 0.002 as the meshes are refined. The densest mesh (Mesh 4 in Figure 5.3) consists of 947 number of elements and 3082 number of nodes. Following the procedure explained in Section 5.3,

Figure 5.4 shows the plots of $\ln(\Delta v^{FE})$ versus the radial distance $\ln(r)$ from the notch tip along the notch flanks along with the superposed lines having slope equals to λ_1^I (= 0.5122, see Table 4.1).

Table 5.1. Details of geometric and loading parameters of the mode I example problems.

	SENT	DENT	CNT	3PB	SCB
a/w	0.2, 0.4	0.2, 0.4	0.2, 0.4	0.2, 0.4	-----
h/w	1.2	2.0	2.0	2.0	-----
γ	0° to 120°	0° to 120°	0° to 120°	0° to 120°	0° to 90°
w	10.0	10.0	10.0	10.0	-----
R	-----	-----	-----	-----	40
a/R	-----	-----	-----	-----	0.3 and 0.5
σ	10.0	10.0	10.0	-----	-----
F_E	-----	-----	-----	1.0	1.0

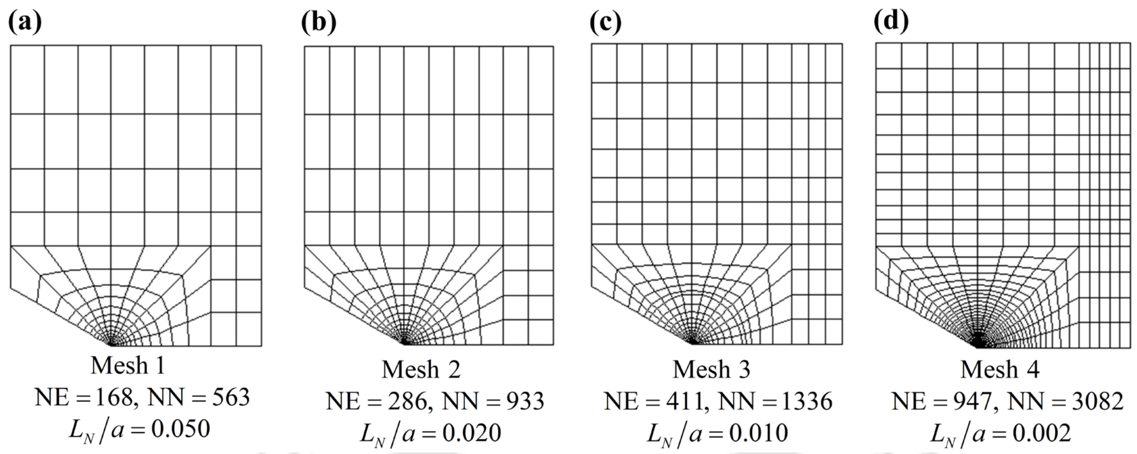

Figure 5.3. Typical FE meshes used for the convergence study.

As predicted by the theory (Section 5.3), the nodes on the right-hand side beyond the star symbol in Figure 5.4 do not obey the Eq. (5.2) and deviate from the superposed straight line due to the presence of the higher-order Williams coefficients at those radial distances. Following the recommendations made in Section 5.3, i.e., the first 6 nodes from the notch tip and the nodes that deviate from the straight line on the right are omitted from the list of the valid collocation nodes.

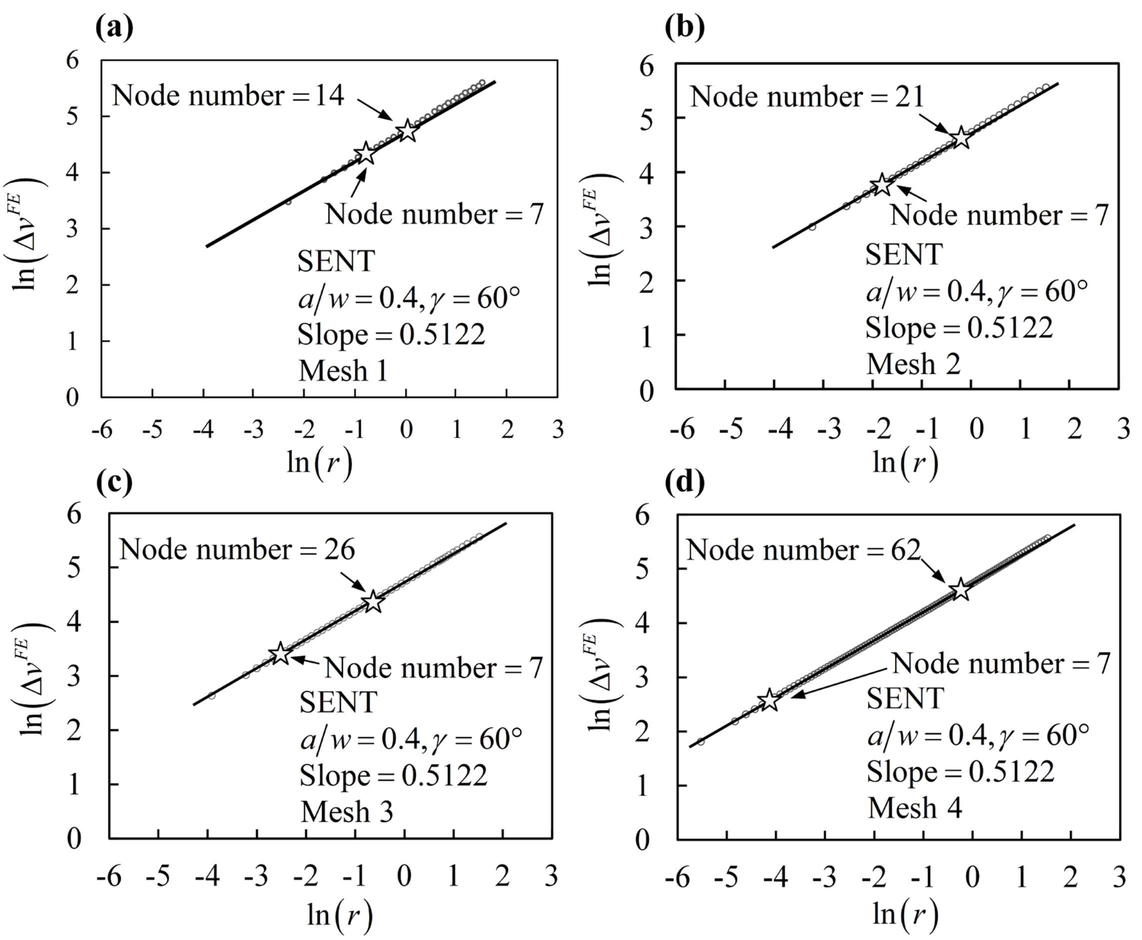

Figure 5.4. Plot of $\ln\left(\Delta v^{FE}\right)$ versus $\ln(r)$ for the FE meshes shown in Figure 5.3.

Table 5.2 shows the estimated normalized NSIF F_I using the proposed method with the actual number (those obtained from Figure 5.4) of the valid collocation nodes along with the published results and the percent relative error in F_I. This constitutes error in the first approach discussed in Section 5.3. Chen (1995) results are considered as the reference solution in Eq. 4.29. Table 5.2 also shows error in the computed F_I for the number of valid collocation nodes limited to 20 numbers as suggested in the second approach in Section 5.3. It can be noticed from the results presented in Table 5.2 that no significant changes in the estimated F_I values in the relatively dense meshes using the first and second approaches of the selection of the collocation nodes. Thus, instead of plotting graphs of the type as in Figure 5.4 (for assessment of the actual number of collocation nodes), one would omit the first 6 or 7 nodes from the notch and select the following 20 numbers of nodes as the valid collocation nodes as suggested in the second approach. Such a procedure leads to a simple and robust approach for the selection of the collocation points. Results of Table

5.2 also indicate the convergence results, and it can be seen that in both cases, the results are converging and are in good agreement with the reference solution as the meshes are refined.

Table 5.2. Converge of F_I with mesh refinement for the SENT specimen $\left(a/w = 0.4 \text{ and } \gamma = 60°\right)$.

Mesh	NE	NN	Actual number of collocation nodes	F_I Present	F_I Chen (1995)	% Rel. error	% Rel. error with 20 number of collocation nodes
Mesh 1	168	563	8	2.2441	2.2230	0.95	3.55
Mesh 2	286	933	14	2.2404		0.78	1.61
Mesh 3	411	1336	19	2.2325		0.43	0.52
Mesh 4	947	3082	55	2.2305		0.34	0.43

It can be noticed from results in Table 5.2 that in the case of coarse meshes (such as Mesh 1 and Mesh 2 in Figure 5.3), due to the availability of less number of nodes on the notch flank, selection of the valid nodes by plotting them as in Figure 5.2b (first approach in Section 5.3) gives more accurate results than selecting 20 numbers of nodes as suggested in the second approach. On the other hand, in the case of reasonably fine meshes, 20 numbers of nodes can be readily available and which can be used to provide the accurate results. Nevertheless, convergence to the reference NSIF can be noticed by selecting 20 numbers of nodes as the meshes are refined, as shown in the last column of Table 5.2. Henceforth, in all the subsequent examples, the second approach with 20 number of nodes has been adopted for the computation of the NSIFs.

To validate the efficacy of the proposed method, the mode I NSIFs have been determined for the SENT, DENT, CNT and 3PB specimens having a/w = 0.2 and 0.4 and SCB specimen having a/R = 0.3 and 0.5. Various notch angles considered are $\gamma = 0° - 120°$ for the SENT, DENT, CNT and 3PB specimens and $\gamma = 0° - 90°$ for the SCB specimen (See Table 5.1). Results of the SENT and DENT specimens are listed in Tables 5.3 – 5.6, along with the available published results for the purpose of comparison. A hyphen (–) is used wherever published results are not available in the above tables. For a better understanding of the performance of the proposed method, results using the meshes Mesh 1, Mesh 2 and Mesh 4 (Figure 5.3) have also been presented for these two problems in the above tables. For determining the mode I NSIFs, 6, 10 and 20 number of collocation nodes are considered for the Mesh 1, Mesh 2 and Mesh 4, respectively. Conversely, the first approach has been adopted for the Mesh 1 and Mesh 2 for the selection of the collocation points. On the other hand, the second approach is used for the selection of the nodes for the Mesh 4.

Table 5.3. Values of the normalized NSIF F_I for the SENT specimen ($a/w = 0.2$).

	F_I								
$\gamma \rightarrow$	0°	15°	30°	45°	60°	75°	90°	105°	120°
Present (Mesh 1)	1.3265	1.3377	1.3555	1.3847	1.4294	1.4952	1.5875	1.7127	1.8759
Present (Mesh 2)	1.3410	1.3498	1.3655	1.3924	1.4352	1.4992	1.5901	1.7138	1.8758
Present (Mesh 4)	1.3547	1.3594	1.3717	1.3960	1.4371	1.4998	1.5900	1.7133	1.8749
Chen (1995)	–	–	1.3810	–	1.4450	–	1.5970	–	–
Gross and Mendelson (1972)	1.3688	–	1.3807	–	1.4460	–	1.6042	–	1.8891
Zhao and Hahn (1992)	1.3738	–	1.3769	–	1.4374	–	1.5714	–	1.7812

Table 5.4. Values of the normalized NSIF F_I for the SENT specimen ($a/w = 0.4$).

	F_I								
$\gamma \rightarrow$	0°	15°	30°	45°	60°	75°	90°	105°	120°
Present (Mesh 1)	2.0953	2.1083	2.1308	2.1707	2.2366	2.3399	2.4950	2.7228	3.0531
Present (Mesh 2)	2.0974	2.1074	2.1271	2.1641	2.2273	2.3278	2.4801	2.7047	3.0318
Present (Mesh 4)	2.0960	2.1016	2.1177	2.1520	2.2133	2.3122	2.4632	2.6864	3.0117
Chen (1995)	–	–	2.1290	–	2.2230	–	2.4720	–	–
Gross and Mendelson (1972)	2.1133	–	2.1283	–	2.2230	–	2.4734	–	3.0215
Zhao and Hahn (1992)	2.1062	–	2.1140	–	2.2230	–	2.4854	–	2.9597
Kim and Cho (2008)	2.1130	–	2.1300	–	2.2250	–	2.4740	–	–
Ayatollahi and Nejati (2011a)	2.1100	2.1125	2.1273	2.1610	2.2250	2.3214	2.4718	–	–
Yi et al. (2017)	2.1100	–	2.1270	–	2.2240	–	2.4690	–	3.195

Table 5.5. Values of the normalized NSIF F_I for the DENT specimen ($a/w = 0.2$).

	F_I								
$\gamma \rightarrow$	0°	15°	30°	45°	60°	75°	90°	105°	120°
Present (Mesh 1)	1.0741	1.0836	1.0988	1.1232	1.1602	1.2135	1.2865	1.3816	1.4976
Present (Mesh 2)	1.0879	1.0954	1.1087	1.1313	1.1666	1.2185	1.2903	1.3844	1.4995
Present (Mesh 4)	1.1013	1.1053	1.1156	1.1360	1.1698	1.2206	1.2917	1.3855	1.5004
Treifi et al. (2009b)	1.1110	–	1.1220	1.1250	1.1650	–	1.3020	–	–
Chen (1995)	–	–	1.1230	–	1.1760	–	1.2980	–	–

Table 5.6. Values of the normalized NSIF F_I for the DENT specimen ($a/w = 0.4$).

	F_I								
$\gamma \rightarrow$	0°	15°	30°	45°	60°	75°	90°	105°	120°
Present (Mesh 1)	1.0907	1.1006	1.1163	1.1413	1.1790	1.2333	1.3078	1.4055	1.5267
Present (Mesh 2)	1.1065	1.1142	1.1279	1.1510	1.1871	1.2399	1.3132	1.4098	1.5302
Present (Mesh 4)	1.1218	1.1259	1.1365	1.1573	1.1917	1.2435	1.3162	1.4125	1.5328
Treifi et al. (2009b)	1.1320	–	1.1430	1.1530	1.1910	–	1.3230	–	–
Chen (1995)	–	–	1.1450	–	1.1990	–	1.3230	–	–
Ayatollahi and Nejati (2011a)	1.1326	1.1343	1.1439	1.1641	1.1984	1.2499	1.3221	–	–
Yi et al. (2017)	–	–	1.1400	1.1560	1.1900	–	1.3280	–	–

An inspection of the results presented in Tables 5.3 – 5.6 shows that the NSIFs obtained from the proposed method using the Mesh 4 (Figure 5.3d) are in excellent agreement with the published results for all the notch angles as compared to the results using the Mesh 1 and Mesh 2 specifically when $\gamma \leq 30°$. As expected, this is mainly due to the less density in the Mesh 1 and Mesh 2 to model the strong singularity for the notch angles $\gamma \leq 30°$. On the other hand, relatively fine mesh such as the Mesh 4 provides accurate solutions for any notch angle. From the observation of the results presented in Tables 5.3 – 5.6, the NSIFs of all example problems of this chapter have been analyzed with the help of the meshes whose mesh densities are similar to that of the Mesh 4 where L_N/a has a value of 0.002, as shown in Figure 5.3d. Thus, meshes having L_N/a=0.002 are considered for the determination of the NSIFs in all the example problems considered in this chapter.

Estimated normalized mode I NSIFs of the CNT specimen have been shown in Tables 5.7 and 5.8. While the 3PB specimen results have been presented in Tables 5.9 and 5.10. Finally, Tables 5.11 and 5.12 show the results of the SCB specimen. The typical mesh used for the SCB specimen in shown in Figure 5.5. The typical mesh consists of NE = 1234 and NN= 3907 (for $\gamma = 60°$ and $a/R = 0.5$). In all these tables, published results are also presented for the purpose of comparison of the accuracy of extraction of the proposed method. As stated in the previous chapter, only very limited results are available for the SCB specimen, i.e., only for $\gamma = 0°$. Using Ayatollahi and Nejati (2011a) overdeterminstic method, the results of the SCB specimen have been computed and presented in Tables 5.11 and 5.12 for all notch angles. It can be observed from the results presented in Tables 5.7 – 5.12 that the NSIFs obtained from the proposed collocation method are in very good agreement with the published results for all the notch angles, a/w and a/R values considered.

Table 5.7. Values of the normalized NSIFs F_I for the CNT specimen ($a/w = 0.2$).

	F_I								
$\gamma(°)\rightarrow$	0	15	30	45	60	75	90	105	120
Present	1.0137	1.0253	1.0489	1.0866	1.1407	1.2140	1.3103	1.4313	1.5806
Triefy et al. (2009b)	1.0240	–	1.0530	1.0670	1.1310	–	1.3210	–	–

Table 5.8. Values of the normalized NSIFs F_I for the CNT specimen ($a/w = 0.4$).

	F_I								
$\gamma(°) \rightarrow$	0	15	30	45	60	75	90	105	120
Present	1.0980	1.1153	1.1466	1.1949	1.2642	1.3595	1.4900	1.6632	1.9031
Triefy et al. (2009b)	1.1090	–	1.1510	1.1840	1.2610	–	1.4970	–	–

Table 5.9. Values of the normalized NSIFs F_I for the 3PB specimen ($a/w = 0.2$).

	F_I								
$\gamma(°) \rightarrow$	0	15	30	45	60	75	90	105	120
Present	0.7687	0.7708	0.7940	0.7942	0.8242	0.8739	0.9513	1.0681	1.2418
Gross and Mendelson (1972)	0.7770	–	0.7850	–	0.8320	–	0.9630	–	1.2610
Zhao and Hahn (1992)	0.7780	–	0.7810	–	0.8300	–	0.9550	–	1.2150

Table 5.10. Values of the normalized NSIFs F_I for the 3PB specimen ($a/w = 0.4$).

	F_I								
$\gamma(°) \rightarrow$	0	15	30	45	60	75	90	105	120
Present	1.3081	1.3098	1.3182	1.3396	1.3814	1.4533	1.5689	1.7495	2.0298
Gross and Mendelson (1972)	1.3180	–	1.3250	–	1.3900	–	1.5780	–	2.0340
Zhao and Hahn (1992)	1.3150	–	1.3220	–	1.4040	–	1.6170	–	2.0050

Table 5.11. Values of normalized NSIFs F_I for the SCB specimen (a/R =0.3).

	F_I						
$\gamma(°)\rightarrow$	0	15	30	45	60	75	90
Present	2.5587	2.5650	2.5836	2.6242	2.6979	2.8182	3.0035
Ayatollahi and Aliha (2006)	2.6040	–	–	–	–	–	–
Tutluoglu and Keles (2011)	2.5380	–	–	–	–	–	–
Using Ayatollahi and Nejati (2011a) method	2.5752	2.5809	2.5984	2.6374	2.7091	2.8271	3.0096

Table 5.12. Values of normalized NSIFs F_I for the SCB specimen (a/R =0.5).

	F_I						
$\gamma(°)\rightarrow$	0	15	30	45	60	75	90
Present	3.5923	3.6023	3.6316	3.6968	3.8180	4.0203	4.6082
Ayatollahi et al. (2011a)	3.6000	–	–	–	–	–	–
Tutluoglu and Keles (2011)	3.5500	–	–	–	–	–	–
Using Ayatollahi and Nejati (2011a) method	3.6198	3.6286	3.6555	3.7174	3.8340	4.0307	4.6126

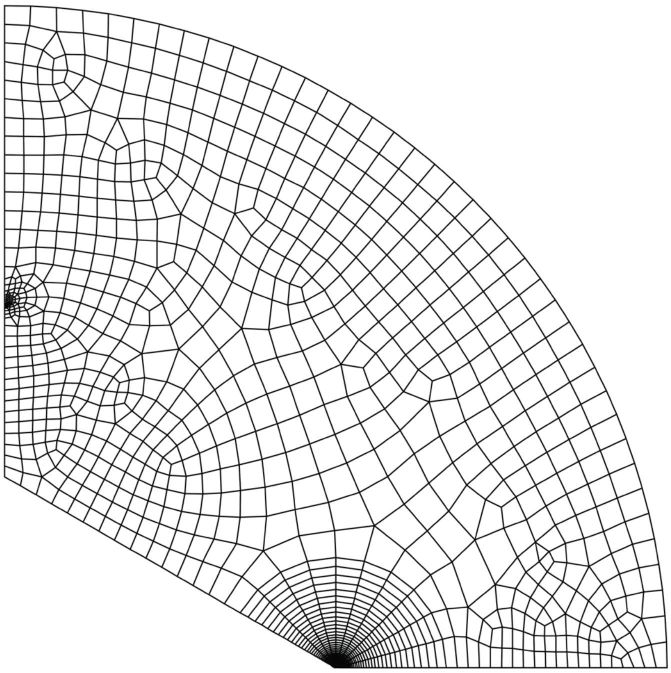

Figure 5.5. Typical FE mesh used for the SCB specimen (NE = 1234, NN = 3907).

In order to validate further the performance of the proposed method, variation of the F_I of the CNT and 3PB specimens with the notch angle has been made, as shown in Figure 5.6. It can be seen from the plots of Figure 5.6 that as expected F_I value increases with the notch angle being minimum at $\gamma = 0°$ (Savruk and Kazberuk, 2007; 2009; 2010; 2017). It can also be seen from Figure 5.6 that as expected F_I values increase with the increase in a/w ratio. Similar trends have also been noticed from the results of the other example problems considered in this section. It is worth mentioning here that such trends have been presented in the previous chapter for the SENT and DENT specimens.

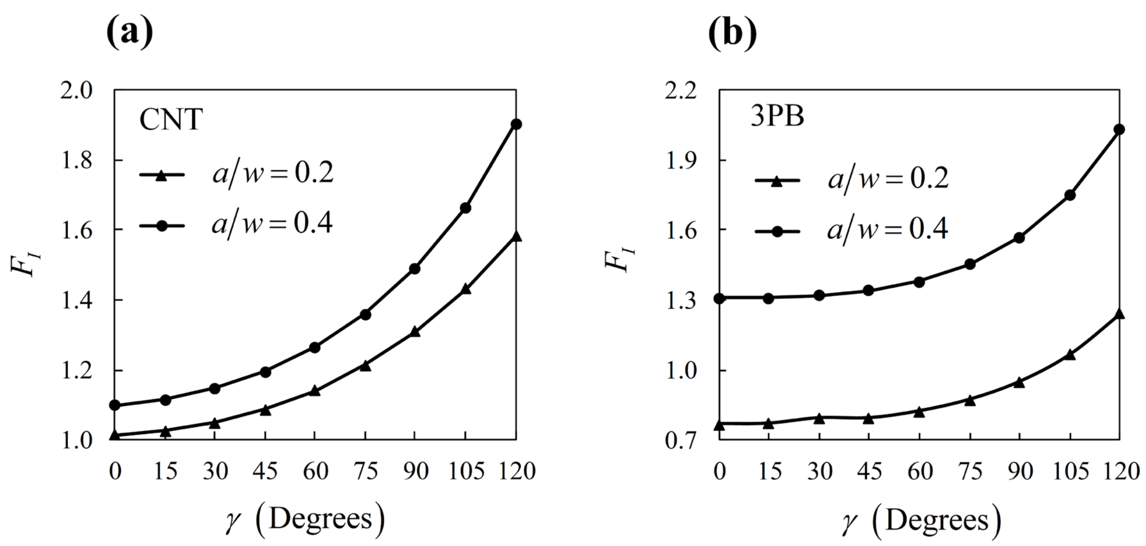

Figure 5.6. Variation of F_I with the notch angle γ for the (a) CNT and (b) 3PB specimens.

5.4.2 Mode II examples

The SENS specimen (Figure 4.15) is again considered here to demonstrate the efficacy of the proposed method under pure mode II loading conditions. The boundary conditions are also shown in Figure 4.15. Mode II NSIF is determined for this specimen for $\gamma = 0°$, 15°, 30°, 45°, 60°, 75° and 90° and $a/w = 0.2$ and 0.4 with $h/w = 1.0$. Further, for the notch angle $\gamma = 50°$ the NSIFs have been determined for $a/w = 0.2 - 0.5$.

Similar to the case of mode I loading, for calculating F_{II}, Δu^{FE} is obtained at 20 number of consecutive nodes (starting from the 7th node from the notch tip) along the notch flanks ($\theta = +\alpha$ and $\theta = -\alpha$) and along two additional radial lines at $\theta = +\alpha'$ and $\theta = -\alpha'$ (Figure

5.1b). To substantiate the applicability of the previously suggested collocation nodes for the mode II problems, graphs of $\ln\left(\Delta u_{eff}^{FE}\right)$ versus $\ln(r)$ (Eq. 5.10) have been plotted from the 7th node to the next consecutive 20 numbers of nodes as shown in Figure 5.7, for $a/w = 0.4$ and $\gamma =$ 0°, 30°, 60° and 90°. As expected, linearity can be observed in the plot between $\ln\left(\Delta u_{eff}^{FE}\right)$ versus $\ln(r)$ up to a relatively long distance with slope equals to the corresponding λ_1^I value (See Table 4.1 in Chapter 4). These results once again ensure that for the mode II problems also the suggested 7 – 20 combination of numbers of nodes forms a conservative set.

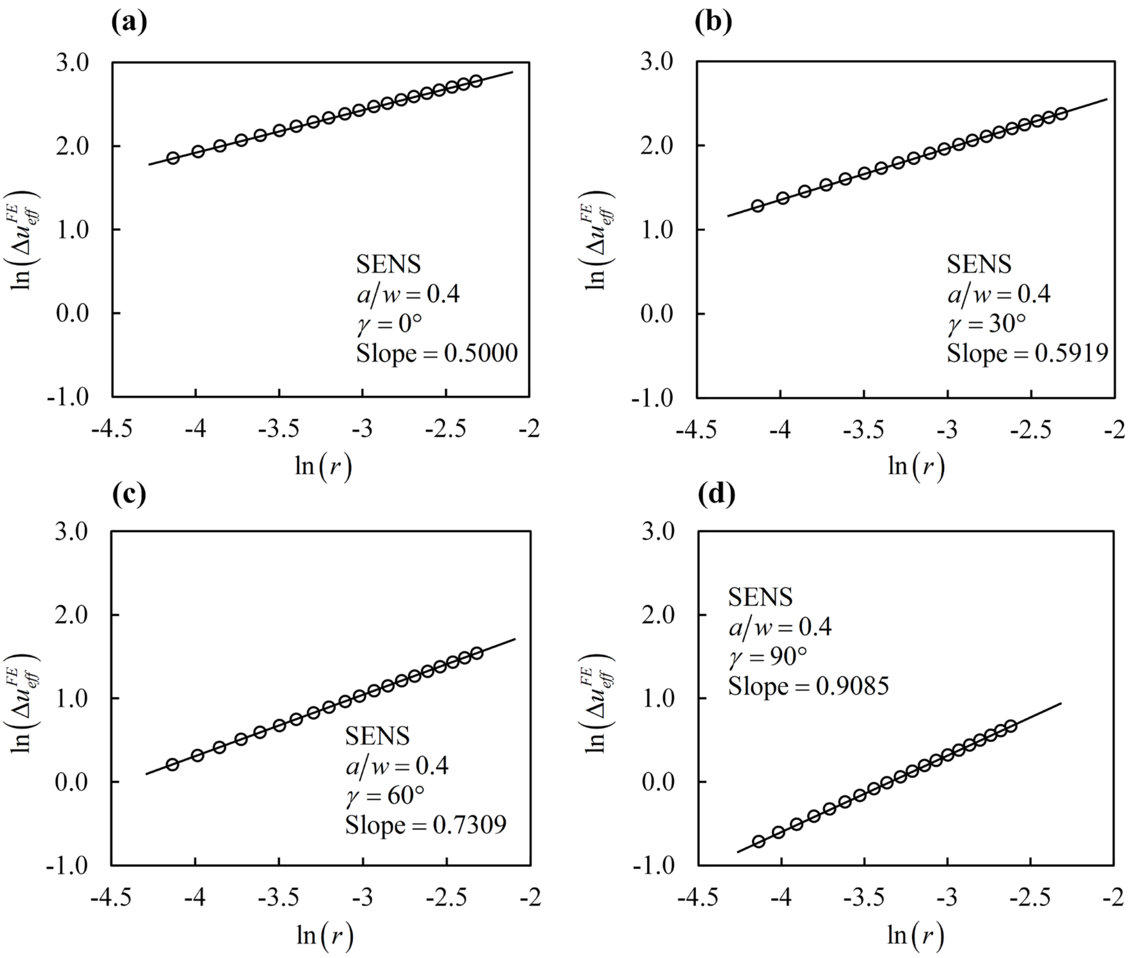

Figure 5.7. Variation of $\ln\left(\Delta u_{eff}^{FE}\right)$ with $\ln(r)$ for the SENS specimen (a) $\gamma = 0°$, (b) $\gamma = 30°$, (c) $\gamma = 60°$ and (d) $\gamma = 90°$.

Tables 5.13 and 5.14 show the computed mode II NSIF using the proposed method for the SENS specimen with $a/w = 0.4$ and 0.2, respectively, for the notch angles $\gamma = 0°$, 15°, 30°, 45°, 60°, 75° and 90°. For the purpose of comparison, Tables 5.13 and 5.14 also show the available published results. However, only a few published results are available for the configuration $a/w = 0.2$. It can be noticed from the results of Tables 5.13 and 5.14 that the NSIF obtained using the proposed collocation method for both $a/w = 0.4$ and 0.2 are in excellent agreement with the published results. These results also further substantiate the proposed approach for the selection of the valid collocation nodes for use in Eq. 5.13. The results of $a/w = 0.2 - 0.5$ for the notch angle $\gamma = 50°$ are listed in Table 5.15 and compared with the results of Treify et al. (2008). Here also a very good agreement has been observed between the present and available results.

Table 5.13. Values of the normalized NSIF F_{II} for the SENS specimen $(a/w = 0.4)$.

	F_{II}							
$\gamma \rightarrow$	0°	15°	30°	45°	50°	60°	75°	90°
Present (Eq. (5.13))	1.1585 (0.64)*	1.3691 (–)	1.6248 (0.01)	1.9323 (–)	2.0474 (–)	2.2975 (0.24)	2.7229 (–)	3.2067 (0.23)
Present Omitting B_2 in Eq. (5.6)	1.1585 (0.64)	–	1.6265 (0.09)	–	–	2.2158 (7.25)	–	1.6194 (49.63)
Zhao and Hahn (1991)	1.1660	–	1.6250	–	–	2.2920	–	3.2150
Treifi et al. (2008)	1.1800	–	1.6350	–	2.0610	2.3070	–	3.1750
Ayatollahi and Nejati (2011a)	1.1735	1.3817	1.6287	1.9365	–	2.2986	2.7309	3.2134
Zhao and Hahn (1992)	1.1500	–	1.8630	–	–	2.3550	–	3.1260
Kim and Cho (2009)	1.1780	–	1.6330	–	–	2.2970	–	3.2040
Yi et al. (2017)	1.1820	–	1.6290	–	–	2.3040	–	3.1760

*Bracketed values are percent relative error with respect to Zhao and Hahn (1991)

Table 5.14. Values of the normalized NSIF F_{II} for the SENS specimen $(a/w = 0.2)$.

	F_{II}						
$\gamma \rightarrow$	0°	15°	30°	45°	60°	75°	90°
Present (Eq. (5.13))	0.6817	0.8092	0.9647	1.1528	1.3757	1.4345	1.9248
Treifi et al. (2008)	0.6960	–	–	–	–	–	–

Table 5.15. Values of the normalized NSIF F_{II} for the SENS specimen ($\gamma = 50^{o}$).

	F_{II}			
$a/w \rightarrow$	0.2	0.3	0.4	0.5
Present (Eq. (5.13))	1.2226	1.6741	2.0474	2.3805
Treifi et al. (2008)	1.2580	1.6980	2.0610	2.3880

Introduction of substantial error in the estimated NSIFs due to the negligence of the rigid body displacements is also shown in Table 5.13, corresponding to $a/w = 0.4$. The NSIFs and percent relative error have also been computed by omitting the B_2 term in Eq. (5.6) for the various notch angles. It is observed from Table 5.13 that for the crack $(\gamma = 0°)$, the NSIFs obtained with or without considering the term B_2 are the same and very accurate with respect to the reference solutions of Zhao and Haun (1991). Nonetheless, as the notch angle increases the error in the NSIFs also increases (around 50% for $\gamma = 90°$) if the B_2 term is neglected. On the other hand, the computed mode II NSIFs using Eqs. (5.13) are in excellent agreement with the solutions of Zhao and Haun (1991) where B_2 term is considered implicitly for the calculation of the NSIFs and the percent relative error is less than 0.7% for all the notch angles. Thus, these results clearly show that rigid body modes have a significant effect on the accuracy of the computed NSIFs and cannot be neglected arbitrarily.

To substantiate further the efficacy of the proposed method in the extraction of the mode II NSIFs, a plot of the NSIF versus the notch angle is made, as shown in Figure 5.8 for $a/w = 0.2$ and 0.4. Similar to the mode I examples, F_{II} increases with the increase in the notch angle γ as expected (Savruk and Kazberuk, 2007; 2009; 2010, 2017). Moreover, F_{II} is also increasing with the increase in a/w.

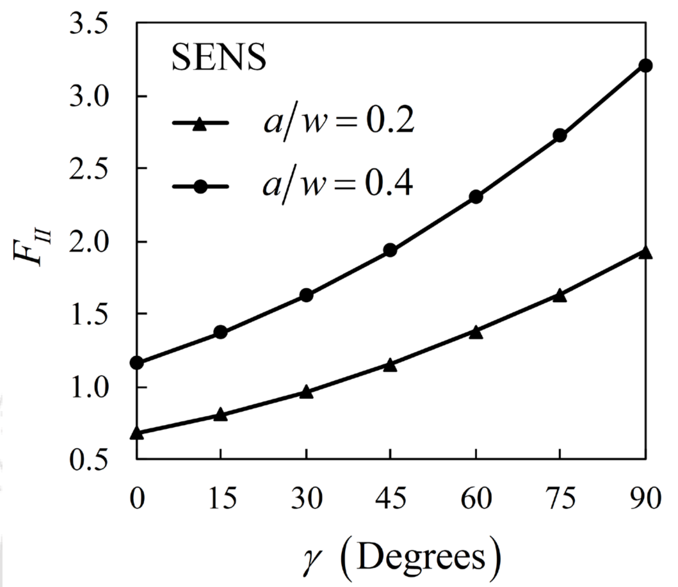

Figure 5.8. Variation of F_{II} with notch angle γ for the SENS specimen.

5.4.3 Mixed mode (I/II) examples

Five example problems viz. (a) ASENT, (b) ADENT, (c) ODENT, (d) OCNT, and (e) SV-BD (Figures 4.17 – 4.19) considered in the previous chapter are also considered here to investigate the efficacy of the proposed collocation method in the mixed mode (I/II) loading conditions. The width $w = 10$ is considered for the ASENT, ADENT, ODENT and OCNT specimens. The radius of the SV-BD specimen is considered as $R = 60$. Table 5.16 summarizes the geometric and loading parameters of the above configurations used in this section.

Table 5.16. Summary of the geometry and loading parameters of the mixed mode specimens.

	ASENT	ADENT	ODENT	OCNT	SV-BD
a/w	0.2, 0.4	0.2, 0.4	0.2, 0.4	0.2, 0.4	-----
γ	0° – 90°	0° – 90°	0° – 90°	0° – 90°	30° – 90°
β	15° – 45°	15° – 45°	-----	-----	0° – 35°
$h_c/2h$	-----	-----	0.1 – 0.4	0.1 – 0.4	-----
a/R	-----	-----	-----	-----	0.3, 0.5
h/w	3.5	3.5	2.0	2.0	-----
σ	10.0	10.0	10.0	10.0	-----
F_E	-----	-----	-----	-----	1.0
w	10	10	10	10	-----
R	-----	-----	-----	-----	60

In this section, meshes with $L_N/a = 0.002$ are considered for the computation of the NSIFs as mentioned in the discussion of the mode I problems. The FE meshes used for the mixed mode examples are shown in Figures 5.9 and 5.10 along with the mesh region near the notch tip. The typical mesh used for the ASENT and ADENT specimens consists of 860 number of elements and 2808 number of nodes. The typical mesh used for the ODENT and OCNT specimens consists of NE = 860 and NN = 2808. Finally, the typical mesh used for the SV-BD specimen in the collocation method consists of NE = 2969 and NN = 9169. For determining F_I and F_{II} for all the mixed mode specimens, Δv^{FE} has been evaluated at 20 number of consecutive nodes (starting from the 7th node from the notch tip) along the notch flanks. Similarly, Δu_{eff}^{FE} has been evaluated at the same nodes at the notch flanks and at two additional radial lines at $\theta = \alpha'$ and $\theta = -\alpha'$ as is done for the case pure mode II examples. The graphs of $\ln\left(\Delta v^{FE}\right)$ and $\ln\left(\Delta u_{eff}^{FE}\right)$ versus $\ln(r)$ are plotted (starting from 7th node from the notch tip to the next consecutive 20 numbers of nodes) in Figure 5.11 for the ASENT specimen with $a/w = 0.4$, $\beta = 30°$ and $\gamma = 0°$, 30°, 60° and 90° to demonstrate the applicability of the suggested collocation nodes for the mixed mode (I/II) problems. It can be observed from Figure 5.11 that the plots between $\ln\left(\Delta v^{FE}\right)$ and $\ln\left(\Delta u_{eff}^{FE}\right)$ versus $\ln(r)$ are linear up to a relatively long distance with slopes equal to the respective λ_1^I and λ_1^{II} values, respectively.

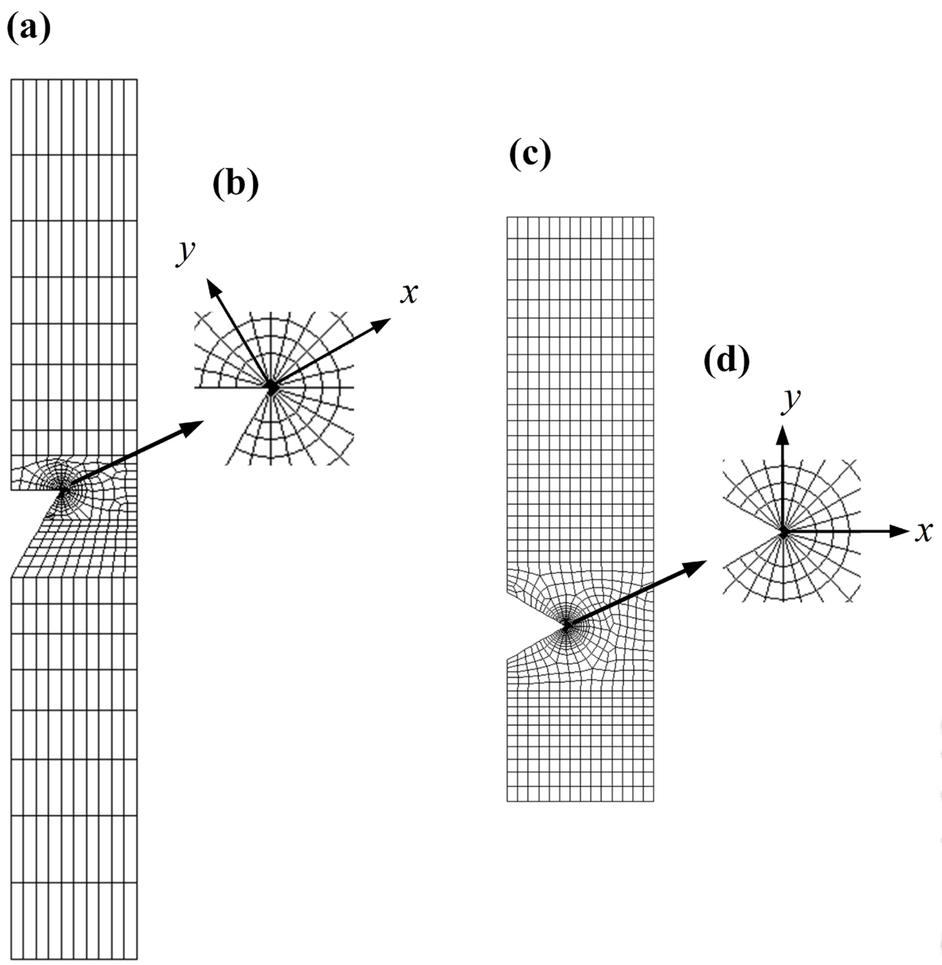

Figure 5.9. (a) Typical meshes used for the ASENT and ADENT specimens in the collocation method (NE=860, NN=2808), (b) enlarged view of the notch tip portion of the ASENT and ADENT specimens, (c) typical meshes used for the ODENT and OCNT specimens in the collocation method (NE=1438, NN=4592) and (d) enlarged view of the notch tip portion of the ODENT and OCNT specimens.

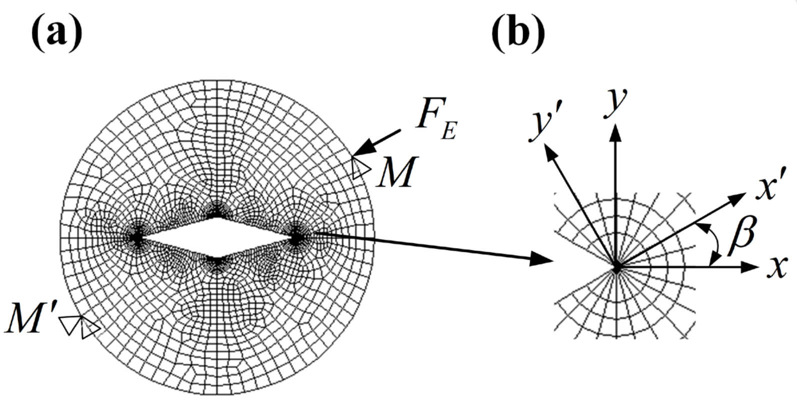

Figure 5.10. (a) Typical meshes used for the SV-BD specimen in the collocation method (NE=2969, NN=9169), (b) enlarged view of the notch tip portion.

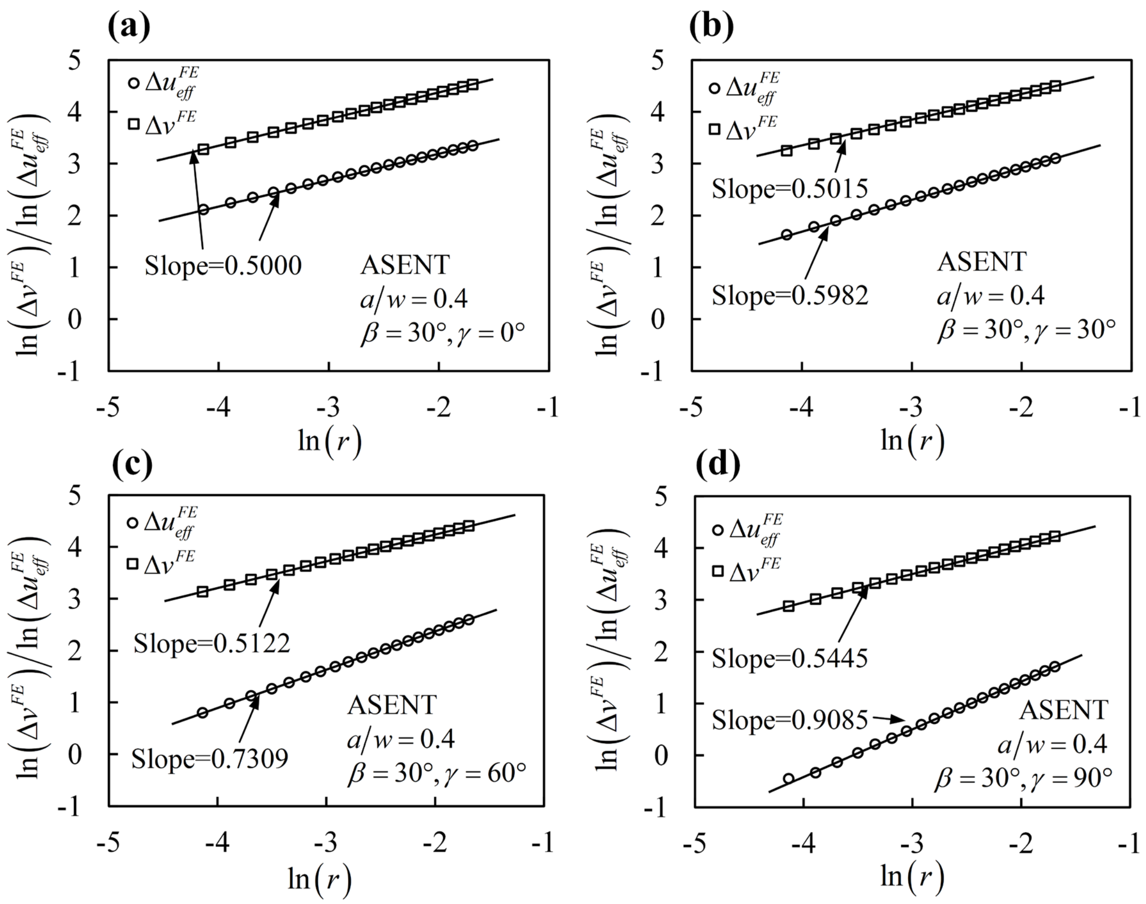

Figure 5.11. Variation of $\ln(\Delta v^{FE})$ and $\ln(\Delta u_{eff}^{FE})$ with $\ln(r)$ for the ASENT specimen (a) $\gamma = 0°$, (b) $\gamma = 30°$, (c) $\gamma = 60°$ and (d) $\gamma = 90°$.

The results of the mixed mode normalized NSIFs F_I and F_{II} for the ASENT and ADENT specimens using the proposed method for $a/w = 0.2$ and 0.4 and for the notch inclination angles $\beta = 15°$, 30° and 45° are presented in Tables 5.17 – 5.20. These tables also contain available published results. An excellent agreement between the present results obtained using the proposed collocation method and those available results can be observed from the results of Tables 5.17 – 5.20. This is true for both the NSIFs F_I and F_{II} for all a/w, notch angles and for all the notch inclination angles.

Table 5.17. Values of the normalized NSIFs F_I and F_{II} for the ASENT specimen ($a/w = 0.2$).

$\beta(°)$	$\gamma(°)$	F_I		F_{II}	
		Present	Chen (1995)	Present	Chen (1995)
15	0	1.3161	–	0.2085	–
	30	1.3310	1.3360	0.2908	0.2940
	60	1.3873	1.3920	0.4025	0.4020
	90	1.5213	1.5250	0.5231	0.5220
30	0	1.2000	–	0.3878	–
	30	1.2035	1.2100	0.5330	0.5360
	60	1.2361	1.2420	0.7168	0.7170
	90	1.3224	1.3280	0.9133	0.9050
45	0	1.0240	–	0.5134	–
	30	1.0126	1.0200	0.6831	0.6870
	60	1.0132	1.0200	0.8802	0.8830

Table 5.18. Values of the normalized NSIFs F_I and F_{II} for the ASENT specimen ($a/w = 0.4$).

$\beta(°)$	$\gamma(°)$	F_I			F_{II}		
		Present	Chen (1995)	Ayatollahi and Nejati (2011a)	Present	Chen (1995)	Ayatollahi and Nejati (2011a)
15	0	2.0446	–	2.0482	0.3024	–	0.3086
	30	2.0639	2.0660	2.0648	0.4213	0.4240	0.4238
	60	2.1525	2.1540	2.1525	0.5856	0.5870	0.5869
	90	2.3901	2.3910	2.3902	0.8033	0.8060	0.8062
30	0	1.8754	–	1.8761	0.5649	–	0.5747
	30	1.8863	1.8890	1.8870	0.7783	0.7830	0.7835
	60	1.9570	1.9600	1.9600	1.0754	1.0760	1.0770
	90	2.1637	2.1660	2.1645	1.4921	1.4900	1.4900
45	0	1.6210	–	–	0.7560	–	–
	30	1.6234	1.6260	–	1.0250	1.0300	–
	60	1.6719	1.6770	–	1.4066	1.4080	–

Table 5.19. Values of the normalized NSIFs F_I and F_{II} for the ADENT specimen ($a/w = 0.2$).

$\beta(°)$	$\gamma(°)$	F_I		F_{II}	
		Present	Chen (1995)	Present	Chen (1995)
15	0	1.0689	–	0.1723	–
	30	1.0812	1.0870	0.2410	0.2430
	60	1.1265	1.1310	0.3338	0.3340
	90	1.2272	1.2310	0.4306	0.4300
30	0	0.9733	–	0.3204	–
	30	0.9745	0.9810	0.4403	0.4440
	60	0.9938	1.0000	0.5887	0.5890
	90	1.0318	1.0370	0.7158	0.7140
45	0	0.8272	–	0.4231	–
	30	0.8116	0.8180	0.5596	0.5630
	60	0.7876	0.7940	0.6972	0.6990

Table 5.20. Values of the normalized NSIFs F_I and F_{II} for the ADENT specimen ($a/w = 0.4$).

$\beta(°)$	$\gamma(°)$	F_I			F_{II}		
		Present	Chen (1995)	Ayatollahi and Nejati (2011a)	Present	Chen (1995)	Ayatollahi and Nejati (2011a)
15	0	1.0878	–	1.0979	0.1759	–	0.1789
	30	1.1003	1.1070	1.1076	0.2462	0.2480	0.2474
	60	1.1477	1.1530	1.1531	0.3372	0.3380	0.3373
	90	1.2541	1.2590	1.2591	0.4250	0.4260	0.4241
30	0	0.9902	–	0.9995	0.3269	–	0.3309
	30	0.9932	1.0000	1.0005	0.4482	0.4520	0.4491
	60	1.0176	1.0240	1.0263	0.5939	0.5960	0.5944
	90	1.0846	1.0900	1.0920	0.7210	0.7220	0.7194
45	0	0.8419	–	–	0.4315	–	–
	30	0.8317	0.8390	–	0.5687	0.5740	–
	60	0.8305	0.8370	–	0.7187	0.7210	–

To understand further the performance of the proposed collocation method, the variation of the F_I and F_{II} with the notch inclination angle β for the notch angles $\gamma = 0°$, 30°, 60°

and 90° and $a/w = 0.4$ are plotted for the ADENT specimen as shown in Figure 5.12. Results correspond to the pure mode I condition (i.e., $\beta = 0°$) are taken from the Table 5.6. It can be observed from the plots in Figure 5.12 and results presented in the above tables that (a) when loading changes from pure mode I ($\beta = 0°$) to the mixed mode, F_I decreases and F_{II} increases with the increase in β for a given notch angle, (b) when $\beta = 0°$, F_I is zero for all the notch angles and for all a/w values, (c) both the NSIFs increase with the increase in the notch angle for a given β, (d) in the specimens like ADENT, F_I exhibits higher value than F_{II} regardless of the notch angle and (e) both the NSIFs increase with the increase in the value of a/w. Similar trends can also be noticed for the ASENT specimen. It should be noted that trends of the ASENT specimen have been presented in the previous chapter.

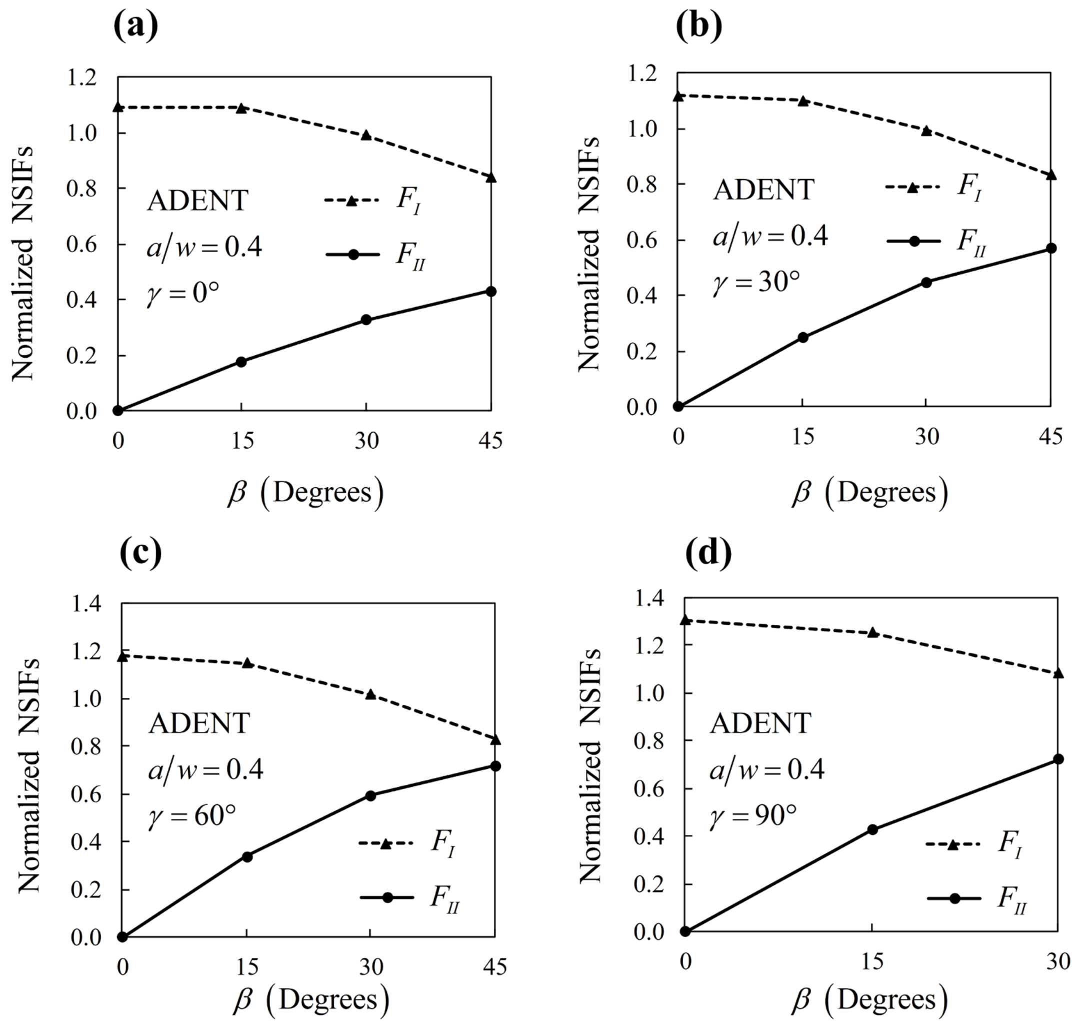

Figure 5.12. Variation of F_I and F_{II} with notch inclination angle β for the ADENT specimen.

Tables 5.21 and 5.22 list the results of the ODENT and OCNT specimens, respectively, for $a/w = 0.2$ and 0.4 and for the notch positions $h_c/2h$ =0.1, 0.2, 0.3 and 0.4 (see Table 5.16). To assess the efficacy of the proposed method, available published results are also presented in Tables 5.21 and 5.22 for the various notch angles. It can be clearly seen from the results of the above tables that once again, the present results show an excellent agreement in values of both the NSIFs F_I and F_{II} with the published results for all a/w, $h_c/2h$, and the notch angles.

Table 5.21. Values of the normalized NSIFs F_I and F_{II} for the ODENT specimen (a/w = 0.2 and 0.4).

$\frac{h_c}{2h}$	$\gamma(°)$	$a/w = 0.2$		$a/w = 0.4$			
		F_I	F_{II}	F_I		F_{II}	
		present	present	present	Treifi et al. (2009b)	present	Treifi et al. (2009b)
0.1	0	1.4312	0.0830	1.9292	1.9300	0.3652	0.3770
	30	1.4478	0.1181	1.9486	1.9490	0.5102	0.5110
	60	1.5138	0.1639	2.0333	2.0470	0.7197	0.7030
	90	1.6716	0.2296	2.2536	2.2500	1.0636	1.0230
0.2	0	1.1755	0.0178	1.2866	1.2950	0.0923	0.0960
	30	1.1909	0.0256	1.3015	1.3060	0.1293	0.1310
	60	1.2479	0.0363	1.3604	1.3610	0.1796	0.1800
	90	1.3779	0.0514	1.4983	1.5030	0.2510	0.2480
0.3	0	1.1162	0.0042	1.1537	1.1630	0.0217	0.0230
	30	1.1310	0.0060	1.1686	1.1740	0.0305	0.0310
	60	1.1860	0.0086	1.2243	1.2230	0.0422	0.0440
	90	1.3093	0.0121	1.3500	1.3550	0.0586	0.0590
0.4	0	1.1041	0.0007	1.1267	1.1360	0.0038	0.0040
	30	1.1189	0.0010	1.1418	1.1470	0.0053	0.0060
	60	1.1732	0.0014	1.1972	1.1950	0.0073	0.0090
	90	1.2952	0.0020	1.3216	1.3270	0.0092	0.0120

Table 5.22. Values of the normalized NSIFs F_I and F_{II} for the OCNT specimen (a/w = 0.2 and 0.4).

$\frac{h_c}{2h}$	$\gamma(°)$	$a/w=0.2$		$a/w=0.4$			
		F_I	F_{II}	F_I		F_{II}	
		present	present	present	Treifi et al. (2009b)	present	Treifi et al. (2009b)
0.1	0	1.1616	0.0346	1.5612	1.5640	0.1715	0.1740
	30	1.2132	0.0637	1.6769	1.6770	0.3322	0.3330
	60	1.3316	0.1111	1.8759	1.8800	0.5860	0.5770
	90	1.5430	0.1839	2.2541	2.1850	0.8167	0.8350
0.2	0	1.0475	0.0053	1.2107	1.2190	0.0372	0.0390
	30	1.0876	0.0098	1.2831	1.2850	0.0708	0.0720
	60	1.1888	0.0169	1.4449	1.4400	0.1293	0.1320
	90	1.3738	0.0255	1.7554	1.7590	0.2240	0.2280
0.3	0	1.0227	0.0015	1.1235	1.1320	0.0101	0.0110
	30	1.0593	0.0028	1.1784	1.1810	0.0201	0.0210
	60	1.1546	0.0052	1.3104	1.3040	0.0395	0.0420
	90	1.3298	0.0072	1.5669	1.5720	0.0799	0.0810
0.4	0	1.0167	0.0003	1.1032	1.1120	0.0020	0.0030
	30	1.0519	0.0005	1.1526	1.1550	0.0042	0.0050
	60	1.1443	0.0012	1.2734	1.2670	0.0088	0.0110
	90	1.3154	0.0030	1.5048	1.5100	0.0197	0.0220

Figure 5.13 shows the plots of variation of the NSIFs with the $h_c/2h$ of the OCNT specimen for $a/w = 0.4$ and $\gamma = 0°$, 30°, 60° and 90°. In Figure 5.13, the results of the mode I are taken from Table 5.8. From the results of the above tables and Figure 5.13, the following observations can be made (a) when the notch is at the center position, i.e., $h_c/2h = 0.5$ the OCNT is under pure mode I loading condition (CNT in Figure 4.17). At this ratio, for all the notch angles, the value of F_{II} is zero, (b) as the notch moves towards the bottom of the plate, i.e., when the $h_c/2h$ decreases, the asymmetry in the plate increases and thus both the F_{II} and F_I increases, (c) both the NSIFs increase with the increase in the value of a/w for all the notch angles and $h_c/2h$ values, (d) both the NSIFs increases with the increase in the notch angle for a given $h_c/2h$ value and (e) the mode II NSIF is less than the mode I NSIF regardless of the notch angle. All the above observations are

anticipated and are inline with the previous predictions. Similar observations have also been noticed from the results of the ODENT specimen.

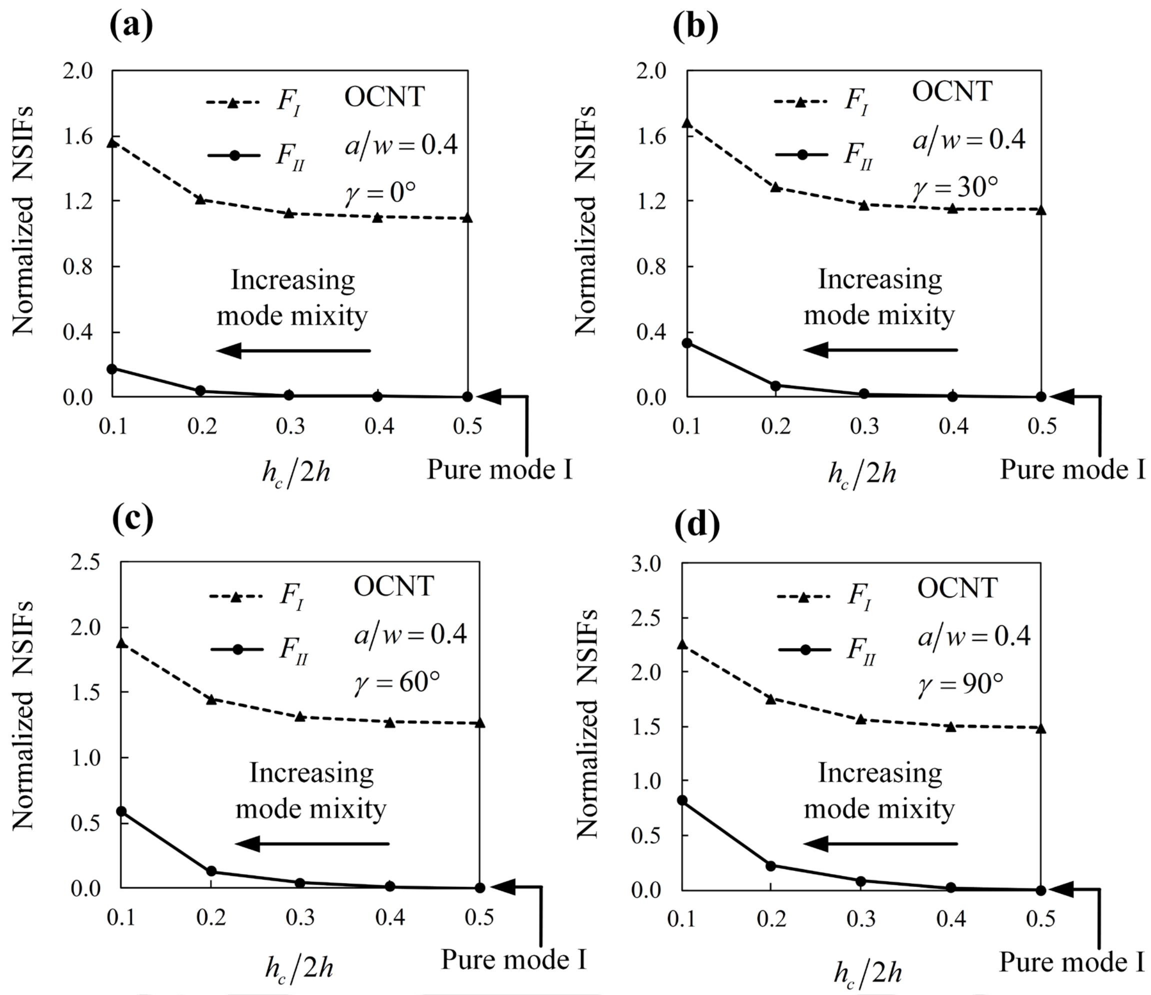

Figure 5.13. Variation of and F_{II} with $h_c/2h$ for the OCNT specimen.

The results for SV-BD specimen for a/w=0.3 and 0.5 and for the notch inclination angles $\beta = 0°$, 10°, 20°, 25°, 29° and 35° are listed in Table 5.23. To assess the efficacy of the proposed method, available published results are also presented in Table 5.23 for the various notch angles. It can be clearly seen in Table 5.23 that once again, the present results show an excellent agreement in values of both the NSIFs F_I and F_{II} with the published results for all a/R, the notch angles and for all the notch inclination angles.

Table 5.23. Comparison of the normalized NSIFs F_I and F_{II} for the SV-BD specimen ($a/w = 0.3$ and 0.5).

$\beta(°)$	$\gamma(°)$	$a/w = 0.3$ F_I Present	$a/w = 0.3$ F_{II} Present	$a/w = 0.5$ F_I Present	F_I Ayatollahi and Nejati (2011b) (FEM)	F_I Ayatollahi and Nejati (2011b) (Exp.)	F_{II} Present	F_{II} Ayatollahi and Nejati (2011b) (FEM)	F_{II} Ayatollahi and Nejati (2011b) (Exp.)
0	30	0.4191	0.0005	0.7245	0.7100	0.7400	0.0004	0.0000	0.0200
	60	0.5992	0.0023	1.1564	1.1300	1.1700	0.0016	0.0000	0.0500
	90	1.0213	0.0153	2.3174	2.2900	2.2900	0.0106	0.0000	0.0600
10	30	0.3564	0.3889	0.5743	0.5600	0.6000	0.7151	0.7200	0.7200
	60	0.5200	0.6034	0.9586	0.9400	0.9900	1.1583	1.1700	1.1100
	90	0.9213	1.1066	2.0286	2.0000	1.9500	1.9520	2.0200	2.1300
20	3 F_I 0	0.1965	0.7051	0.2157	0.2000	0.2200	1.1755	1.1800	1.1800
	60	0.3252	1.0920	0.4953	0.4800	0.4800	1.8650	1.8600	1.8900
	90	0.6319	1.8587	1.3070	1.2900	1.2700	3.0447	3.1200	3.0300
25	30	0.0884	0.8151	0.0000	0.0000	0.0100	1.2815	1.2800	1.2600
	60	0.1904	1.2672	0.2204	–	–	2.0001	–	–
	90	0.4418	2.0695	0.8787	–	–	3.3123	–	–
29	30	0.0316	0.8964	0.1991	–	–	1.3292	–	–
	60	0.0431	1.3929	0.0553	-0.0100	0.0900	2.0416	2.0200	1.9200
	90	0.2316	2.3709	0.4416	–	–	3.3027	–	–
35	30	0.1569	0.2250	0.3949	–	–	1.3179	–	–
	60	0.1049	1.2049	0.3206	–	–	1.9950	–	–
	90	0.0000	2.2467	0.0124	0.0100	0.1500	3.1639	3.1900	3.3100

Performance of the proposed method for the SV-BD specimen is further demonstrated with the help of Figure 5.14. It shows the variation of F_I and F_{II} of the SV-BD specimen with respect to the notch inclination angle β for $a/R = 0.5$ and $\gamma = 30°$, 60° and 90°. The following observations can be made using the results presented in Figure 5.14 and Table 5.23 that (a) at $\beta = 0°$, the specimen is under pure mode I loading condition and consequently the values of F_{II} is zero for all the notch angles, (b) when the loading changes from pure mode I $(\beta = 0°)$ to the mixed mode, F_I decreases, becomes zero and then increases. On the other hand, F_{II} increases with the increase in β and then decreases for a given notch angle, (c) when $a/R = 0.5$, for some combination of the γ and β (as mentioned in the previous chapter) F_I becomes zero and the specimen will be under pure mode II loading condition, (d) both the NSIFs increase with the increase in the value of a/R, (e) in most of the cases both the NSIFs increases with the increase in the notch angle and (f) unlike rectangular boundary specimens, this specimen exhibits higher F_{II} values than F_I for the different notch angles. Most of these expected trends are similar to those of the previous specimens considered in this section. Similar predictions were also observed in Chapter 4.

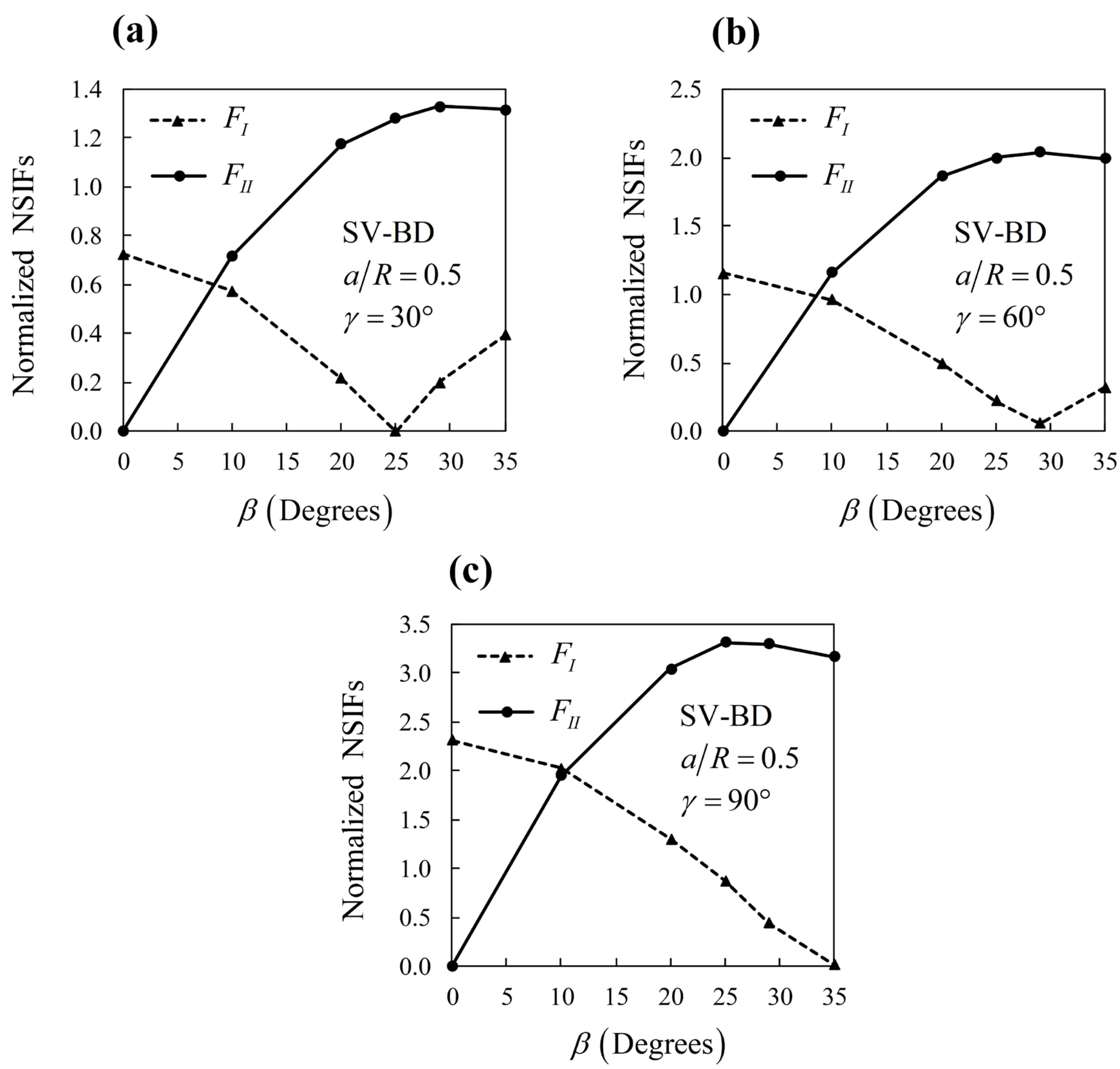

Figure 5.14. Variation of F_I and F_{II} with β for the SV-BD specimen ($a/R = 0.5$).

Finally, the results and comparisons presented in this section clearly demonstrate that very accurate mode I, mode II and mixed mode NSIFs can be easily computed using the proposed collocation method in a simple way by considering the NOD and NSD values at the collocation points in Eqs. (5.5) and Eq. (5.13), respectively.

5.5 Summary

In the present chapter, a simple, efficient, and robust collocation method has been proposed for the accurate determination of the mixed mode NSIFs of the sharp V-notched configurations. The proposed method employs the notch opening and sliding displacements on the notch flanks and obtains the NSIFs in an overdeterministic manner. No rigid body displacements have been neglected but elegantly eliminated from the formulation by choosing the notch opening and notch sliding displacements. Further, two approaches for the selection of valid collocation points for the sampling of the displacements have also been suggested and implemented. The second approach of selecting 20 nodes starting from the 7th node from the notch tip is found to be conservative, less time-consuming, and easy to implement. Normalized NSIFs of the mode I, mode II and mixed mode (I/II) benchmark problems have been extracted using the proposed method. The convergence of the results with the mesh refinement has also been demonstrated. An excellent agreement between the present and published results have been noticed in all classes of the problems considered in the present chapter. The results indicate that the proposed method is simple, robust, and can easily be incorporated in the existing codes. Some new results of the NSIFs of V-notched specimens are also presented in this work.

Chapter 6

Comparison of methods for computation of the NSIFs

6.1 Introduction

In this chapter, various FE based post-processing methods for the computation of the NSIFs are compared along with the present proposed methods on a common set of problems to study their efficacy in terms of accuracy of the computed NSIFs of the sharp V-notched 2D bodies. It has been discussed in Chapter 2 that many FE based methods have been developed over a few decades for the computation of the NSIFs under mixed mode (I/II) loading conditions. As stated in Chapter 1, such a comparative study is needed due to the following reasons

1. Survey of the literature reveals that no comparison among the developed methods on a common set of problems is available till date. One of the advantages of such comparison is the selection of the most appropriate methods by the researchers/practicing engineers for the analysis of the notched geometries.
2. Among the stress, displacement, and energy-based methods, displacement-based methods are seriously affected by the presence of the rigid body displacements. A comparison among the above methods reveals the influence of these rigid body terms in the displacement-based methods when compared with the stress and energy-based methods.

3. Another reason for comparison among the various methods required is due to the use of the collapsed conventional Q8 elements at the notch tip, despite knowing that the region around the tip of a sharp V-notch is a singular zone. A comparison of methods is, therefore, necessary to study the influence of the use of the conventional elements in finding the accurate NSIFs using different field variables such as the stresses, displacements and strain energy, etc.
4. Comparisons on the common set of problems provide better insight into their strengths and limitations due to the different approaches adopted by each method in their formulation of the methodology. For example, type of field variables used their sampling locations/areas, number of sampling points, rigid body components, use of conventional elements at the notch tip, etc.

Comparison of the various methods has been made in terms of the accuracy of the computed mixed mode (I/II) NSIFs on the same FE meshes and on the same common set of problems. Five most widely referred methods in the literature that are based on stress, displacement, and energy are considered in this study in addition to the proposed two methods of the present investigation. The theoretical formulations of all the seven methods are succinctly presented in this chapter.

6.2 Stress and displacement fields due to a sharp V-notch

In this section, the equations of field variables presented in Chapter 3 have been given here in a fashion that is suitable for the presentation of the formulation of the seven selected methods. For a 2D sharp V-notched (Figure 4.1) linear elastic body with notch angle $\gamma\left(=360°-2\alpha\right)$ made of an isotropic material, the leading terms of the stress field (i.e., $n=1$), in the vicinity of the notch tip under the mixed mode (I/II) loading conditions can be obtained using Eq. (3.53) as

$$\begin{Bmatrix}\sigma_{xx}\\ \sigma_{yy}\\ \sigma_{xy}\end{Bmatrix}=\frac{\lambda_1^I A_1}{r^{1-\lambda_1^I}}\begin{Bmatrix}(2+\lambda_1^I\cos 2\alpha+\cos 2\alpha\lambda_1^I)\cos(\lambda_1^I-1)\theta-(\lambda_1^I-1)\cos(\lambda_1^I-3)\theta\\ (2-\lambda_1^I\cos 2\alpha-\cos 2\alpha\lambda_1^I)\cos(\lambda_1^I-1)\theta+(\lambda_1^I-1)\cos(\lambda_1^I-3)\theta\\ -(\lambda_1^I\cos 2\alpha+\cos 2\alpha\lambda_1^I)\sin(\lambda_1^I-1)\theta+(\lambda_1^I-1)\sin(\lambda_1^I-3)\theta\end{Bmatrix}$$

$$+\frac{\lambda_1^{II} B_1}{r^{1-\lambda_1^{II}}}\begin{Bmatrix}-(2+\lambda_1^{II}\cos 2\alpha-\cos 2\alpha\lambda_1^{II})\sin(\lambda_1^{II}-1)\theta+(\lambda_1^{II}-1)\sin(\lambda_1^{II}-3)\theta\\ (-2+\lambda_1^{II}\cos 2\alpha-\cos 2\alpha\lambda_1^{II})\sin(\lambda_1^{II}-1)\theta-(\lambda_1^{II}-1)\sin(\lambda_1^{II}-3)\theta\\ -(\lambda_1^{II}\cos 2\alpha-\cos 2\alpha\lambda_1^{II})\cos(\lambda_1^{II}-1)\theta+(\lambda_1^{II}-1)\cos(\lambda_1^{II}-3)\theta\end{Bmatrix} \quad (6.1)$$

$$=\frac{A_1}{r^{1-\lambda_1^I}}\begin{Bmatrix}f_{xx}\\ f_{yy}\\ f_{xy}\end{Bmatrix}+\frac{B_1}{r^{1-\lambda_1^{II}}}\begin{Bmatrix}g_{xx}\\ g_{yy}\\ g_{xy}\end{Bmatrix}$$

where f_{xx}, f_{yy}, f_{xy}, g_{xx}, g_{yy} and g_{xy} are functions of θ.

Similarly, considering the leading terms and the rigid body terms, the displacement field near the tip of a V-notched linear elastic body (Figure 4.1) under combined loading can be written as (Eqs. (3.63) and (3.64))

$$u=\frac{\kappa+1}{2G}A_0+\frac{A_1}{2G}r^{\lambda_1^I}\left\{\left(\kappa+\lambda_1^I\cos 2\alpha+\cos 2\alpha\lambda_1^I\right)\cos\lambda_1^I\theta-\lambda_1^I\cos\left(\lambda_1^I-2\right)\theta\right\}$$

$$+\frac{B_1}{2G}r^{\lambda_1^{II}}\begin{Bmatrix}\left(-\kappa-\lambda_1^{II}\cos 2\alpha+\cos 2\alpha\lambda_1^{II}\right)\sin\lambda_1^{II}\theta\\ +\lambda_1^{II}\sin\left(\lambda_1^{II}-2\right)\theta\end{Bmatrix}-\frac{\kappa+1}{2G}B_2 r\sin\theta \quad (6.2)$$

$$=A_0 f_0+A_1 r^{\lambda_1^I}f_1+B_1 r^{\lambda_1^{II}}g_1-B_2 r g_2$$

and

$$v=\frac{A_1}{2G}r^{\lambda_1^I}\left\{\left(\kappa-\lambda_1^I\cos 2\alpha-\cos 2\alpha\lambda_1^I\right)\sin\lambda_1^I\theta+\lambda_1^I\sin\left(\lambda_1^I-2\right)\theta\right\}+\frac{\kappa+1}{2G}B_0$$

$$+\frac{B_1}{2G}r^{\lambda_1^{II}}\begin{Bmatrix}\left(\kappa-\lambda_1^{II}\cos 2\alpha+\cos 2\alpha\lambda_1^{II}\right)\cos\lambda_1^{II}\theta\\ +\lambda_1^{II}\cos\left(\lambda_1^{II}-2\right)\theta\end{Bmatrix}+\frac{\kappa+1}{2G}B_2 r\cos\theta \quad (6.3)$$

$$=A_1 r^{\lambda_1^I}f_1'+B_0 g_0+B_1 r^{\lambda_1^{II}}g_1'+B_2 r g_2'$$

where $f_0, f_1, f_1', g_0, g_1, g_2, g_1'$ and g_2' are functions of θ and α, and u, v are displacements in x and $y-$directions, respectively (Figure 4.1). The above near field equations (Eqs. (6.1) – (6.3)) will be used in formulating the selected methods.

6.3 Formulation of the selected methods

In this section, the theoretical formulations of the selected seven post-processing methods for determining the mixed mode (I/II) NSIFs are briefly described.

6.3.1 Ju and Chung (2007) stress-based method

The first stress-based method was proposed by Ju and Chung (2007). In their approach, the mixed mode (I/II) NSIFs are obtained by minimizing the error between the analytical (Eq. (6.1)) and the FE stresses using the least-squares technique. In their method, nodal stresses at m number of nodes around the notch tip in an annulus region between the radii $R_{\min}$ and $R_{\max}$ are considered (shaded region in Figure 6.1a). Minimizing the error in a least-squares sense at each of the m numbers of the selected nodes, a set of linear equations can be shown to be obtained as (Ju and Chung, 2007)

$$[D]\begin{Bmatrix} A_1 \\ B_1 \end{Bmatrix} = \{H\} \tag{6.4}$$

where

$$\begin{aligned}[D] = \sum_{i=1}^{m} & \begin{Bmatrix} r_i^{\lambda_1^I-1} f_{xx,i} \\ r_i^{\lambda_1^{II}-1} g_{xx,i} \end{Bmatrix} \begin{bmatrix} r_i^{\lambda_1^I-1} f_{xx,i} & r_i^{\lambda_1^{II}-1} g_{xx,i} \end{bmatrix} + \begin{Bmatrix} r_i^{\lambda_1^I-1} f_{yy,i} \\ r_i^{\lambda_1^{II}-1} g_{yy,i} \end{Bmatrix} \begin{bmatrix} r_i^{\lambda_1^I-1} f_{yy,i} & r_i^{\lambda_1^{II}-1} g_{yy,i} \end{bmatrix} \\ & + \begin{Bmatrix} r_i^{\lambda_1^I-1} f_{xy,i} \\ r_i^{\lambda_1^{II}-1} g_{xy,i} \end{Bmatrix} \begin{bmatrix} r_i^{\lambda_1^I-1} f_{xy,i} & r_i^{\lambda_1^{II}-1} g_{xy,i} \end{bmatrix}\end{aligned} \tag{6.5}$$

and

$$[H] = \sum_{i=1}^{m} \sigma_{xx,i}^{FE} \begin{Bmatrix} r_i^{\lambda_1^I-1} f_{xx,i} \\ r_i^{\lambda_1^{II}-1} g_{xx,i} \end{Bmatrix} + \sigma_{yy,i}^{FE} \begin{Bmatrix} r_i^{\lambda_1^I-1} f_{yy,i} \\ r_i^{\lambda_1^{II}-1} g_{yy,i} \end{Bmatrix} + \tau_{xy,i}^{FE} \begin{Bmatrix} r_i^{\lambda_1^I-1} f_{xy,i} \\ r_i^{\lambda_1^{II}-1} g_{xy,i} \end{Bmatrix} \tag{6.6}$$

$\sigma_{xx,i}^{FE}$, $\sigma_{yy,i}^{FE}$ and $\sigma_{xy,i}^{FE}$ are the FE stresses at the node i and r_i is the distance of the node i from the notch tip. Thus, by computing the FE stresses at m number of nodes in the annular region (Figure 6.1a), the Williams coefficients A_1 and B_1 can be obtained by solving Eq. (6.4), and then the mixed mode NSIFs can be obtained using Eqs. (3.71) and (3.72).

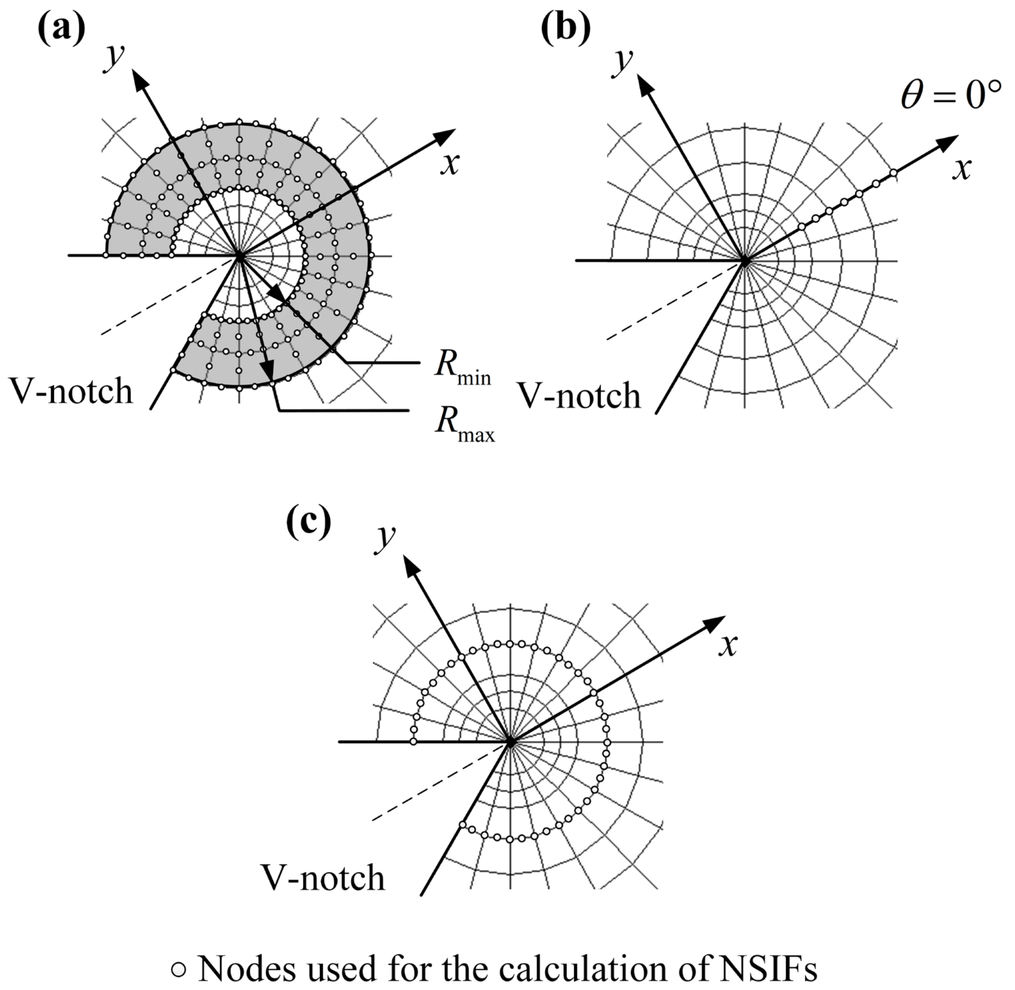

Figure 6.1. Nodes considered for the FE analysis using (a) Ju and Chung (2007) method, (b) Liu et al. (2008) method, and (c) Ayatollahi and Nejati (2011a) method.

It can be noticed from the above discussion that the selection of the radii R_{min} and R_{max} plays a vital role in the accuracy of the computed NSIFs. Ju and Chung (2007) have made some recommendations on the selection of the values of these radii. According to them R_{min} is set at 0.001 times the notch length. While R_{max} values are suggested based on the number of terms considered in the stress series. Obviously, higher-order stress terms provide R_{max} values considerably away from the notch tip. In the present work, Eq. (6.4) is derived using the singular stress field, and no higher-order terms are considered therein. Keeping in view of the use of the leading stress terms and following the recommendations made by Ju and Chung (2007), the radii $R_{\min}\left(=0.001a\right)$ and $R_{\max}\left(=0.3a\right)$ values are set at 0.003 (i.e., the mid-side nodes of the first layer of elements of the spider-web pattern) and 0.9 (the 42nd layer of the elements of the spider-web pattern), respectively, for all the example problems of this chapter. Thus, the NSIFs have been determined using this method at the nodes which fall in an annulus region between the above values of the radii $R_{\min}$ and $R_{\max}$ (Figure 6.1a).

6.3.2 Liu et al. (2008) stress-based method

Another stress-based method was proposed by Liu et al. (2008), and in their method, the NSIFs are determined from the FE stresses along a radial direction from the notch tip, as shown in Figure 6.1b. To compute the mixed mode (I/II) NSIFs, l number of nodes along this radial direction $\left(\theta=0°\right)$, i.e., along the $x-$axis (the notch bisector line as shown in Figure 6.1b) and close to the notch tip, need to be considered (Liu et al., 2008) due to the use of the singular stress terms (Eq. (6.1)). The selection of nodes plays a vital role in the accuracy of the NSIFs; therefore, to get a suitable set of nodes, Liu et al. (2008) suggested applying the least-squares technique between the theoretical stresses (Eq. (6.1)) and the FE stresses (at l number of selected nodes) to find the numerical eigenvalues λ_1^{I*} and λ_1^{II*} as (Liu et al., 2008)

$$\lambda_1^{I*}-1=\frac{l\sum_{i=1}^{l}\left(\ln\left|\sigma_{yy,i}^{FE}\right|\ln r_i\right)-\sum_{i=1}^{l}\ln\left|\sigma_{yy,i}^{FE}\right|\sum_{i=1}^{l}\ln r_i}{l\sum_{i=1}^{l}\left(\ln r_i\right)^2-\left(\sum_{i=1}^{l}\ln r_i\right)^2} \tag{6.7}$$

and

$$\lambda_1^{II*}-1=\frac{l\sum_{i=1}^{l}\left(\ln\left|\sigma_{xy,i}^{FE}\right|\ln r_i\right)-\sum_{i=1}^{l}\ln\left|\sigma_{xy,i}^{FE}\right|\sum_{i=1}^{l}\ln r_i}{l\sum_{i=1}^{l}\left(\ln r_i\right)^2-\left(\sum_{i=1}^{l}\ln r_i\right)^2} \tag{6.8}$$

If the numerical eigenvalues of λ_1^{I*} and λ_1^{II*} approach their corresponding theoretical values determined using Eqs. (3.27) and (3.28), respectively, for a selected set of nodes, then this set of nodes is recommended for the calculation of the NSIFs (Liu et al., 2008). It should be noted that according to Liu et al. (2008), these valid set of nodes could be different for the mode I and mode II loading conditions. Finally, using the FE stresses from the valid set of nodes and the theoretical stresses (Eq. (6.1), they showed that the Williams coefficients A_1 and B_1 can be obtained using the least-squares approach as (Liu et al., 2008)

$$A_1 = \frac{\exp\left[\frac{1}{l}\sum_{i=1}^{l}\ln\left|\sigma_{yy,i}^{FE}\right| r_i^{1-\lambda_1^I}\right]}{\left|f_{yy}\right|} \quad \text{and} \quad B_1 = \frac{\exp\left[\frac{1}{l}\sum_{i=1}^{l}\ln\left|\sigma_{xy,i}^{FE}\right| r_i^{1-\lambda_1^{II}}\right]}{\left|g_{xy}\right|} \tag{6.9}$$

To check whether finite element values λ_1^{I*} and λ_1^{II*} approached their theoretical values or not, the following measure of error is employed in this method

$$e_{\lambda_1^{I(II)}}(\%) = \frac{\lambda_1^{I(II)} - \lambda_1^{I(II)*}}{\lambda_1^{I(II)}} \times 100 \tag{6.10}$$

where $\lambda_1^{I/II}$ is the analytical eigenvalue. The recommended procedure by Liu et al. (2008) is to consider 8 (eight) number of consecutive nodes on the line $\theta = 0°$, starting from a valid node from the notch tip. By choosing different starting nodes and considering the next subsequent 7 number of nodes, the percent relative error in the estimated eigenvalues using Eqs. (6.7), (6.8), and (6.10) is evaluated. The starting node for which Eqs. (6.7) and (6.8) yield minimum error (using Eq. (6.10)) is considered as the valid starting node, and Eq. (6.9) needs to be solved using this node and its subsequent 7 number of nodes. It may be noted that the starting node does not necessarily have to be the same for all the notch angles. This suggested procedure has been implemented in the present work.

6.3.3 Ayatollahi and Nejati (2011a) displacement-based method

An overdeterministic displacement-based method was proposed by Ayatollahi and Nejati (2011a) to determine the mixed mode (I/II) NSIFs. In their method, the NSIFs are determined from the FE displacements at the nodes along a circular ring around the notch tip, as shown in Figure 6.1c. Their method allows to consider both the singular and higher-order terms of the displacement series in order to determine the NSIFs and other higher-order unknown Williams coefficients. Since the NSIFs are only of interest here, only the singular terms along with the rigid body displacement terms are considered in the present work. According to this method, by equating the FE displacement field with the theoretical values in Eqs. (6.2) and (6.3) at j number of nodes along a circular ring (Figure 6.1c), a system of linear equations can be obtained as (Ayatollahi and Nejati, 2011a)

$$[U]_{2j\times1}=[C]_{2j\times5}[X]_{5\times1} \tag{6.11}$$

in which

$$[C]=\begin{bmatrix} f_0 & r_1^{\lambda_1^I} f_1^1 & 0 & r_1^{\lambda_1^{II}} g_1^1 & -r_1 g_2^1 \\ \vdots & \vdots & \vdots & \vdots & \vdots \\ f_0 & r_j^{\lambda_1^I} f_1^j & 0 & r_j^{\lambda_1^{II}} g_1^j & -r_j g_2^j \\ 0 & r_1^{\lambda_1^I} f_1'^1 & g_0 & r_1^{\lambda_1^{II}} g_1'^1 & r_1 g_2^1 \\ \vdots & \vdots & \vdots & \vdots & \vdots \\ 0 & r_j^{\lambda_1^I} f_1'^j & g_0 & r_j^{\lambda_1^{II}} g_1'^j & r_j g_2^j \end{bmatrix},\ U=\begin{Bmatrix} u_1^{FE} \\ \vdots \\ u_j^{FE} \\ v_1^{FE} \\ \vdots \\ v_j^{FE} \end{Bmatrix},\ \text{and}\ X=\begin{Bmatrix} A_0 \\ A_1 \\ B_0 \\ B_1 \\ B_2 \end{Bmatrix} \tag{6.12}$$

In the above equation, $[U]$ contains the nodal FE displacements, $[C]$ contains the angular functions of the displacement components (Eqs. (6.2) and (6.3)), and $[X]$ contains the unknown Williams coefficients. u_j^{FE} and v_j^{FE} are the FE displacements of the j-th node on the circular ring along x and $y-$ directions, respectively (Figure 6.1c). Finally, using the least-squares approach, the Williams coefficients can be obtained as (Ayatollahi and Nejati, 2011a)

$$[X]=\left([C]^T[C]\right)^{-1}[C]^T[U] \tag{6.13}$$

To solve Eq. (6.13), Ayatollahi and Nejati (2011a) suggested to consider nodes lying on the 15$^{\text{th}}$ circular ring from the notch tip. In their work, the radius of this ring is found lying between $a/4$ and $a/2$. Taking into account the use of only the leading terms of the displacements in Eq. (6.11) and following their recommendation, the nodes on the 15$^{\text{th}}$

circular ring from the notch tip have been employed in the present work for solving Eq. (6.13). In the present FE meshes of the example problems, the radial distance of the 15th circular ring is located at a radial distance of 0.0727 from the notch tip.

6.3.4 The proposed point substitution method

The point substitution displacement-based method has been proposed in Chapter 4. In the proposed method, the mode I and mode II NSIFs can be obtained as (rewriting Eqs. (4.19) and (4.23))

$$A_1 = \frac{Ar_{op}^2 + Br_{op}}{C_1 r_{op}^{\lambda_1^I}} = \frac{\left.\Delta v^{FE}\right|_{r=r_{op}}}{C_1 r_{op}^{\lambda_1^I}} \tag{6.14}$$

and

$$B_1 = \frac{\Delta u_{r_{op}}^{FE} r'_{op} - \Delta u_{r'_{op}}^{FE} r_{op}}{2C_2 r_{op} r'_{op}\left(r_{op}^{\lambda_1^{II}-1} - r_{op}'^{\lambda_1^{II}-1}\right)} \tag{6.15}$$

where

$$r = r_{op} = -\frac{B\left(1-\lambda_1^I\right)}{A\left(2-\lambda_1^I\right)} \tag{6.16}$$

and

$$\begin{gathered}
C_1 = \frac{1}{2G}\begin{bmatrix} \left(-\kappa - \lambda_1^I \cos 2\alpha - \cos 2\alpha\lambda_1^I\right)\sin\lambda_1^I\alpha \\ +\lambda_1^I \sin\left(\lambda_1^I - 2\right)\alpha \end{bmatrix} \\
C_2 = \frac{1}{2G}\begin{bmatrix} \left(-\kappa - \lambda_1^{II} \cos 2\alpha + \cos 2\alpha\lambda_1^{II}\right)\sin\lambda_1^{II}\alpha \\ +\lambda_1^{II} \sin\left(\lambda_1^{II} - 2\right)\alpha \end{bmatrix}
\end{gathered} \tag{6.17}$$

As explained in Chapter 4, according to this method, the FE values of Δv^{FE} at r_{op} and Δu^{FE} at $r_{op} = r_{opt} \times L_N$ and $r'_{op} = r_{op} - 0.002 \times L_N$ are substituted in Eqs. (6.14) and (6.15), respectively, for the determination of the NSIFs. The procedure mentioned in Chapter 4 has been adopted in all the example problems of this chapter.

6.3.5 The proposed collocation method

Another displacement-based method is proposed in Chapter 5 for the calculation of the mixed mode (I/II) NSIFs using the FE notch opening and sliding displacements. By collocating the FE NOD and NSD at N number of consecutive nodes lying on the notch flanks, the Williams coefficient A_1 and B_1 can be obtained as (rewriting Eqs. (5.5) and (5.13))

$$A_1 = \frac{\exp\left[\frac{1}{N}\sum_{i=1}^{N}\ln\left(\Delta v_i^{FE} r_i^{-\lambda_1^I}\right)\right]}{2C_1} \tag{6.18}$$

and

$$B_1 = \frac{\exp\left[\frac{1}{N}\sum_{i=1}^{N}\ln\left(\Delta u_{eff,i}^{FE} r_i^{-\lambda_1^{II}}\right)\right]}{2C_4} \tag{6.19}$$

where

$$C_4 = \frac{1}{2G}\left[\begin{array}{c}(\kappa+1)\left(-\kappa-\lambda_1^{II}\cos 2\alpha+\cos 2\alpha\lambda_1^{II}\right)\left\{\sin\lambda_1^{II}\alpha'\sin\alpha-\sin\lambda_1^{II}\alpha\sin\alpha'\right\} \\ +\lambda_1^{II}(\kappa+1)\left\{\sin\left(\lambda_1^{II}-2\right)\alpha'\sin\alpha-\sin\left(\lambda_1^{II}-2\right)\alpha\sin\alpha'\right\}\end{array}\right] \tag{6.20}$$

According to this method, 20 numbers of consecutive nodes on each of the notch flanks from the notch tip starting from the 7th node are employed for solving Eq. (6.18). On the other hand, the above sequence of the nodes on each of the notch flanks and on the two additional lines at $\theta = \alpha'$ and $\theta = -\alpha'$ (Figure 5.1) are employed for solving Eq. (6.19).

The procedure mentioned in Chapter 5 has been adopted in all the example problems of this chapter.

6.3.6 Lazzarin et al. (2010) energy-based method

The first energy-based method was proposed by Lazzarin et al. (2010). In their approach, the NSIFs are calculated using the averaged strain energy density (SED) in two controlled areas around the notch tip, as shown in Figure 6.2a. The SED values (W_1 and W_2) for the controlled areas of radii R_1 and R_2 $\left(R_2 > R_1\right)$, respectively, can be written in terms of A_1 and B_1 as (Lazzarin et al., 2010)

$$W_1 = \frac{1}{2E}\left[\frac{I_1}{2\lambda_1^I\gamma}\times\frac{A'^2A_1^2}{R_1^{2\left(1-\lambda_1^I\right)}}+\frac{I_2}{2\lambda_1^{II}\gamma}\times\frac{B'^2B_1^2}{R_1^{2\left(1-\lambda_1^{II}\right)}}\right]=C_aA_1^2+D_aB_1^2 \tag{6.21}$$

and

$$W_2 = \frac{1}{2E}\left[\frac{I_1}{2\lambda_1^I\gamma}\times\frac{A'^2A_1^2}{R_2^{2\left(1-\lambda_1^I\right)}}+\frac{I_2}{2\lambda_1^{II}\gamma}\times\frac{B'^2B_1^2}{R_2^{2\left(1-\lambda_1^{II}\right)}}\right]=C_bA_1^2+D_bB_1^2 \tag{6.22}$$

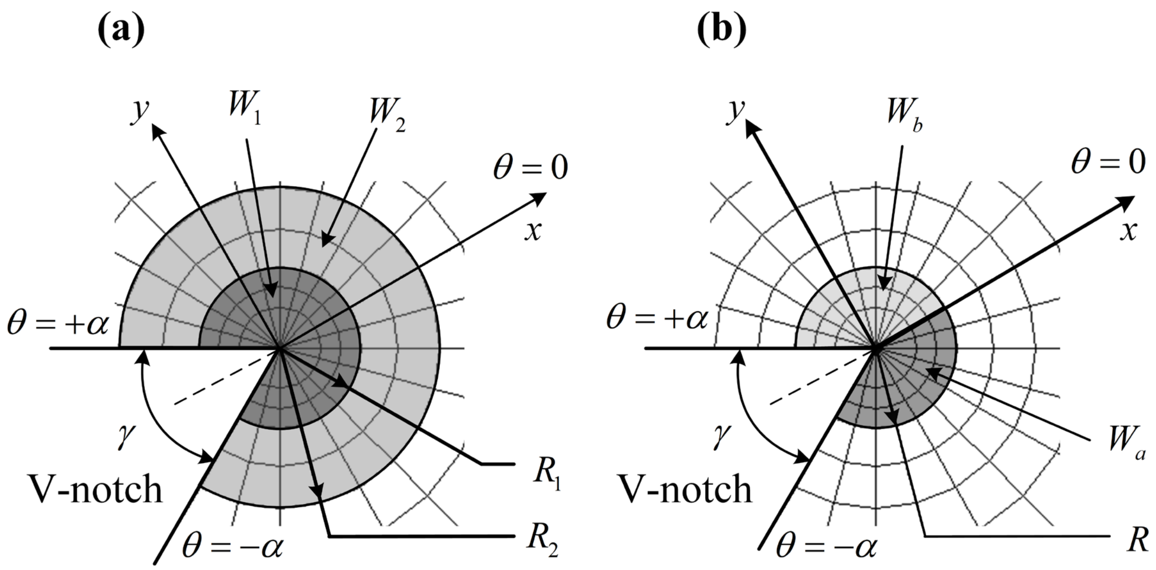

Figure 6.2. Control volumes in (a) Lazzarin et al. (2010) method and (b) Treifi and Oyadiji (2013c) method.

where
$$A' = \sqrt{2\pi}\lambda_1^{I}\left(1+\lambda_1^{I}-\lambda_1^{I}\cos 2\alpha-\cos 2\alpha\lambda_1^{I}\right)$$
$$B' = \sqrt{2\pi}\lambda_1^{II}\left(-1+\lambda_1^{II}-\lambda_1^{II}\cos 2\alpha+\cos 2\alpha\lambda_1^{II}\right) \tag{6.23}$$

and I_1 and I_2 are the integrals of the angular functions of the stress (Eq. (6.1)) and can be calculated as (Lazzarin and Zambardi, 2001)

$$I_1 = \int_{-\alpha}^{+\alpha}\left(f_{xx}^2+f_{yy}^2-2\nu f_{xx}f_{yy}+2\left(1+\nu\right)f_{xy}^2\right)d\theta$$
$$I_2 = \int_{-\alpha}^{+\alpha}\left(g_{xx}^2+g_{yy}^2-2\nu g_{xx}g_{yy}+2\left(1+\nu\right)g_{xy}^2\right)d\theta \tag{6.24}$$

Solving the system of equations given by Eqs. (6.21) and (6.22), the Williams coefficients A_1 and B_1 under the mixed mode (I/II) loading conditions can be calculated as (Lepore et al., 2019)

$$A_1 = \sqrt{\frac{D_a\times W_2-D_b\times W_1}{D_a\times C_b-D_b\times C_a}} \quad \text{and} \quad B_1 = \sqrt{\frac{W_1-C_a\times A_1^2}{D_a}} \tag{6.25}$$

On the other hand, under the pure mode I and pure mode II loading conditions, the coefficients A_1 and B_1 can be obtained using the controlled area of radius R_1 as

$$A_1 = \sqrt{\frac{W_1}{C_a}} \quad \text{and} \quad B_1 = \sqrt{\frac{W_1}{D_a}} \tag{6.26}$$

It is to be noted that this method cannot be used to determine the stress intensity factors (SIFs) of crack problems ($\gamma = 0°$) under the mixed mode loading conditions as Eqs. (6.21) and (6.22) would produce an indeterminate pair of equations (Lazzarin et al., 2010). As the singular terms are employed in deriving the above equations, therefore, it is expected that radii R_1 and R_2 need to be very close to the notch tip. Further, a controlled area with the radius R_1 is only required for pure mode I problems. On the other hand, both the control areas are defined by R_1 and R_2 are needed in the case of the mixed mode (I /II) problems.

No explicit recommendations for the value of R_1 and R_2 are made by Lazzarin et al. (2010) for determining the mixed mode NSIFs. However, the values of the control radius R_1 and R_2 suggested by Treifi and Oyadiji (2013c) for this method are implemented in the present work. Accordingly, the radius of the 3rd circular ring from the notch tip is chosen as R_1 and R_2 is taken as the radius of the 5th circular ring of the spider-web pattern. This comes out to be $R_1 = 0.012$ and $R_2 = 0.020$ for the mesh gradation chosen in the example problems of this chapter.

6.3.7 Treifi and Oyadiji (2013c) energy-based method

The second energy-based method was developed by Treifi and Oyadiji (2013c). In their method, the averaged SED values are evaluated at two controlled symmetric areas (shaded areas in Figure 6.2b) defined by the radius R. Unlike in Lazzarin et al. (2010) method, this method deals with a single region identified by the radius R. The SED values for the bottom (W_a), and top (W_b) half semi-circular areas in terms of the Williams coefficients A_1 and B_1 can be written as (Treifi and Oyadiji, 2013c)

$$\begin{aligned} W_a &= \frac{1}{2E}\left[\frac{I_{1,a}}{\lambda_1^I \gamma}\times\frac{A'^2 A_1^2}{R^{2(1-\lambda_1^I)}}+\frac{I_{2,a}}{\lambda_1^{II}\gamma}\times\frac{B'^2 B_1^2}{R^{2(1-\lambda_1^{II})}}+\frac{2\times I_{12,a}}{\left(\lambda_1^I+\lambda_1^{II}\right)\gamma}\times\frac{A' A_1 B' B_1}{R^{2-\lambda_1^I-\lambda_1^{II}}}\right] \\ &= M_a \times A_1^2 + N_a \times B_1^2 + Q_a \times A_1 \times B_1 \end{aligned} \tag{6.27}$$

and

$$\begin{aligned} W_b &= \frac{1}{2E}\left[\frac{I_{1,b}}{\lambda_1^I \gamma}\times\frac{A'^2 A_1^2}{R^{2(1-\lambda_1^I)}}+\frac{I_{2,b}}{\lambda_1^{II}\gamma}\times\frac{B'^2 B_1^2}{R^{2(1-\lambda_1^{II})}}-\frac{2\times I_{12,b}}{\left(\lambda_1^I+\lambda_1^{II}\right)\gamma}\times\frac{A' A_1 B' B_1}{R^{2-\lambda_1^I-\lambda_1^{II}}}\right] \\ &= M_b \times A_1^2 + N_b \times B_1^2 + Q_b \times A_1 \times B_1 \end{aligned} \tag{6.28}$$

where A' and B' are constants and can be obtained using Eq. (6.23). $I_{1,a}$, $I_{2,a}$, $I_{12,a}$, $I_{1,b}$, $I_{2,b}$ and $I_{12,b}$ are the integrals of the angular functions of stress (Eq. (6.1)) and given as (Treifi and Oyadiji, 2013c)

$$
\begin{aligned}
I_{1,a} &= \int_{-\alpha}^{0} \left(f_{xx}^2 + f_{yy}^2 - 2\nu f_{xx} f_{yy} + 2(1+\nu) f_{xy}^2 \right) d\theta \\
I_{2,a} &= \int_{-\alpha}^{0} \left(g_{xx}^2 + g_{yy}^2 - 2\nu g_{xx} g_{yy} + 2(1+\nu) g_{xy}^2 \right) d\theta \\
I_{12,a} &= \int_{-\alpha}^{0} \left(2 f_{xx} g_{xx} + 2 f_{yy} g_{yy} - 2\nu \left(f_{xx} g_{yy} + f_{yy} g_{xx} \right) \right) d\theta \\
I_{1,b} &= \int_{0}^{+\alpha} \left(f_{xx}^2 + f_{yy}^2 - 2\nu f_{xx} f_{yy} + 2(1+\nu) f_{xy}^2 \right) d\theta \\
I_{2,b} &= \int_{0}^{+\alpha} \left(g_{xx}^2 + g_{yy}^2 - 2\nu g_{xx} g_{yy} + 2(1+\nu) g_{xy}^2 \right) d\theta \\
I_{12,b} &= \int_{0}^{+\alpha} \left(2 f_{xx} g_{xx} + 2 f_{yy} g_{yy} - 2\nu \left(f_{xx} g_{yy} + f_{yy} g_{xx} \right) \right) d\theta
\end{aligned}
\qquad (6.29)
$$

Due to the symmetry of the geometry about the notch bisector line, it is found that (Treifi and Oyadiji, 2013c)

$$
\begin{aligned}
I_{1,a} &= I_{1,b} \\
I_{2,a} &= I_{2,b} \\
I_{12,a} &= -I_{12,b}
\end{aligned}
\qquad (6.30)
$$

From Eqs. (6.27) – (6.30), the following relations hold (Treifi and Oyadiji, 2013c)

$$
\begin{aligned}
M_a &= M_b \\
N_a &= N_b \\
Q_a &= -Q_b
\end{aligned}
\qquad (6.31)
$$

After some algebraic manipulations, the coefficients A_1 and B_1 under mixed mode (I/II) loading can be obtained as (Lepore et al., 2019)

$$
A_1 = \sqrt{\frac{(W_a + W_b) \pm \sqrt{(W_a + W_b)^2 - \dfrac{4 \times M_a \times N_a \times (W_a - W_b)^2}{Q_a^2}}}{4 \times M_a}} \quad \text{and} \qquad (6.32)
$$

$$
B_1 = \frac{W_a - W_b}{2 \times Q_a \times A_1}
$$

Under the pure mode I and pure mode II loading conditions, the coefficients A_1 and B_1 can be calculated as (Treifi and Oyadiji, 2013c)

$$A_1 = \sqrt{\frac{W_a}{M_a}} \quad \text{and} \quad B_1 = \sqrt{\frac{W_a}{N_a}} \tag{6.33}$$

Unlike Lazzarin et al. (2010) method, this method can be employed for crack ($\gamma = 0°$) problems due to the presence of $(A_1 \times B_1)$ in Eqs. (6.27) and (6.28). As per the suggestion of Treifi and Oyadiji (2013c), the controlled radius R is chosen as the radius of the 3rd circular ring from the notch tip ($R = 0.012$) in the present analyses.

6.4 Numerical analysis, results, and discussion

In this section, the NSIFs are determined for the various benchmark example problems under the mode I, mode II and mixed mode (I/II) loading conditions using the above seven FE post-processing methods. Commercially available software ANSYS® (ANSYS, 2007) is used in the present investigation for the FE analyses of all the example problems. All these seven post-processing methods have been implemented in MATLAB® (MATLAB, 2015) individually, which requires the corresponding inputs such as the stresses, displacements, and strain energy density for the computation of the Williams constants A_1 and B_1 (and hence NSIFs). Moreover, the suggested procedure for the computation of these coefficients is also implemented in MATLAB® (MATLAB, 2015) codes.

For ease of convenience, the final equations to be used for the determination of the NSIFs (i.e., A_1 and B_1) in all the selected seven methods are summarized in Table 6.1. Further, Table 6.2 summarizes the recommended nodes/areas by the selected methods for the calculation of the mixed mode (I/II) NSIFs. These recommendations are implemented in all example problems of the present chapter. In all the examples, Young's modulus E=1.0, Poisson's ratio ν=0.25, and applied stress σ=1 are considered. Plane stress conditions are assumed and width/semi-width w=10 and thickness = 1.0 are considered. All units are consistent. The NSIFs, K_I and K_{II} are normalized using Eq. (4.25).

Table 6.1. List of final equations to be used for the determination of the NSIFs.

Method	Input quantity	A_1	B_1
Ju and Chung (2007) method	Stresses	Eq. (6.4)	Eq. (6.4)
Liu et al. (2008) methid	Stresses	Eq. (6.9)	Eq. (6.9)
Ayatollahi and Nejati (2011a) method	Displacements	Eq. (6.13)	Eq. (6.13)
Proposed point substitution method	Displacements	Eq. (6.14)	Eq. (6.15)
Proposed collocation method	Displacements	Eq. (6.18)	Eq. (6.19)
Lazzarin et al. (2010) method	Strain energy density	Eqs. (6.25) and (6.26)	Eqs. (6.25) and (6.26)
Treifi and Oyadiji (2013c) method	Strain energy density	Eqs. (6.32) and (6.33)	Eqs. (6.32) and (6.33)

Table 6.2. Recommended nodes/controlled areas of the selected methods.

Methods	Suggested nodes/controlled areas
Ju and Chung (2007) method	$R_{\min}$ = 0.003 (mid-side nodes of the first layer of elements) $R_{\max}$ = 0.9 (42^{nd} layer of elements)
Liu et al. (2008) method	Eight consecutive nodes starting from the valid starting node
Ayatollahi and Nejati (2011a) method	Nodes on the 15^{th} circular ring from the notch tip (the radial distance from the notch tip = 0.0727)
Proposed point substitution method	Optimum point, (r_{op}/L_N) Eq. (6.16)
Proposed collocation method	20 consecutive nodes stating from the 7^{th} node from the notch tip along the notch flanks and the radial lines at $\theta=\alpha'$ and $\theta=-\alpha'$
Lazzarin et al. (2010) method	R_1 = 3^{rd} circular ring (=0.012) R_2 = 5^{th} circular ring (=0.020)
Treifi and Oyadiji (2013c) method	R = 3^{rd} circular ring (=0.012)

Due to the complex nature of the sharp V-notched problems, analytical or experimental results of the NSIFs are scarcely available. Therefore, a comparison of values of NSIFs obtained using all the selected seven methods is made based on the results reported by Chen (1995) and Zhao and Hahn (1991). This is mainly due to the reason that the results of these references (Chen, 1995; Zhao and Hahn, 1991) have been widely employed in the past for the NSIF verification purpose. In Chen (1995) method, the NSIFs are calculated using the body force method. The basic density functions of the body forces are introduced to characterize the stress singularity at the notch tip. Finally using the densities of the distributed point forces at the notch tip, the mixed mode (I/II) NSIFs are calculated in his method.

6.4.1 Mode I examples

For the purpose of comparison of the methods in the class of the mode I problems, two benchmark example problems, viz., the SENT and DENT as shown in Figure 4.5 are analyzed. Both the plates have been analyzed for the various notch angles equal to $\gamma = 30^{\circ}$, 60°, and 90°. The notch length to width ratio $a/w = 0.3$ is considered for both the specimens. It should be noted that in the numerical examples of the previous chapters $a/w = 0.2$ and 0.4 have been considered. The height to width ratios $h/w = 1.2$ and 2.0 are chosen for the SENT and DENT specimens, respectively. As stated earlier, the main purpose of the present investigation is to compare the efficacy of the selected methods on the same FE meshes, on the same common set of problems, and by observing the recommendations made by them. For this purpose, a typical mesh, as shown in Figure 5.3d with $L_N/a = 0.002$ has been considered here for both the example problems. The typical mesh considered in this section consists of number of elements (NE) = 947 and number of nodes (NN) = 3082.

Following the guidelines mentioned in Tables 6.1 and 6.2, the mode I NSIFs of the selected specimens have been obtained using all the seven methods. Tables 6.3 and 6.4 show the results of the mode I normalized NSIFs F_I estimated using all these seven methods for the SENT and DENT specimens, respectively. As may be seen from the results presented in Tables 6.3 and 6.4 that the error e_k is less than 1% in all of the methods and in both the specimens except Liu et al. (2008) in the SENT specimen. These errors are well within the general acceptable range for the numerical solutions (i.e., less than 1%). The results in the above tables clearly suggest that nearly all the selected methods determined the mode I NSIF very accurately, considering 1% error as the basis.

Table 6.5 shows the number of nodes or points (in the meshes of the SENT and DENT specimens) according to Table 6.2, at which various field variables are sampled for the computation of the NSIF by the each of the seven methods. A reference solution is also presented in the above tables for the calculation of the percent relative error e_k. As may be noticed from the data of the above tables that relatively very less number of nodes are used for the determination of the NSIFs in the 2nd, 3rd, 4th and 5th methods as compared to the remaining methods. Nonetheless, the methods 3rd, 4th and 5th, though sampled at relatively less number of nodes, they still provided very accurate mode I NSIFs. Interestingly enough, the 3rd, 4th and 5th are the displacement-based methods. From Table 6.5, it clear that Ju and Chung (2007) method uses large number of sampling nodes and yet extracts the NSIF with accuracy comparable to that of the displacement-based methods. Amongst all the methods, the proposed point substitution method which employs the lowest possible number of sampling points (i.e., only a single point) and yet extracts very accurate mode I NSIFs, as is evident from the results of Tables 6.3 and 6.4. Relatively large error in Liu et al. (2008) method may be due to the use of less number of sampling nodes in the stress-based approach.

Table 6.3. Comparison of F_I for the SENT specimen ($a/w = 0.3$).

	F_I		
$\gamma(°)\rightarrow$	30º	60º	90º
Ju and Chung (2007) method	1.6591	1.7453	1.9367
	(0.94) #	(0.32)	(0.12)
Liu et al. (2008) method	1.6560	1.7227	1.9136
	(1.13)	(1.05)	(1.31)
Ayatollahi and Nejati (2011a) method	1.6747	1.7499	1.9369
	(0.02)	(0.06)	(0.11)
Proposed point substitution method	1.6612	1.7425	1.9325
	(0.82)	(0.49)	(0.34)
Proposed collocation method	1.6645	1.7419	1.9313
	(0.63)	(0.52)	(0.40)
Lazzarin et al. (2010) method	1.6768	1.7534	1.9399
	(0.11)	(0.14)	(0.05)
Treifi and Oyadiji (2013c) method	1.6768	1.7534	1.9399
	(0.11)	(0.14)	(0.05)
Reference solution (Chen, 1995)	1.6750	1.7510	1.9390

#Bracketed values are percentage relative error (e_k) with respect to Chen (1995)

Table 6.4. Comparison of F_I for the DENT specimen ($a/w = 0.3$).

	F_I		
$\gamma(°) \rightarrow$	30º	60º	90º
Ju and Chung (2007) method	1.1158	1.1770	1.3019
	(0.99) #	(0.25)	(0.01)
Liu et al. (2008) method	1.1204	1.1707	1.2936
	(0.59)	(0.79)	(0.65)
Ayatollahi and Nejati (2011a) method	1.1262	1.1789	1.3001
	(0.07)	(0.09)	(0.15)
Proposed point substitution method	1.1174	1.1742	1.2971
	(0.85)	(0.49)	(0.38)
Proposed collocation method	1.1211	1.1759	1.2982
	(0.52)	(0.35)	(0.29)
Lazzarin et al. (2010) method	1.1272	1.1813	1.3021
	(0.02)	(0.11)	(0.01)
Treifi and Oyadiji (2013c) method	1.1272	1.1813	1.3021
	(0.02)	(0.11)	(0.01)
Reference solution (Chen, 1995)	1.1270	1.1800	1.3020

#Bracketed values are percentage relative error (e_k) with respect to Chen (1995)

Table 6.5. List of number of collocation nodes or points used for the mode I problems.

Methods	Number of collocation points
Ju and Chung (2007) method	1848 for $\gamma = 30°$, 1848 for $\gamma = 60°$ and 1597 for $\gamma = 90°$
Liu et al. (2008) method	8 for all notch angles
Ayatollahi and Nejati (2011a) method	29 for $\gamma = 30°$, 29 for $\gamma = 60°$ and 25 for $\gamma = 90°$
Proposed point substitution method	1 for all angles
Proposed collocation method	20 for all angles
Lazzarin et al. (2010) method	133 for $\gamma = 30°$, 133 for $\gamma = 60°$, 115 for $\gamma = 90°$
Treifi and Oyadiji (2013c) method	133 for $\gamma = 30°$, 133 for $\gamma = 60°$, 115 for $\gamma = 90°$

6.4.2 Mode II examples

The same mode II problem, i.e., a single edge notched specimen under shear (SENS) (Figure 4.15) described in Section 4.3.2 has been considered again here for the comparison purpose. The specimen has been analyzed for the various notch angles equal to $\gamma = 30$º, 60º, and 90º. The notch length to width ratio $a/w = 0.4$ and height and width ratio $h/w = 1.0$ are considered for the specimen. The same mesh and the same boundary conditions as considered in Section 4.3.2 are adopted here. The highest density mesh in this section consists of NE = 947 and NN = 3082 (for $\gamma = 30°$). The computed normalized mode II NSIF F_{II} using all the selected seven methods along with the available published results has been shown in Table 6.6. The percentage relative error e_k is also provided in Table 6.6. Table 6.7 shows the number of nodes or points at which various field variables are sampled (Table 6.2) for the computation of the NSIF by each of the seven methods.

Table 6.6. Comparison of F_{II} for the SENS specimen ($a/w = 0.4$).

	F_{II}		
$\gamma(°) \rightarrow$	30°	60°	90°
Ju and Chung (2007) method	1.6318	2.2842	3.1861
	(0.42) #	(0.34)	(0.90)
Liu et al. (2008) method	1.6508	2.3049	3.2107
	(1.59)	(0.56)	(0.13)
Ayatollahi and Nejati (2011a) method	1.6311	2.2920	3.2065
	(0.38)	(0.20)	(0.27)
Proposed point substitution method	1.6338	2.3063	3.1909
	(0.54)	(0.62)	(0.75)
Proposed collocation method	1.6248	2.2975	3.2067
	(0.01)	(0.24)	(0.23)
Lazzarin et al. (2010) method	1.6309	2.2978	3.2067
	(0.37)	(0.25)	(0.26)
Treifi and Oyadiji (2013c) method	1.6309	2.2978	3.2067
	(0.37)	(0.25)	(0.26)
Reference solution (Zhao and Hahn, 1991)	1.6250	2.2920	3.2150

#Bracketed values are percentage relative error (e_k) with respect to Zhao and Hahn (1991)

Table 6.7. List of number of collocation nodes or points used for the mode II problems.

Methods	Number of collocation points
Ju and Chung (2007) method	1504 for $\gamma = 30°$, 1408 for $\gamma = 60°$, 1520 for $\gamma = 90°$
Liu et al. (2008) method	8 for all notch angles
Ayatollahi and Nejati (2011a) method	31 for $\gamma = 30°$, 29 for $\gamma = 60°$ and 25 for $\gamma = 90°$
Proposed point substitution method	2 for all angles
Proposed collocation method	40 for all angles
Lazzarin et al. (2010) method	142 for $\gamma = 30°$, 133 for $\gamma = 60°$, 115 for $\gamma = 90°$
Treifi and Oyadiji (2013c) method	142 for $\gamma = 30°$, 133 for $\gamma = 60°$, 115 for $\gamma = 90°$

It can be seen from the results presented in Table 6.6 that, except Liu et al. (2008) method, the error e_k is less than 1% in all the remaining methods. As stated earlier, these errors are well within the general acceptable range. The results in the above tables clearly suggest that all the selected methods except Liu et al. (2008) method determined the mode II NSIF very accurately, considering 1% error as the basis.

As may be noticed from the data in Table 6.7 that, relatively very less number of nodes are used for the determination of the NSIFs in the 2nd, 3rd, 4th and 5th methods as compared to the remaining methods, and they still provide very accurate mode II NSIFs except the 2nd method. On the other hand, Ju and Chung (2007) method uses the largest number of sampling points than any other method; however, its accuracy is of the order of the displacement-based methods. Relatively large error in Liu et al. (2008) stress-based approach probably due to the use of less number of sampling nodes along $\theta = 0°$ line (Figure 6.1b) in their stress-based approach. Amongst all the methods, the proposed point substitution method employs two numbers of sampling points and yet computes very accurate mode II NSIFs as is evident from the results of Table 6.6.

6.4.3 Mixed mode (I/II) examples

Two example problems viz. ASENT and ADENT, as shown in Figure 4.17, are considered for comparing the selected methods under the mixed mode (I/II) loading conditions. For both the ASENT and ADENT specimens, the notch length to width ratio $a/w = 0.3$, and notch angles γ =30° and 60° are considered. It is to be noted that in Chapters 4 and 5, $a/w = 0.2$ and 0.4 have been employed for the above configurations. The height to width ratio $h/w = 3.5$ is chosen for both the specimens. The notch inclination angle (β) is considered as 45° for both the specimens. The boundary conditions and typical FE meshes used here are shown in Figure 5.8. Nearly L_N/a = 0.002 value is set in the typical mesh. The maximum number of elements and nodes in the mesh of the ASENT and ADENT specimens are 1421 and 4543, respectively. This dense mesh has been provided for the notch angle $\gamma = 30°$.

Considering the suggested nodes/areas in Table 6.2 and following the procedure of the selected methods as described in the previous sections, the normalized mixed mode NSIFs F_I and F_{II} have been computed for the various notch angles using the seven methods. These results are presented in Tables 6.8 and 6.9 for the ASENT and ADENT specimens, respectively. The published results of Chen (1995) and the percent relative error (e_k) with respect to this reference solution are also listed in Tables 6.8 and 6.9. Moreover, the average value of e_k across all the notch angles (e_k^{avg}) for a given method is also presented in Tables 6.8 and 6.9 for both the specimens. Table 6.10 shows the total number of nodes or points (in the meshes of the ASENT and ADENT specimens) at which various field variables are sampled for the computation of both F_I and F_{II} by each of the seven methods for the various notch angles.

Table 6.8. Comparison of F_I and F_{II} for the ASENT specimen ($a/w = 0.3$, $\beta = 45°$).

	F_I			F_{II}		
$\gamma(°) \rightarrow$	30°	60°	e_k^{avg}	30°	60°	e_k^{avg}
Ju and Chung (2007) method	1.2729	1.2917		0.8224	1.0880	
	(1.35) #	(0.91)	1.13	(0.19)	(0.27)	0.23
Liu et al. (2008) method	1.2346	1.2647		0.8282	1.0945	
	(1.70)	(1.20)	1.45	(0.51)	(0.32)	0.42
Ayatollahi and Nejati (2011a) method	1.2514	1.2746		0.8220	1.0893	
	(0.37)	(0.42)	0.40	(0.24)	(0.16)	0.20
Proposed point substitution method	1.2458	1.2720		0.8215	1.0949	
	(0.81)	(0.63)	0.72	(0.30)	(0.36)	0.33
Proposed collocation method	1.2472	1.2708		0.8178	1.0889	
	(0.70)	(0.72)	0.71	(0.75)	(0.19)	0.47
Lazzarin et al. (2010) method	1.2683	1.2856		0.8151	1.0760	
	(0.98)	(0.44)	0.71	(1.08)	(1.37)	1.23
Treifi and Oyadiji (2013c) method	1.2641	1.2860		0.8241	1.0723	
	(0.64)	(0.47)	0.56	(0.01)	(1.71)	0.86
Reference solution (Chen 1995)	1.2560	1.2800		0.8240	1.0910	

#Bracketed values are percentage relative error (e_k) with respect to Chen (1995)

Table 6.9. Comparison of F_I and F_{II} for the ADENT specimen ($a/w = 0.3$, $\beta = 45°$).

	F_I			F_{II}		
$\gamma(°) \rightarrow$	30°	60°	e_k^{avg}	30°	60°	e_k^{avg}
Ju and Chung (2007) method	0.8328 (1.31) #	0.8135 (0.93)	1.12	0.5637 (0.23)	0.7019 (0.30)	0.27
Liu et al. (2008) method	0.8106 (1.39)	0.8018 (0.52)	0.96	0.5684 (0.60)	0.7075 (0.50)	0.55
Ayatollahi and Nejati (2011a) method	0.8166 (0.66)	0.8016 (0.55)	0.61	0.5636 (0.25)	0.7032 (0.11)	0.18
Proposed point substitution method	0.8145 (0.91)	0.8004 (0.69)	0.80	0.5629 (0.37)	0.7072 (0.45)	0.41
Proposed collocation method	0.8143 (0.94)	0.7990 (0.87)	0.91	0.5606 (0.78)	0.7015 (0.36)	0.57
Lazzarin et al. (2010) method	0.8279 (0.72)	0.8091 (0.38)	0.55	0.5604 (0.81)	0.6935 (1.49)	1.15
Treifi and Oyadiji (2013c) method	0.8271 (0.62)	0.8095 (0.43)	0.53	0.5624 (0.46)	0.6898 (2.02)	1.24
Reference solution (Chen 1995)	0.8220	0.8060		0.5650	0.7040	

#Bracketed values are percentage relative error (e_k) with respect to Chen (1995)

Table 6.10. List of number of collocation nodes or points used for the mixed mode (I/II) problems.

Methods	Number of collocation points
Ju and Chung (2007) method	1791 for $\gamma = 30°$, 1633 for $\gamma = 60°$
Liu et al. (2008) method	8 for all the notch angles
Ayatollahi and Nejati (2011a) method	45 for $\gamma = 30°$, 41 for $\gamma = 60°$
Proposed point substitution method	4 for all the angles
Proposed collocation method	80 for all the angles
Lazzarin et al. (2010) method	336 for $\gamma = 30°$, 296 for $\gamma = 60°$
Treifi and Oyadiji (2013c) method	202 for $\gamma = 30°$, 178 for $\gamma = 60°$

The following observations can be made from the results presented in Tables 6.8 – 6.10 as

1. As opposed to mode I problems, noticeably large error ($e_k > 1\%$) has been observed in the computation of F_I by Ju and Chung (2007) and Liu et al. (2008) methods in both the specimens. Interestingly these two are stress-based methods. It

is worth noting from Table 6.10 that, like in the example problems of the previous sections, Ju and Chung (2007) method uses large number of sampling nodes as compared to the other methods. On the other hand, Lazzarin et al. (2010) and Treifi and Oyadiji (2013c) methods exhibited large errors in the calculation of F_{II} of both the specimens.

2. Most of the methods have shown less error in the determination of the mode II NSIF than the mode I NSIF.
3. Quite interestingly, like in the pure mode I and pure mode II problems, both the NSIFs have been computed very accurately in both the specimens by all the three displacement-based methods (i.e., 3rd, 4th and 5th methods) with the percent relative error $e_k < 1\%$.
4. All three displacement-based methods provided more accurate NSIFs than the other methods considered.
5. The highest e_k value in the displacement-based methods is 0.94% in F_I by the proposed collocation method and 0.78% in F_{II} by the proposed collocation method.
6. It is observed that in stress-based methods, the highest e_k value is 1.70% in F_I (Liu et al., 2008 method) and 0.60% in F_{II} (Liu et al., 2008 method).
7. It can be seen that in the energy-based methods, the highest e_k value is 0.98% in F_I (Lazzarin et al., 2010 method) and as high as 2.02% in F_{II} (Treifi and Oyadiji, 2013c method).
8. As may be noticed from the data of Table 6.10 that relatively very less number of nodes are used for the determination of F_I and F_{II} in the 2nd, 3rd, 4th and 5th methods as compared to the remaining methods. Nonetheless, amongst them, in the methods 3rd, 4th and 5th, though, sampled at relatively less number of nodes, they still provided very accurate mixed mode NSIFs.
9. Amongst the seven methods considered here, the proposed point substitution method employs the lowest possible number of sampling points (i.e., two points for F_I and four points for F_{II}) and nevertheless extracts very accurate mixed mode NSIFs as is evident from the results of Tables 6.8 and 6.9 for the same mesh gradation.

10. Both the proposed methods compute very accurate mixed mode NSIFs F_I and F_{II} with errors well below the 1%.

To further validate the above conclusions, among the e_k^{avg} values of a given method shown in Tables 6.8 and 6.9, the maximum value ($e_k^{\text{avg-max}}$) is selected and listed in Table 6.11. The results in Table 6.11 clearly show that the maximum of averaged errors ($e_k^{\text{avg-max}}$) in both the F_I and F_{II} are less than 1% for all the three displacement-based methods (Ayatollahi and Nejati, 2011a; and the proposed two methods). Thus, taking into account the above observations, the results presented in Table 6.11, and the requirement for acceptable accuracy in both the NSIFs, it is evident that all the three displacement-based methods have shown superior performance consistently in estimating both the NSIFs F_I and F_{II} as compared to the other methods.

Table 6.11. Maximum of averaged errors ($e_k^{\text{avg-max}}$) in F_I and F_{II}.

	$e_k^{\text{avg-max}}$	
	F_I	F_{II}
Ju and Chung (2007) method	1.31	0.27
Liu et al. (2008) method	1.45	0.55
Ayatollahi and Nejati (2011a) method	0.61	0.20
Proposed point substitution method	0.80	0.41
Proposed collocation method	0.91	0.57
Lazzarin et al. (2010) method	0.71	1.23
Treifi and Oyadiji (2013c) method	0.56	1.24

6.5 Summary

In this chapter, two stress-based, three displacement-based, and two energy-based finite element post-processing methods for the estimation of the mixed mode NSIFs have been compared to understand their performance on the same FE meshes and for the common set of example problems. The performance has been observed by keeping the conventional elements at the notch tip and following the recommendations made by each of the selected methods. Amongst, two displacement-based methods have been proposed in the present study. Pure mode I, pure mode II and mixed mode (I/II) benchmark example problems have been analyzed for the various notch angles. The results of the present study are compared with the results available in the literature. From the comparison of all the selected methods, conclusions are of practical relevance have been presented in this chapter.

Chapter 7

Conclusions and scope of future work

7.1 Summary

In this work, two simple, robust, and effective FE based methods have been developed to determine accurate mixed mode (I/II) NSIFs of the sharp V-notched 2D configurations. The main concern of the present investigation is to develop the above methods based primarily on the displacement field of the notched bodies. Particular attention is paid to propose the methods without being neglecting the rigid body displacement components from the formulation.

The first method proposed is a point substitution displacement method. In this method, an optimum point in the conventional Q8 elements that are attached to the notch flanks is found based on the least-squares minimization of the error in the notch opening and notch sliding displacement quantities. It has been shown that at this optimum point, both the displacement components and their slopes are highly accurate. Using the FE displacements at this optimum point, the mode I, mode II and mixed mode (I/II) NSIFs are calculated and compared with the available published results. To the author's knowledge, this is the first study to locate such an optimum point in the conventional Q8 elements when used in the sharp V-notch problems.

The second method developed in the present study is a collocation method. In this method, the NSIFs are determined using the notch opening and sliding displacements at the selected number of nodes along the notch flanks. The rigid body translation and the rotation components are not neglected rather nicely bypassed using a simple approach. Using this method also, the NSIFs of the various benchmark example problems have been determined and compared with the existing results. It has been observed that both methods are simple, rugged, and efficient and can be used in the existing FE codes.

A performance examination has been carried out in the present work to analyze the efficacy of the proposed two methods along with other available and widely referred methods. These methods include methods based on the FE stress, displacements, and energy. A total of seven methods have been compared on the common set of benchmark example problems and on the same meshes.

The salient conclusions from the present study have been presented categorically as general conclusions and specific conclusions. Finally, a possible extension of the present work is stated in the subsection of the scope of future work.

7.2 General conclusions

7.2.1 Conclusions from the proposed point substitution method

The point substitution method has been employed to calculate the NSIFs under mode I, mode II and mixed mode (I/II) loading of the sharp V-notched planar bodies. The results obtained using the present method are compared with the results available in the literature. Based on the results obtained, the following general conclusions have been drawn.

- The numerical results clearly establish that there exists an optimum point $\left(r_{opt} = r_{op}/L_N\right)$ in the conventional Q8 elements attached to the flanks of the sharp V-notched bodies subjected to the mode I loading.
- r_{opt} depends only on the notch angle and does not depend on the geometry of the configuration. It is obtained for the various notch angles, and interestingly its value is centered around 0.785 regardless of the notch angle.

- In the mode I problems only a strong theoretical and numerical support can be provided for the existence of r_{opt}.
- It has been observed that $v_{\theta=+\alpha}^{FE}$ (i.e., A_1) is most accurate at r_{opt} for all the notch angles and in all the example problems considered.
- Further, it has also been observed that the slope of the $v_{\theta=+\alpha}^{FE}$ along the notch flank is equal to the respective theoretical slope λ_1^I only at r_{opt} for all the notch angles.
- Convergence of the normalized mode I NSIF, F_I with the mesh refinement, has been observed.
- Results of the mode I NSIF of various benchmark problems obtained using the proposed point substitution method clearly show that an excellent agreement between the present mode I NSIFs and the available published data.
- Very accurate mode I NSIFs can be computed even on the relatively coarse meshes.
- An excellent agreement between the published results and that of the present mode II NSIF of various benchmark problems obtained using the proposed point substitution method is observed.
- Very accurate estimation of the mode II NSIFs implicitly establishes the fact that the optimum location obtained in Q8 elements for the mode I problems is also an optimum location for the mode II problems.
- Results of the mixed mode NSIFs F_I and F_{II} of various benchmark problems obtained using the proposed point substitution method clearly show that an excellent agreement between the present results and the available published data.
- Apart from matching the present results with the published ones, variation of the computed F_I and F_{II} with the notch angle and a/w is found consistent with the theoretical and published trends. This is true in the mode I, mode II and mixed mode (I/II) example problems.
- By using the optimum point(s), the NOD and NSD quantities, the present proposed method elegantly bypasses the rigid body terms.
- The results of this chapter clearly indicate that the proposed point substitution method is a simple, robust, and efficient method to determine the accurate mixed mode (I/II) NSIFs of the V-notched configurations using relatively coarse meshes and can be implemented in the existing codes.

7.2.2 Conclusions from the proposed collocation method

The proposed collocation method is applied to determine the mode I, mode II and mixed mode (I/II) NSIFs of the sharp V-notched configurations. The results of F_I and F_{II} are also compared with the available results. The conclusions from the proposed collocation method are as follows

- The rigid body terms are neatly bypassed in the mode I problems by choosing the NOD along the notch flanks for the determination of the NSIFs.
- The rigid body terms are elegantly avoided in the mode II problems by choosing two additional lines, one above the top notch flank and one below the bottom notch flank.
- It has been observed that error in the mode II NSIF can be up to 50% if the rigid body terms are forcibly neglected in the field equations.
- The plot of $\ln\left(\Delta v^{FE}\right)$ and $\ln\left(r\right)$ shows distinct linear and non-linear portions. The linear portion is in line with the theoretical prediction where the slope of the line in log-log plot is equal to λ_1^I.
- It is shown that the nodes that fall on the straight-line portion of the above graph are the valid collocation nodes.
- An approach has been suggested to automatically select 20 numbers of the valid collocation nodes without being making graphs such as $\ln\left(\Delta v^{FE}\right)$ versus $\ln\left(r\right)$.
- It is also observed that the plot of $\ln\left(\Delta u_{eff}^{FE}\right)$ and $\ln\left(r\right)$ for the mode II configurations shows a straight line with the slope equals to λ_1^{II} with 20 numbers of the valid collocation nodes.
- Similarly, the plots of $\ln\left(\Delta v^{FE}\right)$ and $\ln\left(\Delta u_{eff}^{FE}\right)$ versus $\ln\left(r\right)$ for mixed mode (I/II) specimens show linear portions with the slopes equal to λ_1^I and λ_1^{II}, respectively, with 20 numbers of the valid collocation nodes
- The results using the collocation method clearly demonstrated that the above-suggested approach infallibly provides a conservative and valid set of the collocation points for the accurate determination of the NSIFs in a relatively fine mesh.

- It is observed that the estimated NSIFs using the collocation method converge with the mesh refinement.
- The computed mode I NSIFs using the proposed collocation method on the benchmark problems have shown excellent agreement with the available published data.
- Similarly, the computed mode II and mixed mode (I/II) NSIFs (F_I and F_{II}) using the proposed collocation method on the benchmark problems have shown excellent agreement with the available published data.
- For $\gamma > 30°$, even the coarse meshes can be used for determining the NSIFs accurately. On the other hand, relatively fine meshes are needed for $\gamma \leq 30°$ due to the increase in strength of the singularity.
- Aside from matching the present results with the published ones, the variation of the computed F_I and F_{II} with the notch angle, notch inclination angle/notch location and a/w is consistent with the theoretical and published trends. This is true in the mode I, mode II and mixed mode (I/II) example problems.
- The results of the present investigation clearly demonstrate that the proposed collocation method is simple, rugged, and straightforward and can be implemented in the existing FE codes.

7.2.3 Conclusions from the comparison of methods for computation of the NSIFs

Seven post-processing methods for the determination of the NSIFs have been compared on the common problem set and on common meshes to understand the performance of each of the methods chosen. The performance has also been studied with respect to the number of sampling points employed by each method for the computation of the NSIFs F_I and F_{II}. Two stress-based, three displacement-based, and two energy-based methods are considered in the present investigation. Out of the seven methods considered, two displacement-based methods have been proposed in this study. The conclusions drawn from the comparative analysis are as follows

- Among all the methods considered, Ju and Chung (2008) method employs a large number of sampling points or nodes as compared to the remaining methods. The energy-based methods by Lazzarin et al. (2010) and Treifi and Oyadiji (2013c) also use relatively large number of sampling points for the determination of the NSIFs as compared to the displacement-based methods.
- Relatively less number of sampling points are employed by all the three displacement-based methods, viz., Ayatollahi and Nejati (2011a) method and the proposed two methods of the present work and the stress-based approach by Liu et al. (2008).
- Amongst all the methods, the proposed point substitution method employs the lowest possible number of sampling points.
- In the pure mode I problems, very accurate NSIFs have been determined by all the methods except Liu et al. (2008) method, which is a stress-based method with less number of sampling points.
- In the pure mode I problems, the relative percentage error $\left(e_k\right)$ in all the above methods except Liu et al. (2008) is found to be less than 1% for all the notch angles when compared with the published reference solution.
- Although Ju and Chung (2008) method employs the highest number of sampling points, the accuracy of this method is of the order of the displacement-based methods wherein relatively less number of sampling points or nodes are used. This aspect has been observed in the pure mode I, pure mode II and mixed-mode (I/II) benchmark example problems.
- Again in the pure mode II problems, very accurate NSIFs have been determined by all the methods except Liu et al. (2008) method, wherein the error is more than 1%. Here also conclusions that are similar to the mode I problems have been noticed.
- As opposed to the mode I and mode II problems, noticeably more error ($e_k > 1\%$) has been observed in the computation of F_I by Ju and Chung (2007) and Liu et al. (2008) methods in all the mixed mode (I/II) problems considered. On the other hand, Lazzarin et al. (2010) and Treifi and Oyadiji (2013c) methods exhibited more errors in the calculation of F_{II} in the mixed mode example problems.
- Most of the methods have shown less error in the determination of the mode II NSIF than the mode I NSIF.

- All the three displacement-based methods provided more accurate mixed mode NSIFs $(e_k < 1\%)$ than the other methods considered. This is true in all the problems considered under mixed mode (I/II) loading conditions.
- It has been observed in the displacement-based methods that the highest percentage relative error e_k is 0.94% in F_I by the proposed collocation method and 0.78% in F_{II} by the proposed collocation method.
- It has been noticed that in the stress-based methods, the highest e_k value is 1.70% in F_I (Liu et al., 2008 method) and 0.60% in F_{II} (Liu et al., 2008 method). Among the stress-based methods, Ju and Chung (2007) have extracted the mixed mode NSIFs with better accuracy than the Liu et al. (2008) method.
- It can be seen that in energy-based methods, the highest e_k value is 0.98% in F_I (Lazzarin et al., 2010 method) and as high as 2.02% in F_{II} (Treifi and Oyadiji, 2013c method).
- All the three displacement-based methods, though sampled at relatively less number of nodes, they still provided very accurate mixed mode NSIFs $(e_k < 1\%)$ in all the problems considered. This may be due to the fact that the displacement field is more accurate as compared to the stress field in the finite element solutions.
- Amongst the seven methods considered here, the proposed point substitution method employs the lowest possible number of sampling points (i.e., a single point for F_I and two points for F_{II}) and nevertheless extracts very accurate NSIFs. This has been observed in problems of pure mode I, pure mode II and mixed mode (I/II).
- Considering the accuracy in both the NSIFs F_I and F_{II}, all the three displacement-based methods have shown consistent superior performance in extraction of the NSIFs.
- Finally, both the proposed methods consistently computed very accurate NSIFs in the mode I, mode II and mixed mode loading problems with errors well below 1%.

7.3 Specific conclusions

The specific conclusions of the present investigation are summarized as

1. There exists an optimum point $\left(r_{opt} = r_{op}/L_N\right)$ in the conventional Q8 elements attached to the flanks of the sharp V-notch bodies subjected to the arbitrary in-plane loading. This point depends only on the notch angle and is independent of the geometry of the notched configuration.
2. The ratio of the radius of this optimum point to the length of the notch tip element is around 0.785 regardless of the notch angle.
3. To the author's knowledge, this is the first study to locate such an optimum point in the conventional Q8 elements used in the sharp V-notch problems.
4. The proposed point substitution displacement-based method provides highly accurate mode I, mode II and mixed mode (I/II) NSIFs for the sharp V-notched configurations though it uses very less number of sampling points.
5. The proposed displacement-based collocation method also calculates the mode I, mode II and mixed mode (I/II) NSIFs with very good accuracy.
6. Both these methods are found to be simple, robust, effective, and can be easily implemented in the existing codes. The formulations of both these methods are very general and can be used to determine the mixed mode (I/II) NSIFs of any 2D configurations under in-plane loading conditions using relatively coarse meshes.
7. It is found that the displacement-based methods viz., Ayatollahi and Nejati (2011a) method and the proposed two methods of the present work consistently provide very accurate NSIFs in the mode I, mode II and mixed mode problems. Further, they also employ relatively less number of sampling points for the determination of the NSIFs.
8. Stress-based methods, although they are free from problems introduced by the rigid body displacement terms; however, require a large number of sampling points to achieve the similar accuracy level as that of the displacement-based methods.

7.4 Scope of future work

1. On the basis of the promising results presented in the present work, the possibility of extending the proposed methods to determine the accurate NSIFs of blunt or rounded V-notches can be explored.
2. A significant future research would be the extension of the proposed methods to compute the NSIFs of the three-dimensional notched bodies.
3. Another important and practically relevant direction to extend the proposed methods is to determine the NSIFs of the sharp V-notches with curved flanks.
4. It is well-known that the quarter-point elements (QPEs) are extensively used to model the singularity at the crack tip in the computational fracture mechanics where the singularity does not change with change in the geometry of the crack. It is worth investigating the applicability of the QPEs in the sharp V-notched problems, although it seems not feasible in the current context.
5. As the engineering materials are not limited to isotropic materials, it would be a good development to extend the proposed methods to compute the NSIFs for orthotropic, bi-metallic and anisotropic materials.
6. The proposed methods could be extended to compute the plastic NSIFs of the V-notches.
7. It is of direct practical relevance to investigate whether such optimum points are available in other 2D/3D finite elements and/or other classes of linear elasticity problems in 2D and 3D. A further deeper investigation into these optimum locations is very useful.

7.5 Contributions of the present work

It is well-known that the finite element displacement field solutions are more accurate than the stress fields. This fact has been widely reflected in the case of crack fracture mechanics, wherein a large number of displacement-based methods for the accurate computation of the SIFs have been developed over the years. Indeed, many commercial software incorporated such displacement-based methods. As far as sharp V-notched problems are concerned, to the best of the author’s knowledge, very limited displacement-based methods for the computation of the NSIFs were available. One reason for the seldom use of the displacement field in the notch problems may be due to the presence of the rigid body terms in the displacement components. Due to the growing interest in the notch fracture mechanics in the last few years and due to the importance of the NSIFs in brittle fracture of the notched components, the present work develops two simple, rugged, and efficient displacement-based methods which uses less number of sampling points for the accurate determination of the NSIFs. The scientific originality of the proposed methods lies in the fact that for the first time (a) an optimum point is identified in the Q8 element where the displacements and their gradients are found to be very accurate, (b) extended the familiar definitions of the crack opening displacement (COD) and crack sliding displacement (CSD) to the notch problems in the form of notch opening displacement (NOD) and notch sliding displacement (NSD), (c) proposing a collocation approach on the notch flanks and along the lines close to the notch flanks. By using the optimum point, NOD and NSD concepts, the proposed point substitute technique elegantly bypasses the notch rigid body terms appear in the displacement field and determines very accurate NSIFs. On the other hand, by employing the NOD and NSD concepts along with the developed collocation method on the notch flanks and long the adjacent lines, the second method, viz., the collocation method determines very accurate NSIFs in all loading conditions by neatly bypassing the rigid body terms. Furthermore, review of the literature indicates that no comparison of the various published stress-based, displacement-based, and energy-based methods available till date to assess the performance of the methods for the accurate estimation of the NSIFs. Looking at the need of such comparisons, the present work attempts a reasonably exhaustive numerical comparison of the various NSIF extraction methods on the common set of benchmark problems and on the common finite element meshes and makes the useful conclusions for the researchers.

7.6 Limitations of the present work

1. The present work limits to the 2D sharp V-notched linear elastic bodies made of isotropic materials and subjected arbitrary in-plane static loads
2. The notch flanks of the V-notches are straight.
3. The methods have been developed within the context of linear elastic notch fracture mechanics.

REFERENCES

Anderson, T.L., 2015. Fracture Mechanics: Fundamentals and Applications, Third ed, Taylor and Francis, Boca Raton.

ANSYS, 2007. Theory reference manual. Release 11. Swanson Analysis Systems, Inc.

Atkinson, C., Bastero, J.M., Martínez-Esnaola, J.M., 1988. Stress analysis in sharp angular notches using auxiliary fields. Eng. Fract. Mech. 31 (4), 637–646.

Atzori, B., Lazzarin, P., Filippi, S., 2001. Cracks and notches: analogies and differences of the relevant stress distributions and practical consequences in fatigue limit predictions. Int. J. Fatigue. 23, 355–362.

Atzori, B., Lazzarin, P., Tovo, R., 1999. Stress field parameters to predict the fatigue strength of notched components. J. Strain Anal. 34 (6), 437–453.

Ayatollahi, M.R., Aliha, M.R.M., 2006. On determination of mode II fracture toughness using semi-circular bend specimen. Int. J. Solids Struct. 43, 5217–5227.

Ayatollahi, M.R., Nejati, M., 2011a. Determination of NSIFs and coefficients of higher order terms for sharp notches using finite element method. Int. J. Mech. Sci. 53 (3), 164–177.

Ayatollahi, M.R., Nejati, M., 2011b. Experimental evaluation of stress field around the sharp notches using photoelasticity. Mater. Des. 32, 561–569.

Ayatollahi, M.R., Torabi, A.R., 2010. Brittle fracture in rounded-tip V-shaped notches. Mater. Des. 31, 60–61.

Ayatollahi, M.R., Aliha, M.R.M., Saghafi, H., 2011a. An improved semicircular bend specimen for investigating mixed mode brittle fracture. Eng. Fracture Mech. 78, 110–123.

Ayatollahi, M.R., Torabi, A.R., Azizi, P., 2011b. Experimental and theoretical assessment of brittle fracture in engineering components containing a sharp V-notch. Exp. Mech. 51, 919–932.

Bahrami, B., Ayatollahi, M.R., Torabi, A.R., 2018. Predictions of fracture load, crack initiation angle, and trajectory for V-notched Brazilian disk specimens under mixed mode I/II loading with negative mode I contributions. Int. J. Damage Mech. 27(8), 1173–1191.

Bahrami, B., Ayatollahi, M.R., Torabi, A.R., 2020a. Application of digital image correlation method for determination of mixed mode stress intensity factors in sharp notches. Opt. Lasers Eng. 124, 105830.

Bahrami, B., Ayatollahi, M.R., Torabi, A.R., 2020b. In-situ brittle fracture analysis of sharp V-notched components using digital image correlation. Theor. Appl. Fract. Mec. 106, 102484.

Barroso, A, Graciani, E., Mantic, V., Paris, F., 2012. A least squares procedure for the evaluation of multiple generalized stress intensity factors at 2D multimaterial corners by BEM. Eng. Anal Bound. Elem. 36 (3), 458–470.

Barsoum, R.S., 1976. On the use of isoparametric finite elements in linear fracture mechanics. Int. J. Numer. Methods Eng. 10 (1), 25–27.

Berto, F., Lazzarin, P., Afshar, R., 2012. Simple new expressions for the notch stress intensity factors in an array of narrow V-notches under tension. Int. J. Fract. 176, 237–244.

Berto, F., Razavia, S.M.J., Ayatollahi, M.R., 2017. Some methods for rapid evaluation of the mixed mode NSIFs. Procedia Struct. Int. 3, 126–134.

Blandford, G.E., Ingraffea, A.R., Liggett, J.A., 1981. Two-dimensional stress intensity factor computations using the boundary element methods. Int. J. Numer. Meth. Eng. 17, 387–404.

Boukharouba, T., Tamine, T., Niu, L., Chehimi, C., Pluvinage, G., 1995. The use of notch stress intensity factor as a fatigue crack initiation parameter. Eng. Fract. Mech. 52 (3) 503–512.

Carpenter, W.C., 1984a. A collocation procedure for determining fracture mechanics parameters at a corner. Int. J. Fract. 24 (4), 255–266.

Carpenter, W.C., 1984b. Calculation of fracture mechanics parameters for a general corner. Int. J. Fract. 24, 45–58.

Carpenter, W.C., 1984c. Mode I and mode II stress intensities for plates with cracks of finite opening. Int. J. Fract. 26 (3), 201–214.

Carpinteri, A., 1987. Stress-singularity and generalized fracture toughness at the vertex of re-entrant corners. Eng. Fract. Mech. 26 (1), 143–155.

Carpinteri, A., Cornetti, P., Pugno, N., Sapora, A., Taylor, D., 2008. A finite fracture mechanics approach to structures with sharp V-notches. Eng. Fract. Mech. 75, 1736–1752.

Chang, J.H., Fan, J.F., 2009. Evaluation of mixed-mode stress intensity factors for a sharp notch-tip with curved and stressed edges. J. Appl. Mech. 76, 031004-1-9.

Chang, J.H., Kang, L.K., 2002. Evaluation of the stress field around a notch tip using contour integrals. Int. J. Eng. Sci. 40 (5), 569–586.

Chang, J.H., Wu, W.H., 2003. Calculation of mixed-mode stress field at a sharp notch tip using $M_{1\varepsilon}$ −integral. Comput. Mech. 31, 419–427.

Chen, D.H., 1995. Stress intensity factors for V-notched strip under tension or in-plane bending. Int. J. Fract. 70 (1), 81–97.

Cheng, C., Ge, S., Yao, S., Niu, Z., 2016. Thermal stress singularity analysis for V-notches by natural boundary element method. Appl. Math. Model. 40 (19–20), 8552–8563.

Cheng, C., Niu, Z., Zhou, H., Recho, N., 2009. Evaluation of multiple stress singularity orders of a V-notch by the boundary element method. Eng. Anal Bound. Elem. 33 (10), 1145–1151.

Dehnavi, M.R.Y., Eshraghi, I., Soltani, N., 2013. Investigation of fracture parameters of edge V-notches in a polymer material using digital image correlation. Polym. Test. 32, 778-784.

Dunn, M.L., Suwito, W., 1997. Cunningham S. Fracture initiation at sharp notches: Correlation using critical stress intensities. Int. J. Solids Struct. 34 (29), 3873–3883.

Dunn, M.L., Suwito, W., Cunningham, S., 1997b. Stress intensities at notch singularities. Eng. Fract. Mech. 57 (4), 417–430.

Dunn, M.L., Suwito, W., Cunningham, S., May, C.W., 1997a. Fracture initiation at sharp notches under mode I, mode II, and mild mixed mode loading. Int. J. Fract. 84 (4), 367–381.

Erdogan, F. Sih, G.C., 1963. On the crack extension in plates under plane loading and transverse shear. J. Basic Eng. ASME 85(4), 519–525.

Espion, B., 2012. The Vierendeel bridges over the Albert Canal, Belgium – their significance in the story of brittle failures. Steel Constr. 5 (4), 238–243.

Fischer, C., Feltz, O., Fricke W., Lazzarin, P., 2011. Application of the notch stress intensity and crack propagation approaches to weld toe and root fatigue. World Weld. 55, 30–39.

Fischer, C., Fricke W., Rizzo, C.M., 2012. N-SIF based fatigue assessment of hopper knuckle details. Sustainable Maritime Transportation and Exploitation of Sea Resources, Rizzuto & Guedes Soares (eds.) At: London: Taylor & Francic Group.

Fischer, C., Fricke, W., Rizzo, C.M., 2016a. Experiences and recommendations for numerical analyses of notch stress intensity factor and averaged strain energy density. Eng. Fract. Mech. 165, 98–113.

Fischer, C., Fricke, W., Rizzo, C.M., 2016b. Review of the fatigue strength of welded joints based on the notch stress intensity factor and SED approaches. Int. J. Fatigue. 84, 59–66.

Gomez, F.J., Elices, M., 2003. Fracture of components with V-shaped notches. Eng. Fract. Mech. 70, 1913–1927.

Griffith, A.A., 1920. The phenomena of rupture and flow in solids. Philos. Trans. Royal Soc. A. 221, 163–198.

Gross, B., Mendelson, A., 1972. Plane elastostatic analysis of V-notched plates. Int. J. Fract. Mech., 8 (3), 267–276.

Gross, B., Srawley, J.E., 1965. Stress intensity factors of three point bend specimens by boundary collocation. NASA Technical Note D-2603.

Han, Z., Cheng, C., Yao, S., Niu, Z., 2019. Determination of stress intensity factors of V-notch structures by characteristic analysis coupled with isogeometric boundary element method. Eng. Fract. Mech. 222, 106717.

Hart, D.J., 1976. A note on the plate width and notch angle correction factors for single edge V-notched plates in tension. Eng. Fract. Mech. 8, 47–48.

Hartranft, R.J., Sih, G.C., 1968. Effect of plate thickness on the bending stress distribution around through cracks. J. math. Phys. 47, 276–291.

Hartranft, R.J., Sih, G.C., 1969. The use of eigen function expansions in the general solution of three dimensional crack problems. J. Math. Mech. 19, 123–138.

Hasebe, N., Kutanda, Y., 1978. Calculation of stress intensity factor from stress concentration factor. Eng. Fract. Mech. 10, 215–221.

Henshel, R.D., Shaw, K.G., 1976. Crack tip finite elements are unnecessary. Int. J. Numer. Methods Eng. 9, 495–507.

Horn, A.J.V., Wilso, R., 1977. The potential risks of liquefied natural gas. Energy J. 2, 375–389.

Hu, Y., Yan R., Shen W., Liu, K., 2019. Notch stress analysis and fatigue strength assessment of tube-flange welded joints under torsion loading. Ocean Eng. 186, 106074.

Hwu, C., Kuo, T.L., 2007. A unified definition for stress intensity factors of interface corners and cracks. Int. J. Solids Struct. 44, 6340–6359.

Inglis, C.E., 2013. Stresses in a plate due to the presence of cracks and sharp croners. Transactions of the Royal Institution of Naval Architects. 60, 219–241.

Irwin, G.R., 1948. Fracture dynamics, Fracture of metals. American Society for Metals, Cleveland. 147–166.

Irwin, G.R., 1957. Analysis of stresses and strains near the end of a crack traversing a plate. J. Appl. Mech. 24, 361–364.

Irwin, G.R., 1958. Fracture, handbuch der physic. S. Flugge (ed.), Springer-Verlag, Berlin, 6, 551–590.

Ju, S.H., 2010. Calculation of notch H-integrals using image correlation experiments. Exp. Mech. 50, 517–525.

Ju, S.H., Chung, H.Y., 2007. Accuracy and limit of a least-squares method to calculate 3D notch SIFs. Int. J. Fract. 148 (2), 169–183.

Ju, S.H., 2014. A hybrid analytical–numerical solution for 3D notched plates. Int. J. Solids Struct. 51, 4113–4121.

Kim, J.K., Cho, S.B., 2009. Effect of second non-singular term of mode I near the tip of a V-notched crack. Fatigue Fract. Eng. Mater. Struct. 32 (4), 346–356.

Knesl, Z., 1991. A criterion of V-notch stability. Int. J. Fract. 48, R79-R83.

Kobayashi, A.S., Cherepy, R.B., and Kinsel, W.C., 1964. A numerical procedure for estimating the stress intensity factor of a crack in a finite plate. J. Basic Eng. Vol. 86, 681–684.

Kondo, T., Kobayashi, M., Sekine, H., 2001. Strain gage method for determining stress intensities of sharp-notched strips. Exp. Mech. 41 (1), 1–7.

Kondo, T., Kurabe, Y., Sasaki, T., Kurahashi, T., Miyashita, Y., 2014. Use of strain gages for determining generalized stress intensity factors of sharp V-notched plates under transverse bending. Eng. Fract. Mech. 124-125, 248–261.

Kundu, T., 2008. Fundamentals of fracture mechanics. CRC Press, Taylor & Francis Group, Boca Raton.

Labossiere, P.E.W., Dunn, K.L., 1998. Calculation of stress intensities at sharp notches in anisotropic media. Eng. Fract. Mech. 61 (5-6), 635–654.

Larrosa, N.O., Treifi, M., Ainsworth, R.A., 2015. Rapid parametric analysis of SEN(T) specimens using algorithmic modelling: Evaluation of strain energy density and notch stress intensity factors. Mater. Des. 85, 771–777.

Lazzarin, P., Berto, F., 2005. Some expressions for the strain energy in a finite volume surrounding the root of blunt V-notches. Int. J. Fract.135, 161–185.

Lazzarin, P., Berto, F., Zappalorto, M., 2010. Rapid calculations of notch stress intensity factors based on averaged strain energy density from coarse meshes: Theoretical bases and applications. Int. J. Fatigue. 32 (10), 1559–1567.

Lazzarin, P., Filippi, S., 2006. A generalized stress intensity factor to be applied to rounded V-shaped notches. Int. J. Solids Struct. 43, 2461–2478.

Lazzarin, P., Livieri, P., 2001. Notch stress intensity factors and fatigue strength of aluminium and steel welded joints. Int. J. Fatigue. 23 (3), 225–232.

Lazzarin, P., Tovo, R., 1998. A notch intensity factor approach to the stress analysis of welds. Fatigue Fract. Eng. Mater. Struct. 21 (9), 1089–1103.

Lazzarin, P., Zambardi, R., 2001. A finite-volume-energy based approach to predict the static and fatigue behavior of components with sharp V-shaped notches. Int. J. Fract. 112, 275–298.

Lazzarin, P., Zambardi, R., 2002. The equivalent strain energy density approach reformulated and applied to sharp V-shaped notches under localised and generalised plasticity. Fatigue Fract. Eng. Mater. Struct. 25, 917–928.

Lazzarin, P., Zappalorto, M., 2008. Plastic notch stress intensity factors for pointed V-notches under antiplane shear loading. Int. J. Fract. 152, 1–25.

Leguillon, D., Yosibash, Z., 2003. Crack onset at a v-notch. Influence of the notch tip radius. Int. J. Solids Struct., 122, 1–21.

Leguillon, D., Yosibash, Z., 2017. Failure initiation at V-notch tips in quasi-brittle materials. Int. J. Solids Struct., 122, 1–13

Lepore, M., Solberg, K., Berto, F., 2019. A comparison between numerical and approximate methods for rapid calculation of NSIFs. Theor. Appl. Fract. Mec. 101, 67–79.

Liu, Y., Wu, Z., Liang, Y., Liu, X., 2008. Numerical methods for determination of stress intensity factors of singular stress field. Eng. Fract. Mech. 75 (16), 4793–4803.

Livieri, P., 2003. A new path independent integral applied to notched components under mode I loadings. Int. J. Fract. 123, 107–125.

Livieri, P., Lazzarin, P., 2005. Fatigue strength of steel and aluminium welded joints based on generalised stress intensity factors and local strain energy values. Int. J. Fract. 33, 247–276

Loua, B., Barltrop, N., 2020. Universal hybrid method and approximate closed-form solution for V-notched and V-notch-cracked plate under tensile and in-plane bending. Theor. Appl. Fract. Mec. 108, 102579.

Mahinfalah, M., Zackery, L., 1995. Photoelastic determination of mixed mode stress intensity factors for sharp reentrant corners. Eng. Fract. Mech. 52 (4), 639–645.

MATLAB, 2015. The MathWorks Inc., Natick, USA.

Mehraban, M.R., Ayatollahi, M.R., Bahrami, B., Berto, F., 2021. Higher order stress terms in sharp notch problems under pure-out-of-plane loading. Fatigue Fract. Eng. Mater. Struct. 1–14.

Meneghetti, G., 2012. The use of peak stresses for fatigue strength assessments of welded lap joints and cover plates with toe and root failures. Eng. Frac. Mech. 89, 40–51.

Meneghetti, G., Campagnolo, A., Avalle, M., et al., 2018. Rapid evaluation of notch stress intensity factors using the peak stress method: Comparison of commercial finite element codes for a range of mesh patterns. Fatigue Fract. Eng. Mater. Struct. 41 (5), 1044–1063.

Meneghetti, G., Guzzella, C., 2014. The peak stress method to estimate the mode I notch stress intensity factor in welded joints using three-dimensional finite element models. Eng. Fract. Mech. 115, 154–171.

Meneghetti, G., Lazzarin, P., 2007. Significance of the elastic peak stress evaluated by FE analyses at the point of singularity of sharp V-notched components. Fatigue Fract. Eng. Mater. Struct. 30, 95–106.

Minora, H.E., Kifani, A., Louah, M. Azari, Z., Pluvinage, G., 2003. Fracture toughness of high strength steel—using the notch stress intensity factor and volumetric approach. Struct. Saf. 25 (1), 35–45.

Mohammadi, H., Salavati, H., Alizadeh, Y., Berto, F., Panin, S.V., 2017. Fracture investigation of V-notch made of tungsten-copper functionally graded materials. Phys. Mesomech. 20 (4), 457–464.

Murthy, S.N., Rakesh, N., Srinath, L.S., 1983. Effect of specimen thickness on mode I stress intensity factor in photoelastic investigations. Eng. Fract. Mech. 18 (6), 1201–1205.

Murthy, S.N., Rao, P.R., 1985. Determination of mode 1 notch stress intensity factor by the photoelastic technique. Eng Fract Mech. 21, 557–562.

Niu, Z., 1993. Nonlinear bending of the shallow spherical shells with variable thickness under axisymmetrical loads. Appl. Math. Mech. 14 (11), 1023–1031.

Niu, Z., Cheng, C., Ye, J., Recho, N., 2009. A new boundary element approach of modeling singular stress fields of plane V-notch problems. Int. J. Solids Struct. 46 (16), 2999-3008.

Noda, N.A., Oda, K., Inoue, T., 1996. Analysis of newly-defined stress intensity factors for angular corners using singular integral equations of the body force method. Int. J. Fract. 76 (3), 243–261.

Noda, N.A., Takase, Y., 2003. Generalized stress intensity factors of V-shaped notch in a round bar under torsion, tension, and bending. Eng. Fract. Mech. 70 (11), 1447–1466.

Paris, P.C., Gomez, M.P., Anderson, W.E., 1961. A rational analytic theory of fatigue. Trends. Eng. 13, 9–14.

Paul, P., Murthy, K.S.R.K., Chakraborty, D., 2018. A strain gage technique for mode I notch stress intensity factor of sharp V-notched configurations. Theor. Appl. Fract. Mec. 94, 57–70.

Pittarello, L., Campagnolo, A., Berto, F., 2016. NSIFs estimation based on the averaged strain energy density under in-plane mixed mode loading. Procedia Struct. Int. 2, 1829–1836.

Portela, A., Aliabadi, M.H., Rooke, D.P., 1991. Efficient boundary element analysis of sharp notched plates. Int. J. Numer. Methods Eng. 32 (3), 445–470.

Prassianakis, J.N., Theocaris, P.S., 1980. Stress intensity factors at V-notched elastic, symmetrically loaded, plates by the method of caustics. J. Phys. D: Appl. Phys. 13, 1043–1053.

Press, W.H., Flannery, B.P., Teukolsky, S.A., Vettenling, W.T., 2007. Numerical recipes, the art of scientific computing, third ed., Cambridge University Press, New York.

Razavi, S.M.J., Ferro, P., Berto, F., Torgersen, J., 2018. Fatigue strength of blunt V-notched specimens produced by selective laser melting of Ti-6Al-4V. Theor. Appl. Fract. Mech. 97, 376–384.

Reed, K., 2016. Equipment Failure: Crane Gearbox Failure. https://www.taproot.com/equipment-failure-crane-gearbox-failure/ (accessed 14 January 2021).

Rezaee, A., Adnan, A., 2018. On the elastic stress singularities and mode I notch stress intensity factor for 3D printed polymers. Eng. Fract. Mech. 204, 235–245.

Reitz, W., 2013. Failure of bolt threads exposed to shear stress. J. Fail. Anal. Prev. 13, 551–554.

Sanford, R.J., 1980. Application of the least squares method to the photoelastic analysis. Exp. Mech. 20 (6), 192–197.

Savruk, M. P., Kazberuk A., 2007. A unified approach to problems of stress concentration near V-shaped notches with sharp and rounded tip. Int. Appl. Mech.. 43 (2), 182-197.

Savruk, M. P., Kazberuk A., 2009. Problems of fracture mechanics of solid bodies with V-shaped notches. Mater. Sci. 45, 162–180.

Savruk, M. P., Kazberuk A., 2010. Two-dimensional fracture mechanics problems for solids with sharp and rounded V-notches. Int. J. Fract. 161, 79–95.

Savruk, M. P., Kazberuk A., 2017. Stress concentration at notches. Springer International Publishing.

Seweryn, A., 1994. Brittle fracture criterion for structures with sharp notches. Eng. Fract. Mech. 47 (5), 673–681.

Seweryn, A., 2002. Modeling of singular stress fields using finite element method. Int. J. Solids Struct. 39 (18), 4787–4804.

Seweryn, A., Mroz, Z., 1995. A non-local stress failure condition for structural elements under multiaxial loading. Eng. Fract. Mech. 51 (6), 955–973.

Seweryn, A., Molski, K., 1996. Elastic stress singularities and corresponding generalized stress intensity factors for angular corners under various boundary conditions. Eng. Fract. Mech. 55 (4), 529–556.

Seweryn, A., Poskrobko, S., Mroz, Z., 1997. Brittle fracture in plane elements with sharp notches under mixed-mode loading. J. Eng. Mech. 123 (6), 535–543.

Sih, G.C., 1974a. Strain-energy-density factor applied to mixed mode crack problems. Int. J. Fract. 10 (3), 305–321.

Sih, G.C., Macdonald, B., 1974b. Fracture mechanics applied to engineering problems-strain energy density fracture criterion. Eng. Fract. Mech. 6, 361–386.

Sinclair, G.B., Okajima, M., Griffin, J.H., 1984. Path independent integrals for computing stress intensity factors at sharp notches in elastic plates. Int. J. Numer. Methods Eng. 20 (6), 999–1008.

Stern, M., Soni, M.L., 1976. On the computation of stress intensities at fixed-free corners. Int. J. Solids Struct. 12, 331–337.

Stojceveski, F., Hendlmeier, A., Randall, J.D., Arnold, C.L., Stanfield, M.K., Eyckens, D.J., Alexander, R., Henderson, L.C., 2018. Effect of tow size and interface interaction on interfacial shear strength determined by iosipescu (V-Notch) testing in epoxy resin. Materials. 11 (9), 1786.

Tanaka, K., 1974. Fatigue crack propagation from a crack inclined to the cyclic tensile axis. Eng. Fract. Mech. 6, 493–507.

Timoshenko, S.P., Goodier, J.N., 1970. Theory of Elasticity. McGraw-Hill, Third Ed., New York.

Tomari, K., Tonogai, S., Harada, T., et al., 1990. The V-notch at weld lines in polystyrene injection moldings. Polym. Eng. Sci. 30 (15), 931–936.

Torabi, A.R., 2012. Estimation of tensile load-bearing capacity of ductile metallic materials weakened by a V-notch: The equivalent material concept. Mater. Sci. Eng. A. 536, 249–255.

Torabi, A.R., Bahrami, B., Ayatollahi, M.R., 2019. Experimental determination of the notch stress intensity factor for sharp V-notched specimens by using the digital image correlation method. Theor. Appl. Fract. Mec.103, 102244.

Treifi, M., 2012. Fractal-like finite element method and strain energy approach for computational modelling and analysis of geometrically V-notched plates. PhD Thesis Desertation. School of Mechanical, Aerospace and Civil Engineering, University of Manchester, UK.

Treifi, M., Oyadiji, S.O., 2013a. Bi-material V-notch stress intensity factors by the fractal-like finite element method. Eng. Fract. Mech. 105, 221–237.

Treifi, M., Oyadiji, S.O., 2013b. Evaluation of mode III stress intensity factors for bi-material notched bodies using the fractal-like finite element method. Comput. Struct. 129, 99–110.

Treifi, M., Oyadiji, S.O., 2013c. Strain energy approach to compute stress intensity factors for isotropic homogeneous and bi-material V-notches. Int. J. Solids Struct. 50 (14-15), 2196–2212.

Treifi, M., Oyadiji, S.O., Tsang, D.K.L., 2008. Computations of modes I and II stress intensity factors of sharp notched plates under in-plane shear and bending loading by the fractal-like finite element method. Int. J. Solids Struct. 45 (25-26), 6468–6484.

Treifi, M., Oyadiji, S.O., Tsang, D.K.L., 2009a. Computation of the stress intensity factors of sharp notched plates by the fractal-like finite element method. Int. J. Numer. Meth. Engng. 77, 558–580.

Treifi, M., Oyadiji, S.O., Tsang, D.K.L., 2009b. Computations of the stress intensity factors of double-edge and centre V-notched plates under tension and anti-plane shear by the fractal-like finite element method. Eng. Fract. Mech. 76, 2091–2108.

Tutluoglu. L., Keles, C., 2011. Mode I fracture toughness determination with straight notched disk bending method. Int. J. Rock Mech. Min. Sci. 48, 1248–1261.

Verreman, Y., Nie, B., 1996. Early development of fatigue cracking at manual fillet welds. Fatigue Fract. Eng. Mater. Struct. 19 (6), 669–681.

Westergaard, H.M., 1939. Bearing pressures and cracks. J. Appl. Mech. 61, 49–53.

Williams, M.L., 1952. Stress singularities resulting from various boundary conditions in angular corners of plates in extension. J. Appl. Mech. 19 (4), 526–528.

Williams, M.L., 1957. On the stress distribution at the base of a stationary crack. J. Appl. Mech. 24, 109–114.

Xu, Z.Q., Liu, Y.H., Wang, X.G., 1999. Numerical methods for the determination of multiple stress singularities and related stress intensity coefficients. Eng. Fract. Mech. 63, 775–790.

Xu, W., Yao, X.F., Xua, M.Q., Jin, G.C., Yeh, H.Y., 2004. Fracture characterizations of V-notch tip in PMMA polymer material. Polym. Test. 23, 509–515.

Yang, Y., Pan, W., Yao, S., Cheng, C., Wu, Q., 2021. Analysis of the non-singular stress terms for the sharp notches under anti-plane loading. Eng. Fract. Mech. 245, 107583.

Yao, X.F., Yeh, H.Y., Xu, W., 2006. Fracture investigation at V-notch tip using coherent gradient sensing (CGS). Int. J. Solids Struct. 43, 1189–1200.

Yazdanmehr, A., Soltani, N., 2014. Evaluation of stress intensity factors of rounded V and U notches under mixed mode loading, using the experimental method of caustics. Theor. Appl. Fract. Mec. 74, 79–85.

Yi, G., Yu, T., Bui, T.Q., Tanaka, S., 2018. Bi-material V-notched SIFs analysis by XFEM and conservative integral approach. Comput. Struct. 196, 217–232.

Yi, G., Yu, T., Quoc, T., Ma, C., Hirose, S., 2017. SIFs evaluation of sharp V-notched fracture by XFEM and strain energy approach. Theor. Appl. Fract. Mec. 89, 35–44.

Yu, T., Shi, L., 2012. Determination of sharp V-notch stress intensity factors using the extended finite element method. J. Strain Anal. Eng. Des. 47(2), 95–103.

Zappalorto, M., 2019. Mode I generalised stress intensity factors for rounded notches in orthotropic plates. Theor. Appl. Fract. Mech. 101, 356–364.

Zappalorto, M., Carraro, P.A., 2020. An efficient energy-based approach for the numerical assessment of mode I NSIFs in isotropic and orthotropic notched plates. Theor. Appl. Fract. Mec. 108, 102612.

Zappalorto, M., Lazzarin, P., Berto, F., 2009. Elastic notch stress intensity factors for sharply V-notched rounded bars under torsion. Eng. Fract. Mech. 76, 439–453.

Zappalorto, M., Ricotta, M., 2019. Effect of material orthotropy on the notch stress intensity factors of sharp V-notched plates under tension, Theor. Appl. Fract. Mech. 104, 102375.

Zhang, J., Dong, Y., Ju, C., Lin, W., 2018. A new singular element for evaluating stress intensity factors of V-shaped notches under mixed mode load. Eng. Anal Bound. Elem. 93, 161–166.

Zhang, J., Lin, W., Dong, Y., Ju, C., 2017. A double-layer interpolation method for implementation of BEM analysis of problems in potential theory. Appl. Math. Model. 51, 250–269.

Zhao, B., Fuyuan, L., Qingtong, W., 1988. Determining K_I of a V-notch from the existing results of a linear crack. Eng. Fract. Mech. 31 (6) 923–929.

Zhao, Z., Hahn, H.G., 1991. A path independent integral for computing stress intensities of V-notched cracks and mixed-mode problems. Int. Conf. MMFF, Vienna, Austria.

Zhao, Z., Hahn, H.G., 1992. Determining the SIF of a V-notch from the results of a mixed-mode crack. Eng. Fract. Mech. 43 (4), 511–518.

LIST OF PUBLICATIONS

Journal publications

1. **M. K. Hussain** and K. S. R. K. Murthy (2018). A point substitution displacement technique for estimation of elastic notch stress intensities of sharp V-notched bodies, ***Theoretical and Applied Fracture Mechanics***, 97:87-97.

2. **M. K. Hussain** and K. S. R. K. Murthy (2019). Calculation of mixed mode (I/II) stress intensities at sharp V-notches using finite element notch opening and sliding displacements, ***Fatigue & Fracture of Engineering Materials & Structures***, 42(5):1130-1147.

3. **M. K. Hussain** and K. S. R. K. Murthy (2019). Evaluation of mixed mode (I/II) notch stress intensity factors of sharp V-notches using point substitution displacement technique, ***Frattura ed Integrità Strutturale***, 13(48):599-610.

4. **M. K. Hussain** and K. S. R. K. Murthy. Comparison of different methods for estimating the notch stress intensities at sharp V-notches, ***Journal of Mechanics of Materials and Structures*** (*In Press*).

5. **M. K. Hussain** and K. S. R. K. Murthy. A review on the determination of notch stress intensity factors of sharp V-notches (**Under preparation**).

Book chapter publications

1. **M. K. Hussain** and K. S. R. K. Murthy (2020). Numerical examination of sharp V-notches using notch-flank displacement collocation method. In: L. Li, D. Pratihar, S. Chakrabarty, P. Mishra (eds) *Advances in Materials and Manufacturing Engineering*. Lecture Notes in Mechanical Engineering. Springer, Singapore; 329-335.

2. **M. K. Hussain** and K. S. R. K. Murthy (2021). Calculation of NSIFs and shape factors of four-point bend specimens containing sharp V-notches, In: S. K. Saha, M. Mukherjee (eds) *Recent Advances in Computational Mechanics and Simulations*. Lecture Notes in Mechanical Engineering. Springer, Singapore; 133-140.

Conference publications

1. **M. K. Hussain** and K. S. R. K. Murthy (2018). Determination of notch stress intensity factors of sharp V-notches by least-squares method, *National Conference on Shipbuilding & Offshore Engineering*, 23rd March, Academy of Marine Education and Training (AMET), Chennai.

2. **M. K. Hussain** and K. S. R. K. Murthy (2018). Numerical estimation of notch stress intensity factors of sharp V–notches, *3rd International Conference on Design, Analysis, Manufacturing & Simulation* (ICDAMS-2018), 6-7 April, Saveetha School of Engineering, Chennai.

3. **M. K. Hussain** and K. S. R. K. Murthy (2018). Comparison of some least-squares methods for evaluation of the notch stress intensities of sharp V-notched configurations, *3rd International Conference on Advances in Materials and Manufacturing Applications* (IConAMMA-2018), 16-18 August, Amrita School of Engineering, Bengaluru.

4. **M. K. Hussain** and K. S. R. K. Murthy (2018). Evaluation of notch stress intensities at sharp V-notches using a point substitution method, *Second International Conference On Structural Integrity* (ICONS-2018), 14-17 December, Indian Institute of Technology Madras, Chennai.

5. **M. K. Hussain** and K. S. R. K. Murthy (2019). Numerical examination of sharp V-notches using notch-flank displacement collocation method, *International Conference on Advances in Material and Manufacturing Engineering* (ICAMME-2019), 15-17 March, Kalinga Institute of Industrial Technology, Bhubaneshwar.

6. **M. K. Hussain** and K. S. R. K. Murthy (2019). NSIFs of 2D Elastic Bodies with Straight and Curved Sharp V-Notches. *1st International Conference on manufacturing, material science and engineering* (ICMMSE-2019), 16-17 August, CMR Institute of Technology, Hyderabad.

7. **M. K. Hussain** and K. S. R. K. Murthy (2019). Calculation of NSIFs and shape factors of four-point bend specimens containing sharp V-notches, *7th International Congress on Computational Mechanics and Simulation* (ICCMS 2019), 11-13 December, Indian Institute of Technology Mandi, Mandi.

8. **M. K. Hussain** and K. S. R. K. Murthy (2021). Mixed mode (I/II) notch stress intensities at sharp V-notches under in-plane shear and bending loading, *12th International Conference on Structural Integrity and Failure* (SIF2021), 6-7 December, Monash University, Melbourne, Australia.

About the author

Mirzaul Karim Hussain is the elder son of Mr. Moslem Hussain and Ms. Merina Hussain. He completed his Class-X from Board of Secondary Education, Assam and Class-XII from Assam Higher Secondary Education Council, securing 1st division in both the examinations. He completed his Bachelor of Engineering (B.E.) in Mechanical Engineering, securing 1st class from Gauhati University in the year 2010. He completed his Master of Technology (M.Tech) in Mechanical Engineering (Machine Design) from Indian Institute of Technology Guwahati in the year 2013. He joined Mechanical Engineering Department at Indian Institute of Technology Guwahati as a regular research scholar in the year 2014. His areas of academic interest are computational fracture mechanics, notch fracture mechanics, error estimation, finite element method, etc.